

2000

FUNDAMENTAL STUDIES OF INTERFERENCES IN ICP - MS

ROWLEY, LINDA KATHLEEN

<http://hdl.handle.net/10026.1/1918>

<http://dx.doi.org/10.24382/4432>

University of Plymouth

All content in PEARL is protected by copyright law. Author manuscripts are made available in accordance with publisher policies. Please cite only the published version using the details provided on the item record or document. In the absence of an open licence (e.g. Creative Commons), permissions for further reuse of content should be sought from the publisher or author.

**FUNDAMENTAL STUDIES OF INTERFERENCES IN
ICP - MS**

By

LINDA KATHLEEN ROWLEY, BSc (Hons), MSc

A thesis submitted to the University of Plymouth

in partial fulfilment for the degree of

DOCTOR OF PHILOSOPHY

Department of Environmental Sciences

Faculty of Science

In collaboration with

VG Elemental, Winsford, Cheshire

November 2000

90 0470386 4



UNIVERSITY OF PLYMOUTH	
Item No.	9004703864
Date	11 JUL 2001 S
Class No.	543.0858 ROW
Cont. No.	X70427865X
PLYMOUTH LIBRARY	

LIBRARY STORE

REFERENCE ONLY

ABSTRACT

FUNDAMENTAL STUDIES OF INTERFERENCES IN ICP - MS

Linda Kathleen Rowley

Methods of temperature measurement by mass spectrometry have been critically reviewed. It was concluded that the most appropriate method depended critically on the availability of fundamental data, hence a database of fundamental spectroscopic constants, for diatomic ions which cause interferences in ICP-MS, was compiled. The equilibration temperature, calculated using the different methods and using various diatomic ions as the thermometric probes, was between c.a. 400 – 10,000 K in the central channel, and between c.a. 600 – 16,000 K when the plasma was moved 1.8 mm off-centre. The wide range in temperature reflected the range of temperature measurement methods and uncertainty in the fundamental data.

Optical studies using a fibre optic connected to a monochromator were performed in order to investigate the presence of interferences both in the plasma and the interface region of the ICP-MS, and the influence of a shielded torch on these interferences. It was possible to determine the presence of some species in the plasma, such as the strongly bound metal oxides, however, no species other than OH were detected in the interface region of the ICP-MS. The OH rotational temperature within the interface region of the ICP-MS was calculated to be between 2,000 – 4,000 K.

The effect of sampling depth, operating power, radial position and solvent loading, with and without the shielded torch, on the dissociation temperature of a variety of polyatomic interferences was investigated. These calculated temperatures were then used to elucidate the site of formation for different polyatomic interferences. Results confirmed that strongly bound ions such as MO^+ were formed in the plasma, whereas weakly bound ions such as ArO^+ were formed in the interface region due to gross deviation of the calculated temperatures from those expected for a system in thermal equilibrium.

CONTENTS

Title	i
Abstract	ii
Contents	iii
List of Figures	ix
List of Tables	xv
List of Abbreviations	xvii
Acknowledgements	xxii
Authors Declaration	xxiii
CHAPTER 1: INTRODUCTION	1
1.1: General Introduction	2
1.1.1: History and Development of ICP - MS	2
1.1.2: The Inductively Coupled Plasma - Mass Spectrometer:	
System Set - up and Operation	3
1.1.2.1: Forming and Sustaining the Plasma	6
1.1.2.2: Sample Introduction	7
1.1.2.3: Detection	11
1.1.3: Strengths and Weaknesses of ICP - MS	14
1.1.4: Applications of ICP - MS	17
1.2: Interferences in ICP - MS	18
1.2.1: Spectroscopic Interferences	18
1.2.1.1: Isobaric Interferences	18
1.2.1.2: Doubly Charged Species	20
1.2.1.3: Polyatomic Ion Interferences	21

1.2.2: Methods for Removing Interferences	23
1.2.2.1: Multivariate Correction Methods	23
1.2.2.2: Alternative Sample Preparation Methods	24
1.2.2.3: Alternative Sample Introduction Methods	27
1.2.2.4: Instrumental Methods	29
1.2.3: Non-Spectroscopic Interferences	39
1.3: Fundamental Studies	41
1.3.1: Excitation Mechanisms	42
1.3.1.1: Formation Mechanisms of Analyte Ions	42
1.3.1.2: Formation Mechanisms of Molecular Ions	45
1.3.2: Ion Sampling and Formation of Secondary Discharge	47
1.3.2.1: Ion Sampling	47
1.3.2.2: Formation of the Secondary Discharge	49
1.4: Aims of Study	51
CHAPTER 2: EXPERIMENTAL	52
2.1: Instrumentation	53
2.1.1: PlasmaQuad 2+ ICP - MS	53
2.1.2: PlasmaQuad 3 ICP - MS	54
2.2: Reagent Preparation	56
CHAPTER 3: PRELIMINARY OPTICAL STUDIES	57
3.1: Introduction	58
3.2: Experimental	58
3.2.1: Plasma Studies (Effect of Sampling Depth)	58
3.2.2: Interface Studies (Effect of Power)	62

3.3: Results and Discussion	65
3.3.1: Plasma Studies (Effect of Sampling Depth)	65
3.3.2: Interface Studies (Effect of Power)	73
3.3.2.1: OH Rotational Temperature	75
3.4: Conclusions	77

CHAPTER 4: CRITICAL COMPARISON OF TEMPERATURE

DETERMINATION METHODS BY ICP - MS	79
4.1: Introduction	80
4.1.1: Ionisation Temperature	81
4.1.2: Dissociation Temperature	83
4.2: Experimental	84
4.3: Results and Discussion	85
4.3.1: Radial Profile of ArX^+ and MO^+ Species	85
4.3.2: Temperature Determination	90
4.3.2.1: Method A	90
4.3.2.2: Method B	94
4.3.2.3: Method C	98
4.3.2.4: Method D	105
4.3.2.5: Method E	108
4.4: Conclusions	111
4.4.1: Method A	111
4.4.2: Method B	112
4.4.3: Method C	112
4.4.4: Method D	113
4.4.5: Method E	114

4.4.6: Overall Conclusions	114
----------------------------	-----

CHAPTER 5: EFFECT OF SAMPLING DEPTH ON POLYATOMIC IONS AND THEIR DISSOCIATION TEMPERATURES

118

5.1: Introduction	119
5.2: Experimental	120
5.3: Results and Discussion	121
5.3.1: Variation of Dissociation Temperature with Sampling Depth	121
5.3.1.1: Dissociation Temperature of MO^+	121
5.3.1.2: Dissociation Temperature of ArX^+	127
5.3.2: Effect of Sampling Depth on M^+ Signal	129
5.3.3: Effect of Sampling Depth on MO^+ Signal	131
5.3.4: Effect of Sampling Depth on ArX^+ Signal	136
5.4: Conclusions	143

CHAPTER 6: EFFECT OF POWER ON POLYATOMIC IONS AND THEIR DISSOCIATION TEMPERATURES

146

6.1: Introduction	147
6.2: Experimental	147
6.3: Results and Discussion	148
6.3.1: Variation of Dissociation Temperature with Power	148
6.3.1.1: Dissociation Temperature of MO^+	148
6.3.1.2: Dissociation Temperature of ArX^+	150
6.3.2: Effect of Power on M^+ Signal	152
6.3.3: Effect of Power on MO^+ Signal	155

6.3.4: Effect of Power on ArX ⁺ Signal	159
6.4: Conclusions	164
CHAPTER 7: EFFECT OF SOLVENT LOADING ON POLYATOMIC IONS AND THEIR DISSOCIATION TEMPERATURES	165
7.1: Introduction	166
7.2: Experimental	167
7.3: Results and Discussion	169
7.3.1: Effect of Solvent Loading on Dissociation Temperature	169
7.3.2: Effect of Solvent Loading on Ion Signals	171
7.4: Conclusions	175
CHAPTER 8: DETERMINATION OF THE SITE AND MECHANISMS OF FORMATION OF POLYATOMIC ION INTERFERENCES	176
8.1: Introduction	177
8.2: Experimental	178
8.3: Results and Discussion	180
8.3.1: Temperature Determination	180
8.4: Conclusions	185
CHAPTER 9: CONCLUSIONS AND SUGGESTIONS FOR FURTHER WORK	187
9.1: Conclusions	188
9.2: Suggestions for Further Work	191

References	193
Appendices	215
Appendix 1: Table of Fundamental Data	216
Appendix 2: Conferences and Courses Attended	219
Appendix 3: Presentations	221
Appendix 4: Publications	222

LIST OF FIGURES

1.1	Schematic diagram of VG PlasmaQuad 3 ICP - MS instrumentation	4
1.2	Schematic diagram of a standard "Fassel" ICP torch	5
1.3	Temperature regions of the ICP	7
1.4	ICP -MS sample introduction system	7
1.5	Concentric Meinhard nebuliser, showing enlarged nebuliser tip	8
1.6	Typical spray chamber designs. A: Scott double pass and B: single pass with impact bead	9
1.7	Fate of a sample droplet after introduction into an ICP discharge	10
1.8	Two stage rotary pump ICP interface	11
1.9	Schematic of the supersonic expansion formed in the expansion chamber	13
1.10	Comparison of (A) standard inverted load coil system; and (B) centre - tapped load coil system	33
1.11	Schematic diagram of the shielded torch system	33
1.12	Comparison of background spectra using standard plasma conditions and shielded plasma conditions	34
3.1	Schematic diagram of the optical arrangement used to image the plasma onto the tip of the fibre optic	60
3.2	Schematic diagram to show optical sampling of the plasma where the plasma is moved to create a sampling depth profile	61
3.3	Schematic diagram to show optical sampling of the plasma where the fibre optic is moved to create a sampling depth profile	62
3.4	Schematic diagram of the fibre optic arrangement used to observe the interface region of the ICP - MS	64
3.5	Schematic diagram of the tip of the fibre optic and spacer	64

3.6	Mass spectrometric sampling depth profile for Ti^+ within the plasma. Errors = 3 σ for n = 3	66
3.7	Optical sampling depth profile for Ti^+ within the plasma. Errors = 3 σ for n = 3	66
3.8	Mass spectrometric sampling depth profile for TiO^+ within the plasma. Errors = 3 σ for n = 3	69
3.9	Optical sampling depth profile for TiO within the plasma. Errors = 3 σ for n = 3	69
3.10	Comparison of optical sampling depth profiles for TiO within the plasma, at different sampling depth positions. Errors = 3 σ for n = 3	72
3.11	Typical optical spectrum of OH (0 - 0) band emission showing Q_1 branches	73
3.12	Effect of power on the signal for the Q_1^1 branch of the OH (0 - 0) band emission at 307.844 nm within the interface. Errors = 3 σ for n = 3	74
3.13	Comparison of the optical signal for the Hg reference line (546.07 nm) through the interface and without the interface	74
3.14	Example of Boltzmann plot used to calculate the OH rotational temperature within the interface	76
3.15	Effect of power on the OH rotational temperature within the interface region of the ICP. Errors = 3 σ for n = 3	77
4.1	Radial profile for $^{115}\text{In}^+$. Errors = 3 σ for n = 3	86
4.2	Radial profile for Ba^+ . Errors = 3 σ for n = 3	87
4.3	Radial profile for Ba^{2+} . Errors = 3 σ for n = 3	87

4.4	Comparison of the radial profiles for MO^+ . Signals normalised to 100% abundance (Signals divided by molecular abundance then multiplied by 100). Molecular abundances of the metal oxides are given in Table 4.1. D_0 values given are for MO^+ . Errors = 3σ for $n = 3$	88
4.5	Radial profile for ArO^+ . Errors = 3σ for $n = 3$	89
4.6	Example of plot used to calculate the temperature using Method A	91
4.7	Comparison of the radial profiles for the temperature calculated using Method A, with data for D_0 (MO) and D_0 (MO^+). Errors = 3σ for $n = 3$	93
4.8	Example of plot used to calculate the temperature using Method B	96
4.9	Radial profile for the temperature calculated using Method B. Errors = 3σ for $n = 3$	97
4.10	Comparison of the radial profiles for the temperature calculated using Method C, with D_0 values for MO. Errors = 3σ for $n = 3$	102
4.11	Comparison of the radial profiles for the temperature calculated using Method C, with data for AlO and AlO^+ . Errors = 3σ for $n = 3$	104
4.12	Radial profile for the temperature calculated using Method D. Errors = 3σ for $n = 3$	106
4.13	Comparison of the radial profiles for the temperature calculated using Method E, for equilibration in the plasma and interface. Errors = 3σ for $n = 3$	110
4.14	Comparison of the radial profiles for the temperature calculated using all methods. Errors = 3σ for $n = 3$	116
5.1	Schematic diagram of an ICP showing the different zones within the plasma	119

5.2	Comparison of the sampling depth profiles for the MO^+ temperature. Errors = 3σ for $n = 3$	122
5.3	Comparison of the sampling depth profiles for the MO^+ temperature up to a sampling depth of 25 mm. Errors = 3σ for $n = 3$	123
5.4	Comparison of the sampling depth profiles for the ArO^+ temperature. Errors = 3σ for $n = 3$	127
5.5	Sampling depth profile for Ba^+ . Errors = 3σ for $n = 3$	129
5.6	Sampling depth profile for BaO^+ . Errors = 3σ for $n = 3$	132
5.7	Comparison of the sampling depth profiles for MO^+ at 1350 W. Signals normalised to 100% abundance. Molecular abundances of metal oxides are given in Table 5.1. D_0 values given are for MO^+ . Errors = 3σ for $n = 3$	134
5.8	Comparison of the sampling depth profiles for MO^+ with the shield torch at 620 W. Signals normalised to 100% abundance. Molecular abundances of metal oxides are given in Table 5.1. D_0 values given are for MO^+ . Errors = 3σ for $n = 3$	135
5.9	Comparison of the sampling depth profiles for MO^+ at 620 W. Signals normalised to 100% abundance. Molecular abundances of metal oxides are given in Table 5.1. D_0 values given are for MO^+ . Errors = 3σ for $n = 3$	135
5.10	Sampling depth profile for ArO^+ . Errors = 3σ for $n = 3$	136
5.11	Comparison of the sampling depth profiles for the ArX^+ species at 1350W. Signals normalised (Signals divided by highest signal in profile). Errors = 3σ for $n = 3$	138

5.12	Comparison of the sampling depth profiles for the ArX ⁺ species at 620W. Signals normalised. Errors = 3 σ for n = 3	138
5.13	Comparison of the sampling depth profiles for the ArX ⁺ species with the shield torch at 620 W. Signals normalised. Errors = 3 σ for n = 3	139
6.1	Comparison of the effect of power for the MO ⁺ temperature. Errors = 3 σ for n = 3	149
6.2	Comparison of the effect of power for the ArO ⁺ temperature. Errors = 3 σ for n = 3	151
6.3	Effect of power on the signal for La ⁺ . Errors = 3 σ for n = 3	153
6.4	Effect of power on the signal for Al ⁺ . Errors = 3 σ for n = 3	154
6.5	Effect of power on the signal for LaO ⁺ . Errors = 3 σ for n = 3	156
6.6	Comparison of the effect of power for the MO ⁺ / M ⁺ ratio with standard conditions. MO ⁺ and M ⁺ signals normalised to 100%. Molecular and atomic abundances are given in Table 6.1. D ₀ values given are for MO ⁺	157
6.7	Comparison of the effect of power for the MO ⁺ / M ⁺ ratio with the shield torch. MO ⁺ and M ⁺ signals normalised to 100%. Molecular and atomic abundances are given in Table 6.1. D ₀ values given are for MO ⁺	157
6.8	Effect of power on the signal for ArO ⁺ . Errors = 3 σ for n = 3	159
6.9	Comparison of the effect of power for the ArX ⁺ species with standard conditions. Signals normalised. Errors = 3 σ for n = 3	161
6.10	Comparison of the effect of power for the ArX ⁺ species with the shield torch. Signals normalised. Errors = 3 σ for n = 3	162
7.1	Schematic diagram of apparatus used for the introduction of water vapour via a temperature controlled Dreschel bottle	167

7.2	Effect of solvent loading for the ArO^+ temperature. Errors = 3σ for $n = 3$	169
7.3	Effect of solvent loading for the ArX^+ species at 1350 W. Signals normalised. Errors = 3σ for $n = 3$	171
7.4	Effect of solvent loading for the ArX^+ species at 700 W. Signals normalised. Errors = 3σ for $n = 3$	174
7.5	Effect of solvent loading for the ArX^+ species with the shield torch. Signals normalised. Errors = 3σ for $n = 3$	174

LIST OF TABLES

1.1	Detection limits (3σ) for ICP - MS, ICP - AES and GF - AAS, for selected elements	15
1.2	Examples of isobaric interferences encountered in ICP - MS	19
1.3	Commonly observed M^{2+} ions in ICP - MS and the affected isotopes	20
1.4	Common polyatomic interferences and the affected isotopes	22
1.5	Interferences of iron and selenium	23
2.1	ICP - MS operating parameters for PQ2+	53
2.2	ICP - MS data collection parameters	54
2.3	ICP - MS operating parameters for PQ3	55
3.1	Operating conditions for the SPEX 1704 monochromator used for optical observation of the plasma	59
3.2	Operating conditions for the SPEX 1704 monochromator used for optical observation of the interface	63
3.3	Wavelengths of the Q_1 branches of the OH (0 - 0) band monitored optically within the interface of the ICP	65
3.4	Assignment, wavelengths, energies and transition probabilities for the Q_1 branches of the OH (0 - 0) band	77
4.1	Isotopes studied during radial profile experiment	85
4.2	Comparison of D_o (MO) and D_o (MO ⁺) values	92
4.3	Comparison of spectroscopic constants for AlO and AlO ⁺	102
4.4	Comparison of the temperature calculated using all methods	115
5.1	Isotopes studied during effect of sampling depth experiment	121
6.1	Isotopes studied during effect of power experiment	148
7.1	Isotopes studied during the effect of solvent loading experiment	168

8.1	Isotopes studied during the introduction of 2% HNO ₃ for the site of formation experiment	178
8.2	Isotopes studied during the introduction of 1% HCl for the site of formation experiment	179
8.3	Isotopes studied during the introduction of 1% MeOH for the site of formation experiment	179
8.4	Isotopes studied during the introduction of 10 ng ml ⁻¹ MO solution for the site of formation experiment	179
8.5	Dissociation temperatures calculated for the polyatomic ions (K)	182

LIST OF ABBREVIATIONS

α	Degree of ionisation
ΔE	Energy difference
ϵ_{neb}	Nebuliser efficiency
λ	Wavelength
σ	Standard deviation for 3 replicates
ω	Vibrational constant
A	Transition probability
AAS	Atomic absorption spectrometry
AFS	Atomic fluorescence spectrometry
Ar_m[*]	Metastable excited argon atom
ArX	Argon polyatomic molecule
ArX⁺	Argon polyatomic ion
B	Rotational constant
BCR	Community Bureau of Reference
C	Solution concentration of indicated element
CCT	Collision cell
CE	Capillary electrophoresis
CID	Collision induced dissociation
D	Sampling diameter
dc / DC	Direct current
dM	Mass difference between peaks
D₀	Dissociation energy
DSI	Direct sample introduction / insertion

- E** Energy
- e⁻** Electron
- EIE** Easily ionised element
- ETV** Electrothermal vaporisation
- F** Solution uptake rate
- FIA** Flow injection analysis
- g** Statistical weight of ground electronic state
- GC** Gas chromatography
- GF - AAS** Graphite furnace - atomic absorption spectrometry
- h** Plancks constant
- HR - ICP - MS** High resolution - inductively coupled plasma - mass spectrometry
- h ν _{cont}** Continuum photon
- h ν _{line}** Spectral line photon
- I** Signal intensity
- ICP** Inductively coupled plasma
- ICP - AES** Inductively coupled plasma - atomic emission spectroscopy
- ICP - MS** Inductively coupled plasma - mass spectrometry
- IE** Ionisation energy
- IE'** Second ionisation energy
- INAA** Instrument neutron activation analysis
- IR** Induction region
- IRZ** Initial radiation zone
- k** Boltzmann constant
- K** Equilibrium constant
- K_d** Equilibrium constant for dissociation of diatomic molecule

K_{ion}	Equilibrium constant for ionisation of metal atom
K'_{ion}	Equilibrium constant for ionisation of metal ion
LC	Liquid chromatography
LTE	Local thermodynamic equilibrium
M	Mass
M	Metal atom
M⁺	Metal Ion
M²⁺	Doubly charged metal ion
MAr⁺	Metal argide ion
MASSCAL	Mass calibration solution
MH⁺	Metal hydride ion
MIP	Microwave induced plasma
MLR	Multiple linear regression
MO	Metal oxide molecule
MO⁺	Metal oxide ion
MO / M	Metal oxide to metal atom ratio
MO⁺ / M⁺	Metal oxide ion to metal ion ratio
[MO⁺] / [M⁺]	Measured ratio of metal oxide ion to metal ion signal
MOH⁺	Metal hydroxide ion
M_p	Low energy (ground) state metal atom
M_p⁺	Low energy (ground) state metal ion
M_q	High energy state (excited) metal atom
M_q⁺	High energy state (excited) metal ion
MS	Mass spectrometry
m / z	Mass to charge ratio

n Number density

NAZ Normal analytical zone

Nd:YAG Neodymium - yttrium aluminium garnet

n_{e-} Number density of electrons

n_M Number density of metal atom

n_{M+} Number density of metal ion

n_{MO} Number density of metal oxide molecule

n_O Number density of oxygen atom

N_o Avagadro's number

n_{X(plasma)} Density of species X in plasma

n_{X(int)} Density of species X in interface

P Vapour pressure

PCR Principle components regression

PII Polyatomic ion interference

PLS Partial least squares

p - LTE Partial local thermodynamic equilibrium

ppb Parts per billion

ppt Parts per trillion

PS Plasma screen

Q Gas flow rate

R Universal gas constant

RF Radio frequency

R_p Resolution

RSD Relative standard deviation

SFC Supercritical fluid chromatography

SI	Spectroscopic interference
S_{M+}	Measured M ⁺ signal
S_{MO+}	Measured MO ⁺ signal
ST	Standard mode
T	Temperature
TB	Torchbox
T_{diss}	Dissociation temperature
T_e	Electron temperature
T_{exc}	Excitation temperature
T_{gas}	Gas kinetic temperature
T_{ion}	Ionisation temperature
T_{kin}	Kinetic temperature
T_{plasma}	Plasma temperature
T_{room}	Room temperature
T_{rot}	Rotational temperature
T_{spray}	Spray chamber temperature
x	Position downstream from sampling orifice
X	Metal or non - metal atom
X⁺	Metal or non - metal ion
XRF	X - ray fluorescence
XY⁺	Diatomic molecular ion
Z	Partition function

ACKNOWLEDGEMENTS

I would like to offer my thanks to Dr Hywel Evans and Professor Les Ebdon for their guidance and support throughout this PhD. I would also like to thank Professor Steve Hill for the loan of the monochromator.

I would like to thank the EPSRC and VG Elemental for a CASE research grant, and providing the spare expansion chamber which was modified for the optical measurements in the interface, and to my industrial supervisor Dr Martin Liezers.

Thanks to everyone I have worked with during my time in Plymouth, past and present, including Fishcake, Gav, Neil, Wobbly Bob, Elena, Jason, Anita, various mad Spaniards (with varying degrees of madness!), Matt, Hugh, Warren, Jackie and anyone else I've forgotten to mention. Special thanks to James who, even though he's in America, found the time to proof read my thesis - Cheers Scouse!!!. Further special thanks to Rob Harvey who was just down the corridor whenever Gordon or Thomas "went bang"!!!

Extra special thanks to Rob for putting up with me throughout the PhD and the writing of this thesis - I told you I'd get it done eventually!!

Finally, I would like to dedicate this work to my parents, who have been there all through my student life providing constant support in the form of both finance and food parcels, to Grandma and to the memory of my other grandparents. I hope I've done you proud.

AUTHORS DECLARATION

At no time during the registration for the degree of Doctor of Philosophy has the author been registered for any other University award.

The study was financed with the aid of a CASE studentship from the Engineering and Physical Sciences Research Council in collaboration with VG Elemental, Winsford, Cheshire.

The work described in this thesis has entirely been carried out by the author. Relevant scientific seminars and conferences were regularly attended at which work was presented, external institutions were visited for consultation purposes, and several papers were prepared for publication.

Signed *L. Karley*.....

Dated *22/5/2001*.....

CHAPTER 1

Introduction

1 INTRODUCTION

1.1 GENERAL INTRODUCTION

1.1.1 History and Development of ICP - MS

The need for ultra - trace level elemental analysis has been a major driving force for the development and improvement of analytical techniques. Plasma source mass spectrometry is one technique that is currently of interest for multi - element analysis at the part per billion (ppb) and part per trillion (ppt) levels¹.

The original concept of ICP - MS developed from a requirement, expressed in 1970, for the next generation of multi - element analytical instrument systems needed to complement the rapidly developing technique of ICP - AES², which suffered from a number of matrix interferences³. Following a survey of available and emerging techniques, including atomic fluorescence spectrometry (AFS), instrumental neutron activation analysis (INAA), atomic absorption spectrometry (AAS) and X - ray fluorescence (XRF), it was concluded that atomic mass spectrometry was the only basic spectrometric technique that potentially had the wide element coverage, element specificity and relatively uniform sensitivity across the Periodic Table that was essential.

The ICP operating at atmospheric pressure was first utilised by Reed⁴⁻⁶ in 1961 to grow crystals under high temperature conditions. The analytical potential of the ICP as an optical source was realised by Greenfield *et al.*⁷ in 1964 and Wendt and Fassel⁸ in 1965. Initial work on plasma MS was carried out by Gray^{9,10}, who used a small direct current (dc) plasma, which was being used for emission studies, as an ion source for mass spectrometry. However, the ionisation temperature was too low to provide adequate ionisation of elements whose ionisation energy was greater than about 8 eV,

and severe ionisation suppression was caused by easily ionised elements (EIEs)¹¹. This ultimately led to the replacement of the capillary dc arc by an ICP by Gray and Houk¹², whereas Douglas¹³ at the University of Toronto began work with a microwave induced plasma (MIP).

The first paper describing the coupling of an argon plasma and a mass spectrometer was published in 1980 by Houk *et al.*¹², as a result of the collaboration between the research group at the Ames Lab, Iowa State University and Gray at the University of Surrey. Work was also underway by Douglas and colleagues¹⁴ at Sciex in Canada. The first mass spectra from an ICP source were obtained by Date and Gray^{15,16} in 1982. By 1983 two commercial instruments were launched, the PlasmaQuad, based on the Surrey system, by VG Isotopes Ltd. (now TJA Solutions) in the UK¹⁷, and the Elan in Canada by Sciex Inc. (now Perkin Elmer Ltd.), based on the work of the Toronto group¹⁸. Since this time ICP - MS has experienced rapid growth and there are now at least six manufacturers, with the original quadrupole ICP - MS being continuously modified. Many features, such as the shield torch system¹⁹ and collision cell technology^{19,20}, have also been introduced to overcome interferences. In addition to the original quadrupole ICP - MS some manufacturers also produce a high resolution magnetic sector ICP - MS. A schematic diagram of a typical quadrupole ICP - MS is given in Figure 1.1.

1.1.2 Inductively Coupled Plasma - Mass Spectrometer: System Set - up and Operation

The ICP is an electrode - less discharge in a gas at atmospheric pressure, maintained by energy coupled to it from a radio frequency generator. The gas used is commonly argon, although other gases, such as nitrogen and helium, have been used²¹.

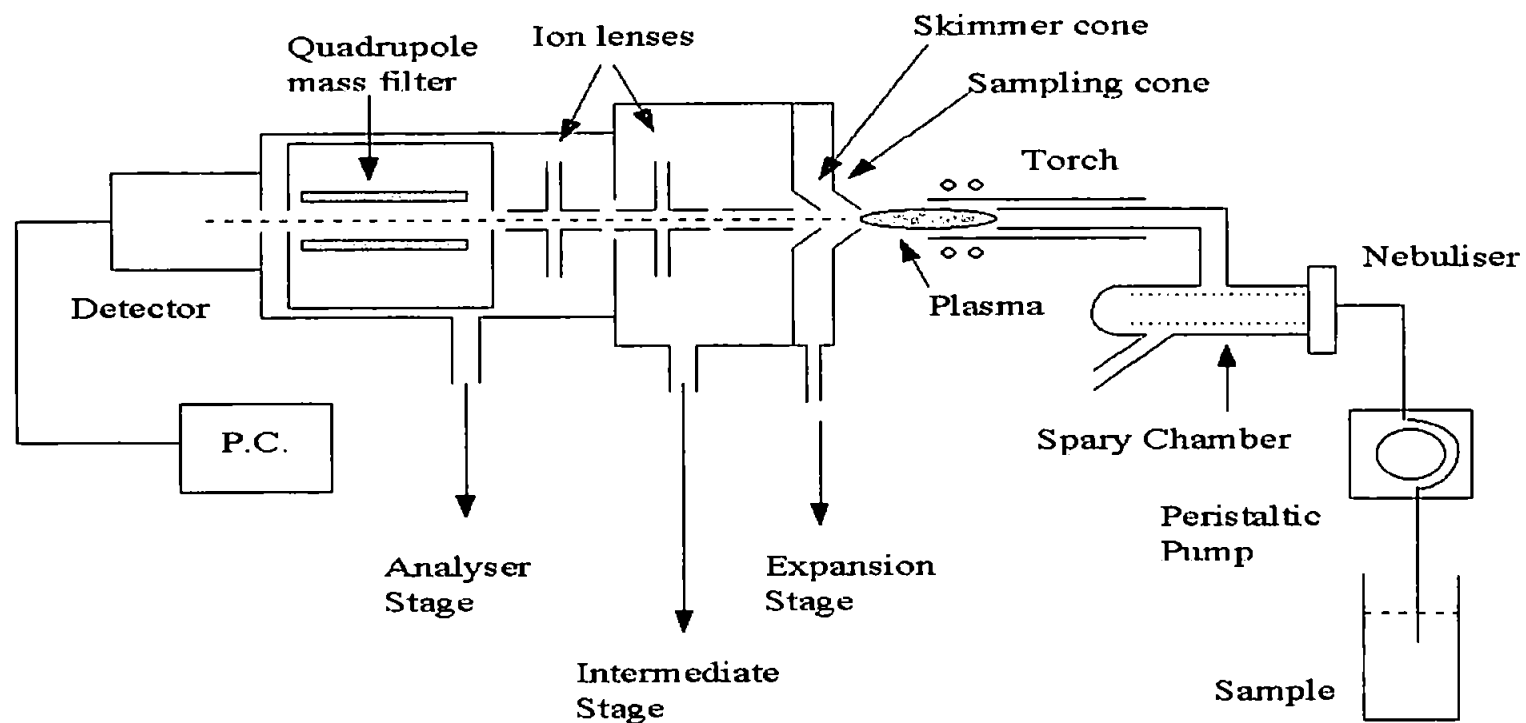


Figure 1.1: Schematic diagram of VG PlasmaQuad 3 ICP - MS instrumentation²²

The plasma is generated inside and at the end of an assembly of quartz tubes known as the torch. The standard Fassel type torch is shown in Figure 1.2.

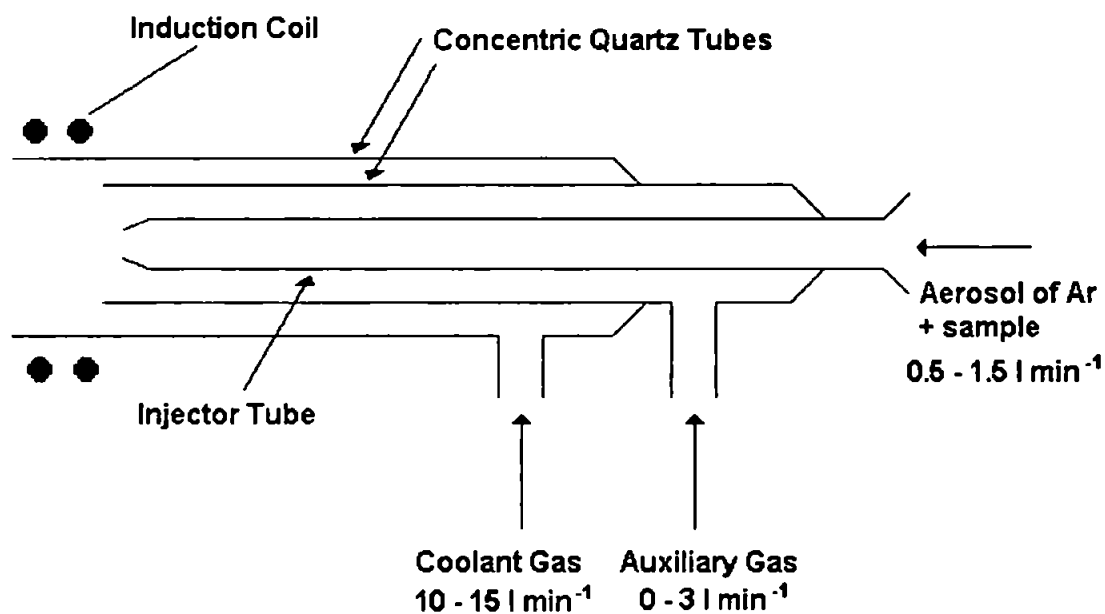


Figure 1.2: Schematic diagram of a standard "Fassel" ICP torch

This consists of an outer tube within which are two concentric tubes terminating short of the torch mouth. Each annular region formed by the tubes is supplied with gas by a side tube entering tangentially, so that it creates a vorticular flow. The innermost of the three gas flows (the nebuliser or injector gas) carries the aerosol from the sample introduction system at about 1.0 l min^{-1} . This produces a high velocity jet of gas which punches a hole in the base of the plasma. This central, or axial, tunnel is cooler than the rest of the plasma, but at $5000 - 6000 \text{ K}$ is hot enough to atomise most samples and cause varying degrees of ionisation of the constituent elements²³. The outer, or coolant, gas flow (usually $10 - 15 \text{ l min}^{-1}$) protects the torch walls and acts as the main plasma support gas. The second, or auxiliary, gas flow ($0 - 1.5 \text{ l min}^{-1}$) ensures that the hot plasma is kept clear of the tip of the injector tube.

1.1.2.1 Forming and Sustaining the Plasma

Upon emerging at the tip of the torch the argon gas is surrounded by a 2 or 3 - turn water cooled copper induction coil, which is located with its outer turn about 5 mm below the mouth of the torch. An alternating current flows through this coil, typically at a frequency of either 27.12 or 40.68 MHz and power levels of 1 - 3 kW²⁴. The argon gas stream that enters the coil is initially seeded with free electrons from a Tesla discharge coil. These seed electrons quickly interact with the magnetic field of the coil and gain sufficient energy to ionise argon atoms by collisional excitation. Cations and electrons generated by the initial Tesla spark are accelerated by the magnetic field in a circular flow perpendicular to the stream that emerges from the tip of the torch. The fast moving cations and electrons, known as an eddy current, collide with more argon atoms to produce further ionisation and intense thermal energy. This collisional ionisation continues in an "avalanche" reaction forming the ICP discharge.

The ICP is sustained by continuous energy transfer between the radio frequency (RF) generator and the torch. A flame shaped plasma is formed near the top of the torch, with a temperature of 6000 - 10,000 K²⁴, although the degree of ionisation of argon is only about 0.1 % at these temperatures²⁵. The temperature distribution throughout the system is shown in Figure 1.3.

A plasma with torroidal, or annular, geometry results from the aerosol gas punching the plasma, which lengthens the residence time (approx. 2 ms) of the sample in the interior, high temperature zone of the plasma, thereby increasing sensitivity for many elements. The sample stream then forms a long, well defined tail emerging from the high temperature region within the load coil. This tail is the spectroscopic source, containing all the analyte atoms and ions that have been excited and ionised.

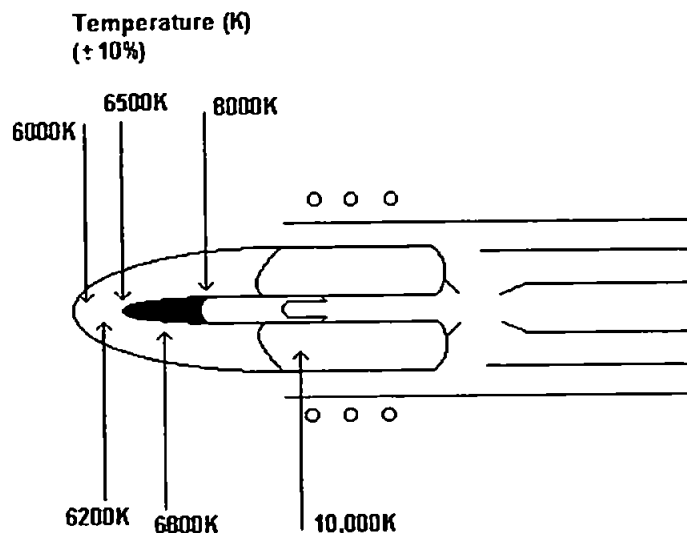


Figure 1.3: Temperature regions of the ICP

1.1.2.2 Sample Introduction

There are a number of different ways that samples can be introduced to an ICP, but the most common method is by aspiration of aqueous samples. The sample introduction system for simple aqueous samples consists of a peristaltic pump, a nebuliser, a spray chamber and a torch, and this set - up is shown in Figure 1.4.

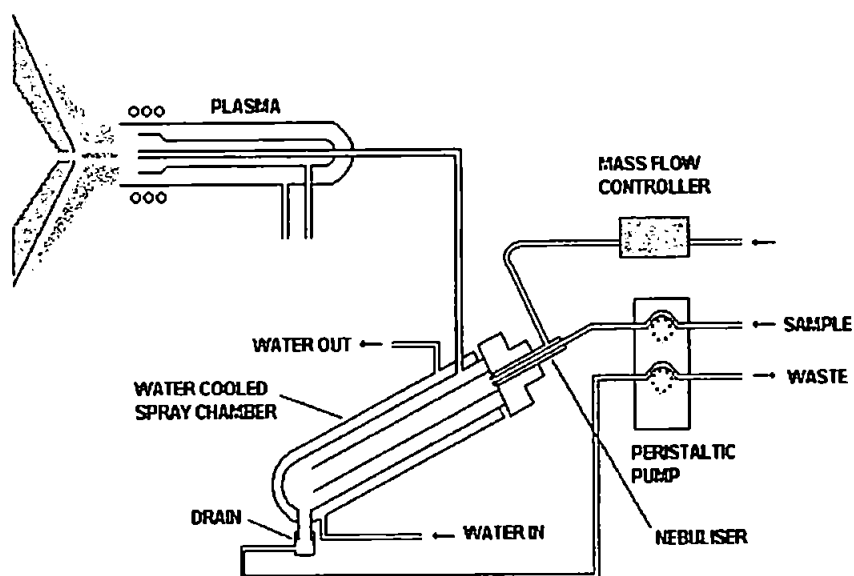


Figure 1.4: ICP - MS sample introduction system

The sample is pumped via a peristaltic pump to a nebuliser, normally a pneumatic²⁶ or ultrasonic nebuliser²⁷, where it comes into contact with argon gas, regulated by a mass flow controller, generating an aerosol. The pneumatic method, in which a high velocity gas stream produces a fine droplet dispersion of the analyte solution, is the most popular because of its convenience, reasonable stability and ease of use. Various pneumatic nebuliser designs exist and include the concentric glass nebulisers, such as the Meinhard, shown in Figure 1.5, cross flow nebulisers, and V-groove nebulisers.

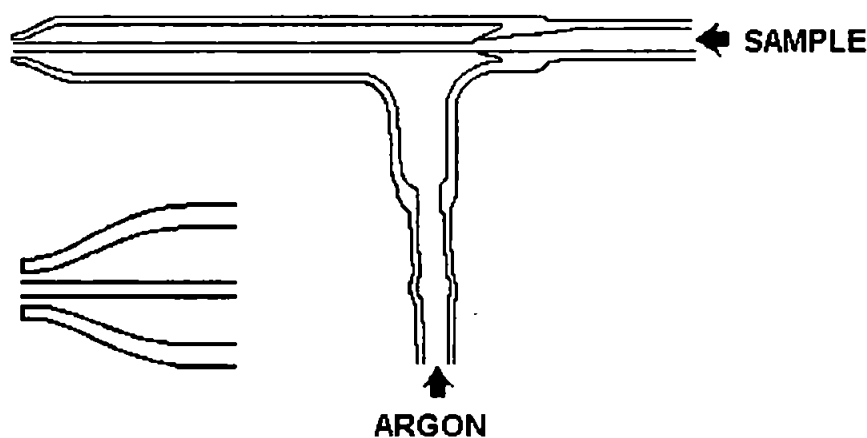


Figure 1.5: Concentric Meinhard nebuliser, showing enlarged nebuliser tip

However, other techniques are also becoming more widely used, with liquid sample introduction being achieved using ultrasonic nebulisers²⁷⁻³⁰, thermospray vaporisers^{28,31,32} and direct injection nebulisers³³⁻³⁵, which can improve nebulisation and transport efficiencies.

Liquid samples, either aqueous or organic, have also been introduced into the plasma using chromatographic techniques, including liquid chromatography (LC)^{33,34,36-42}, gas chromatography (GC)^{36,37,39,43}, flow injection analysis (FIA)⁴⁴⁻⁴⁹, supercritical fluid chromatography (SFC)^{36,38,50,51} and capillary electrophoresis (CE)^{50,52}.

Gaseous sample introduction into the ICP offers several advantages over liquid sample introduction. Unlike pneumatic nebulisation, where > 90 % of the sample is discarded using most nebulisation systems, the transport efficiency of a gas to the plasma approaches 100 %. Thus, more sample reaches the plasma, resulting in improved signal - to - background ratios and detection limits. The introduction of gaseous samples to the ICP has been performed using hydride generation⁵³ and direct injection⁵⁴.

The analysis of solid samples employs either vaporisation of the sample, i.e. electrothermal vaporisation (ETV)⁵⁵⁻⁶¹ or laser ablation⁶²⁻⁶⁴, or direct analysis, i.e. slurry nebulisation⁶⁵⁻⁶⁷.

After the aerosol has been formed it must be transported, via a spray chamber, to the torch for introduction to the plasma. Figure 1.6 shows some typical spray chamber designs.

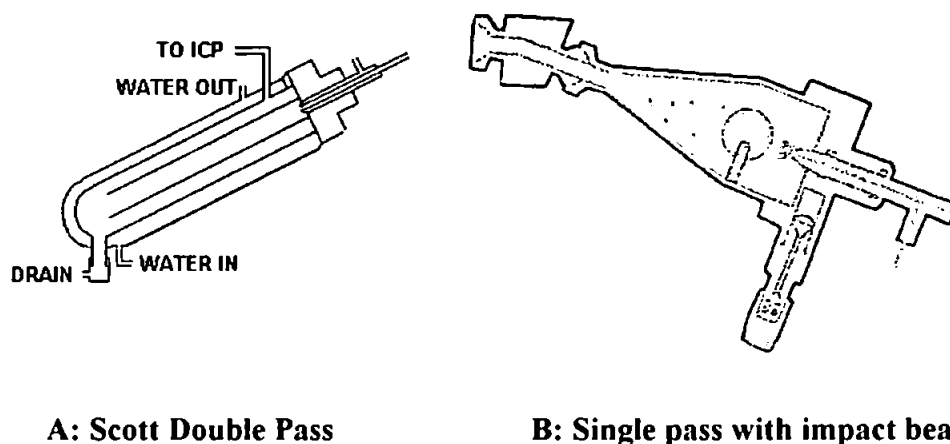


Figure 1.6: Typical spray chamber designs. A: Scott double pass and B: single pass with impact bead

The spray chamber is placed between the nebuliser and the torch and serves to remove the large aerosol droplets and to smooth out pulses occurring during nebulisation due to pumping of the solution. Only droplets less than about 10 μm reach the plasma after passing through the spray chamber, which constitutes about 1 - 2 % of the sample that is introduced to a pneumatic nebuliser⁶⁸. For an ultrasonic nebuliser the percentage efficiency is significantly greater. The spray chamber is required because these larger droplets would cause signal fluctuations, plasma instability and eventually could extinguish the plasma.

Once the sample has entered the plasma it undergoes a sequence of kinetically controlled processes, shown in Figure 1.7.

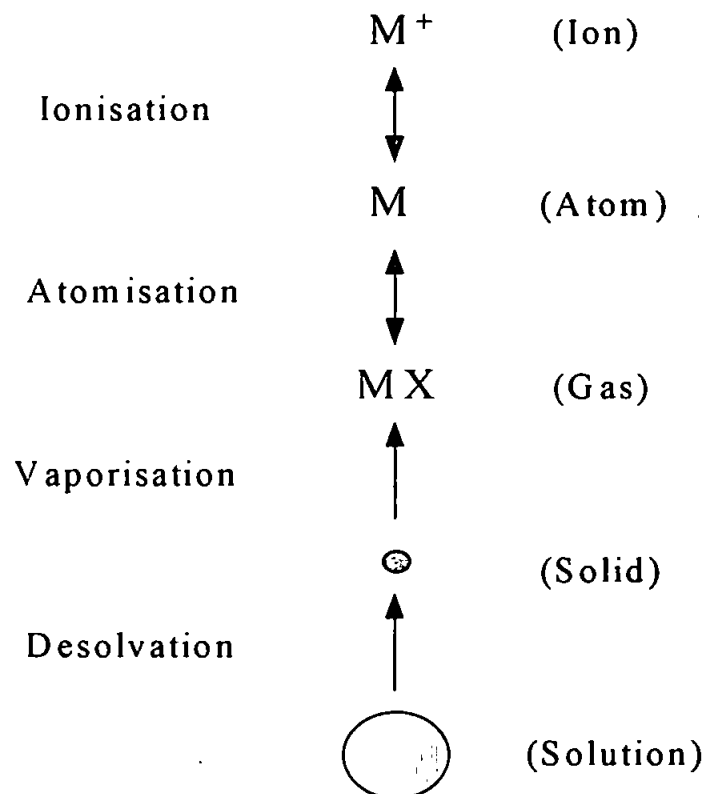


Figure 1.7: Fate of a sample droplet after introduction into an ICP discharge⁶⁹.

A droplet of sample undergoes desolvation until a dry or nearly dry particle remains. The particle is heated by the plasma, and vaporisation begins when the particle surface temperature is sufficiently hot. Molecules or atoms are released into the plasma at rates that depend on either the transfer of heat to the particle surface, or the transfer of vaporised sample away from the particle surface⁶⁹. Molecules are atomised and atoms are ionised in the plasma, and the vaporisation products diffuse. The ions produced in the ICP are then transported through the sampling orifice, skimmer, ion optics, the mass spectrometer and then strike the ICP - MS detector.

1.1.2.3 Detection

The use of an ICP as an ion source for mass spectrometry has several intrinsic problems because the plasma operates at atmospheric pressure while the mass spectrometer operates under high vacuum. This extraction is achieved using a two stage rotary pumped interface, shown in Figure 1.8.

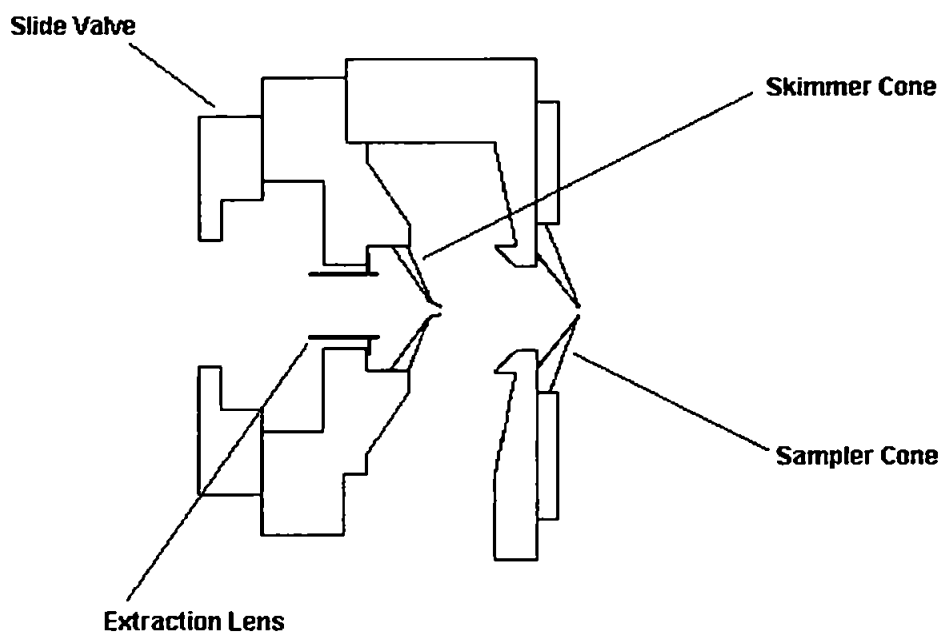


Figure 1.8: Two stage rotary pump ICP interface

The interface consists of two nickel or platinum cones enclosing a region of intermediate pressure between the plasma and mass spectrometer. The ions are extracted through a 1 mm sampling cone into a low pressure expansion chamber. As the gas emerges through the sampling orifice it undergoes rapid adiabatic expansion, where the kinetic temperature of the gas falls but the total enthalpy remains constant, and the flow becomes supersonic. Under these conditions, the kinetic energy of the sample is converted into a directed flow along this axis. In effect, a free jet is formed that is bounded by a shock wave known as "barrel shock". The barrel shock helps prevent the gas jet from mixing with any surrounding gas and hence helps prevent the formation of molecular species. A second shock wave exists across this axis. This is formed when the expansion is halted by the background gas pressure. This second shock wave is called the Mach disc. The position of the Mach disc is dependent on the diameter of the aperture in the sampling cone and on the pressure, and is typically 10 mm behind the aperture. Behind the Mach disc the ion beam becomes subsonic again and may mix with any surrounding gas. To prevent this a skimmer cone is placed at a distance of just over 6 mm away from the aperture of the sampling cone, as shown in Figure 1.9. This allows the gas jet to pass through to the next stage of the spectrometer. Once through the skimmer, the gas jet becomes random and requires focusing onto the detector by a set of electrostatic ion lenses.

The function of the ion lenses is to focus as many ions as possible from the cloud formed behind the skimmer cone through a differential pumping aperture into an axial beam of circular cross section at the entrance to the quadrupole mass analyser. The ion lenses are basically metal rings with electric potentials applied to them, and are housed in the intermediate region of the instrument. Several different systems are in use, and many have a photon stop present on the axis to prevent photons from the plasma reaching the detector and adding to the background signal.

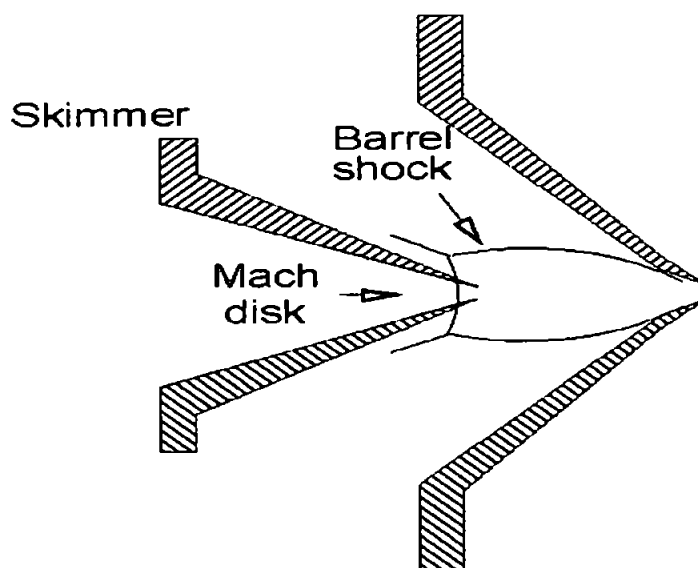


Figure 1.9: Schematic of the supersonic expansion formed in the expansion chamber

The function of the quadrupole is to produce an electric field that selectively allows a stable trajectory for ions that have a narrow mass - to - charge ratio (m / z). It is comprised of four electrically conducting rods that are arranged to produce an oscillating electric field between them. Before the main mass analyser there is often a series of pre - rods which are used to improve the transmission of the lighter ions and to prevent contamination of the main analyser. Similarly, at the end of the main analyser a set of rods can be used to improve extraction of the ions. The entire assembly is under high vacuum to ensure that there is no residual gas that can disrupt the ion trajectories by scattering, and hence causing decreased sensitivity. The ions of selected m / z “corkscrew” their way through the filter while other ions strike the rods and are lost.

The ions transmitted from the quadrupole mass analyser are detected by an electron multiplier. In a single dynode multiplier a positive ion strikes the funnel of the multiplier to produce one or more secondary electrons which are ejected from the

surface and accelerated down the tube. During the passage down the tube they collide with the walls dislodging further electrons and thus an avalanche effect quickly builds up. At the bottom of the tube the cloud of electrons leave the base of the channel and is attracted by a collector electrode. The signal is therefore measured as an electrical pulse, which is transferred to a computer. Once stored on the computer the data can be manipulated as appropriate.

1.1.3 Strengths and Weaknesses of ICP - MS

ICP - MS has both a number of advantages over its rival techniques, but also some disadvantages. The coupling of the highly efficient ICP ion source with the sensitivity and selectivity of the mass spectrometer means that the ICP - MS is a highly sensitive instrument, with detection limits in the sub ppt range, although these are usually obtained under ideal conditions using ultra pure deionised water. These detection limits are, for most elements, at least three orders of magnitude better than ICP - AES and better than, or equivalent to, detection limits obtainable with GF - AAS. Some examples of this are summarised in Table 1.1^{19,70}. In addition to being sensitive the technique has a linear calibration range of at least six orders of magnitude, which is far superior to that obtainable with GF - AAS. Another key advantage of the ICP - MS is the semi - quantitative capability. This allows the operator to measure the concentration of over 60 elements, in under sixty seconds, to within a factor of 2 or 3 of the true value. Another feature of the quadrupole mass spectrometer is multi - element analysis, with the possibility of fully quantitative calibrations for elements across the mass range. ICP - AES also offers a multi - element facility, but this is limited by the monochromator or the polychromator used. GF - AAS is typically a single element technique and as a result the sample throughput is far lower than for the ICP techniques.

Table 1.1: Detection limits (3σ) for ICP - MS¹⁹, ICP - AES⁷⁰, and GF - AAS⁷⁰, for selected elements.

Element	ICP - MS (ppt)^a	ICP - AES (ppb)^b	GF - AAS (ppb)^b
Li	0.01 - 0.1 (PS)	1	0.1
B	10 - 100 (ST)	0.5	43
Na	0.1 - 1 (PS)	1.0	0.05
S	>1000 (ST)	20	-
Ca	1 - 10 (PS)	0.03	0.04
Mn	0.1 - 1 (ST / PS)	0.3	0.03
Fe	0.1 - 1 (PS)	1	0.06
Ni	0.1 - 1 (PS)	6	0.24
Co	0.1 - 1 (ST)	2	0.5
Cu	0.1 - 1 (PS / CCT)	2	0.07
Zn	0.1 - 1 (PS)	1	0.008
As	1 - 10 (ST / CCT)	12	0.33
Rb	0.01 - 0.1 (ST)	35	0.06
Mo	0.01 - 0.1 (ST)	4	0.14
Cd	0.01 - 0.1 (ST)	1	0.02
Te	1 - 10 (ST)	27	0.5
La	0.01 - 0.1 (ST)	0.02	-
Lu	0.01 - 0.1 (ST)	0.05	-
Au	0.01 - 0.1 (ST)	0.5	0.05
Hg	1 - 10 (ST)	9	18
Pb	0.01 - 0.1 (ST)	14	0.04
U	0.01 - 0.1 (ST)	3.5	-

a) ICP - MS data obtained in multi - element mode with 10 s integrations, data from TJA Solutions product literature¹⁹ (ST = standard mode, PS = plasma screen, CCT = collision cell)

b) ICP - AES data and GF - AAS data represent the technique, not a particular instrument⁷⁰

Most instruments have single - ion monitoring and time - resolved analysis. These are software packages that monitor the signal at one isotope for single - ion monitoring or at several isotopes in a rapid sequential manner for time - resolved analysis. They are most useful with transient signals, such as those obtained with laser ablation, flow injection, electrothermal vaporisation, or when chromatography is being coupled with ICP - MS. Another advantage is that the ICP - MS can be used to determine isotope ratios for geological, or other applications, and isotope dilution analysis.

The ICP - MS is extremely flexible with respect to sample introduction, being able to admit samples as gas, liquid or solid. Manufacturers offer laser ablation and electrothermal vaporisation (ETV) accessories for solid sample introduction and hydride generators for gaseous sample introduction into the ICP - MS. These options are also available for ICP - AES but have been less extensively exploited commercially. GF - AAS can take samples as liquid or solid, but sample loading is time consuming and awkward.

While ICP - MS has a number of distinct advantages over competitive techniques it has some notable drawbacks. Firstly, it is expensive both to purchase and maintain, with instruments costing > £100 K and accessories up to £20 K, while the running costs amount to about £5 K per annum. This is some two to three times and five to seven times the cost incurred in buying and running an ICP - AES and GF - AAS instrument respectively. In addition to these costs an ICP - MS instrument should ideally be kept in a temperature controlled clean room in order to function at its best, which can be expensive. The biggest problem encountered in ICP - MS is the occurrence of interferences, which is discussed in Section 1.2.

1.1.4 Applications of ICP - MS

The advantages of ICP - MS over competitive techniques has resulted in its rapid application in a wide range of fields. ICP - MS is now used in many areas including:

- **Clinical**⁷¹⁻⁷⁹, i.e. analysis of body fluids for toxic metal levels or for vital trace elements.
- **Biological**⁸⁰⁻⁸⁷, i.e. analysis of animal or plant materials, or sediments for toxic metal levels.
- **Geological**⁸⁸⁻⁹³, i.e. analysis of potential ore materials or isotopic ratio measurements for dating rocks.
- **Nuclear industry**⁹⁴⁻⁹⁷, where the sensitivity and speed of analysis make it more favourable than traditional techniques for the analysis of radioactive materials or dosimetry of nuclear industry workers.
- **Water industry**^{98,99}, where high sample throughput and multi - element capabilities make it well suited to the analysis of potable waters.
- **Chemicals and petroleum industries**^{47,100-104}, for both routine and more specialised applications, i.e. ultratrace analysis of high purity chemicals or analysis of impurities in materials, such as steel.
- **Environmental**¹⁰⁵⁻¹¹⁶, i.e. analysis of environmentally sensitive elements such as Cd, As or Pb.
- **Certification and validation**¹¹⁷⁻¹²⁰, i.e. Certification of Community Bureau of Reference (BCR) reference materials (now the Measurements and Testing Programme).
- **Higher education establishments**, for both fundamental and applied research.

1.2 INTERFERENCES IN ICP - MS

Interferences which occur in ICP - MS can be defined as either spectroscopic or non - spectroscopic. Spectroscopic interferences are caused by atomic or molecular ions having the same nominal mass as the analyte of interest, thereby interfering with the analysis by causing an erroneously large signal at the m / z of interest¹²¹. Non - spectroscopic interferences (or matrix effects) are complex, not specific to one particular element and not apparent in the spectrum. They can be divided into¹²¹:

- a) suppression and enhancement effects,
- b) physical effects caused by high total dissolved solids.

1.2.1 Spectroscopic Interferences

Spectroscopic interferences (SIs) can be divided into 3 main areas¹²¹:

- a) isobaric overlap,
- b) doubly charged ions,
- c) polyatomic ion interferences.

1.2.1.1 Isobaric Interferences

Isobaric interferences occur when two or more elements have isotopes at the same nominal mass. In fact, masses may differ by a small amount (0.005 m / z) which cannot be resolved by a conventional quadrupole mass analyser. Some examples of these isobaric interferences are shown in Table 1.2. Isobaric overlaps are well documented, and hence easy to predict, and can be overcome by the use of elemental equations¹²²⁻¹²⁴. However, in practice, isobaric interferences are not always a problem because all

elements, with the exception of In at m/z 113 and 115 (which overlap with ^{113}Cd and ^{115}Sn), have at least one isotope which is free from isobaric overlap.

Table 1.2: Examples of isobaric interferences encountered in ICP - MS

Isotope	Isobaric Interference
^{36}S (0.02)	^{36}Ar (0.34)
^{40}K (0.01)	^{40}Ar (99.6) & ^{40}Ca (96.9)
^{50}V (0.25)	^{50}Ti (5.30) & ^{50}Cr (4.35)
^{64}Ni (0.95)	^{64}Zn (48.9)
^{84}Sr (0.56)	^{84}Kr (57.0)
^{92}Zr (17.1)	^{92}Mo (14.8)
^{113}In (4.3)	^{113}Cd (12.2)
^{115}In (95.7)	^{115}Sn (0.35)
^{124}Te (4.60)	^{124}Sn (5.8) & ^{124}Xe (0.01)
^{148}Nd (5.7)	^{148}Sm (11.2)
^{160}Gd (21.7)	^{160}Dy (2.30)
^{176}Lu (2.6)	^{176}Yb (12.7) & ^{176}Hf (5.20)
^{196}Pt (25.3)	^{196}Hg (0.15)
^{204}Pb (1.4)	^{204}Hg (6.8)

Values in brackets are isotopic abundances

1.2.1.2 Doubly Charged Species

Doubly charged ions (M^{2+}) are common for elements with a low second ionisation potential, such as barium, which has a second ionisation potential of 10.0 eV. The alkaline earth elements, the rare earth elements and elements such as U and Th are most likely to form M^{2+} species. The formation of a doubly charged ion results in a loss of sensitivity for the singly charged species and also generates an isotopic overlap at one half of the mass of the parent element. The problem of M^{2+} formation is further exacerbated if the interferent precursor is present in high concentrations, which is often the case with the rare earth elements in geological samples¹²⁵. The range of M^{2+} interferences is shown in Table 1.3.

Table 1.3: Commonly observed M^{2+} ions in ICP - MS and the affected isotopes

M^{2+} Species	Affected Isotope
$^{88}\text{Sr}^{2+}$	^{44}Ca (2.06)
$^{138}\text{Ba}^{2+}$	^{69}Ga (60.2)
$^{140}\text{Ce}^{2+}$	^{70}Ge (20.5)
$^{154}\text{Sm}^{2+}$	^{77}Se (7.58)
$^{170}\text{Er}^{2+}$	^{85}Rb (72.2)
$^{176}\text{Yb}^{2+}$	^{88}Sr (82.5)
$^{232}\text{Th}^{2+}$	^{116}Sn (14.2)
$^{238}\text{U}^{2+}$	^{119}Sn (8.58)

Values in brackets are isotopic abundances.

1.2.1.3 Polyatomic Ion Interferences

This form of spectroscopic interferences is far more of a problem than isobaric interferences and can be much more difficult to overcome. Polyatomic ions are molecular species which are formed in the plasma and interface region of the ICP - MS. These polyatomic ions typically come from precursors in the argon support gas (e.g. Ar, H, O), entrained atmospheric gases (e.g. N, O), from solvents or acids used during sample preparation (e.g. N, Cl, S, P), or from the sample matrix, and are particularly problematic below m/z 80^{12,54,126-133}. Polyatomic ion interferences (PIIs) can be placed into several groupings;

- * **oxides** i.e. ArO^+ , ClO^+ , MO^+
- * **hydroxides** i.e. ArOH^+ , ClOH^+ , MOH^+
- * **hydrides** i.e. ArH^+ , MH^+
- * **argides** i.e. MAr^+ .

Therefore, their occurrence will depend on the sample composition with regard to both the solute and the solvent. Common examples of polyatomic ion interferences are given in Table 1.4, although this is by no means an exhaustive list. Particularly problematic polyatomic interferences are those which interfere with mono - isotopic elements, i.e. $^{75}\text{ArCl}^+$ on $^{75}\text{As}^+$ and $^{103}\text{ArCu}^+$ on $^{103}\text{Rh}^+$. Other problematic elements are Fe and Se, as they suffer from interferences on most of their isotopes, as shown in Table 1.5.

Table 1.4: Common polyatomic interferences and the affected isotopes

Polyatomic interference	Affected Isotope
$^{18}\text{H}_2\text{O}^+$	^{18}O (0.20)
$^{28}\text{N}_2^+$, $^{28}\text{CO}^+$	^{28}Si (92.2)
$^{31}\text{NOH}^+$	^{31}P (100)
$^{32}\text{O}_2^+$	^{32}S (95.0)
$^{44}\text{N}_2\text{O}^+$, $^{44}\text{CO}_2^+$	^{44}Ca (2.08)
$^{52}\text{ArC}^+$	^{52}Cr (83.8)
$^{54}\text{ArN}^+$	^{54}Fe (2.36)
$^{56}\text{ArO}^+$	^{56}Fe (91.7)
$^{57}\text{ArOH}^+$	^{57}Fe (2.14)
$^{68}\text{ArCO}^+$	^{68}Zn (18.6)
$^{75}\text{ArCl}^+$	^{75}As (100)
$^{76}\text{Ar}_2^+$	^{76}Se (7.7)
$^{80}\text{Ar}_2^+$	^{80}Se (50.0)
$^{103}\text{ArCu}^+$	^{103}Rh (100)
$^{154}\text{BaO}^+$	^{154}Sm (22.8) & ^{154}Gd (2.2)
$^{155}\text{BaOH}^+$	^{155}Gd (14.9)
$^{181}\text{HoO}^+$	^{181}Ta (99.9)
$^{192}\text{LuO}^+$	^{192}Os (41.0) & ^{192}Pt (0.78)
$^{254}\text{UO}^+$	$^{254}\text{Es}^*$ & $^{254}\text{Cf}^*$

Values in brackets are natural isotopic abundances

* Radioactive isotopes

Table 1.5: Interferences of iron and selenium

Affected Isotope	Interferent Ion
^{54}Fe (5.8)	^{54}Cr (2.36) & ^{54}ArN
^{56}Fe (91.7)	^{56}ArO
^{57}Fe (2.14)	$^{57}\text{ArOH}$
^{58}Fe (0.31)	^{58}Ni (67.8)
^{74}Se (0.9)	^{74}Ge (36.4)
^{76}Se (9.0)	^{76}Ge (7.7) & $^{76}\text{Ar}_2$
^{77}Se (7.5)	$^{77}\text{ArCl}$
^{78}Se (23.5)	^{78}Kr (0.35) & $^{78}\text{Ar}_2$
^{80}Se (50.0)	^{80}Kr (2.25) & $^{80}\text{Ar}_2$
^{82}Se (9.0)	^{82}Kr (11.6)

Values in brackets are isotopic abundances

1.2.2 Methods for Removing Interferences

The problem of spectroscopic interferences can be dealt with in two ways, either by their removal or by correcting for them. Careful setting of instrumental parameters has been shown to reduce the relative levels of interferences^{125,134-152}, with the nebuliser gas flow, sampling depth and forward power being the most important.

1.2.2.1 Multivariate Correction Methods

One of the simplest methods to correct for spectroscopic interferences is the use of mathematical correction methods^{122-124,131,153-157}, such as elemental equations^{122-124,131} and multivariate techniques^{153,157}. Elemental equations^{122-124,131} have been used to correct for both isobaric and polyatomic interferences. For example, the interference caused by

$^{40}\text{Ar}^{35}\text{Cl}^+$ on $^{75}\text{As}^+$ can be corrected for by measuring the $^{40}\text{Ar}^{37}\text{Cl}^+$ signal at m/z 77 and back calculating the contribution from $^{40}\text{Ar}^{35}\text{Cl}^+$ at m/z 75, assuming the sample does not contain $^{77}\text{Se}^{+131}$.

Multivariate techniques used to overcome spectroscopic interferences include multiple linear regression (MLR)¹⁵³, principle components regression (PCR)¹⁵³ and partial least squares (PLS)¹⁵⁷. MLR and PCR have been used to correct for MoO^+ , ZrO^+ and RuO^+ in the determination of low levels of Cd^+ , In^+ and Sn^+ , respectively¹⁵³. PLS has been used to correct for interferences caused by light rare earth oxides on heavier rare earth elements¹⁵⁷.

1.2.2.2 Alternative Sample Preparation Methods

a) Sample Dissolution Procedures

Polyatomic interferences can be removed by alternative sample preparation, which may be as simple as changing the dissolution media in order to remove the interference precursors from the plasma system. Hence, if V or As is to be determined then hydrochloric acid should be avoided in order to prevent the occurrence of Cl based polyatomic interferences. In general, nitric acid is favoured as a dissolution media as it gives rise to the simplest spectra, with digestion media such as hydrochloric, sulphuric and phosphoric acids all giving rise to a wide range of interferences^{12,129,130,132,133,135,136,138,148}. However, it is not always possible to use an alternative sample digestion media, particularly for geological samples¹²⁴. One answer to this problem has been the use of slurry nebulisation⁶⁵⁻⁶⁷, where the sample is introduced as a finely ground solid in suspension, avoiding the need for sample dissolution.

While it is possible to avoid potential interferences due to acids used for dissolution, if the sample matrix itself contains the interfering species then it is often necessary to separate the analyte completely from the interfering matrix component.

b) Desolvation Techniques

Many of the most serious polyatomic interferences in ICP - MS are caused by species which contain oxygen in combination with an element in the support gas (e.g. argon or nitrogen), in the acids used to dissolve the sample (e.g. chlorine or sulphur), or in the sample itself^{30,158-162}. Since water is the major source of oxygen in the plasma when nebulising aqueous samples, decreasing the water loading decreases the oxygen concentration in the plasma^{30,160}.

An extremely simple method to reduce oxygen - containing interferences derived from injected water is to cool the spray chamber, thereby condensing some of the water vapour. More efficient solvent removal can be achieved by the use of more complex arrangements, such as Peltier coolers¹⁶³, membrane interfaces^{28,160}, or heater / condensers^{31,32}. These methods have reduced the levels of both oxides and polyatomic ion interferences, while increasing the sensitivity for a variety of metal analytes.

The desolvation system generally used with an ultrasonic or thermospray nebuliser can also be used with other nebulisers for attenuating polyatomic ions containing oxygen. The aerosol is first heated to vaporise the solvent. Most of the solvent vapour is then removed in a condenser that is kept at a temperature near the melting point of the solvent, i.e. 0 - 2 °C for water¹⁶⁴. Additional water may be removed by attaching a second device to the outlet of the condenser.

Cryogenic desolvation uses repetitive heating and cooling steps to condense solvent vapour^{30,164,165}. In this method the aerosol generated by the nebuliser is heated to 140 °C and then passed through a series of condensers. The first condenser at 0 °C removes most of the water present. The partially dried aerosol stream is warmed to room temperature before it enters a second glass condenser at - 80 °C. The aerosol stream then

passes into a set of copper loops where it is repeatedly cooled and heated at - 80 °C and 140 °C respectively, before being transported to the ICP³⁰.

Membrane methods also vaporise the solvent, which then passes as a vapour through a porous membrane and is evacuated or purged continuously by a sweep gas^{28,29,160,161,164}. A multi - strand Nafion[®] dryer, located between the spray chamber and torch, has been used to remove 97 % of the total mass of water leaving the spray chamber¹⁶⁶.

c) On - Line Separation methods

Co - precipitation¹⁶⁷⁻¹⁶⁹ and solvent extraction¹⁷⁰ are useful methods of separating the analyte from the matrix component. However, such procedures are time consuming and impurities in the organic solvents or complexing agents can increase blank values. A rapid method of analyte separation is that of preconcentration or matrix removal using chelating resins, ion exchange or chromatographic methods, which can be performed on - line¹⁷¹. Using microcolumns of exchange media analytes can be preconcentrated, the matrix eliminated, and hence interferences removed^{171,172}. This approach has been used for a large number of applications, including the determination of trace analytes in seawater^{40,120,173-184}, concentrated brines^{185,186}, biological samples^{41,45,172,183,187-189}, waters^{46,113,114,182,184,190-193}, and geological samples¹⁸⁶. Many of these applications use ion exchange resins to retain the analytes while the bulk matrix is eluted to waste. Therefore, potentially interfering species have already been removed by the time the analytes reach the ICP.

1.2.2.3 *Alternative Sample Introduction Methods*

ICP - MS has the ability to accept samples in gas, liquid or solid states, and the ability to modify the sample introduction system can be utilised in the removal of interferences.

a) Thermal Vaporisation

Thermal vaporisation as a method of sample introduction for ICP - MS has been performed using electrothermal vaporisation (ETV)⁵⁵⁻⁶¹ and direct sample introduction (DSI)^{54,61,194}. For ETV the normal sample introduction system of the ICP is replaced by a graphite furnace. For the majority of ETV applications the sample is dispensed on a graphite rod or platform, dried, ashed and then vaporised. The vapour is then swept to the plasma by a flow of carrier gas. This technique has the advantage of separating the analytes from the matrix, which is removed during the ashing phase, hence reducing interferences. Interferences arising from solvents are also reduced, since the sample is dry.

ETV has been used to determine trace metals in seawater¹⁹⁵, trace metals in biological samples¹⁹⁶ and radioisotopes in waters¹⁹⁷, where the interferences from the matrix have been eliminated. ETV has also been used to determine sulphur in steel¹⁹⁸, where the background interferences of $^{16}\text{O}^{16}\text{O}^+$, $^{16}\text{O}^{16}\text{O}^1\text{H}^+$, and $^{16}\text{O}^{18}\text{O}^+$ on $^{32}\text{S}^+$, $^{33}\text{S}^+$, and $^{34}\text{S}^+$ respectively, have been reduced.

However, due to the possibility of insufficient vaporisation of some refractory analytes this technique often requires the use of matrix modifiers, which increases the possibility of interferences.

b) Laser Ablation

Laser ablation ICP - MS is a modification of ICP - MS in which a laser is used for initial volatilisation prior to its introduction into the plasma. A laser (often a Nd:YAG laser) is focused onto (or close to) the surface of a solid sample causing it to vaporise. The sample vapour is then swept by a flow of carrier gas to the plasma for ionisation and detection. This enables the introduction of solids directly into the plasma, thereby eliminating time consuming and difficult dissolution, and the risks of contamination from reagents¹⁹⁹. This has been applied to the analysis of geological material²⁰⁰, the analysis of impurities in solid uranium²⁰¹, and the analysis of ceramic layers in solid oxide fuel cells²⁰². The production of a dry vapour of the sample leads to decreased interference effects that normally arise from the solvent. However, the laser only vaporises very small areas of the sample, which can lead to spurious results if the sample is not homogeneous.

c) Hydride Generation

Hydride generation involves the conversion of species in aqueous solution into volatile hydrides by reaction with sodium tetrahydroborate (III)⁵³. The volatile hydride product can be readily removed from the bulk matrix, resulting in the isolation of the analytes from interferences. Another advantage of hydride generation is that the transport efficiency of the analyte to the ion source is far higher than for aqueous nebulisation (close to 100 %), which leads to a substantial increase in sensitivity.

The tetrahydroborate (III) reagent is fairly selective in the compounds with which it will react to yield a volatile product and has been used for the determination of As, Se, Sn, Sb, Ge, Te, Pb, Bi and Hg^{121,203}. Hydride generation has been particularly used for As²⁰³⁻²⁰⁶ and Se²⁰⁷⁻²⁰⁹ analysis for samples with high chloride content, such as HCl²⁰⁶, seawater^{203,205,207,208} and biological samples²⁰⁷, to avoid spectral interferences such as $^{40}\text{Ar}^{35}\text{Cl}^+$ on $^{75}\text{As}^+$, $^{37}\text{Cl}^{37}\text{Cl}^+$ on $^{74}\text{Se}^+$, and $^{40}\text{Ar}^{37}\text{Cl}^+$ on $^{77}\text{Se}^+$.

1.2.2.4 Instrumental Methods

a) Alternative Plasma Sources

Another option is to use an alternative plasma source such as a helium microwave induced plasma (MIP)^{210,211}. The use of helium removes all of the argon based interferences and also allows the more effective analysis of difficult to ionise elements, by virtue of its higher first ionisation potential. Low pressure MIPs²¹¹ and ICPs^{108,212-215} have also been used to reduce interference levels, although helium ICPs are difficult to initiate and sustain. Therefore, mixed gas plasmas, where a molecular or monatomic gas is bled into or replaces one of the three gas flows of the ICP, are more common.

b) Mixed Gas Plasmas

Mixed gas plasmas, using molecular or inert gases bled into, or replacing one of the three gas flows of the ICP - MS, have been employed to reduce polyatomic ion interferences. A mixed gas plasma is formed by the addition of only a few percent of an alternative gas to the outer gas flow, or in some cases to the intermediate or injector gas flows, with alternative gases including nitrogen^{158,162,216-228}, helium²²⁹, oxygen^{225,227}, air^{225,227,230}, xenon²³¹, hydrogen^{162,224,230,232}, methane^{224,233,234}, ethane²³⁵ and trifluoromethane²³⁶. Nitrogen addition has been extensively studied, with nitrogen being added to the nebuliser gas, auxiliary gas and coolant gas. Nitrogen addition in ICP - MS for interference removal was first reported by Evans and Ebdon^{158,228}, with the authors finding the gas to be of use in reducing the ArCl⁺ interference when added to the nebuliser gas flow. Nitrogen addition to the plasma has also been used by other groups to reduce chloride - based interferences^{223,226}. This approach was later applied for improving the determination of As in high chloride matrices^{222,237}. Nitrogen addition has been extensively studied by other groups^{162,217,220,221,225} who found that the addition of nitrogen to the plasma not only enhanced analyte sensitivity but also reduced polyatomic

interference signals. Beauchemin and Craig^{218,219} focused their addition of nitrogen to the outer gas to improve the analysis of ⁵⁶Fe and ⁷⁸Se and also to overcome nonspectral matrix interferences due to Na.

While nitrogen addition to the plasma has been the most popular supplementary gas, others have also been studied. The use of an Ar - He plasma was investigated by Sheppard *et al.*²²⁹, who found that the addition of He produced a plasma that was capable of ionising elements of high ionisation potential more efficiently than a pure Ar plasma. Hydrogen addition has been reported^{162,238} and was found to be useful in reducing MO⁺ interferences, although other interferences such as ArCl⁺ and ArO⁺ were enhanced. Oxygen addition has been used^{158,225} with differing results. Lam and Horlick²²⁵ found no effect on analyte sensitivity with oxygen addition but Evans and Ebdon¹⁵⁸ found that it reduced the levels of ArCl⁺, Ar₂⁺, and Cl₂⁺. The addition of air to the plasma^{225,239} was found to have a similar effect to nitrogen addition, in that analyte sensitivity was improved, particularly for elements with high ionisation potentials. Xenon addition has been investigated by Smith *et al.*²³¹ and they reported a significant reduction of various polyatomic ions (such as N₂⁺, HN₂⁺, NO⁺, ArH⁺, ClO⁺, ClOH⁺, ArC⁺, ArN⁺, and ArO⁺), which facilitated the measurement of Si, K, V, Cr, and Fe. Hydrocarbon gases have also been introduced to the plasma. Allain *et al.*²⁴⁰ used methane addition to achieve analyte enhancement, particularly of poorly ionised elements. Methane has also been used to reduce interferences in ICP - MS^{226,233}, and was found to be even more effective than nitrogen addition for reducing a wide range of interferences. Ethane addition to the plasma has also been investigated²³⁵ and found to greatly reduce the interference levels of species such as ArCl⁺, ArNa⁺, SO₂⁺, S₂⁺, PO₂⁺, ArO⁺, ClO⁺ and CeO⁺. Trifluoromethane has been added to the nebuliser gas by Platzner *et al.*²³⁶, who found an increase in analyte response and a decreased background for the analysis of As, Se, Cu and Zn.

c) High Resolution Instruments

One of the most effective methods of overcoming spectral interferences is to spectrally separate the interfering masses by coupling the Ar ICP source to a high resolution mass spectrometer^{241,242}. The high resolution ICP - MS (HR - ICP - MS) is based on a double focusing magnetic sector mass spectrometer, and it is this double focusing nature of the spectrometer which enables the separation of several species of the same nominal mass. The ability to separate species is described by the resolving power, which is defined by²⁴³

$$R_p = M / dM \quad (1.1)$$

where R_p = resolution
 M = nominal mass peak
 dM = mass difference between the peaks.

Separation of the peaks is said to have occurred if the depth of the valley between the two peaks is 10 % of the peak height (for peaks of equal height). Most predicted interferences in ICP - MS can be resolved from the isotopes of interest with an R_p of up to 10,000, although the separation of isobaric interferences requires an R_p greater than 20,000, which is outside the performance of the spectrometer. Reed *et al.*²⁴³ catalogued and illustrated the polyatomic spectral interferences affecting measurements of Li to Ge for common anion matrices (sulphate, nitrate, chloride) and those species containing C, N, H, O and Ar, and the resolution required in order to separate out these interferences. High resolution ICP - MS has been applied to the determination of 40 ultratrace elements in terrestrial waters²⁴⁴ and the determination of V, Cr, Ga, Ge, and As in HCl²⁴⁵, while Becker and Dietze²⁴⁶ have reviewed other applications of HR - ICP - MS.

The implementation of high resolution is not achieved without compromise, as the sensitivity will decrease as resolution is increased. HR - ICP - MS instruments are also roughly four times as expensive as quadrupole ICP - MS instruments.

d) Alternate Load Coil Geometries / Shielded Torch System

A secondary discharge has been shown to cause interference effects that have a severely detrimental effect on the performance of the instrumentation²⁴⁷. The secondary discharge can promote the formation of polyatomic ions such as ArO^+ , ArH^+ and Ar_2^+ behind the sampling cone²⁴⁸. The formation and implications of the secondary discharge are discussed further in Section 1.3.2.

A centre tapped load coil is often used to minimise the secondary discharge and is compared to the standard load coil in Figure 1.10. With the centre - tapped load coil high voltage of equal amplitude but opposite phase is applied to the two ends of the coil, and the centre is connected to ground. The potential gradient from the left end of the coil to the centre is balanced by that from the right end of the coil to the centre, so the net RF potential coupled into the plasma remains close to zero. Electrical current still flows through the coil, so the inductive coupling remains to sustain the plasma²⁴⁹.

The centre - tapped load coil has been used by Douglas and French²⁵⁰ and Ross *et al.*¹⁵⁰, while Gray¹⁵¹ investigated several alternative load coil geometries as a means of reducing the secondary discharge. Douglas and French²⁵⁰ found a greatly reduced level of M^{2+} , but a slight increase in the oxide level. Ross *et al.*¹⁵⁰ found that the load coil geometry only had a minor effect on M^{2+} and MO^+ formation, but that there was a great difference in the amount of ArH^+ .

One of the load coil configurations investigated by Gray¹⁵¹ involved the insertion of a grounded slotted metal cylinder (the shield torch) between the outer surface of the torch and the load coil, as shown in Figure 1.11.

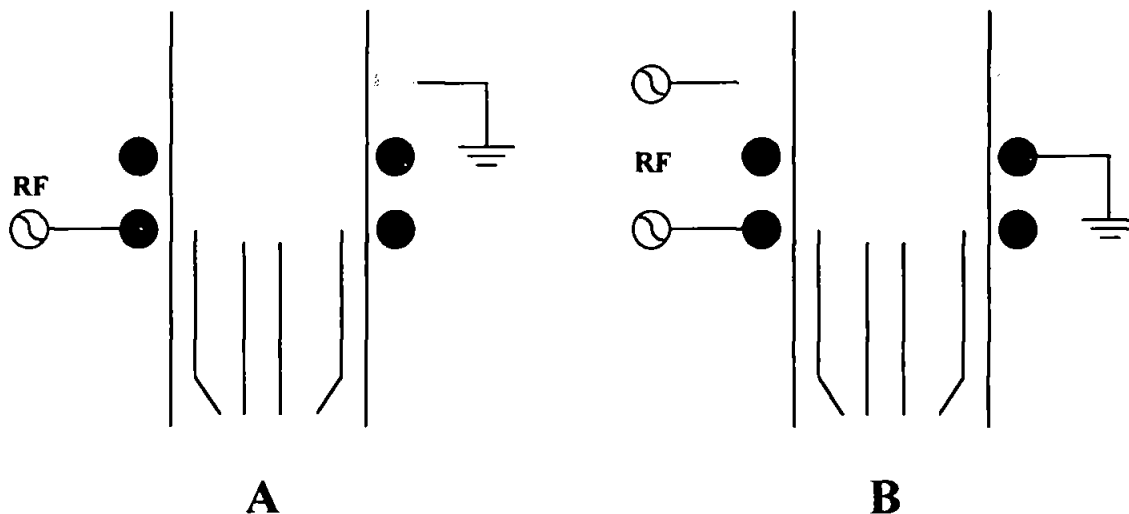


Figure 1.10: Comparison of (A) standard inverted load coil system; and (B) centre - tapped load coil system.

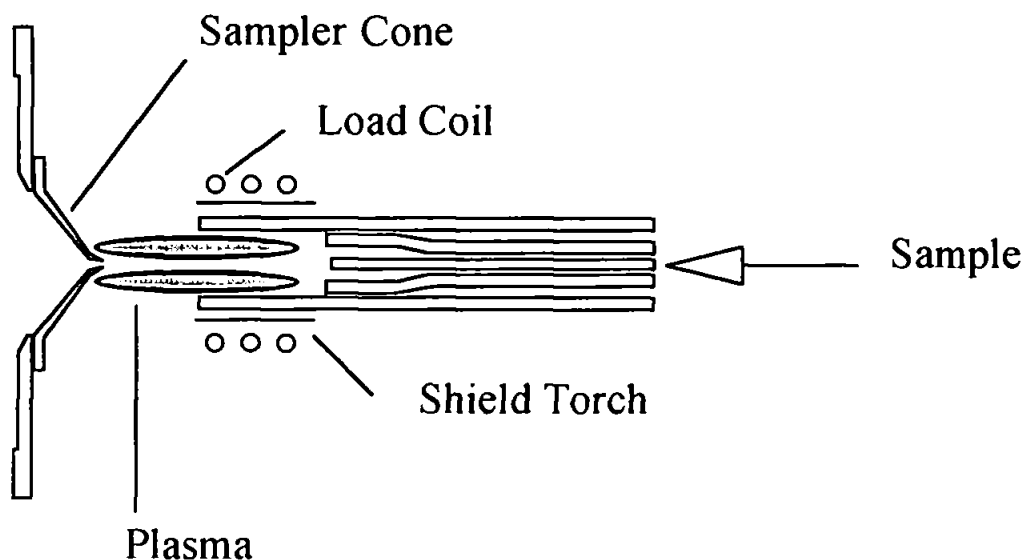


Figure 1.11: Schematic diagram of the shielded torch system

The shielded system minimises capacitive coupling between the electrical fields of the load coil and the plasma¹⁵¹, so that the potential in the plasma is lower than that without the shield torch system. As a result the secondary discharge is eliminated and polyatomic ions are not formed behind the sampler cone²⁴⁸. However, Uchida and Ito¹⁴⁶ stated that while the shield torch reduces the plasma potential a secondary discharge can

still persist, and Sakata *et al.*¹⁵² found that even with the shield torch polyatomic ions were present at significant levels at RF powers above 1200 W. In order to reduce the level of polyatomic ions the plasma conditions must be adjusted to generate a cooler plasma, which can be accomplished by increasing the injector gas flow rate and / or lowering the forward power.

Sakata *et al.*¹⁵² and Nonose *et al.*¹⁴² have investigated the shield torch system to alter the polyatomic spectral interferences, with particular focus on the reduction of ArO^+ level in order to facilitate the determination of iron. They found that when the shield torch system was combined with the cooler plasma the polyatomic ions such as ArH^+ , CO_2^+ and ArO^+ can be reduced, with species such as NO^+ becoming the dominant background ion. This can be seen in Figure 1.12, which shows the background spectra with and without the use of the shield torch system.

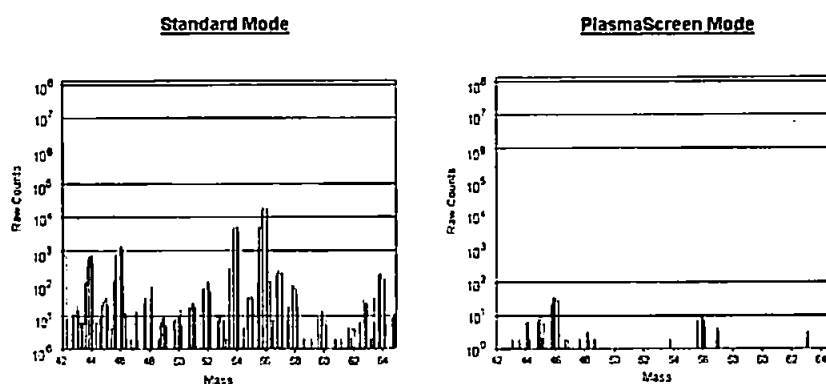


Figure 1.12: Comparison of background spectra using standard plasma conditions and shielded plasma conditions¹⁹.

The shielded ICP system produces remarkably low ion energies compared with the conventional plasma system^{142,151,152}. Therefore, with the shield torch lower ionisation potential elements, such as Li, Mg and Fe, are still ionised at nearly 100 %, while the ionisation efficiencies of elements with higher ionisation potentials are drastically

reduced²⁴⁸. By using a combination of the shield torch system and cool plasma conditions polyatomic ions such as ArO^+ , ArC^+ and ArH^+ can be drastically reduced, while analytes such as Li, Mg and Fe are still ionised efficiently. However, this technique generates other polyatomic ions, such as MO^+ and MOH^+ , and prohibits ionisation of higher ionisation potential elements¹⁵². Hence, while some of the common interferences such as $^{40}\text{Ar}^+$, ArH^+ , ArC^+ , ArOH^+ and ArO^+ can be reduced or even eliminated by applying cool plasma techniques, the plasma stability suffers under these lower temperature conditions. This is particularly the case if there are large amounts of dissolved solids or strong acids present in the sample^{19,251}. Most cool plasma analyses therefore require the use of the standard addition method to overcome matrix - induced signal suppression. Also, if many analytes are to be determined, each sample must be analysed twice, first with a reduced temperature plasma for analytes with a sufficiently low first ionisation potential and a second time with a normal plasma for all other analytes.

e) Collision Cells

One way of overcoming the problems associated with cool plasma conditions is the use of a collision cell, where all analytes can be determined using normal, high temperature plasma conditions, so that there is no need to determine elements such as K, Ca and Fe using cool plasma conditions. This reduces the matrix effects which occur with cool plasma conditions.

Collision cells used in ICP - MS are based on instrumentation developed for the production of fragment ions for structural elucidation and selective analysis of mixtures in organic MS, and for fundamental studies in ion - molecule reactions²⁵², although there is one important difference. In ICP - MS the collision cell should remove polyatomic ions completely, whereas in the other disciplines it is usually sufficient to merely make new ions not already present in the spectrum.

Collision cells provide a means for molecular ion discrimination that is independent of m/z , i.e. collisional dissociation²⁵³. This method of discrimination is also independent of the ICP operating conditions and the nature of the sample. This allows the ICP to be operated at 'normal' RF power, in a conventional 'hot' regime, where the ionisation efficiency is high for most elements²⁵³. Generally, the ions are passed into a multipole ion guide (either quadrupole, hexapole or octapole) in an enclosed housing filled with one or more collision gases²⁵². The target gas density is high enough to remove the undesired ions, while collisional cooling²⁵⁴ and the focusing properties of the multipole help retain many of the analyte ions.

Early studies by Douglas²⁵⁵ and Rowan and Houk²⁵⁶ with quadrupole collision cells for ICP - MS found that collision induced dissociation (CID) reactions, typically used in tandem MS, were not sufficient to remove most polyatomic ions to the extent desired. If the target gas density was increased to values high enough to drive CID to completion then the atomic analyte ions were lost to scattering. Rowan and Houk²⁵⁶ also showed that a chemically reactive collision gas, i.e. CH₄, helped to remove particular polyatomic ions, i.e. ArO⁺, Ar₂⁺ and ArN⁺, with enough efficiency for analytical purposes, although it was found that different collision gases and energies were necessary for different polyatomic ions. They also observed that polyatomic ions were removed by reactions between the polyatomic ions and the neutral collision gas, as well as collision induced dissociation of the polyatomic ions. This resulted in new peaks in the mass spectrum from products of ion - molecule reactions between both interfering ions and background ions with the target gas.

Douglas and French²⁵⁴ showed that a collision cell can also serve to reduce the kinetic energy spread of ions, thus reducing the peak tailing observed in the spectra, and this cooling effect for atomic ions in ICP - MS was also demonstrated by Turner *et al.*²⁵⁷.

Various collision cell gases have been used in order to reduce polyatomic interferences. Turner *et al.*²⁵⁷ have used He in the collision cell to reduce the polyatomic interferences Ar_2^+ , ArCl^+ , ArO^+ , Ar^+ , and ArH^+ on the signals for $^{80}\text{Se}^+$, $^{75}\text{As}^+$ (in 1 % HCl), $^{56}\text{Fe}^+$, $^{40}\text{Ca}^+$ and $^{39}\text{K}^+$, respectively, whilst maintaining the sensitivity for analyte species. Ammonia has been used as a collision cell gas by several workers²⁵⁸⁻²⁶⁰. Vollkopf *et al.*²⁵⁸ used ammonia as a collision cell gas to successfully reduce ArH^+ , Ar^+ , ArC^+ , ArOH^+ , and ArO^+ to enable the analysis of $^{39}\text{K}^+$, $^{40}\text{Ca}^+$, $^{52}\text{Cr}^+$, $^{55}\text{Mn}^+$ and $^{56}\text{Fe}^+$ in high purity hydrogen peroxide. However, they found that the use of methane as a collision cell gas was more effective for removing the Ar_2^+ interference to allow the determination of $^{80}\text{Se}^+$. Ammonia has been used by Bollinger and Schleisman²⁵⁹ to determine Al, As, Ca, Cr, Fe, K, Ni, Ga, Ge, Mn, Sn, Ti, and V in concentrated HNO_3 and HCl, although they found that the ammonia could not eliminate the interferences from hydrochloric acid on V or As. Neubauer and Vollkopf²⁶⁰ have also used ammonia as a collision cell gas to remove chloride and carbon based spectral interferences to allow the determination of Cr, Mn, V and As in sucrose solution, 1 % HCl and NaCl. Bandura and Tanner²⁶¹ have used neon as a collision cell gas to reduce plasma noise during the determination of Pb and Ag isotope ratios.

Most of these polyatomic ions studied are weakly bound, (e.g. Ar_2^+ $D_0 = 1.25$ eV, ArM^+ $D_0 \approx 0.5 - 1$ eV). Usually the ions to be removed also have higher internal energies than the corresponding atomic analyte ions, so both CID and chemical reactions would be expected to be effective. This is not the case for metal oxide ions (MO^+) which are often quite strongly bound (LaO^+ $D_0 = 8.89$ eV). These MO^+ ions often have ion energies similar to those of the analyte ions and thus CID and charge exchange reactions would not be expected to be effective in these cases.

Du and Houk²⁵² have used a hexapole collision cell with a mixture of He and H_2 gas to attenuate metal oxide signals. They found that the MO^+ / M^+ signal ratio was

suppressed by a factor of up to 60 for CeO^+ and LaO^+ , while maintaining $\approx 20\%$ of the original signal for atomic analyte ions. They also found that the conditions used served to remove most of the ArO^+ , Ar_2^+ and ArN^+ from the background spectrum.

Ion traps have been used in a similar fashion for selective storage of the analyte or removal of undesired ions^{253,262-264}, although they differ from collision cells in their position relative to the mass analyser of the ICP. Ion traps are situated after the quadrupole of the ICP - MS, whereas collision cells are located in front of the quadrupole. The use of H_2 ²⁶⁴ and He ²⁶³ in ion traps have been found to reduce the background spectra, with the signals for ArO^+ , Ar^+ , Ar_2^+ , ArN^+ and ClO^+ (in a 2% HCl matrix) being greatly reduced.

Collision cells are now produced commercially by at least two manufacturers, although they differ greatly in their approach to reducing polyatomic interferences. One approach is the use of an inert gas, such as He, as a collision gas to dissociate the polyatomic ions into their component atoms or ions. This selectively reduces all argon-based polyatomic interferences. The other approach is to use a reaction gas to selectively remove interfering polyatomic ions using controlled ion - molecule chemistry^{20,265}.

There are three major considerations in implementing the ICP - MS reaction cell technique²⁶⁶. The first is identifying an appropriate reaction gas which is able to eliminate the interferences of interest. Xenon²⁵⁶, CH_4 ²⁵⁶, He ^{252,257}, ammonia²⁵⁸⁻²⁶⁰, H_2 ²⁶⁰, He / H_2 ²⁵², ethane²⁵⁶, and neon²⁶¹ have been used as reaction gases in order to remove polyatomic ion interferences. These studies have shown that it is necessary to use different reaction gases to remove different interfering species²⁶⁶. The second consideration is the elevation of the chemical background²⁶⁴. This characteristic is associated with the nature of ion - molecule chemistry, which does not eliminate ions from the reaction cell but converts them into other ions. These were overcome by Du and Houk²⁵² by operating at a negative hexapole dc pole bias in relation to that of the quadrupole. This led to most of

the artefact ions produced in the hexapole not having sufficient kinetic energy to enter the quadrupole. The third consideration is associated with the properties of the reaction cell as an ion - molecule reactor, where it is desirable to provide a controlled thermal environment for the promotion of useful reactions²⁶⁶.

The plasma operates at normal power for both systems, when used with a collision cell. This maintains the high sensitivity of the system, since with normal powers the degree of analyte ionisation is very high. Therefore, spectral interferences are significantly reduced, while maintaining high analyte sensitivity. This enables elements such as K, Ca, Cr, Fe, Cu, As and Se to be analysed in one analytical run, without the matrix induced limitations of cool plasma or the need for hydride generation.

1.2.3 Non - Spectroscopic Interferences

Non - spectroscopic interferences are characterised by a reduction or enhancement in analyte signal due to factors exerting an influence on sample transport, ionisation in the plasma, ion extraction and ion throughput in the resultant ion beam¹²¹. Sample introduction and transport are affected by the nebuliser design and nebuliser gas flow, the viscosity, surface tension, density, evaporation rate and vapour pressure of the solvent²⁶⁷⁻²⁶⁹. Therefore, if a different solvent is used, with all other parts of the sample introduction system being equal, changes in sample delivery rates occur and hence interfere with or suppress the signal²⁶⁷. Therefore, it is critical to matrix match samples and standards with respect to the solvent. The sample matrix can also affect the atomisation, excitation and ionisation characteristics by altering the plasma temperature^{270,271}.

An excess of heavy, easily ionisable elements (EIEs) in the matrix creates the most serious non - spectroscopic interferences¹²¹. The presence of easily ionisable

elements can lead to enhancements in analyte signals, but usually result in severe suppression of analyte response²⁴⁹. This effect is particularly severe if the matrix is a heavy element with a low ionisation potential, and the affected element is one of low mass²⁷². The role of the EIEs in suppressing analyte signal has been attributed to space charge effects with the ion optics^{249,272,273}. This effect occurs due to the loss of the negatively charged electrons in the ion optics which are designed to focus positively charged ions. This loss of electrons leads to repulsion between the remaining positive ions which is most pronounced for the light elements²⁷³. The presence of heavy matrix ions increases this repulsion, by further deflecting light elements from the centre of the ion beam. Suppression of the analyte signal and long term stability problems can also result from the physical deposition of material on the sampler and skimmer cones and the subsequent restriction of the orifices¹²¹.

The problems of matrix induced non - spectroscopic interferences can be dealt with by removal of the matrix, or its effect. Internal standardisation has been widely used to correct for the effects of matrix elements^{120,274-277}, with the best results being obtained when the internal standard is as close as possible in mass and ionisation potential to the analyte of interest. Non - spectroscopic interferences can also be reduced by judicious setting of the operating parameters of the ICP - MS^{125,135,277-281}. Mixed gas plasmas have also been explored to reduce matrix effects^{218,219}.

Removal of the matrix from the sample is the alternative to correction for its effects. This can be achieved in a similar fashion to the removal of spectroscopic interferences, e.g. LC or on - line preconcentration^{167,176,178-182,190-193,282} and matrix removal using flow injection can be used^{45,49,175,177,183,184-186,189,203,283}. Flow injection has also been used to introduce samples with very high solids content⁵⁵⁻⁶⁰, or to introduce organic solvents^{61,62}. The use of flow injection for these samples prevents a continual

loading of the plasma with high solids, thereby preventing torch / nebuliser / cone blockage^{55,63}.

1.3 FUNDAMENTAL STUDIES

The fundamental properties of ICPs are of importance for the characterisation of plasmas and for their efficient use for analytical purposes²⁸⁴. The aim of fundamental studies is to identify the pertinent excitation, ionisation, de - excitation and recombination processes that are responsible for observed analyte behaviour²⁸⁵. The elucidation of these processes is called 'excitation mechanisms'. 'Plasma diagnostic' techniques are used to measure the physical properties of the plasma discharge that will yield significant information about the excitation mechanisms²⁸⁵. The fundamental parameters of plasmas are considered to be plasma temperatures, electron number densities, atom and ion emission intensities, number densities of analyte and argon species and spectral line widths²⁸⁴. Spectroscopic diagnostics consist of measuring single emission lines or spectra from species in the plasma and from that emission evaluating temperatures and relative or absolute number densities²⁸⁶. An accurate knowledge of the temperature actually experienced by the analyte species is one of the prerequisites leading to the definitive understanding of solute vaporisation, dissociation, atomisation and ionisation processes occurring in the plasma²⁸⁷. The electron number density is an important indicator of the degree of ionisation²⁸⁴, with free electrons thought to be the primary plasma particle responsible for excitation and ionisation in the ICP²⁸⁶.

The majority of these measurements are determined optically, and a description of the optical methods used in this study can be found in Chapter 3. Descriptions of other optical temperature and electron density methods can be found in the reviews by

Mermet²⁸⁸, Hasegawa *et al.*²⁸⁴ and Cabannes and Chapelle²⁸⁹. Mass spectrometric methods for temperature determination are discussed extensively in Chapter 4.

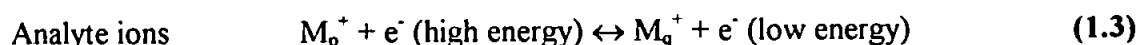
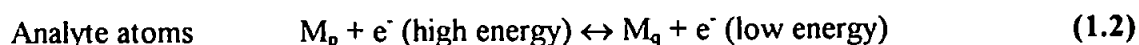
1.3.1 Excitation Mechanisms

The ICP discharge contains a host of species, all of which can interact with one another physically or chemically²⁸⁶. However, comprehensive understanding of how all these species are formed, and how they interact with one another has still not been fully achieved^{286,290}.

1.3.1.1 Formation Mechanisms of Analyte Ions

The majority of research has focused on the processes that act to produce an excited or ionised analyte, known as excitation mechanisms²⁸⁶. These excitation mechanisms show how all the species interact with one another as reactants and products, and common reactions encountered in plasma discharges are given below:

1) Collisional excitation and de - excitation mechanisms



where M_p / M_p^+ = ground state atom / ion

M_q / M_q^+ = excited state atom / ion

e^- = an electron.

In the forward process, kinetic energy is taken up from the electron by the analyte atom or ion, which is left in an excited state. In the reverse process, excitation energy is transferred from the excited atom or ion to the colliding electron. For the forward process the energy of the electron must be equal to, or exceed the transition energy involved²⁸⁵.

2) Collisional ionisation and 3 - body recombination



This process leads to the production of analyte ions, normally in the ground state. The electron energy must match or exceed the ionisation energy. The reverse process, three - body recombination, is an ion decay mechanism through which excited state analyte atoms may be produced²⁸⁵.

3) Radiative recombination of an analyte ion (M^+) producing background emission

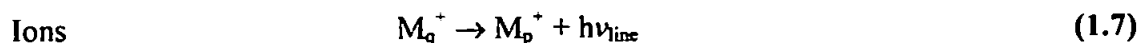
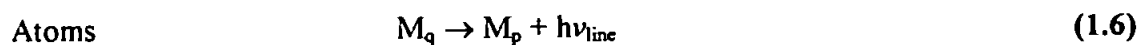
($h\nu_{\text{cont}}$)



where $h\nu_{\text{cont}}$ = continuum photon.

The products of this reaction are excited analyte atoms and a continuum photon ($h\nu_{\text{cont}}$). The reverse process, photo ionisation, is not as important in the ICP because, for the most part, the analyte lines are optically thin for reabsorption²⁸⁵.

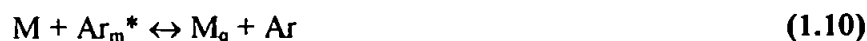
4) Radiative decay to produce spectra ($h\nu_{\text{line}}$)



where $h\nu_{\text{line}}$ = spectral line photon.

These reactions are the most important in ICP - AES, since they create the characteristic line spectra. The reverse process is not favourable in an ICP due to its low optical density²⁸⁵.

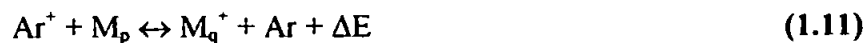
5) Penning ionisation and excitation



where Ar_m^* = an Ar atom excited in a metastable state.

Penning ionisation reactions produce ionised and / or ionised and excited analytes, depending on the energies involved, with excess energy being carried away in the form of kinetic energy of the free electron (1.8 and 1.9). Thus, reaction 1.8 will produce analyte ions for any species whose ionisation energy is less than the Ar metastable energies of 11.55 and 11.71 eV²⁸⁵. Similarly, in reaction 1.9 excited analyte ions are produced. Direct excitation of atoms and ions is also possible (1.10).

6) Charge exchange with Ar



where ΔE = energy difference.

In this process asymmetrical charge transfer takes place between Ar ions and analyte atoms, leading to the production of excited state analyte ions. The difference in energy is dissipated as kinetic energy of the colliding partners²⁸⁵.

1.3.1.2 Formation Mechanisms of Molecular Ions

Ideally, the plasma would produce solely monatomic ions, so that spectroscopic interferences would be few and easy to predict²⁴⁹. Unfortunately, some polyatomic ions are produced in the ICP, although there is some uncertainty as to whether these ions are present in the plasma or made during the extraction process²⁴⁹, and this is discussed further in Chapter 8.

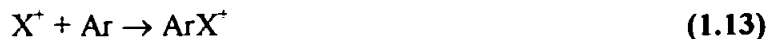
Just as the formation of analyte ions is governed by more than one reaction mechanism, so there are several mechanisms for the formation of molecular ions²⁹¹.

1) Associative ionisation



where Ar_m^* = metastable excited argon atom
X = metal or non metal.

2) Association reaction of an ion (X^+) and an argon atom



3) Ionisation by electron impact of a neutral argon molecule



4) Association reaction of an atomic argon ion with a metal atom



Becker *et al.*²⁹¹ investigated the formation of several metal argide molecular ions. From the similar distribution of metal argide ions and metal ions they assumed that the association reaction (1.13) was dominant for their formation, although associative ionisation (1.12) was also a probable formation mechanism for the formation of argon molecular ions.

Van Heuzen and Nibbering¹²⁸ found an unexpectedly high intensity of the H_2O^+ peak in comparison to that of the OH^+ peak and suggested that an amount of the water in the ICP was not decomposed in the plasma. They also suggested that this undecomposed water may undergo an ion / molecule reaction with an argon ion to form an argon hydride ion, as shown in Equation 1.16.



Nonose *et al.*¹⁴² also suggested that ArO^+ was formed via a collision induced reaction of neutral argon and an oxygen ion (1.17), rather than an ionisation reaction of neutral ArO.



Nonose *et al.*¹⁴² also theoretically calculated the monoxide to analyte (MO / M) ratios, assuming the dissociation equilibrium in the ICP. They proposed that the MO^+ due to analytes was derived from undissociated MO in the ICP because the theoretical MO / M ratios in the ICP agreed satisfactorily with the experimental MO^+ / M^+ ratios.

Therefore, polyatomic ions can be classified into two groups according to their formation mechanism, with argon polyatomic ions in one group and metal monoxide ions, as well as species such as NO^+ and O_2^+ in the other group.

1.3.2 Ion Sampling and Formation of Secondary Discharge

1.3.2.1 Ion Sampling

The ion extraction process is of crucial importance to the analytical performance of an ICP - MS. A key facet of the extraction process is the extent to which the plasma and sampling interface interact electrically²⁹². This interaction affects the kinetic energies of the extracted ions and hence the resolution and peak shapes obtainable with the mass analyser. The discharge also influences the abundance of doubly charged ions, metal oxide ions and other species observed in the mass spectra²⁹².

The first analytical mass spectrometer for ion sampling from an ICP¹² used a stagnant layer sampling interface, subsequently referred to as boundary layer sampling²⁹³. With the small sampling orifice (approx. 0.1 mm) a cooled boundary layer was formed

over the sampler, and the observed mass spectrum corresponded to the ionic composition of this layer rather than to that of the bulk plasma¹². The small sampling orifice was also found to erode rapidly and to clog with solutions of even moderate salt content.

This type of sampling interface was soon replaced by the sampler - skimmer arrangement, which has subsequently been adopted for plasma sampling on commercial ICP - MS systems²⁹⁴. This interface differed in that a much larger sampling orifice (ca. 1 mm) was used, through which the source gas flowed under continuum conditions into an evacuated expansion stage²⁹³. This enlarging of the orifice led to an improvement in the performance of ICP - MS in several respects. The larger sampling orifice resulted in a higher gas flow, which broke through the boundary layer and sheath. These cool layers were still present but they formed obliquely along the inside edge of the sampling orifice rather than across its mouth. The bulk of the gas simply flowed through the sampler without passing through either the boundary layer or sheath. This arrangement provided a) much higher total flow of ions, b) a more representative sample of ions from the plasma, and c) greater resistance to plugging from deposited solids²⁴⁹.

The initial problem with continuum flow sampling in ICP - MS was that an electrical discharge (known as a secondary discharge) formed between the plasma and the sampler through the gas flow into the orifice²⁴⁹. A bad discharge causes crackling of the plasma and is characterised by bright white emission from the gas flowing into the orifice. This caused a very high proton noise level, produced ions of high kinetic energy and energy spread and led to rapid erosion of the orifice²⁵⁰. This erosion of the orifice leads to decreased vacuum in the expansion region which therefore leads to increased interference effects such as more doubly charged ions and more polyatomic ions²⁴⁷.

Initially it was thought that the secondary discharge resulted from an electro - gasdynamic effect which led to an increase in the electron density at the orifice. This

secondary discharge was called the “pinch” effect. Douglas and French²⁵⁰, however, indicated that the secondary discharge resulted simply from a capacitive discharge caused by the large RF voltage swing in the plasma relative to the grounded interface.

1.3.2.2 Formation of the Secondary Discharge

When the plasma is completely inductively coupled with the RF coil, the plasma has only a slight DC potential and there is little potential difference between the plasma and the interface, which is at ground level. However, there is also capacitive coupling between the plasma and the RF coil, which creates a potential in the plasma that oscillates at the radio frequency of the current²⁴⁸. An equal number of positive ions and electrons exist in the plasma in the absence of any external influence. However, because electrons are more mobile than the more massive positive ions, the electrons will be lost to the grounded sampling cone more rapidly and a positive potential builds up in the plasma. Additionally, a sheath of neutral argon atoms builds up between the cool interface and the plasma, acting as a condenser so the plasma potential is grounded to the interface and vacuum chamber through the sheath.

The plasma potential is divided by two capacitances: one is between the plasma and the RF coil and the second is between the plasma and the interface²⁴⁸. Likewise behind the sampling cone the ions and electrons oscillate, with the movement of the electrons much faster than that of the ions, so that the RF potential is rectified to a mean net positive dc voltage. If the plasma potential is too high a strong secondary discharge forms between the plasma and the sampling orifice^{249,250}. This discharge is strongest at low power, high aerosol gas flow rate and high water loads²⁹⁵⁻²⁹⁷. The discharge also becomes more intense as the sampler is retracted further downstream in the plasma¹⁴⁹. The secondary discharge can promote the formation of polyatomic ions such as ArO^+ , ArH^+ and Ar_2^+ behind the sampling cone²⁴⁸.

There have been several methods used to remove the secondary discharge, including careful optimisation of the sampling depth, using a low nebuliser gas flow, and reducing the solvent loading of the plasma^{147,247,295,296,298}. A number of different load coil configurations have been used to minimise the plasma potential and to eliminate the secondary discharge. They include 'reversed' load coils¹⁵⁰, centre tapped load coils^{150,250}, balanced load coils²⁹⁹, and shielded load coils^{142,146,151,152,248,300-302}, while Gray¹⁵¹ investigated several alternative load coil geometries as a means of reducing the secondary discharge.

With the centre - tapped load coil high voltage of equal amplitude but opposite phase is applied to the two ends of the coil, and the centre is connected to ground. The potential gradient from the left end of the coil to the centre is balanced by that from the right end of the coil to the centre, so the net RF potential coupled into the plasma remains close to zero. Electrical current still flows through the coil, so the inductive coupling remains to sustain the plasma²⁴⁹. A centre tapped load coil has previously been compared to the standard load coil in Figure 1.10.

One of the load coil configurations investigated by Gray¹⁵¹ involved the insertion of a grounded slotted metal cylinder (the shield torch) between the outer surface of the torch and the load coil, as previously shown in Figure 1.11.

The shielded system minimises capacitive coupling between the electrical fields of the load coil and the plasma¹⁵¹, so that the potential in the plasma is lower than that without the shield torch system³⁰². As a result the secondary discharge is eliminated²⁴⁸. However, Uchida and Ito¹⁴⁶ stated that while the shield torch reduces the plasma potential a secondary discharge can still persist. The shielded ICP system produces remarkably low ion energies compared with the conventional plasma system^{142,151,152}.

1.4 AIMS OF STUDY

Inductively coupled plasma - mass spectrometry is widely accepted as the leading technique for trace element analysis. It suffers, however, from a range of interferences, both spectral and non - spectral, which limit the range of analytes and substrates which can be analysed successfully. Numerous attempts have been made to reduce these interferences, such as the use of a shield torch, although the mechanisms of how these species are formed, and hence also successfully reduced, are still not fully understood.

The aim of this study was to investigate the use of a shield torch, and the effect of different operating parameters, on the formation of a variety of polyatomic ion interferences, in order to determine how molecular interferences are thermodynamically or kinetically influenced by conditions in the plasma.

The influence of the shield torch and varying operating parameters on the fundamental properties of the plasma, such as temperature and electron number density, was determined in order to elucidate the formation mechanisms and site of formation of the molecular interferences.

Optical measurements, using a monochromator, were carried out in conjunction with the mass spectrometric measurements, in order to obtain as much information about the molecular interferences as possible, to facilitate the understanding into their formation.

CHAPTER 2

Experimental

2 EXPERIMENTAL

2.1 INSTRUMENTATION

2.1.1 PlasmaQuad 2+ ICP - MS

Preliminary experiments were conducted using a PlasmaQuad 2+ ICP - MS (VG Elemental, Ion Path, Road Three, Winsford, Cheshire, UK) fitted with a Meinhard nebuliser and a double pass spray chamber, cooled to 10 °C. The sample solution was delivered to the nebuliser by a peristaltic pump at a flow rate of 1.0 l min⁻¹. Standard nickel sampler and skimmer cones were used, with a 1 mm and 0.7 mm orifice respectively. Results were obtained at 1350 W and operating conditions are given in Table 2.1. Ion lens settings and torchbox position were optimised throughout the experiments to give maximum ¹¹⁵In⁺ signal using 10 ng ml⁻¹ MASSCAL solution. Data collection parameters were kept constant for all experiments and are given in Table 2.2.

Table 2.1: ICP - MS operating parameters for PQ2+

Power (W)	1350
Gas Flow Rate (l min⁻¹)	
Nebuliser	0.9
Auxiliary	0.8
Coolant	13.0

Table 2.2: ICP - MS data collection parameters

Mass Range (amu):	5.6 → 239.40
Detection Mode:	Dual
Dwell Time (μs):	
PC	320
Analog	320
Channels per amu	19
Time / sweep:	0.5

2.1.2 PlasmaQuad 3 ICP - MS

Experiments were conducted using a PlasmaQuad 3 ICP - MS (VG Elemental, Ion Path, Road Three, Winsford, Cheshire, UK) fitted with a Meinhard nebuliser and a double pass spray chamber, cooled to 12.5 °C. The sample solution was delivered to the nebuliser by a peristaltic pump at a flow rate of 1.0 l min⁻¹. Standard nickel sampler and skimmer cones were used, with a 1 mm and 0.7 mm orifice respectively. Results were obtained using three different sets of operating conditions, a) typical conditions (1350 W), b) with the shield torch (620 W / 700 W), and c) at 620 W / 700 W without the shield torch. This last set of conditions were used as a control to ensure that any differences observed were not merely due to a power effect. The operating parameters for the three sets of conditions used are given in Table 2.3. Ion lens settings and torchbox position were optimised throughout the experiments to give maximum ¹¹⁵In⁺ signal using 10 ng ml⁻¹ MASSCAL solution. Data collection parameters were kept constant for all experiments and are given in Table 2.2.

Table 2.3: ICP - MS operating parameters for PQ3

	1350 W	Shield Torch	Control
Power (W)	1350	620 / 700	620 / 700
Gas Flow Rate (l min⁻¹)			
Nebuliser	0.9	0.9	0.9
Auxiliary	0.8	0.4	0.8
Coolant	13.0	12.5	13
Lens Settings (V)*			
Extraction	-210	-141	-180
Collector	-1.3	0.4	-1.3
L1	-2.6	1.7	1.4
L2	-26.8	1.5	-21.8
L3	1.3	0.3	0.3
L4	-41.0	-88.3	-35.0
Pole Bias	3.0	-8.0	4.0
Torchbox position			
(arbitrary units)*			
x axis	803	736	777
y axis	289	297	297
z axis	270	291	277

* These parameters were optimised throughout the experiments. Values stated are typical settings under these conditions.

2.2 REAGENT PREPARATION

All solutions were prepared with deionised water (18 M Ω cm) from a Milli - Q analytical grade water purification system (Millipore, Bedford, MA, USA) in acid washed volumetric flasks, using previously calibrated pipettes and balances. All reagents were Aristar[®] grade unless otherwise stated. All metal standards were Spectrosol[®] grade unless otherwise stated.

10 $\mu\text{g ml}^{-1}$ stock solutions of the analytes (Al, Ba, La, Mn, Ti, Y, and Zr) were prepared from either 10,000 $\mu\text{g ml}^{-1}$ or 100 $\mu\text{g ml}^{-1}$ commercial stock solutions (BDH, Poole, Dorset, UK) and stored in 100 ml acid washed (10 % v / v HNO₃) polypropylene containers. The 10,000 $\mu\text{g ml}^{-1}$ Y stock solution was prepared by dissolving 1.2575 g of Y₂O₃ (Specpure[®]) (Johnson, Matthey and Co., Hatton Garden, London, UK) in 15 ml conc. HCl (BDH, Poole, Dorset, UK) made up to 100 ml with Milli - Q water.

Standard solutions were prepared daily in 100 ml acid washed (10 % v / v HNO₃) volumetric flasks by appropriate dilution of the stock solutions with 2 % v / v nitric acid (2 parts concentrated HNO₃ (BDH, Poole, Dorset, UK) and 98 parts Milli - Q water).

10 ng ml⁻¹ MASSCAL (Be, Mg, Co, In, Pb, U) standard was prepared daily from 10 $\mu\text{g ml}^{-1}$ commercial stock standard (BDH, Poole, Dorset, UK).

1 % v / v MeOH and 1 % v / v HCl were prepared from appropriate dilution of MeOH (BDH, Poole, Dorset, UK) and HCl (concentration 36 %) (BDH, Poole, Dorset, UK) with Milli - Q water.

CHAPTER 3

Preliminary Optical Studies

3 PRELIMINARY OPTICAL STUDIES

3.1 INTRODUCTION

Mass spectrometric studies are widely used to determine the influence of operating parameters on both analytes and interferences^{125,134-152}. The resulting signals, however, may not be representative of the behaviour of these species within the plasma, as the sampled ions may be affected as they travel through the mass spectrometer to the detector. Optical studies can be used to determine the influence of different operating parameters on various species directly in the plasma, without the influence of any external parameters, such as the extraction system. Optical studies, in conjunction with mass spectrometric studies, may therefore provide additional information on the behaviour of the selected species, which would not be possible solely with mass spectrometric studies. It is also possible to perform optical studies in different regions of the ICP - MS, i.e. in the plasma and the interface of the ICP - MS, which may facilitate the determination of the site of formation of molecular ion interferences.

Therefore, simultaneous optical and mass spectrometric studies of species within the ICP - MS may provide a useful tool into the understanding of interference behaviour and formation within the ICP.

3.2 EXPERIMENTAL

3.2.1 Plasma Studies (Effect of Sampling Depth)

Experiments were conducted using a PlasmaQuad 2+ ICP - MS (VG Elemental, Ion Path, Road Three, Winsford, Cheshire, UK), as described in Section 2.1.1. Optical measurements of the plasma were performed using a SPEX 1704 monochromator

(SPEX, Edison, New Jersey, US), with pre - installed Scadas operating software.

Operating parameters are given in Table 3.1.

Table 3.1: Operating conditions for the SPEX 1704 monochromator used for optical observation of the plasma

Slit Widths (μm)	
Entrance	30
Exit	30
Slit Height (mm)	2
Voltage Applied to	
Photomultiplier (V)	600

A 1000 μm core diameter HPSUV1000P optical fibre cable (Oxford Electronics Ltd., Four Marks, Hampshire, UK) was used to transfer the light emitted from the plasma to the monochromator. The fibre optic consisted of a high purity silica core with doped silica cladding and an acrylate coating, and was fitted with SMA connectors at each end. The transmission range of the fibre optic was from 180 to 1200 nm. The fibre optic was held in place in front of the entrance slit of the monochromator using a modified blanking disc, which secured on to the front of the monochromator. The other end of the fibre optic was attached to an XY translation stage using a fibre optic holder (Oriel Ltd., Leatherhead, Surrey, UK) which screwed onto the translation stage. The light from the plasma was focused on to the end of the fibre optic using a 1 cm diameter lens, with a focal length determined to be approx. 8 cm, which was attached to the side of the torchbox. A schematic diagram of this arrangement is shown in Figure 3.1. The region of the plasma being sampled could be altered using the XY translation stage.

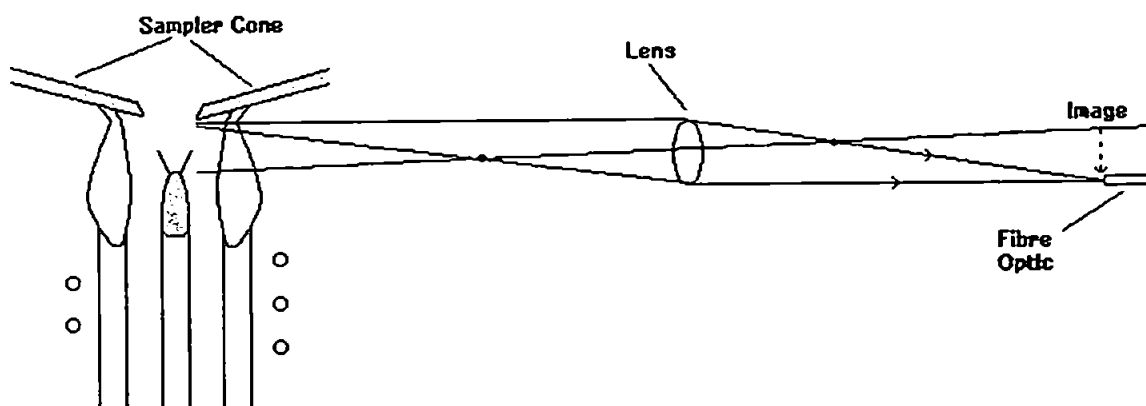


Figure 3.1: Schematic diagram of the optical arrangement used to image the plasma onto the tip of the fibre optic

The central channel of the plasma, at the tip of the sampler cone, was focused on the fibre optic using the emission observed from $10,000 \mu\text{g ml}^{-1}$ yttrium solution. A solution of $10 \mu\text{g ml}^{-1}$ titanium standard was aspirated into the plasma in order to monitor titanium and titanium oxide signals simultaneously by mass spectrometric and optical methods. Ti^+ was monitored mass spectrometrically at $m/z = 49$ and optically at a wavelength of 368.52 nm . TiO^+ was monitored mass spectrometrically at $m/z = 65$. However, there was no wavelength available for the titanium oxide ion and so the neutral titanium oxide was monitored optically at a wavelength of 617.44 nm . A high concentration of Ti solution was necessary in order to observe the optical signals. However, this meant that the ion lens of the mass spectrometer had to be detuned in order to monitor such a high concentration of Ti solution without overloading the detector.

A mass spectrometric sampling depth profile was obtained from 8 to 16 mm by positioning the torchbox as far forward as possible and then moving it back at 1 mm intervals. Sampling depth is defined as the distance between the first turn of the load coil and the tip of the sampling cone. Two methods of observing the axial channel of the plasma were employed, as shown in Figures 3.2 and 3.3. First (Figure 3.2), the observation region was fixed at a point just in front of the tip of the sampling cone, and the plasma was moved, by moving the torchbox, such that the region corresponding to a sampling depth between 8 - 16 mm was observed. This method sampled the optical profile in the same way as the mass spectrometric profile was obtained, and so both profiles were sampled from the same region of the plasma and hence a direct comparison was possible.

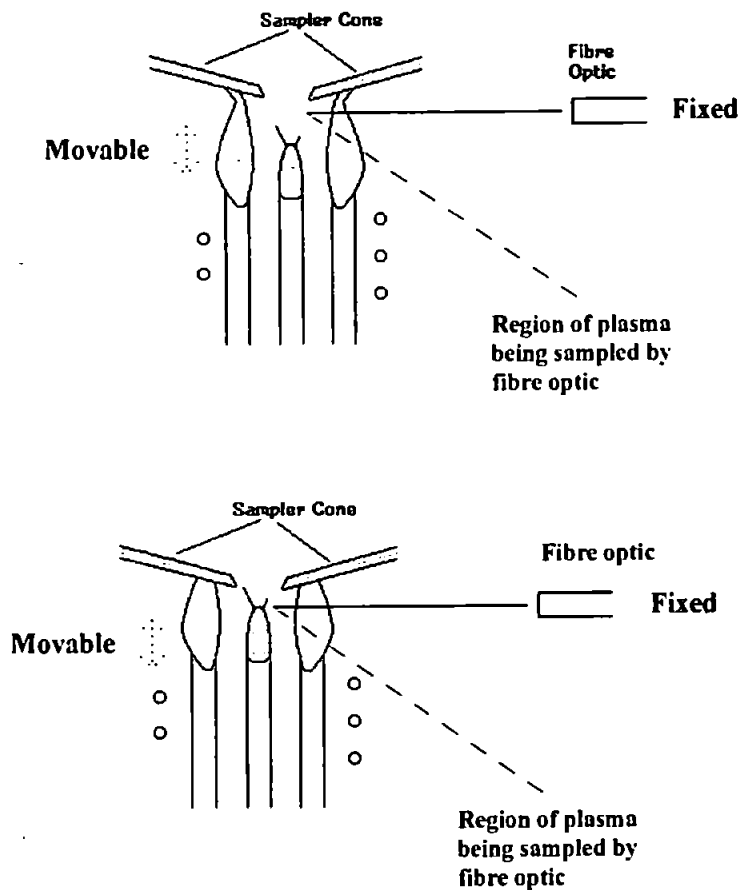


Figure 3.2: Schematic diagram to show optical sampling of the plasma where the plasma is moved to create a sampling depth profile

Second (Figure 3.3), the plasma was fixed at various sampling depths and the optical observation region was moved along the axial channel at 0.66 mm intervals, by moving the focusing lens and fibre optic assembly, from just in front of the top edge of the torch to the tip of the sampling cone. This extended the sampling depth profile down to the base of the plasma and the load coil. Three different sampling depths, of 8 mm, 11.5 mm, and 15 mm were chosen, representing the range of typical sampling depths used in ICP - MS studies. Unfortunately, a comparative mass spectrometric study was not possible since the optical and mass spectrometric probes were sampling from different regions of the plasma.

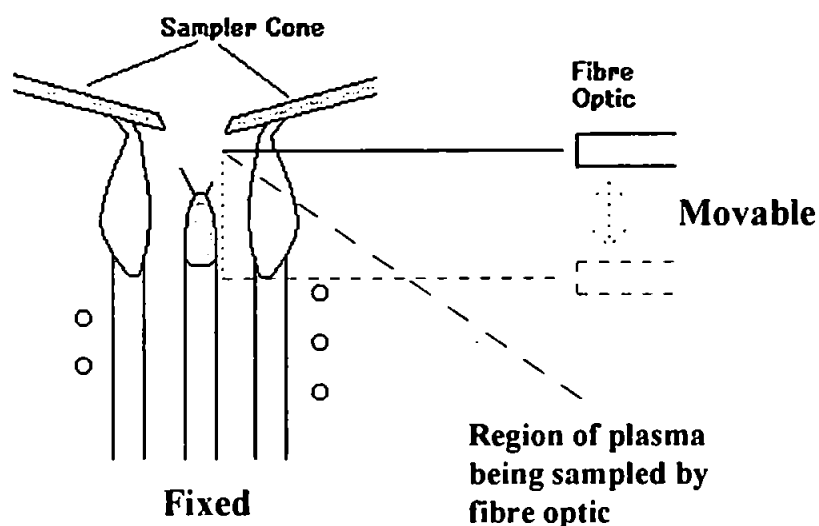


Figure 3.3: Schematic diagram to show optical sampling of the plasma where the fibre optic is moved to create a sampling depth profile

3.2.2 Interface Studies (Effect of Power)

Experiments were conducted using a PlasmaQuad 3 (VG Elemental, Ion Path, Road Three, Winsford, Cheshire, UK), as described in Section 2.1.2. Optical measurements of the interface were performed using a SPEX 1704 monochromator

(SPEX, Edison, New Jersey, US), with Spectrad operating software (Glen Spectra Ltd., Stanmore, Middlesex, UK). Operating parameters are given in Table 3.2.

Table 3.2: Operating conditions for the SPEX 1704 monochromator used for optical observation of the interface

Slit Widths (μm)	
Entrance	30
Exit	30
Slit Height (mm)	2
Voltage Applied to	
Photomultiplier (V)	850

A 1000 μm core diameter HPSUV1000A optical fibre cable (Oxford Electronics Ltd., Four Marks, Hampshire, UK) was used to transfer the light emitted from the interface to the monochromator. The fibre optic consisted of a high purity silica core with doped silica cladding and an aluminium coating, which had an operating temperature up to 400 $^{\circ}\text{C}$, in order to withstand the temperature in the interface. The transmission range of the fibre optic was from 180 to 1200 nm. The fibre optic was fitted with an SMA connector at one end and this was held in place in front of the entrance slit of the monochromator using a modified blanking disc, which secured on to the front of the monochromator. The other end of the fibre optic had a simple polished end, with no connectors, which was inserted in to the end of a modified expansion chamber and held in place with UltraTorr fittings (Bristol Valve & Fitting Co. Ltd., Avonmouth, Bristol, UK), to maintain the pressure inside the expansion chamber. A schematic diagram of this arrangement is shown in Figure 3.4.

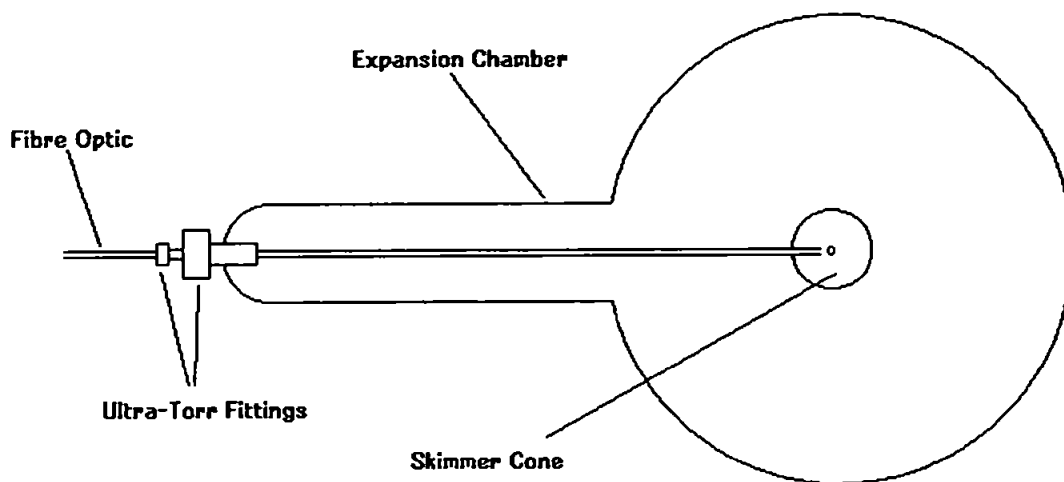


Figure 3.4: Schematic diagram of the fibre optic arrangement used to observe the interface region of the ICP - MS

The fibre optic was positioned to sample light from the tip of the skimmer cone with the use of a ceramic spacer used in the lens stack assembly. This set - up is shown in Figure 3.5. Without the ceramic spacer the fibre optic would be sampling light from the wall of the skimmer cone.

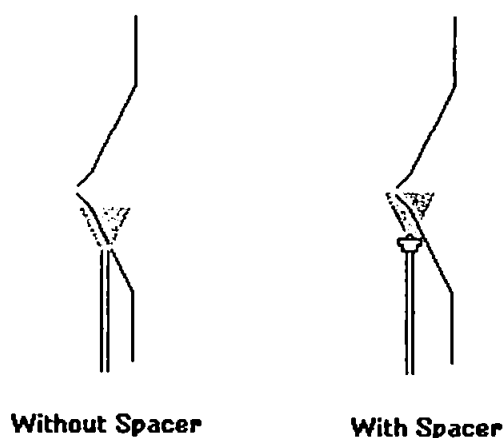


Figure 3.5: Schematic diagram of the tip of the fibre optic and spacer

Deionised water was aspirated into the plasma in order to monitor OH signals. Power profiles of the OH signal were obtained from 550 to 1600 W at 50 W intervals, using standard ICP - MS operating conditions and a sampling depth of 16 mm. The OH signals were monitored optically within the interface using the Q₁ branches of the OH (0 - 0) band at wavelengths between 307.5 and 310 nm. The wavelengths of the Q₁ branches monitored are given in Table 3.3.

Table 3.3: Wavelengths of the Q₁ branches of the OH (0 - 0) band monitored optically within the interface of the ICP.

Q ₁ Branch	Wavelength (nm)
1	307.844
2	307.995
4	308.328
5	308.520
6	308.734
8	309.239
9	309.534

3.3 RESULTS AND DISCUSSION

3.3.1 Plasma Studies (Effect of Sampling Depth)

The mass spectrometric and optical viewing depth profiles for Ti⁺ within the plasma are shown in Figures 3.6 and 3.7 respectively.

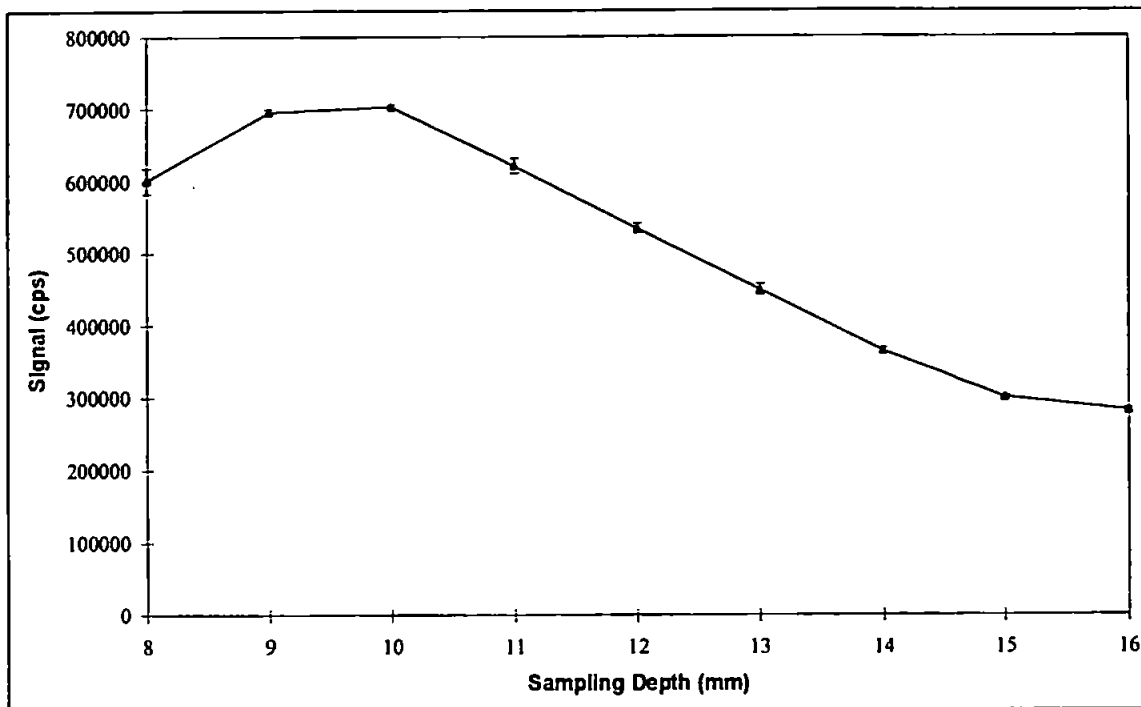


Figure 3.6: Mass spectrometric sampling depth profile for Ti^+ within the plasma.

Errors = 3σ for $n = 3$.

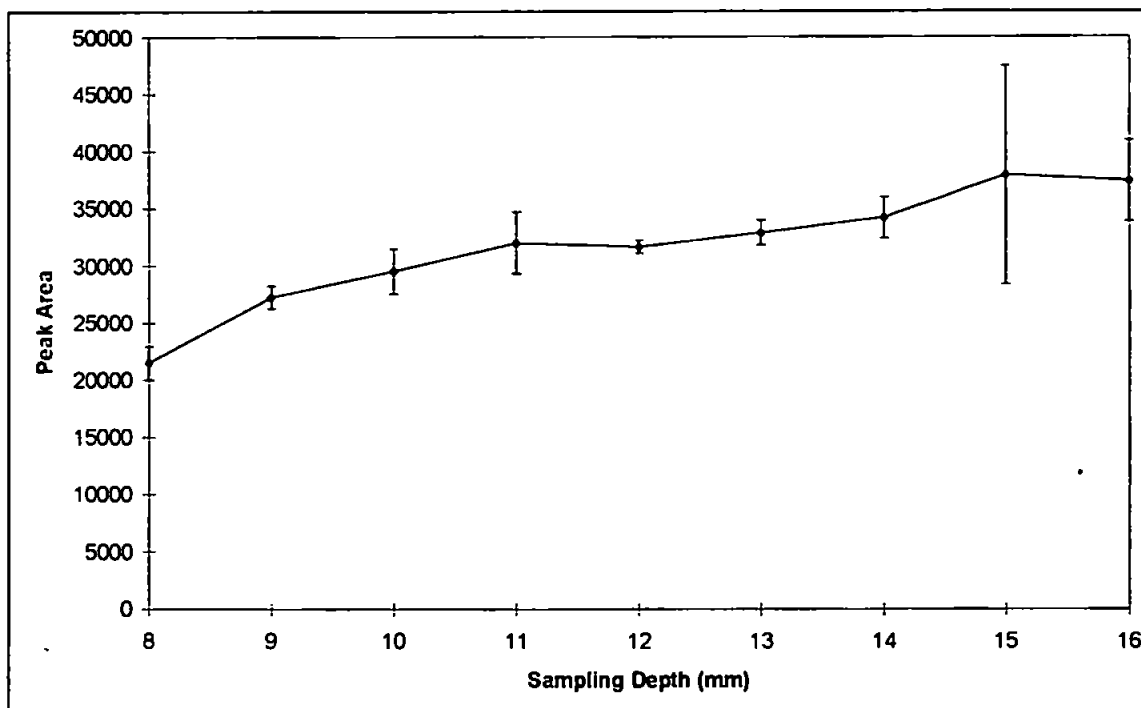


Figure 3.7: Optical sampling depth profile for Ti^+ within the plasma.

Errors = 3σ for $n = 3$.

These results show that the mass spectrometric signal for Ti^+ increased to a maximum at a sampling depth of 10 mm and then decreased as the sampling depth was increased further, while the optical signal for Ti^+ increased as the sampling depth was increased, and levelled off at a sampling depth of 16 mm.

This behaviour can be explained with reference to the two main zones in the ICP, the initial radiation zone (IRZ) and the normal analytical zone (NAZ). In ICP - AES the NAZ is generally associated with the position at which the most intense ion line emission is observed, while the IRZ is where the most intense neutral atom line emission is observed^{136,249}. In ICP - MS the optimum observation zone is somewhere between the IRZ and NAZ¹³⁶, which is at a sampling depth of approximately 5 - 15 mm³⁰³. At small sampling depths, corresponding to the IRZ, analytes introduced into the plasma have a short residence time in the plasma. This short residence time in the plasma leads to reduced ionisation of the analyte species. As the sampling depth is increased the residence time of analytes in the plasma increases, and so the analytes are present in the plasma long enough for efficient ionisation to occur³⁰³. Therefore, as the sampling depth is increased from the IRZ to the NAZ, the analyte signal intensity increases, as the analyte is being more effectively ionised^{304,305}. However, at greater sampling depths the plasma gas becomes cooler and so the ion population is lower, as the analyte is no longer being effectively ionised at the lower temperatures and hence the analyte signal decreases¹³⁸. Therefore a zone of maximum intensity is exhibited³⁸. This zone of maximum intensity was observed for the mass spectrometric signal, while the optical signal had possibly just reached a maximum at a sampling depth of 16 mm.

Previous studies on the effect of sampling depth on metal analyte species include Mg^+ ¹³⁹, Co^+ ^{138,139}, Cd^+ ¹³⁹, Ba^+ ^{138,139,144}, Pb^+ ^{138,139}, Be^+ ¹³⁸, In^+ ¹³⁸, and Ce^+ ¹⁴⁴. All the species were studied over different sampling depth ranges. However, the majority of species reached a maximum signal intensity at sampling depths between 5 and 10 mm,

and then decreased as the sampling depth was increased further. The remainder of the species were studied at sampling depth ranges which started above 15 mm. These species all reached a maximum signal intensity at the lowest sampling depth studied. The effect of sampling depth on the optical emission signals for Pb^{+306} , Cd^{+306} , $\text{Mg}^{+306,307}$ and Y^{+305} have also been studied. All of the signals reached a maximum signal intensity at a sampling depth around 10 mm.

Therefore, other studies show that the maximum analyte signal occurred at sampling depths between 5 and 10 mm, which corresponds to the mass spectrometric results of this study, where the analyte signal reached a maximum at a sampling depth of 10 mm. The optical results showed a maximum analyte signal at a larger sampling depth, around 15 mm. However, this could be explained due to the system which is being monitored optically. The previous optical studies have studied analyte species in an ICP - AES, where the plasma is independent of the detection optics. However, in this study analyte species were studied optically in an ICP - MS, where the plasma is coupled intimately to the extraction system which sits in the middle of the plasma. Therefore, the presence of the extraction system within the plasma may alter the behaviour of the analyte species within the plasma.

Comparison of the optical and mass spectrometric sampling depth profiles for Ti^{+} show no correlation between the two signals, whereas they would be expected to exhibit the same trend as they are sampled from the same region of the plasma. However, while the optical signal is sampled directly from the plasma the mass spectrometric signal has to travel through the mass spectrometer prior to detection. The influence of the sampling process, under high vacuum, is not known and this could explain the difference observed in the optical and mass spectrometric data.

The mass spectrometric and optical sampling depth profiles of TiO^{+} and TiO within the plasma are shown in Figures 3.8 and 3.9 respectively.

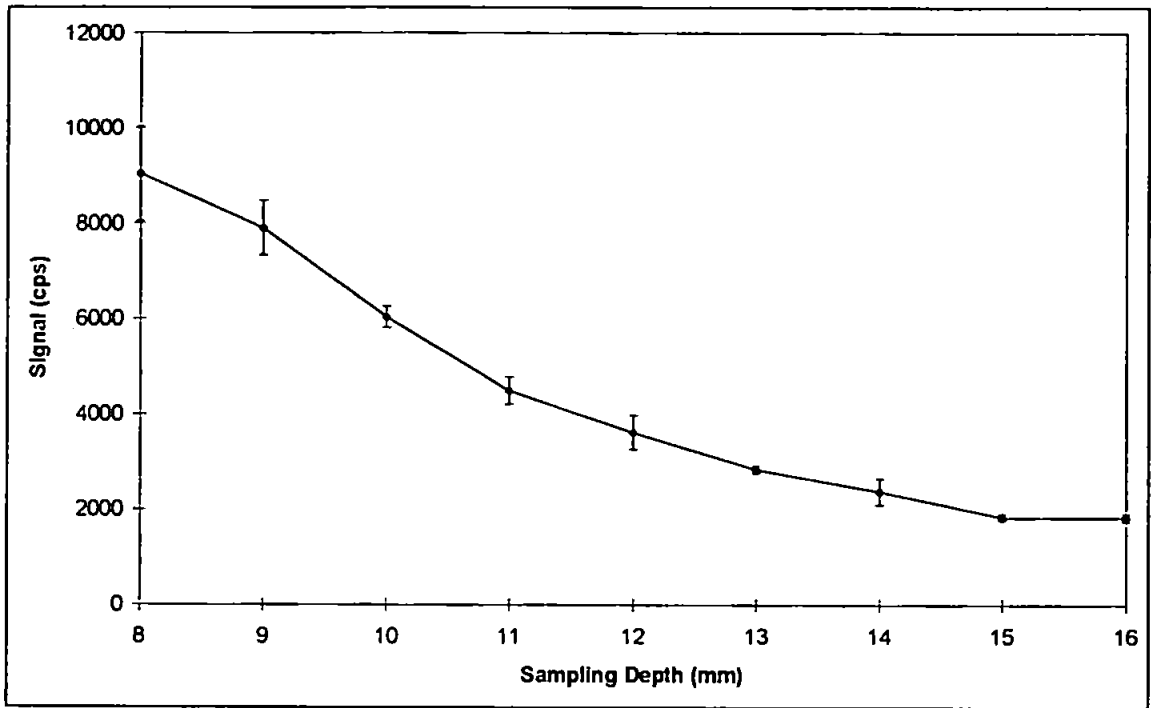


Figure 3.8: Mass spectrometric sampling depth profile for TiO^+ within the plasma.

Errors = 3σ for $n = 3$.

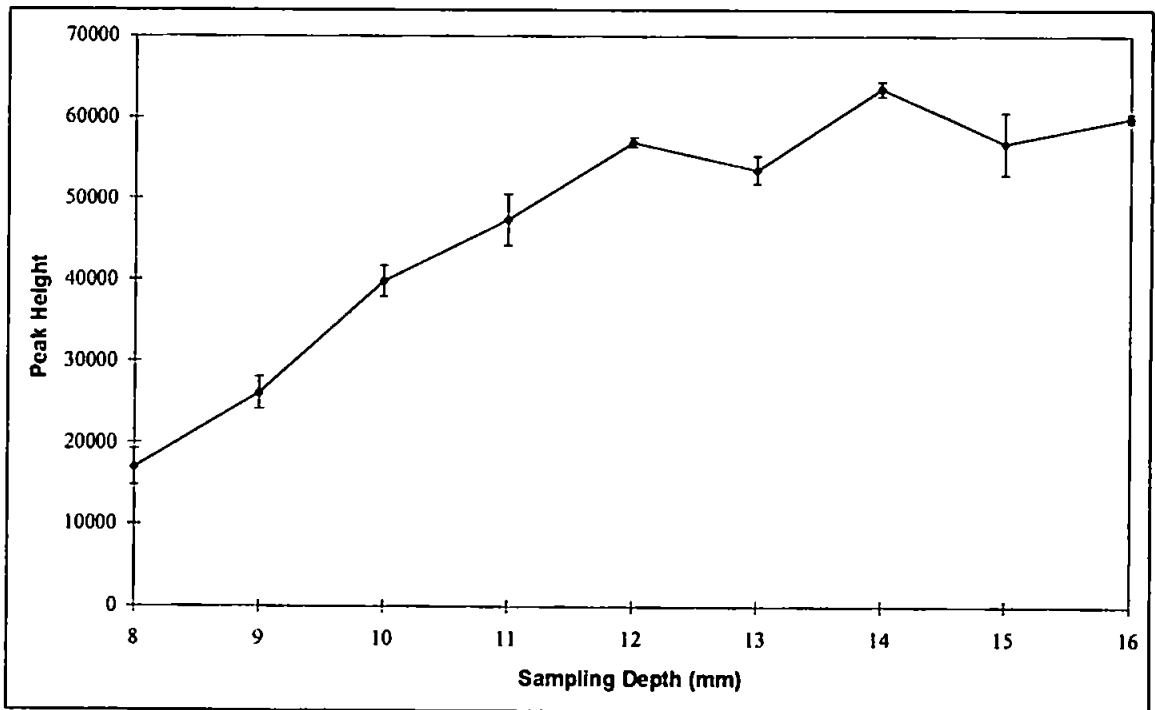


Figure 3.9: Optical sampling depth profile for TiO within the plasma.

Errors = 3σ for $n = 3$.

These results show that the mass spectrometric signal for TiO^+ decreased as the sampling depth was increased. At low sampling depths the analytes are being sampled from the IRZ, where a short residence time in the plasma can lead to insufficient dissociation of any metal oxide species present in the plasma¹⁴⁴. As the sampling depth is increased the sampling region of the ICP moves from the IRZ to the NAZ, resulting in promotion of MO^+ dissociation^{58,142}. Molecular dissociation occurs progressively along the axial channel of the plasma³⁰⁸, because at larger sampling depths a long residence time in the plasma results in effective dissociation of the metal oxide. Therefore, a zone of maximum intensity is exhibited as the oxide is progressively formed and then dissociated again. Therefore, at the sampling depths studied, which started at 8 mm, the maximum signal intensity had probably already occurred lower down in the plasma, and only the decrease in signal, as the sampling depth was increased from this position, was observed.

Previous studies have investigated the effect of sampling depth on various metal oxide species, including CeO^+ ^{125,139}, BaO^+ ¹³⁹, GdO^+ ⁵⁸ and TbO^+ ⁵⁸. In all cases it was found that either the metal oxide signal or the MO^+ / M^+ ratio decreased as the sampling depth was increased, as found in this study.

The optical sampling depth profile for TiO is shown in Figure 3.9. The optical signal for TiO increased as the sampling depth was increased, until a sampling depth of 12 mm, after which the signal remained fairly constant. This differed from the trend observed for YO by Furuta³⁰⁵ using ICP - AES. He found that the YO emission was localised low in the central channel of the plasma, between sampling depths of 0 and 10 mm, with a maximum occurring about 5 mm. However, in this study the analyte species were being sampled from a plasma which is coupled intimately to the extraction system which sits in the middle of the plasma, and may alter the behaviour of the analyte species within the plasma.

Comparison of the mass spectrometric and optical sampling depth profiles show that the optical signal exhibited a different trend from the mass spectrometric signal. The optical signal for neutral TiO increased as the sampling depth was increased, while the mass spectrometric signal for TiO^+ decreased as the sampling depth was increased. As the sampling depth was increased the TiO^+ signal decreased as longer residence times in the plasma resulted in more efficient dissociation of the metal oxide ion. This was reflected in the optical signal for neutral TiO, which increased as the sampling depth was increased. Therefore, an increase in sampling depth resulted in a decrease of the TiO^+ signal and an increase in neutral TiO, as the TiO^+ was reduced to the neutral molecule. Hence, simultaneous optical and mass spectrometric studies show that the TiO^+ ion was not being dissociated in the plasma, but reduced to neutral TiO.

The optical sampling depth profiles for TiO at different positions of the torchbox are shown in Figure 3.10. The plots are arranged so that they are zeroed at the load coil (sampling depth = 0 mm). Hence, the sampler cone was at sampling depths of 8 mm (TB = 0), 11.5 mm (TB = 7) and 15 mm (TB = 14).

These results show that at each position of the torchbox (TB) the TiO signal increased, reached a maximum, and then decreased again. This trend would be expected for neutral metal oxides, which are most probably formed by collisional mechanisms¹⁴². At the load coil a low signal for neutral metal oxides would be expected, since there was little time for these collisional processes to occur, and this signal would increase as the sampling depth was increased, due to increased collisional formation of MO. However, molecular dissociation occurs progressively along the axial channel of the plasma¹⁴⁴, which would lead to a decrease in the signal. Therefore, a maximum signal would occur as the oxide was progressively formed and then dissociated again. In accordance to this theory the plot for the maximum sampling depth profile (TB = 14) would exhibit this trend, with the signal increasing, reaching a maximum and then decreasing again.

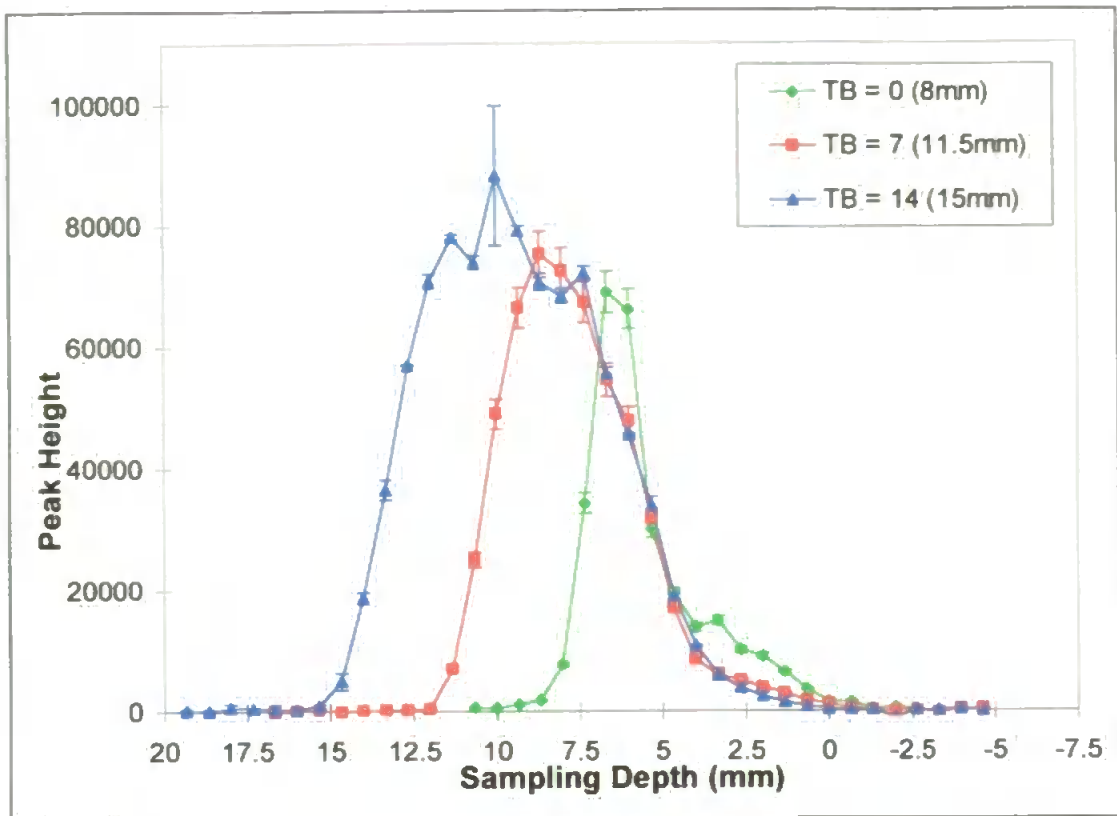


Figure 3.10: Comparison of optical sampling depth profiles for TiO within the plasma, at different sampling depth positions. Errors = 3σ for $n = 3$.

However, the plots for the minimum (TB = 0) and the intermediate (TB = 7) sampling depth profiles had shorter measurable profiles, so it would be expected that the signal was prematurely cut off by the tip of the sampler cone, rather than decreasing naturally. This can be seen in Figure 3.10 where the signal for TB = 14 decreased gradually as the tip of the sampler cone was approached. The signal for TB = 7 decreased more sharply as the tip of the sampler cone was approached, although there was some indication that the signal was beginning to decrease naturally. The signal for TB = 0 decreased very sharply as the tip of the sampler cone was approached. Therefore, these results show that with short sampling depth profiles the signal is greatly affected by the sampler cone, which prematurely cut off the signal. However, with greater sampling depth profiles the sampler cone was less significant as the signal began to decrease naturally.

3.3.2 Interface Studies (Effect of Power)

A typical optical spectrum for (0 - 0) band emission from OH, showing the Q_1 branches is shown in Figure 3.11. The optical power profile, within the interface, for the Q_1^1 branch, at 307.844 nm, of the (0 - 0) band emission from OH is shown in Figure 3.12.

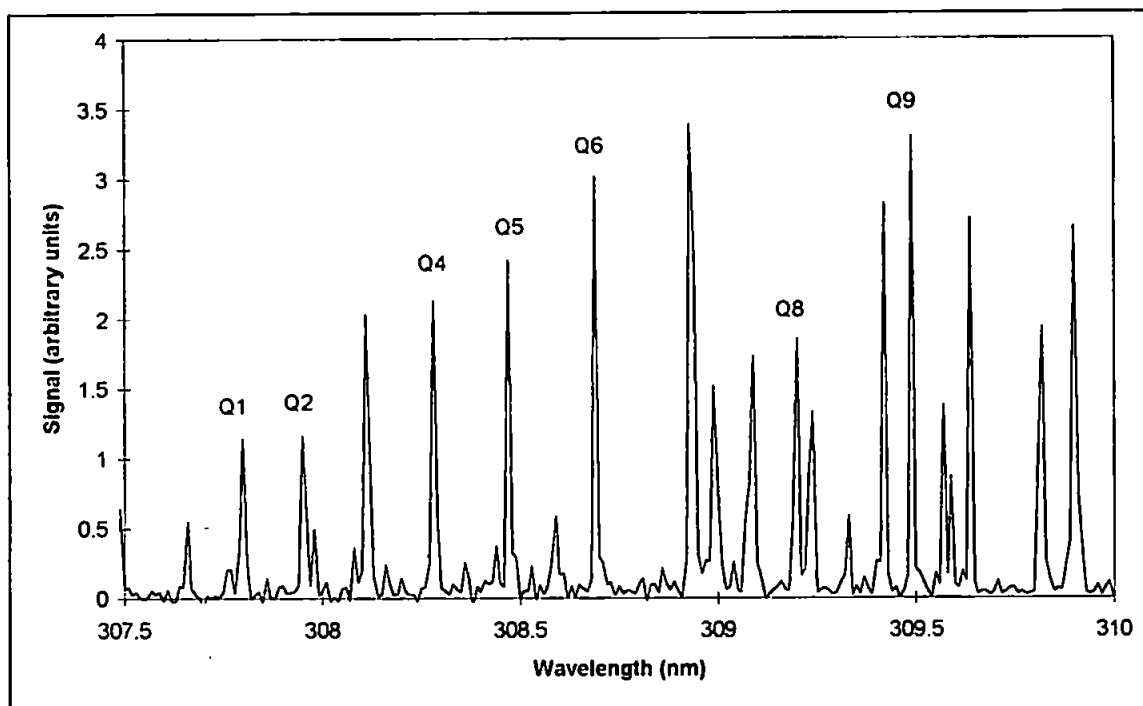


Figure 3.11: Typical optical spectrum of OH (0 - 0) band emission showing Q_1 branches.

These results show that the optical signal for OH in the interface remained fairly constant as the power of the plasma was altered, although the signals obtained were not very reproducible, with large RSDs at all powers studied. However, the sensitivity of the fibre optic through the interface was less than half that through the fibre optic normally. This can be seen in Figure 3.13, where a mercury lamp was used to obtain the mercury line at 546.07 nm, which was used as a reference line throughout the optical studies.

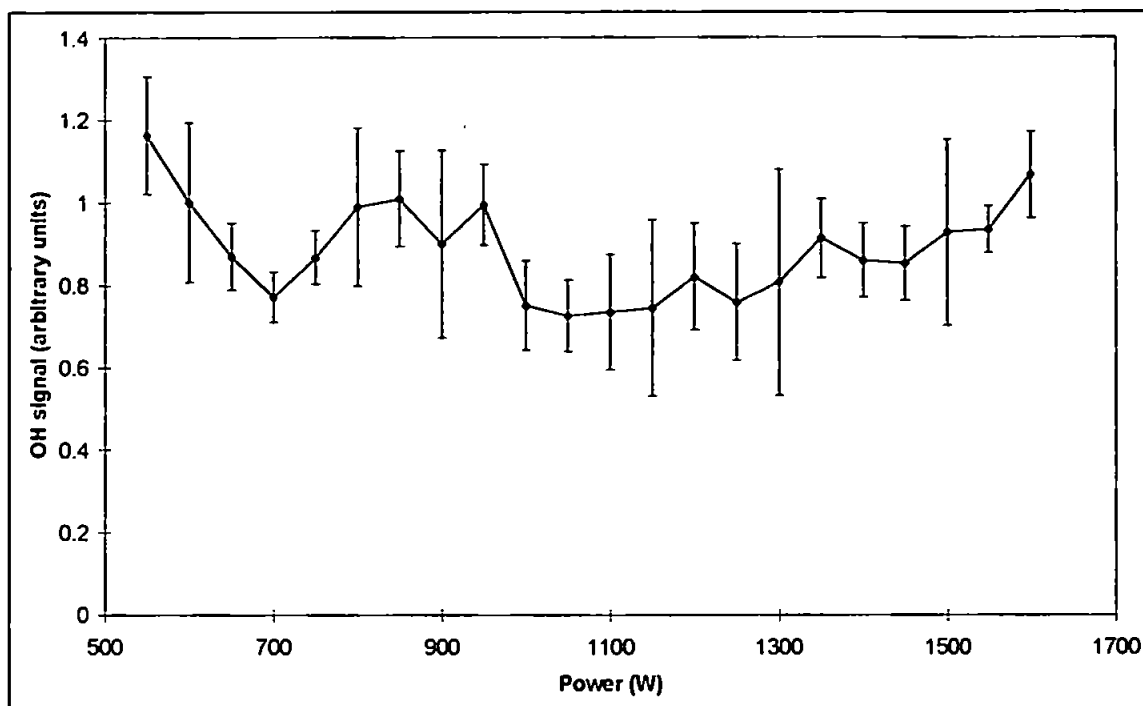


Figure 3.12: Effect of power on the signal for the Q_1^1 branch of the OH (0 - 0) band emission at 307.844 nm within the interface. Errors = 3σ for $n = 3$.

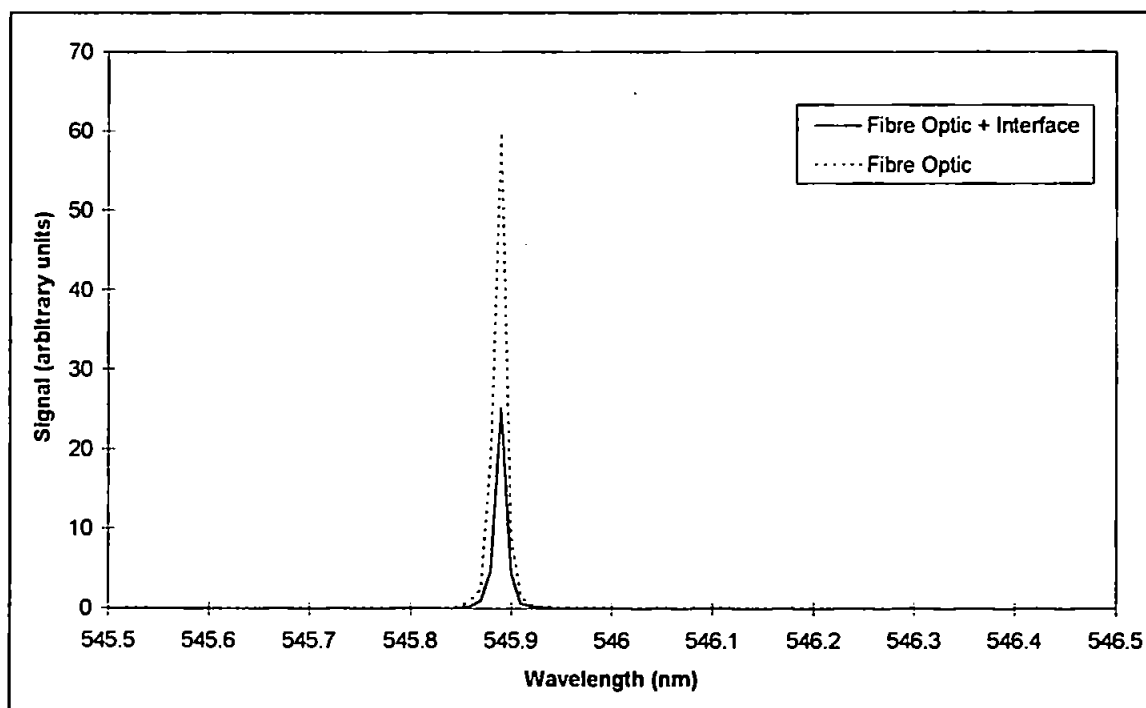


Figure 3.13: Comparison of the optical signal for the Hg reference line (546.07 nm) through the interface and without the interface.

This reduction in signal when monitoring the interface is illustrated in Figure 3.12, where the signal obtained was very low, with poor reproducibility. These low signals and poor RSDs meant that it was not possible to determine a meaningful trend in OH signal with increasing power.

3.3.2.1 OH Rotational Temperature

The OH optical emission data was used to calculate the rotational temperature, from the slope of the graph $\log(I \lambda / A)$ against E , which is given by $-0.625 / T$, where I is the signal intensity, λ is the wavelength, A is the transition probability, E is the energy and T is the temperature, using the assignment, wavelength, energies and transition probability data given in Table 3.4. An example plot is shown in Figure 3.14. This graph was plotted for every power studied, in order to obtain a power profile of the OH rotational temperature within the interface.

Table 3.4: Assignment, wavelengths, energies and transition probabilities for the Q₁ branches of the OH (0 - 0) band²⁸⁸.

K	λ (nm)	E (cm ⁻¹)	A (10 ⁸ s ⁻¹)
1	307.844	32,475	0.0
2	307.995	32,543	17.0
4	308.328	32,779	33.7
5	308.520	32,948	42.2
6	308.734	33,150	50.6
8	309.239	33,652	67.5
9	309.534	33,952	75.8

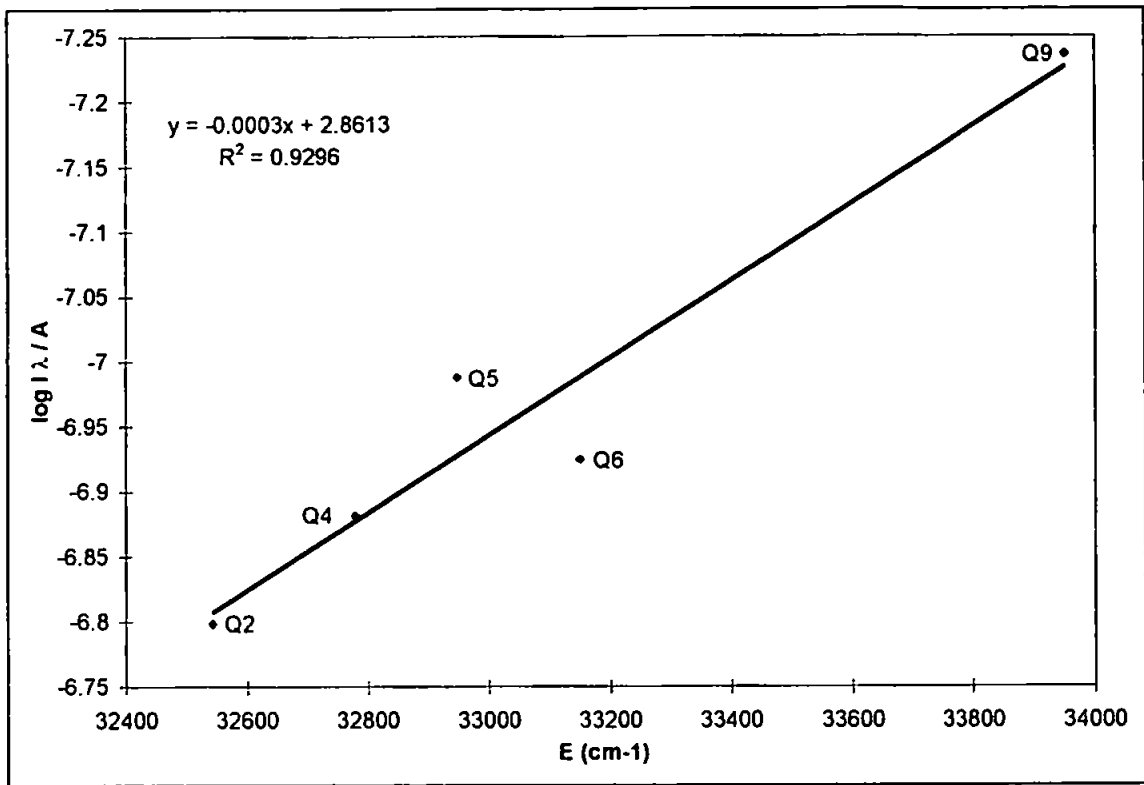


Figure 3.14: Example of Boltzmann plot used to calculate the OH rotational temperature within the interface.

The power profile of the OH rotational temperature within the interface is shown in Figure 3.15. These results show that the temperature within the interface varied from 1700 to 4600 K, although there was no apparent trend in the temperature with the applied forward power. The calculated temperature varied greatly, and this can be seen in the large RSDs obtained for the OH temperature. This could be due to the lack of sensitivity of the fibre optic within the interface, which led to poor reproducibility of the raw OH optical signals obtained. This poor reproducibility in the raw signals would be carried through to the temperatures calculated from this data. Therefore, the low signals and poor reproducibility of the raw OH signals result in a large variation in the calculated temperatures, which also show poor reproducibility, and so it was not possible to determine a meaningful trend in OH rotational temperature with increasing power.

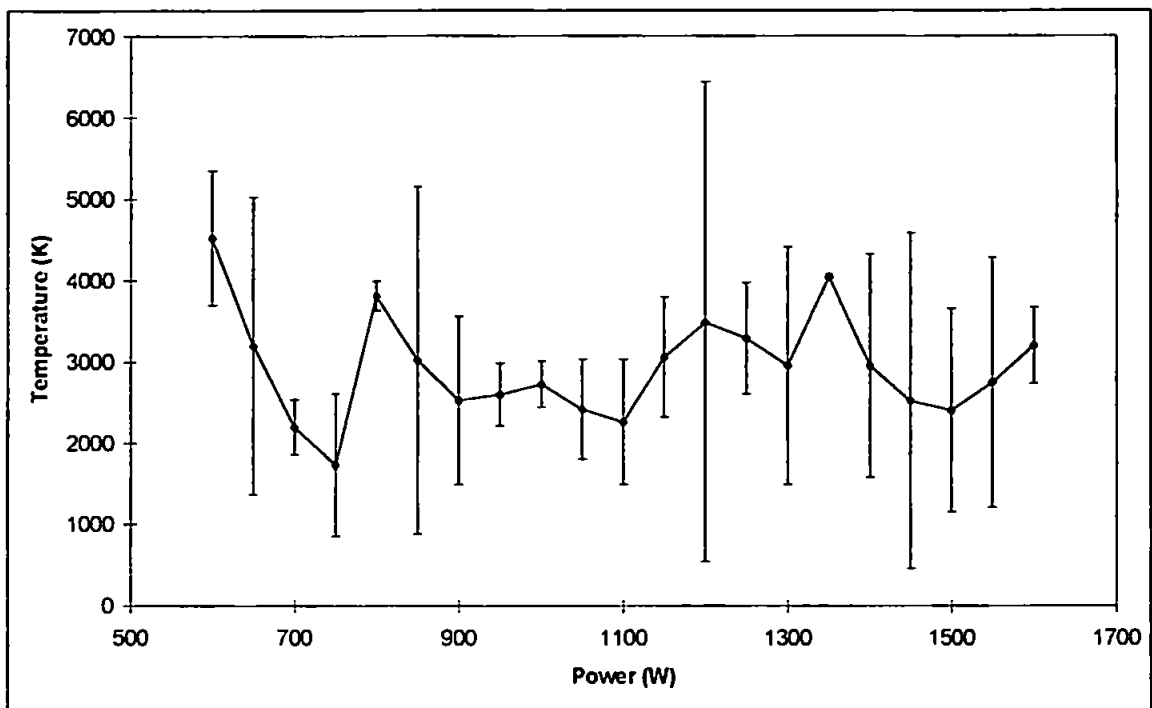


Figure 3.15: Effect of power on the OH rotational temperature within the interface region of the ICP. Errors = 3σ for $n = 3$.

3.4 CONCLUSIONS

There was no correlation between the simultaneous optical and mass spectrometric signals for Ti^+ , although there was a definite correlation between the optical signal of TiO and the mass spectrometric signal for TiO^+ , with the TiO signal increasing as the TiO^+ signal decreased. Therefore, while mass spectrometric studies would indicate that the dissociation of TiO^+ was enhanced with increasing sampling depth, the simultaneous optical studies indicate that the TiO^+ was being reduced to neutral TiO , rather than dissociated Ti^+ and O , due to the increase in the optical TiO signal with increasing sampling depth. Therefore, the simultaneous optical and mass spectrometric studies may provide an insight into the formation mechanisms occurring within the plasma, which would not be possible with only mass spectrometric studies.

Both the Ti^+ and TiO signals monitored optically exhibited trends different to previous studies performed with ICP - AES. This suggests that the extraction system, which sits in the middle of the plasma in ICP - MS, may alter the detected signal of the analyte species, when compared to optical measurements which are independent of the mass detection system.

In the interface region of the ICP - MS the optical signals were very low with poor reproducibility, which affected the OH rotational temperatures calculated from them. This could be due to the reduced signal through the interface, which was half the intensity of the signal not through the interface. However, in general it was very difficult to detect any signal in the interface region of the ICP - MS, with the OH signal being the only signal which could be determined within the interface.

Due to problems with the monochromator it was necessary to change the operating software, and following this it was difficult to obtain signals in the plasma as well as the interface, and so it proved very difficult to obtain signals which would be sensitive enough to perform temperature or electron number density calculations. In addition, the species of most interest to study optically in the plasma and interface, i.e. the argon polyatomic ion interferences, suffered from a lack of available reference wavelength data and so could not be measured optically. Therefore, although simultaneous optical and mass spectrometric studies had the potential to provide information on possible formation mechanisms and sites of formation, it was not possible to study the analytes of interest with the equipment available.

CHAPTER 4

Critical Comparison Of Temperature Determination

Methods By ICP - MS

4 CRITICAL COMPARISON OF TEMPERATURE DETERMINATION METHODS BY ICP - MS

4.1 INTRODUCTION

A single temperature for the ICP cannot be determined explicitly because local thermodynamic equilibrium (LTE) does not prevail in the plasma^{304,309}. If the plasma is in a state of LTE then $T_{kin} = T_e = T_{exc} = T_{ion}$. However, this has been found to not be the case for an argon atmospheric pressure ICP³¹⁰, and the determined temperatures give different values by the definition of the temperature. In general the temperature within the ICP is decreasing in the order of electron temperature (T_e), ionisation temperature (T_{ion}), excitation temperature (T_{exc}) and rotational temperature (T_{rot})³⁰⁴.

The majority of techniques used to determine the temperature within the plasma involve optical measurements, although it is also possible to calculate the temperature of the plasma using mass spectrometric data^{144,249,250,311-314}, and both ionisation temperature, (T_{ion})³¹¹⁻³¹³, and dissociation temperature, (T_{diss})^{144,249,250,314} have been calculated using mass spectrometric means. The ion sampling process in ICP - MS is inherently radially resolved, so there is no need to perform an Abel inversion, which is used in optical emission experiments to construct radial emission profiles from line - of - sight intensity measurements, thereby introducing substantial imprecision in the measured emission profiles. Thus, mass spectrometric methods would be expected to produce more reliable T_{ion} values, provided that the relative ion abundances measured by the mass spectrometer reflect the relative population of ions in the plasma³¹¹.

4.1.1 Ionisation Temperature

The ionisation temperature can be calculated using the Saha equation²⁴⁹
(Equation 4.1)

$$\log K_{\text{ion}}(M) = 1.5 \log T_{\text{ion}} - 5040 (IE_M) / T_{\text{ion}} + \log (Z_{M^+} / Z_M) + 15.684 \quad (4.1)$$

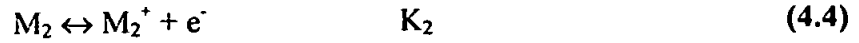
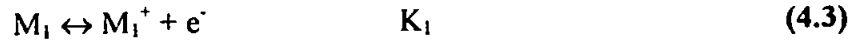
where Z = the partition function
 IE = the ionisation energy
 T_{ion} = ionisation temperature
 K_{ion} = equilibrium constant.

If the relative abundances of the ions, atoms and electrons are known the equilibrium constant can be calculated (Equation 4.2) and used to solve for T_{ion} in the Saha equation.

$$M \leftrightarrow M^+ + e^- \quad K_{\text{ion}}(M) = n_{M^+} n_{e^-} / n_M \quad (4.2)$$

where n_{M^+} = abundance of metal ion
 n_{e^-} = abundance of electrons
 n_M = abundance of metal atom.

It is usual to calculate the temperature from the ratio of singly charged ions of different elements which are similar in mass, thereby reducing the influence of mass bias in the results. This involves the determination of the relative numbers of singly charged ions formed from two elements (M_1 and M_2) of different ionisation energies³¹³. The same T_{ion} is assumed for the reactions:



where K = equilibrium constant.

Subtracting the logarithmic forms of the Saha equation for K_2 from that for K_1 leads to the relationship

$$\log (K_1 / K_2) = [5040 (IE_2 - IE_1) / T_{ion}] + \log (Z_{M1+} / Z_{M1}) - \log (Z_{M2+} / Z_{M2}) \quad (4.5)$$

The ratio of equilibrium constants in Equation 4.5 may be evaluated as follows

$$\log (K_1 / K_2) = \log [(n_{M1+} / n_{M2+}) (n_{M2} / n_{M1})] \quad (4.6)$$

$$n_M \sim (1 - \alpha) C \quad (4.7)$$

$$\sim (n_{e^-} / (n_{e^-} + K)) C \quad (4.8)$$

$$\log (K_1 / K_2) = \log [(n_{M1+} / n_{M2+}) (n_{e^-} + K_1 / n_{e^-} + K_2) (C_2 / C_1)] \quad (4.9)$$

where α = the degree of ionisation

C = the solution concentration of the indicated element.

The ionisation temperature is taken to be that value which results in equivalence of Equation 4.9 using $n_{e^{-}}$ values taken from the literature³¹³. This method has been used to measure the ionisation temperature of the plasma by comparing the ratio of Cd^{+} / I^{+} ^{312,313}, Sb^{+} / In^{+} ³¹¹ and As^{+} / Ga^{+} ³¹¹.

These calculations can be extended to include doubly charged ions (M^{2+})³¹³.

$$M^{+} \leftrightarrow M^{2+} + e^{-} \quad K'_{ion}(M) = n_{M^{2+}} n_{e^{-}} / n_{M^{+}} \quad (4.10)$$

$$\log K'_{ion}(M) = 1.5 \log T_{ion} - 5040 (IE') / T_{ion} + \log (Z_{M^{2+}} / Z_{M^{+}}) + 15.684 \quad (4.11)$$

where IE' = the second ionisation energy of the element M

$Z_{M^{2+}}$ = the electronic partition function of M^{2+} .

2.1.2 Dissociation Temperature

There are several different methods which can be used to determine the dissociation temperature within the plasma, all based on the dissociation of a diatomic molecular ion (XY^{+})

$$XY^{+} \leftrightarrow X^{+} + Y \quad K_d(XY^{+}) = n_Y n_{X^{+}} / n_{XY^{+}} \quad (4.12)$$

where the equilibrium constant K_d is defined as⁵⁸

$$K_d = (Z_{X^{+}} Z_Y / Z_{XY^{+}}) ((2\pi k T) / h^2)^{3/2} ((M_{X^{+}} M_Y) / M_{XY^{+}})^{3/2} (hcB/k (1 - \exp(-hc\omega/kT)) / T) \exp(-D_0 / kT) \quad (4.13)$$

where M = the species mass
 D_0 = the dissociation energy
 k = the Boltzmann constant
 T = the plasma temperature
 Z = the electronic partition function
 B = the rotational constant
 ω = the vibrational constant.

The majority of these methods use the dissociation of metal oxides^{144,249,314} to calculate the temperature, although other diatomic molecules, such as ArO^+ ²⁴⁹ have also been studied. This method could be used to obtain a dissociation temperature from most diatomic molecules, as long as all the necessary fundamental data exists. A table of existing fundamental data is given in Appendix 1³¹⁵⁻³³¹.

2.2 EXPERIMENTAL

Experiments were conducted using a PlasmaQuad 3 ICP - MS (VG Elemental, Ion Path, Road Three, Winsford, Cheshire, UK), as described in Section 2.1.2. Both ArX^+ and MO^+ interferences were studied at the m/z shown in Table 4.1.

A radial profile of the plasma using standard conditions, at 1350 W, was obtained by moving the torchbox from right to left across the tip of the sampler cone at 0.25 mm intervals, at a sampling depth of 16 mm. A solution containing 10 ng ml⁻¹ MASSCAL (Be, Mg, Co, In, Pb and U) and 100 ng ml⁻¹ Al, Ba, La, Mn, Ti, Y and Zr (in order to obtain MO^+ signals) was aspirated into the plasma. At each position of the radial profile the ion lens and torchbox position in the other two axes were adjusted to obtain a maximum signal for ¹¹⁵In⁺.

Table 4.1: Isotopes studied during radial profile experiment

Species	Mass	Abundance	Species	Mass	Abundance
Al ⁺	27	100	Y ⁺	89	100
Ar ⁺	38	0.1	Zr ⁺	96	2.8
ArH ⁺	39	0.1*	YO ⁺	105	99.8*
AlO ⁺	43	99.8*	ZrO ⁺	106	51.3*
Ti ⁺	49	5.5	In ⁺	115	95.8
Mn ⁺	55	100	Ba ⁺	132	0.1
ArO ⁺	56	99.4*	La ⁺	138	0.1
TiO ⁺	64	73.6*	BaO ⁺	154	71.6*
Ba ²⁺	66	0.1	LaO ⁺	155	99.7*
MnO ⁺	71	99.8*			

* The abundances for the molecular species were calculated by combining the abundances of the two constituent elements. Molecular abundances were obtained by multiplying abundances of constituent elements and then dividing by 100.

4.3 RESULTS AND DISCUSSION

4.3.1 Radial Profile of ArX⁺ and MO⁺ Species

Indium was introduced to act as an internal reference to determine the centre of the plasma. Because the indium solution was aspirated into the plasma the majority should pass through the centre of the central channel, with little signal being observed beyond the central channel of the plasma. The results for ¹¹⁵In⁺, shown in Figure 4.1, indicate that as the torchbox was moved from right to left across the tip of the sampler cone the signal increased, reaching a maximum and then decreased again.

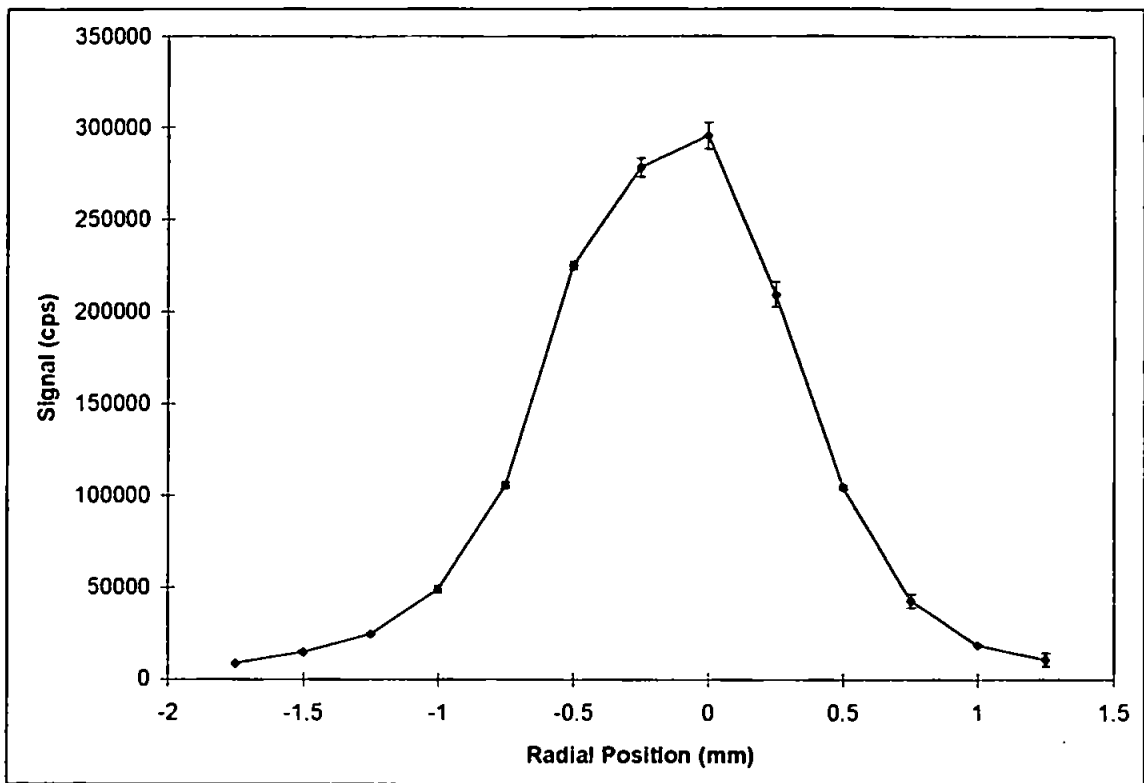


Figure 4.1: Radial profile for $^{115}\text{In}^+$. Errors = 3σ for $n = 3$.

This has been observed for the optical emission of Y^{+305} and Mg^{+307} , where the maximum signal occurs on - axis (i.e. the centre of the plasma) with little signal being observed beyond 3 mm either side of the central axis. Therefore, the position where the maximum In^+ signal was observed in the radial profile of the plasma was taken to be the centre of the plasma. This trend can also be seen for other species which were introduced into the plasma, as shown in Figures 4.2 and 4.3 for $^{132}\text{Ba}^+$ and $^{66}\text{Ba}^{2+}$ respectively.

For these species the signal also exhibited a maximum signal along the central axis, as defined by the In^+ signal, and decreased as the distance from this central axis was increased, with little signal being observed at either edge of the profile. This was also the case for interferences such as metal oxides because, although oxygen is present throughout the plasma, the metals were only introduced through the central channel. This can be seen in Figure 4.4 where the radial profile of all of the seven metal oxides studied, as given in Table 4.1, are compared.

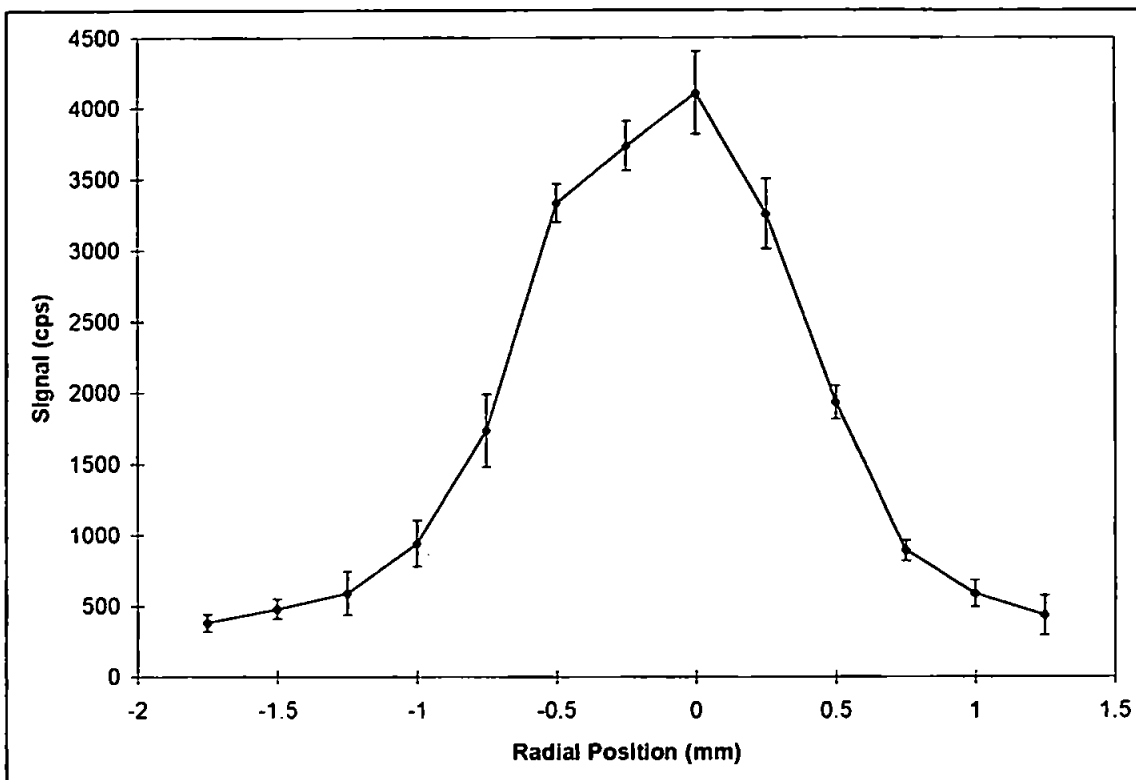


Figure 4.2: Radial profile for Ba⁺. Errors = 3 σ for n = 3.

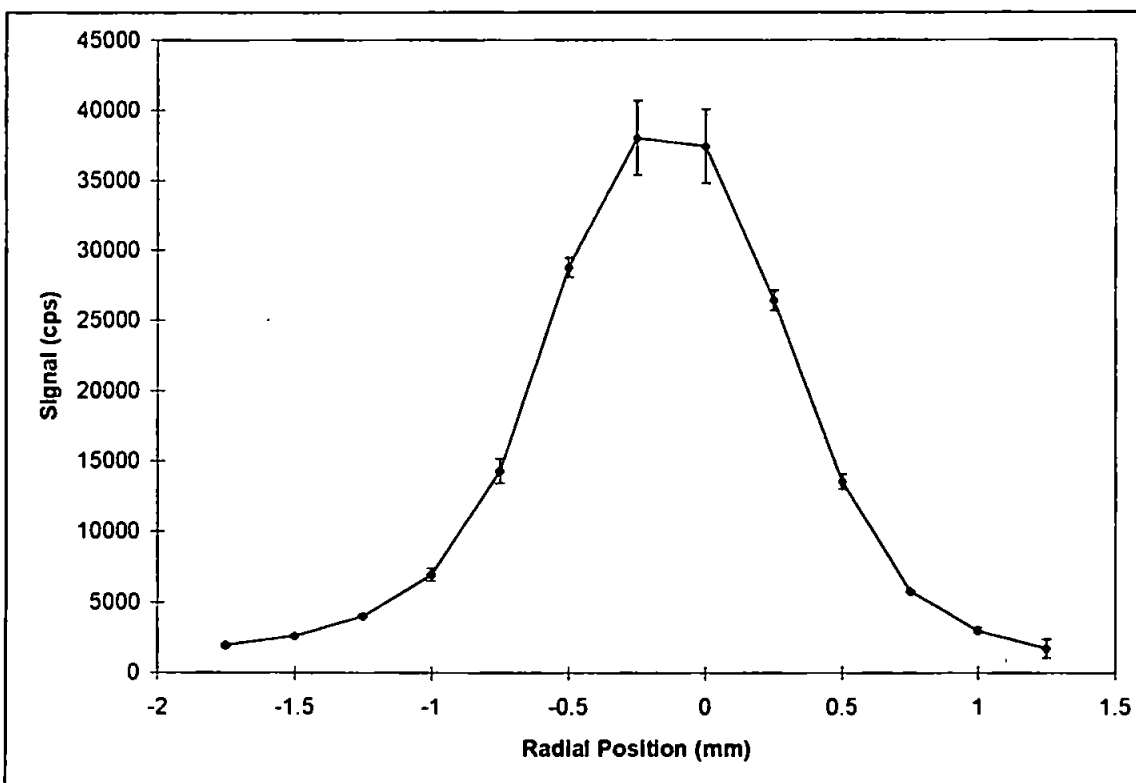


Figure 4.3: Radial profile for Ba²⁺. Errors = 3 σ for n = 3.

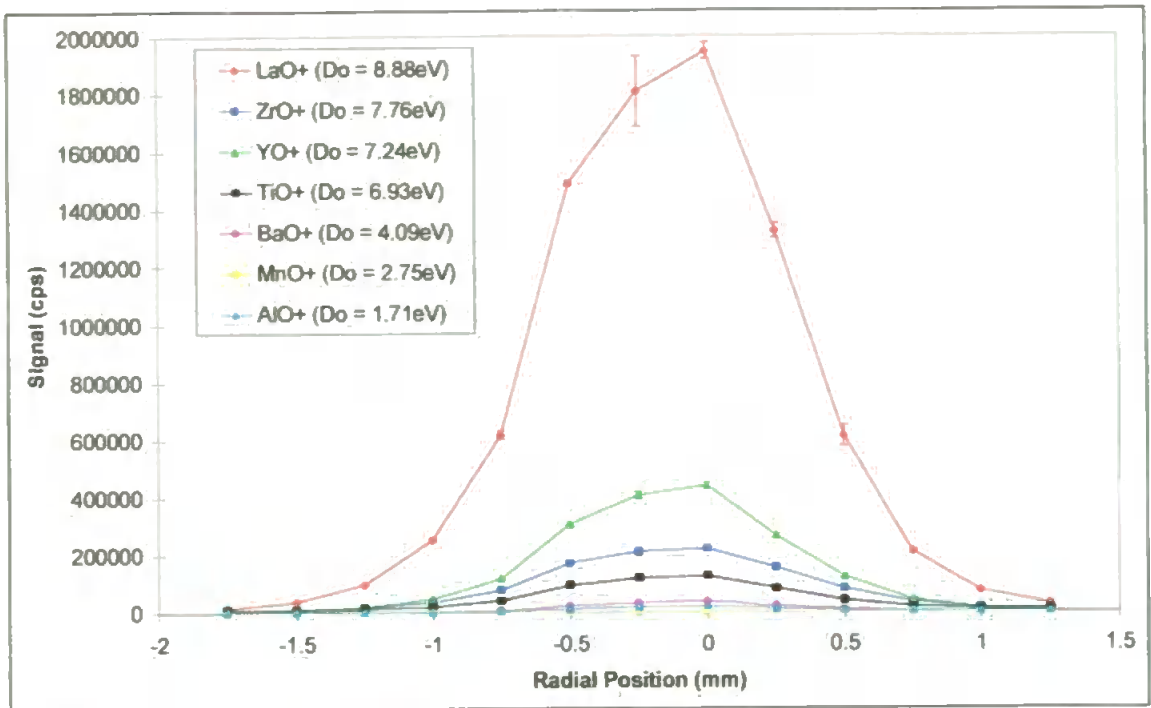


Figure 4.4: Comparison of the radial profiles for MO^+ . Signals normalised to 100% abundance (Signals divided by molecular abundance then multiplied by 100).

Molecular abundances of metal oxides are given in Table 4.1. D_0 values given are for MO^+ . Errors = 3σ for $n = 3$.

Figure 4.4 shows that all of the metal oxides studied exhibited the same trend, with a maximum signal along the central axis of the plasma, and the signal decreasing as the distance from the central axis was increased, with little signal being observed at either edge of the profile. However, the maximum intensity reached varied considerably between each metal oxide species. It can be seen that the intensity of the metal oxide signal varied according to its dissociation energy. Species with a high dissociation energy require large amounts of energy to break the metal oxide bond, so were present in the plasma in large quantities, and hence a large signal was observed. Conversely, species with low dissociation energies require little energy to break the metal oxide bond, were present in the plasma in very small quantities because they have dissociated to a greater

extent, so relatively little signal was observed. This can be seen in Figure 4.4 where LaO^+ , with a high dissociation energy of 8.88 eV, gave rise to a very large signal and AlO^+ , with a low dissociation energy of 1.71 eV, produced virtually no signal.

Other interference ions, such as ArO^+ , showed a broadly similar trend to the metals and metal oxides, as shown in Figure 4.5.

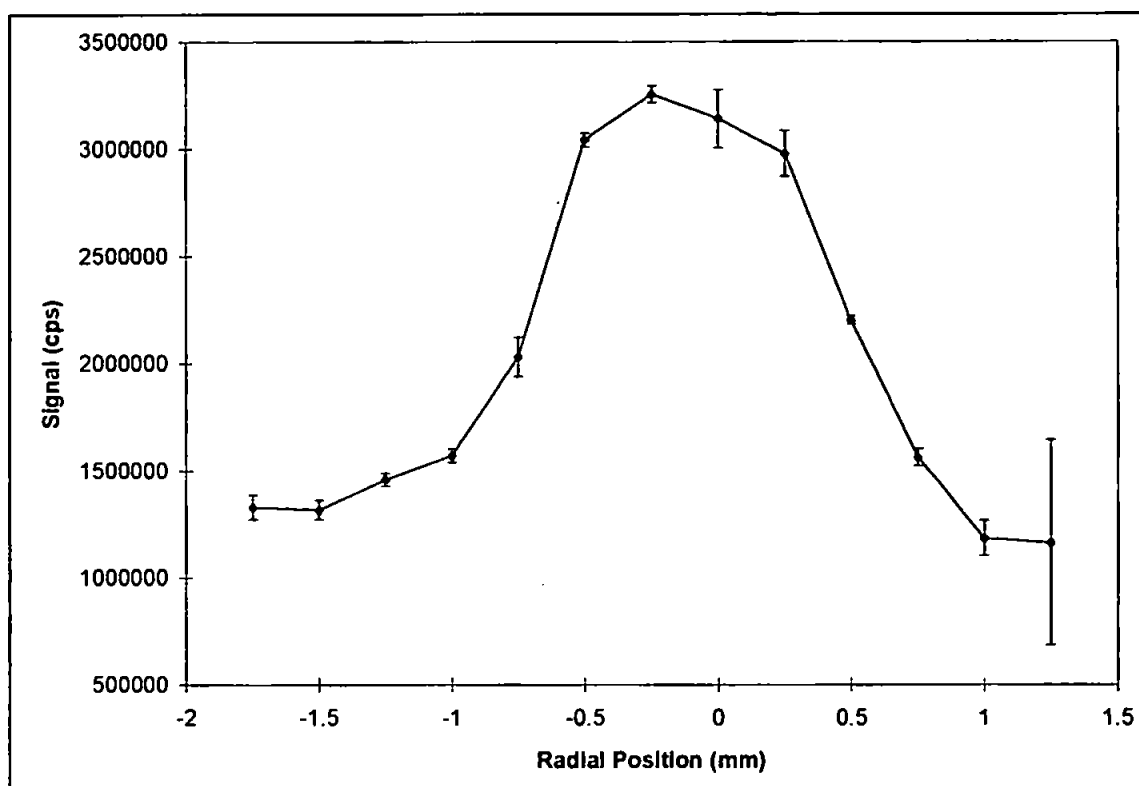


Figure 4.5: Radial profile for ArO^+ . Errors = 3σ for $n = 3$.

Figure 4.5 shows that the signal for ArO^+ still reached a maximum signal intensity, although the maximum was spread over a wider distance than for the metal analyte species. At the edges of the radial profile the signal intensity did decrease but not as rapidly as for the other species, and there was still a relatively large signal at the edges of the radial profile, whereas the signal intensities for the metal oxides were minimal at these positions. These results suggest that, although there is more oxygen entering the plasma through the central channel with the aspiration of the analyte solution in 2 %

HNO₃, there were also significant amounts of both argon and oxygen throughout the rest of the plasma, indicating that there were significant levels of ArO⁺ being formed in parts of the plasma beyond the central channel.

4.3.2 Temperature Determination

The generalised methods for determining the temperature in the plasma, described in Section 3.1, have been used by various workers^{144,249,250,311-314}. However, several problems exist with the application of these methods and the interpretation of their results, as discussed in the following sections.

4.3.2.1 Method A

This method was first proposed by Douglas and French²⁵⁰, and applied by Longerich³¹⁴. The assumption is made that $MO^+ / M^+ \propto e^{D_o / kT}$, and that the temperature can be determined from the energy of formation of the monovalent monoxide ion from the corresponding monovalent metal ion (M^+)³¹⁴.

The equilibrium of the metal oxide monovalent ion with the monovalent metal ion and neutral oxygen is given as



$$D_o = -RT \ln ([MO^+] / [M^+]) \quad (4.15)$$

This equation can be rearranged to

$$\log ([MO^+] / [M^+]) = D_o / [RT \times \ln (10)] + \text{constant} \quad (4.16)$$

where $[MO^+]/[M^+] =$ the measured ratio of the metal oxide and metal ion signals

$D_o =$ the dissociation energy of the metal oxide

$R =$ the universal gas constant

$T =$ the temperature.

A plot of $y = \log ([MO^+] / [M^+])$ versus $x = D_o$ gives a straight line where

$$\text{slope} = 1 / [\ln (10) \times RT] \quad (4.17)$$

Rearrangement of this equation gives

$$T = 1 / [\ln (10) \times R \times \text{slope}] \quad (4.18)$$

The constant (intercept) is a function of the fugacity of oxygen and is constant for a set of elements determined at a given set of operating conditions. This graph was plotted for every point of the radial signal profile, in order to obtain a radial profile of the temperature. An example plot is shown in Figure 4.6.

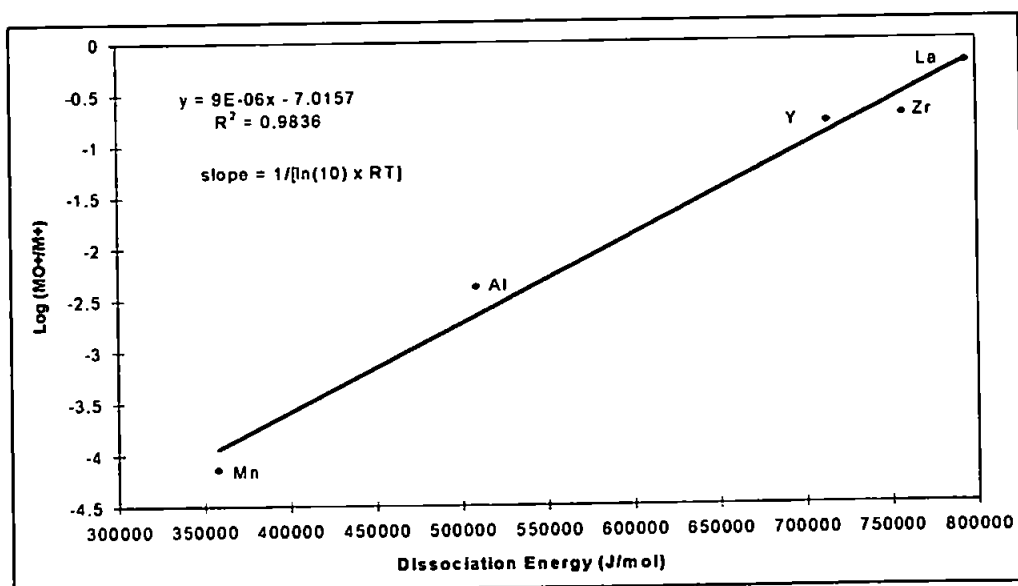


Figure 4.6: Example of plot used to calculate the temperature using Method A.

This was initially plotted with the dissociation energy data for the neutral metal oxides, for a direct comparison with previous calculations which have erroneously used the MO, rather than the MO⁺, dissociation energies due to the limited MO⁺ data. However, the MO⁺ dissociation energy data did exist for most of the metal oxides used in this study and it was possible to calculate the others using Equation 4.19³²⁵.

$$D_0(\text{MO}^+) = D_0(\text{MO}) - \text{IE}(\text{MO}) + \text{IE}(\text{M}) \quad (4.19)$$

These values were then used to calculate the temperature using the D₀(MO⁺) data, in graphs similar to Figure 4.6. These graphs were plotted for every point of the radial signal profile, in order to obtain a radial profile of the temperature using the D₀(MO⁺) data. The differences between D₀(MO⁺) and D₀(MO) are shown in Table 4.2.

Table 4.2: Comparison of D₀(MO) and D₀(MO⁺) values

Metal	D₀(MO) / eV	D₀(MO⁺) / eV
Al	5.27	1.71
Ba	5.79	4.09*
La	8.23	8.88
Mn	3.71	2.95
Ti	6.87	6.93
Y	7.39	7.25
Zr	7.85	7.76

* = value calculated using Equation 4.19.

The radial temperature profiles determined using this method are shown in Figure 4.7.

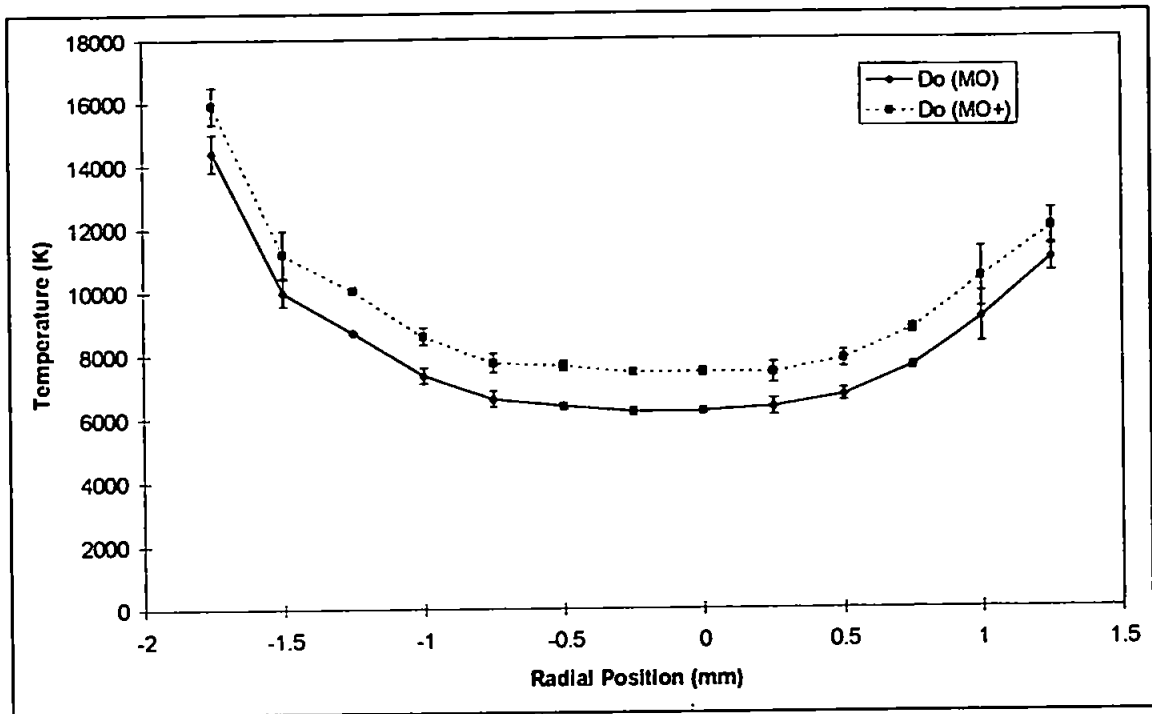


Figure 4.7: Comparison of the radial profiles for the temperature calculated using Method A, with data for D_0 (MO) and D_0 (MO⁺). Errors = 3σ for $n = 3$.

The temperature determined using the MO dissociation energies ranged from 6200 K at the central axis of plasma to 14,500 K at the edges of the radial profile. The temperature calculated using the MO⁺ dissociation energies was slightly higher than that for the MO data, ranging from 7400 K at the central axis of the plasma to 16,000 K at the edges of the radial profile. The temperatures using both sets of dissociation energies were much lower than other temperatures reported using this method, 21,000 K²⁵⁰ and 12,500 K³¹⁴, although Longerich¹²⁵ also reported a lower temperature of 10,100 K using this method. The temperatures calculated using this method, except at the very edges of the radial profiles, were within the range expected in the plasma (5000 - 10,000 K)³³².

The radial profiles of the temperature exhibited the opposite trend to that shown by the raw data, i.e. the temperature was lowest at the central axis and increased as the distance from this central axis was increased. This trend was also observed by Kornblum and De Galan³³³ for the excitation temperatures of Ar, Ca and Mg and the OH rotational

temperature. This would be expected because the aspiration of solution through the central channel cools this region of the plasma relative to the outer regions. Therefore, it would be expected that the central channel of the plasma was the coolest part of the plasma, and that the temperature increased as the distance from the central channel was increased.

The raw data plots used to calculate the temperature, e.g. Figure 4.6, indicate the magnitude of inherent errors in these temperature calculations. Towards the edges of the radial profile, where the raw signals were low, poor R^2 values were obtained, e.g. 0.87. However, near the central axis, where the raw signals were high, the points were much less scattered about the slope of the graph, as demonstrated by R^2 values of 0.98 and higher.

Previous studies using this method have used the dissociation energies of the neutral metal oxides to calculate the dissociation temperature, due to the lack of available data for the MO^+ species. The MO^+ data for the majority of the metal oxides used in this study were available, but in general the available MO^+ data is still limited, with the data for most species not available, and that which is available is not easily obtainable. The use of the MO^+ dissociation energies produced an increase in the calculated temperature, but which was still within the range expected in the plasma.

4.3.2.2 Method B

This method, developed by Kubota *et al.*¹⁴⁴, is also based on the relationship between the measured metal oxide ion to metal ion signal ratio (S_{MO^+} / S_{M^+}) and the oxide bond strength (D_o). However, they devised an expression which uses the dissociation energies of the neutral metal oxides (Equation 4.20), and hence it is not necessary to know the dissociation energies of the metal oxide ions.

$$n_{MO} / n_M = Z_{MO} / (-2\pi M_M M_O kT / h^2 M_{MO})^{3/2} Z_M Z_O \times n_O \exp(D_o / kT) \quad (4.20)$$

where n = the number density

M = the atomic or molecular weight

Z = the partition function

subscripts M, O and MO indicate a metal element, oxygen and a monoxide.

For the ionisation equilibria



and



the equilibrium constants are

$$K_1 = n_{M^+} n_{e^-} / n_M \quad (4.23)$$

and

$$K_2 = n_{MO^+} n_{e^-} / n_{MO} \quad (4.24)$$

The elimination of n_{e^-} from equations 4.23 and 4.24 gives

$$n_{MO^+} / n_{M^+} = K_2 n_{MO} / K_1 n_M \quad (4.25)$$

Substituting equation 4.20 for equation 4.25 and rearranging gives

$$n_{MO^+} Z_O (M_M M_O / M_{MO})^{3/2} / n_{M^+} Z_{MO} = K_2 n_O \exp(D_o / kT) / K_1 (-2\pi kT / h^2)^{3/2} \quad (4.26)$$

Assuming that the signal ratio S_{MO^+} / S_{M^+} equals n_{MO^+} / n_{M^+}

$$\log [S_{MO^+} Z_M Z_O (M_M M_O / M_{MO})^{3/2} / S_{M^+} Z_{MO}] = A + \log (K_2 / K_1) + 5040 D_o / T \quad (4.27)$$

where $A = \log [n_0 / (-2\pi kT / h^2)^{3/2}]$.

Therefore, assuming K_2 / K_1 is constant, the left hand side of Equation 4.27, i.e. the logarithmic term in which the partition functions, atomic weights and molecular weights are taken into consideration, should have a linear relationship with D_o . This was plotted for every point of the radial signal profile, in order to obtain a radial profile of the temperature. An example plot is shown in Figure 4.8.

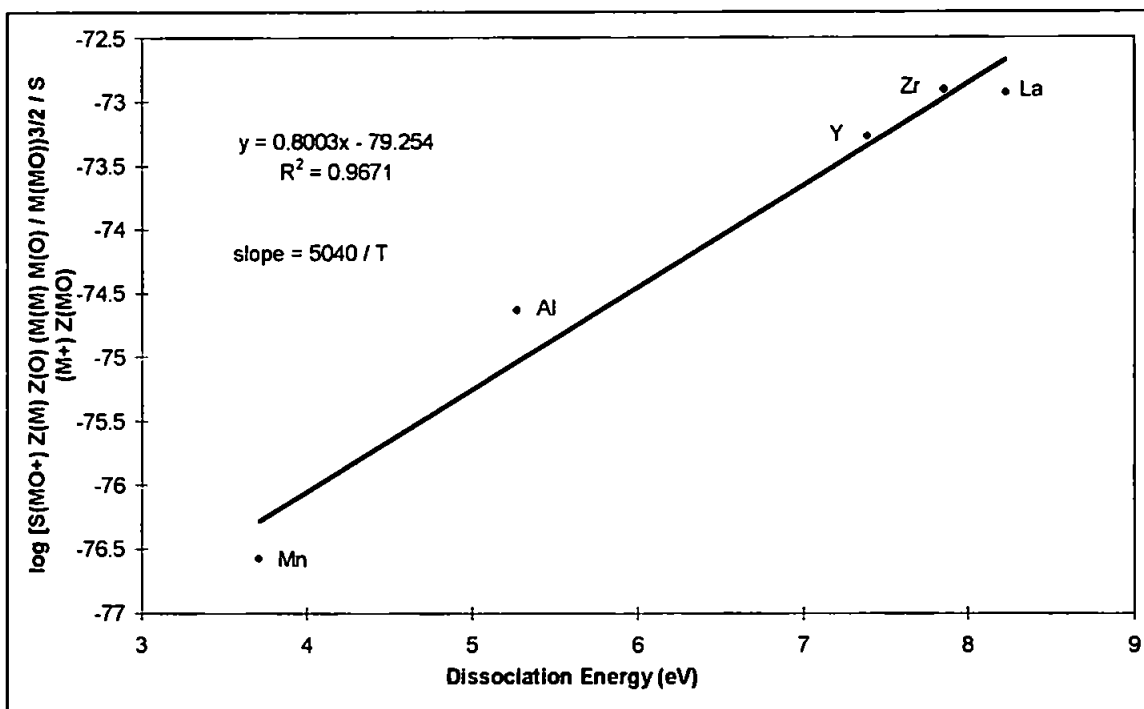


Figure 4.8: Example of plot used to calculate the temperature using Method B

The need to know the dissociation energies of the metal oxide ions has been overcome by this method, but other assumptions have been introduced. The calculation of the temperature using Equation 4.27 assumes that the ratio of K_2 / K_1 is constant for all the different metals and their oxide ions studied. This method introduces the partition functions into the calculation, which are, by definition, a temperature dependent term. Therefore, an assumption about the temperature of the plasma has to be made in order to calculate the partition functions, which may affect the resultant temperature calculated using that data.

The radial temperature profile calculated using Method B is shown in Figure 4.9. The temperature determined ranged from 6200 K at the central axis of plasma to 15,000 K at the edges of the radial profile. These temperature values were almost identical to those calculated for Method A using the MO dissociation data. The temperature profile also followed the same trend as shown for Method A, in that the temperature was coolest at the central axis of the plasma and increased as the distance from this central axis was increased.

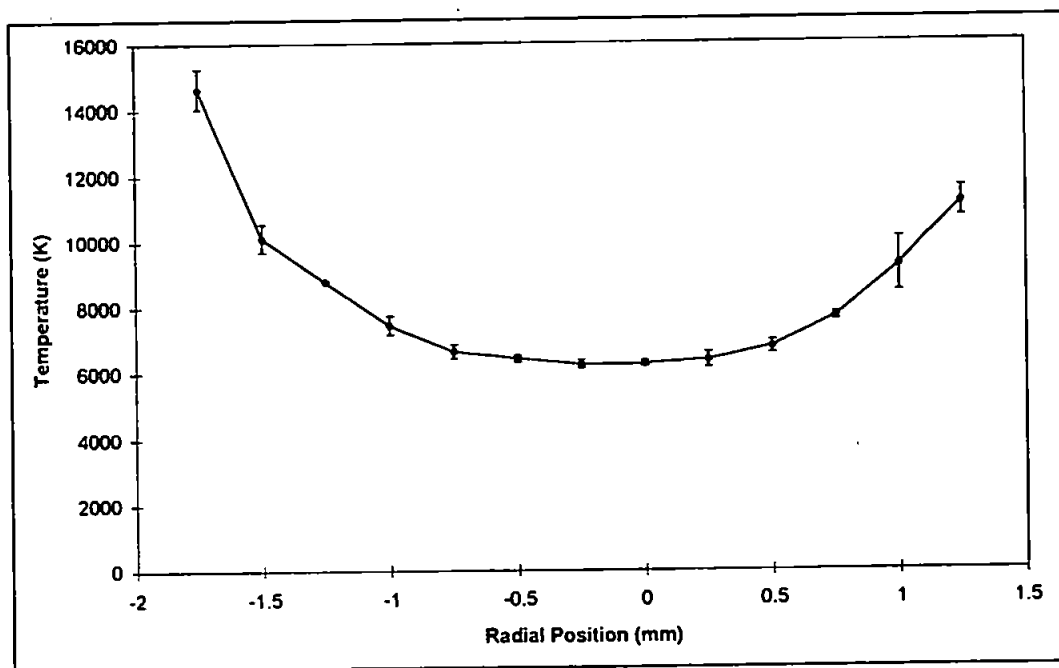


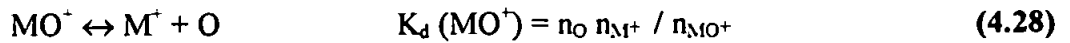
Figure 4.9: Radial profile for the temperature calculated using Method B. Errors = 3σ for $n = 3$.

These temperatures determined using Method B corresponded to other temperatures calculated using this method (6650 K)¹⁴⁴ and lay within the expected values for the plasma (5000 - 10,000 K)³³².

As with Method A the raw plots used to calculate the temperature (e.g. Figure 4.8), were variable, with poor R² values obtained for the edges of the radial profile (e.g. R² ≈ 0.86). However, near the central axis the points were much less scattered about the slope of the graph, with R² values of 0.97.

4.3.2.3 Method C

This method has been suggested by Houk²⁴⁹, and is based on the theory that the dissociation of a diatomic molecule at a gas kinetic temperature (T_{gas}) is governed by an equation similar to the Saha equation²⁴⁹. The main reaction for the dissociation of an oxide ion MO⁺ is



where the equilibrium constant K_d is defined as⁵⁸

$$K_d = ((2\pi M_M M_O) / (h^2 M_{MO}) kT)^{3/2} (Z_M Z_O / Z_{MO}) \exp(-D_o / kT) \quad (4.29)$$

where

- M = the species mass
- D_o = the dissociation energy (eV)
- k = the Boltzmann constant
- T = the plasma temperature
- Z = the partition function.

Equation 4.29 can be rearranged to include the spectroscopic constants of MO^+ rather than the partition function, which is difficult to evaluate, as given in Equation 4.30.

$$\log K_d = \log Z_M Z_O + 0.5 \log T + \log (1 - 10^{-0.625\omega/T}) - 5040 D_o / T + C \quad (4.30)$$

where

$$C = 20.432 + 1.5 \log (M_{M^+} M_O / M_{MO}) + \log (B / g) \quad (4.31)$$

where g = the statistical weight of the ground electronic state of MO^+

ω = a vibrational constant (cm^{-1})

B = a rotational constant (cm^{-1})

M = the atomic or molecular weight.

Combination of Equations. 4.30 and 4.31 gives^{142,249}

$$\begin{aligned} \log K_d (MO^+) &= 0.5 \log T_{gas} - 5040 D_o / T_{gas} + 1.5 \log (M_{M^+} M_O / M_{MO}) + \log (Z_{M^+} Z_O) \\ &+ \log (1 - 10^{-0.625 \omega / T_{gas}}) + \log (B / g) + 20.432 \end{aligned} \quad (4.32)$$

Temperature measurements using this method may be inaccurate due to the use of partition function values, which are, by definition, temperature dependent. However, in the case of ions and neutral atoms the electronic partition function can be calculated using equation 4.33, with the appropriate constants³³⁴.

$$B(T) = a + b (T/10^3) + c (T/10^3)^2 + d (T/10^3)^3 + e (T/10^3)^4 + f (T/10^3)^5 \quad (4.33)$$

For the calculations undertaken here the value for the partition function (Z_x) did not rely upon a single temperature value, because a spreadsheet was set up so that the value for the partition function changed as the temperature value was altered.

The results obtained from Section 4.3.1 were used to calculate an experimental value for $K_d(\text{MO}^+)$ using Equation 4.34.

$$K_d(\text{MO}^+) = n_{\text{O}} n_{\text{M}^+} / n_{\text{MO}^+} \quad (4.34)$$

This was calculated by measuring the signals for M^+ and MO^+ in order to obtain an $n_{\text{M}^+} / n_{\text{MO}^+}$ ratio. This was then multiplied by the theoretical value of oxygen atoms in the plasma, calculated using Equation 4.35²⁴⁹.

$$n_{\text{O}} = \epsilon_{\text{ncb}} F N_{\text{o}} T_{\text{room}} / M_{\text{H}_2\text{O}} Q T_{\text{plasma}} \quad (4.35)$$

where

- ϵ_{ncb} = nebuliser efficiency (= 2 %)
- F = solution uptake rate (= 1.2 ml min⁻¹ = 0.02 g s⁻¹)
- N_{o} = Avagadro's number
- $M_{\text{H}_2\text{O}}$ = molecular weight of water (= 18.015 g mol⁻¹)
- Q = gas flow rate (= 0.9 l min⁻¹ = 15 cm³ s⁻¹)
- T_{room} = room temperature (= 292 K)
- T_{plasma} = plasma temperature (= 5000 K).

This value, of 5.21×10^{16} atom cm⁻³, is the contribution of O atoms from the water droplets. However, there is also a contribution of O atoms from water vapour, calculated using Equation 4.36³³⁵.

$$n_{O(\text{vap})} = P / R T_{\text{spray}} \times (T_{\text{spray}} / T_{\text{plasma}}) \quad (4.36)$$

where

- P = vapour pressure of water (= 1498 Pa)
- R = gas constant (= 8.31451 J K⁻¹ mol⁻¹)
- T_{spray} = temperature of spray chamber (= 289 K)
- T_{plasma} = plasma temperature (= 5000 K).

This value, of 2.17×10^{16} atom cm⁻³, is the contribution of O atoms from the water vapour. The value for the amount of O atoms in the plasma is obtained by combining the contributions from water droplets and water vapour, resulting in a value of 7.38×10^{16} atom cm⁻³.

This experimental value of K_d (MO⁺) was then compared to the theoretical K_d (MO⁺) value, calculated using Equation 4.28. Using a spreadsheet, the value for the temperature was adjusted until the theoretical K_d value was the same as the experimental K_d value. This temperature was then assumed to be the equilibrium dissociation temperature for the MO⁺ species.

Unfortunately, the spectroscopic constants for most of the MO⁺ species do not exist, therefore, the spectroscopic constants for the neutral metal oxides had to be used instead. A table of the spectroscopic constants which are available is given in Appendix 1³¹⁵⁻³³¹. However, the spectroscopic constants for AlO⁺ were available, and a comparison of these with the spectroscopic constants for neutral AlO is shown in Table 4.3. In order for a complete comparison of AlO and AlO⁺ the dissociation energy of AlO⁺ was used.

The radial profiles of the temperatures calculated from the dissociation of each of the seven metal oxides studied, as given in Table 4.1, are shown in Figure 4.10.

Table 4.3: Comparison of spectroscopic constants for AlO and AlO⁺ ³¹⁶⁻³²¹

Spectroscopic Constant	AlO	AlO ⁺
ω / cm^{-1}	979.23	710
B / cm^{-1}	0.64136	0.5066
g	2	6

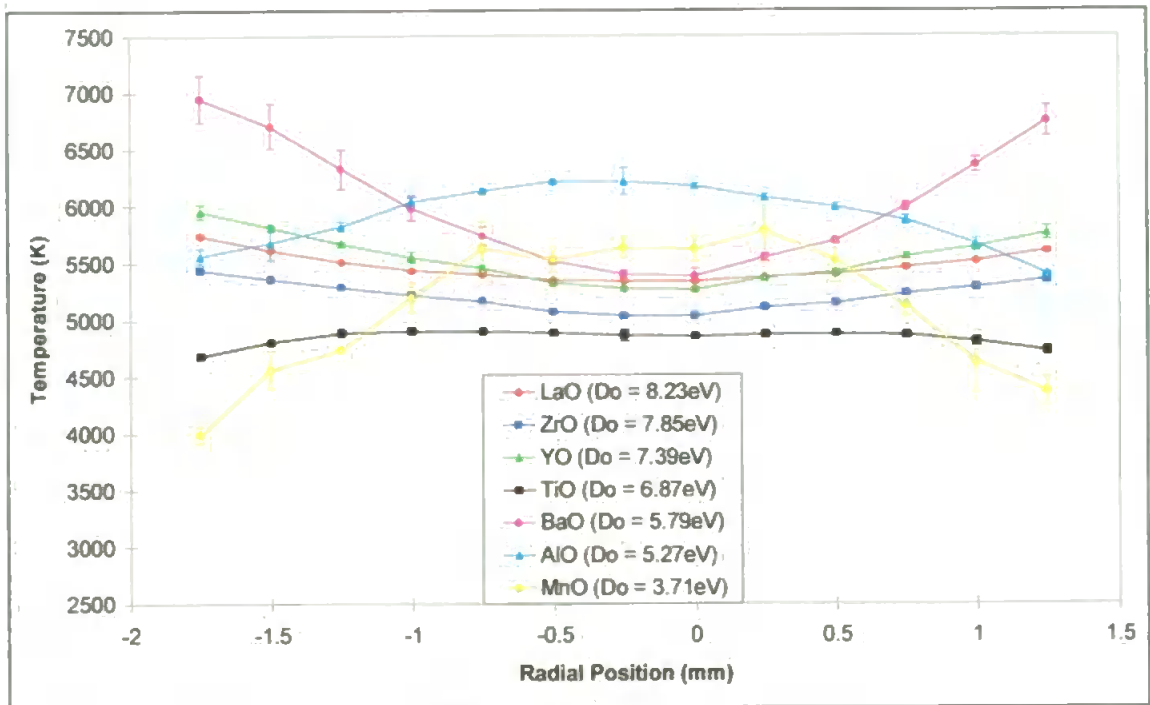


Figure 4.10: Comparison of the radial profiles for the temperatures calculated using Method C, with D_0 values for MO. Errors = 3σ for $n = 3$.

The temperatures calculated for the dissociation of BaO, LaO, YO and ZrO exhibited the same trend as for Methods A and B, in that the temperature was lowest at the central axis of the plasma and increased as the distance from this central axis was increased. The temperature calculated for the dissociation of AlO, MnO and TiO exhibited the opposite trend, in that the temperature was greatest at the central axis of the plasma and decreased as the distance from this central axis was increased.

The results of Methods A and B, and the work of others³³³ all indicate that the temperature should be lowest at the central axis of the plasma and that it increases as the distance from this central axis is increased. This was the case for four of the seven metal oxides studied, i.e. BaO, LaO, YO and ZrO, and indicates that there may be a problem with the temperature calculation for the other three metal oxides, i.e. AlO, MnO and TiO. Inspection of the raw data for these species seems to suggest that this was the case. The raw signal for MnO^+ was negligible and therefore this would lead to a large error in the $\text{Mn}^+ / \text{MnO}^+$ ratio, which in turn would lead to a large error in the temperature calculated from this data. This was also the case for AlO^+ , although not to such an extent as for MnO^+ . There was ample signal for TiO^+ , so this was not the reason for an unusual trend in the temperature calculated for TiO^+ . However, a 10 ng ml^{-1} of MASSCAL was aspirated along with the solution used to obtain the metal oxide signals. The MASSCAL solution contained Be at $m/z = 9$, and so there was the possibility of this reacting with Ar to form the interference ion ArBe^+ , which would interfere with the isotope of Ti^+ monitored at $m/z = 49$. There was also the possibility of a minor isotope of NO_2^+ , formed from the 2 % HNO_3 solution, causing an interference at $m/z = 49$. Therefore, these would lead to a deviation from the correct $\text{Ti}^+ / \text{TiO}^+$ ratio, and hence an error in the temperature calculated from this ratio.

Despite the differences in the trends for the temperatures calculated from the different species, all of the temperatures calculated were within the range 4000 - 7000 K, which is well within the range expected in the plasma³³². The temperatures calculated exhibited no correlation with the dissociation energy of the metal oxide species.

The temperatures calculated from the data for the neutral metal oxide and the metal oxide ion of AlO are compared in Figure 4.11.

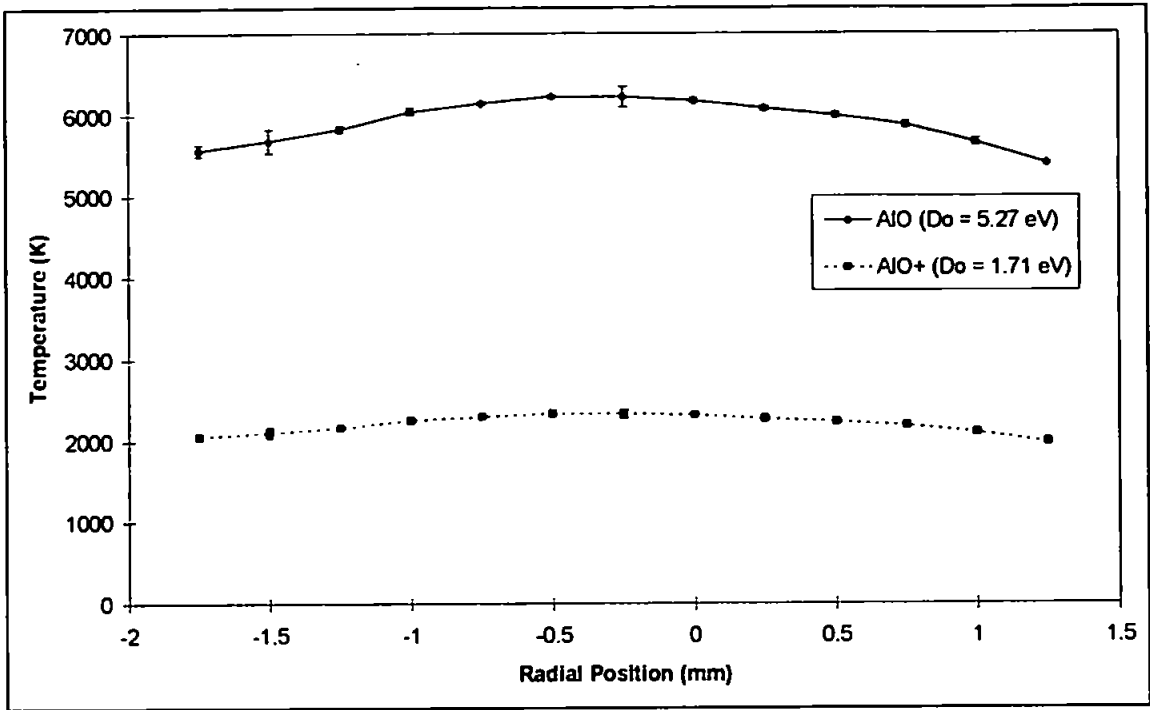


Figure 4.11: Comparison of the radial profiles for the temperature calculated using Method C, with data for AlO and AlO⁺. Errors = 3 σ for n = 3.

The temperature calculated from the data for the metal oxide ion was much lower than that calculated from the data for the neutral metal oxide. The temperature calculated for AlO ranged from 5400 to 6250 K, whereas the temperature calculated for AlO⁺ ranged from 2000 to 2350 K. This is different to Method A where the temperature calculated with the metal oxide ion data was higher than that calculated with the neutral metal oxide data. This may be due to the fact that the dissociation energy of AlO⁺ was much lower than that for neutral AlO (1.71 eV as compared to 5.27 eV). AlO⁺, with a lower dissociation energy than the neutral AlO, would require less energy to dissociate the molecule, resulting in the dissociation equilibrium being reached at a lower temperature, and so a lower temperature would be expected for the dissociation of AlO⁺ compared to that for AlO. However, this lower temperature calculated for the dissociation of AlO⁺ (< 2500 K) was much lower than would be expected within the plasma (5000 - 10,000 K)³³².

4.3.2.4 Method D

This method has been utilised by Houk *et al.*³¹³ and is based on the ionisation of an already ionised metal ion. A set of ionisation reactions can be written for the major plasma constituents (Ar, H and O), the matrix elements (X) from the sample, and the analyte elements (M)²⁴⁹, e.g. for metal analyte



The ionisation constant can be calculated from the Saha equation²⁴⁹

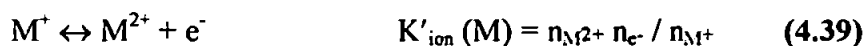
$$\log K_{\text{ion}}(M) = 1.5 \log T_{\text{ion}} - 5040 (IE_M) / T_{\text{ion}} + \log (Z_{M^+} / Z_M) + 15.684 \quad (4.38)$$

where IE_M = the first ionisation energy for the element M (eV)

Z = the partition function

T_{ion} = the ionisation temperature (K).

These calculations can be extended to include doubly charged ions (M^{2+}).



$$\log K'_{\text{ion}}(M) = 1.5 \log T_{\text{ion}} - 5040 (IE') / T_{\text{ion}} + \log (Z_{M^{2+}} / Z_{M^+}) + 15.684 \quad (4.40)$$

where IE' = the second ionisation energy of the element M

$Z_{M^{2+}}$ = the electronic partition function of M^{2+} .

The ionisation temperature was calculated from Equation 4.40 and the measured ratio of M^{2+} / M^+ where M was barium³¹³.

One problem with this method is that since n_e was not measured directly, a set of n_e values based on atomic emission measurements reported by others had to be used. Various n_e measurements have been carried out, mainly using the Stark width of the H_β line method, producing values in the range $10^{14} - 10^{16} \text{ cm}^{-3}$ ³³⁶. A value of $2 \times 10^{15} \text{ cm}^{-3}$ was taken for this calculation, based on the contour maps of n_e at similar operating conditions³³⁷. A further problem was again the use of partition functions to calculate the temperature.

The radial temperature profile calculated using Method D is shown in Figure 4.12, and indicates that the temperature was highest close to, but not exactly at the central axis of the plasma, and decreased as the distance from this central axis was increased.

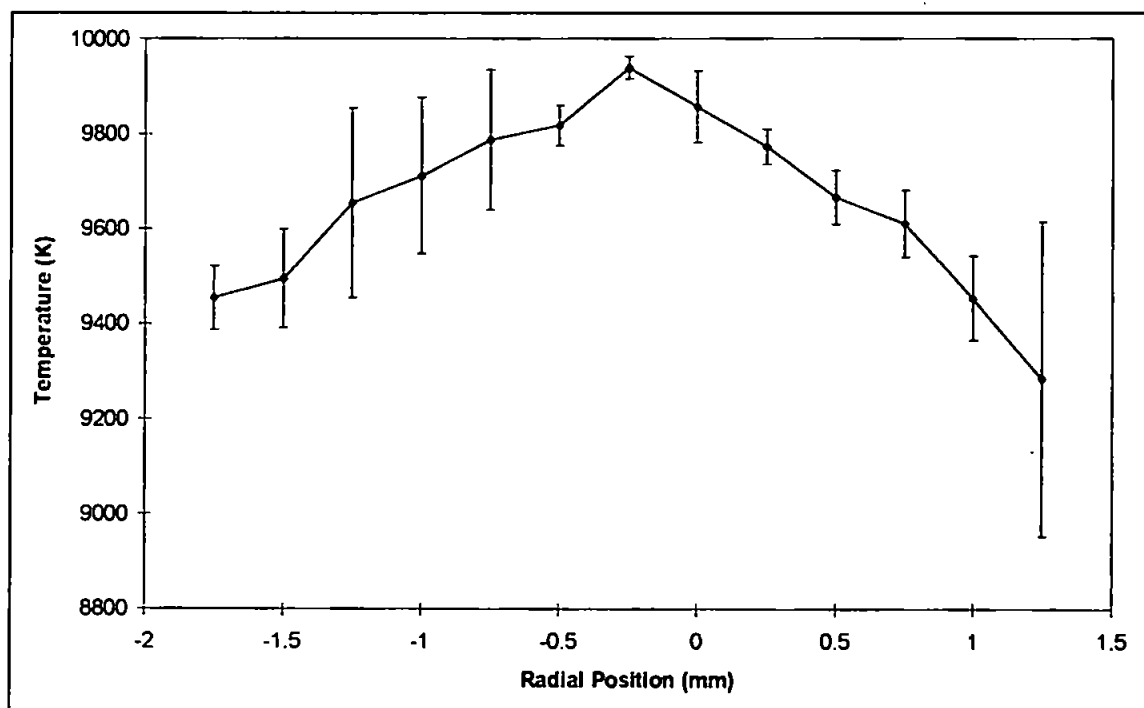


Figure 4.12: Radial profile for the temperature calculated using Method D.

Errors = 3σ for $n = 3$.

The temperature calculated using this method was higher than those calculated using the previous methods, varying from 9300 K at the edges of the radial profile to 10,000 K around the central axis of the plasma. This higher ionisation temperature would be expected because the plasma is not in thermal equilibrium, and values for the ionisation temperature are typically higher than those for the dissociation and excitation temperatures¹²⁵.

Other T_{ion} determinations have also produced temperatures which are higher than those determined for excitation and dissociation temperatures (5000 - 7000 K). Mass spectrometric T_{ion} measurements have produced temperatures of 7600 - 8000 K using $\text{Ba}^{2+}/\text{Ba}^+$ and $\text{Sr}^{2+}/\text{Sr}^+$ ratios, and 7800 - 8400 K using the Cd^+/I^+ ratio, for $n_{\text{e-}}$ values of $2 \times 10^{15} \text{ cm}^{-3}$ ³¹³. The Cd^+/I^+ ratio has also resulted in ionisation temperatures of 6700 - 7400 K³¹², while the ratios of Sb^+/In^+ and As^+/Ga^+ have resulted in ionisation temperatures of 6850 K and 6450 K respectively³¹¹. Optical T_{ion} measurements have resulted in temperatures of 8100 K using $\text{Ca}^{338,339}$, 7600 K using Ba^{339} and 8000 K using Mg^{333} as the thermometric species, at similar $n_{\text{e-}}$ values ($2 \times 10^{15} \text{ cm}^{-3}$). However, the power used for these studies, 1 kW^{338,339} and 530 W³³³, was much lower than used in this experiment. A T_{ion} value of 7200 K for Mg was obtained at the same power as used for this experiment (1350 W)³⁴⁰, although the observation height was very low (2 mm) and the $n_{\text{e-}}$ value used was only $5 \times 10^{14} \text{ cm}^{-3}$. All of the optical T_{ion} measurements were calculated using the M^+/M ratio.

The trend shown by the temperature, with the highest temperature being along the central axis of the plasma, is different to that which would be expected, i.e. with the central channel of the plasma being cooler than the outer areas due to cooling by the solution being aspirated. This could be due to a very minor isotope of Ba^{2+} ($m/z = 66$ at 0.1 % abundance) being monitored, which would probably suffer from interference by a minor isotope of TiO^+ ($m/z = 66$ at 5.4 % abundance) which would also be present

since it was one of the species being studied. However, the isotopic ratio of TiO^+ was known, and so the contribution of the signal at $m/z = 66$ which was due to TiO^+ was calculated and corrected for.

4.3.2.5 Method E

A similar reaction to that described in Section 4.3.2.3, for the metal oxides using Method C, can be written for the dissociation of other polyatomic ions, such as ArO^+ ²⁴⁹.



$$\begin{aligned} \log K_d (\text{ArO}^+) = & 0.5 \log T_{\text{gas}} - 5040 D_o / T_{\text{gas}} + 1.5 \log (M_{\text{Ar}} M_{\text{O}^+} / M_{\text{ArO}^+}) + \log (Z_{\text{Ar}} Z_{\text{O}^+}) \\ & + \log (1 - 10^{-0.625 \omega / T_{\text{gas}}}) + \log (B / g) + 20.432 \end{aligned} \quad (4.42)$$

The results obtained in Section 4.3.1 were used to obtain an $\text{Ar}^+ / \text{ArO}^+$ ratio, which was then divided by the degree of ionisation for argon, in order to obtain the value for Ar / ArO^+ . This value was then multiplied by the theoretical value of oxygen atoms in the plasma, calculated previously in Section 4.3.2.3. This value was then multiplied by the degree of ionisation for oxygen in order to obtain the amount of O^+ (5.99×10^{14} atoms cm^{-3}) in the plasma. However, species such as ArO^+ are thought to form in the interface of the ICP - MS rather than in the plasma and so another K_d value was calculated using the oxygen ions concentration assumed to be in the interface (1.97×10^{12} atoms cm^{-3}), calculated using Equation 4.43³⁴¹

$$n_{\text{X}(\text{int})} = 0.161 n_{\text{X}(\text{plasma})} (D / x)^2 \quad (4.43)$$

where $n_{X(\text{plasma})}$ = the density of the species X in the plasma
 x = the position downstream from the sampling orifice
 D = the sampling diameter.

The experimental $K_d(\text{ArO}^+)$ value, calculated for both the plasma and interface was compared to the theoretical $K_d(\text{ArO}^+)$ value as described previously for Method C in Section 4.3.2.3. Alternatively, $K_d(\text{ArO}^+)$ can be calculated by measuring the $\text{O}^+ / \text{ArO}^+$ ratio, which was then multiplied by the concentration of argon assumed to be in the plasma (1.45×10^{18} atoms cm^{-3}), calculated from the ideal gas law³³⁵, to obtain a $K_d(\text{ArO}^+)$ value for the plasma. The amount of Ar in the interface (4.76×10^{15} atoms cm^{-3}) was calculated using Equation 4.43 and used to obtain a $K_d(\text{ArO}^+)$ value for the interface. These experimental $K_d(\text{ArO}^+)$ values, calculated for both the plasma and interface were then compared to the theoretical $K_d(\text{ArO}^+)$ value as described previously.

The results are shown in Figure 4.13, and indicate that the temperature was lowest at the central axis of the plasma, and increased as the distance from this central axis was increased. This trend is the same as that which would be expected, with the central channel of the plasma being cooler than the outer areas due to cooling by the solution being aspirated.

The temperature calculated for the plasma using this method was much lower than those calculated for the other methods, varying from 650 K at the central axis of the plasma to 2250 K at the edges of the radial profile studied. This is much lower than would be expected in the plasma (5000 - 10,000 K), and this could be due to the low dissociation energy of ArO^+ , which is only 0.43 eV. This is much lower than the metal oxides, the lowest being MnO with a dissociation energy of 3.71 eV. However, AlO^+ also has a dissociation energy much lower than the neutral metal oxides (1.71 eV), and the temperatures calculated for this species were also much lower than those expected

within the plasma (< 2500 K). Therefore, the low temperature calculated for ArO^+ may be due to its low dissociation energy, although the metal oxides showed no trend between the temperature and the dissociation energy of the molecule.

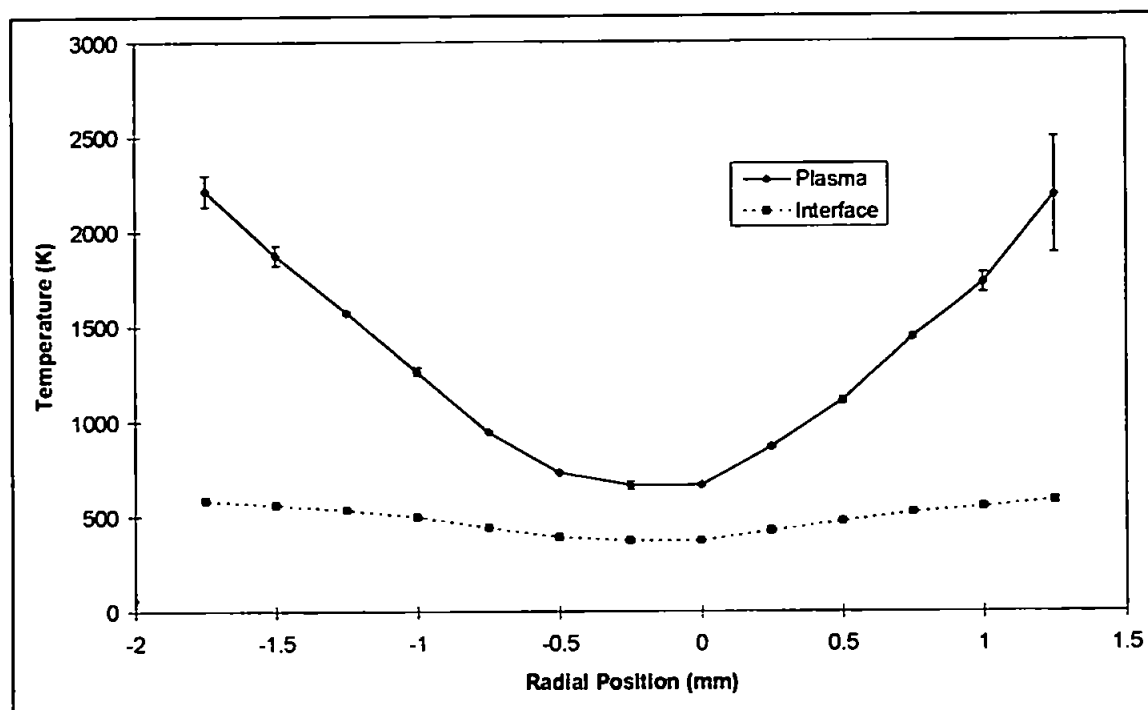


Figure 4.13: Comparison of the radial profiles for the temperature calculated using Method E, for equilibration in the plasma and interface. Errors = 3σ for $n = 3$.

Argon polyatomics, such as ArO^+ , are thought to possibly be formed in the interface rather than in the plasma¹⁴², and this may reflect the low temperature. The temperature calculated for the interface was even lower than that calculated for the plasma, ranging from 350 K at the central axis of the plasma to 600 K at the outer edges of the radial profile studied.

These temperatures calculated for both the plasma and interface were much lower than expected for the plasma. The temperature calculations are based on partial local thermodynamic equilibrium (p - LTE) conditions within the plasma, and therefore the low temperatures calculated using ArO^+ may indicate a deviation from LTE

conditions. LTE conditions are not thought to exist in the interface region of the ICP - MS, suggesting that the ArO^+ species is formed in the interface rather than the plasma. The low temperatures calculated correspond to those thought to prevail in the interface ($< 3500 \text{ K}$)¹⁴², also suggesting formation in the interface rather than the plasma.

4.4 CONCLUSIONS

4.4.1 Method A

The temperature calculated using Method A varied between 6150 and 14,500 K, which was much lower than those previously reported for this method, which were as high as 21,000 K²⁵⁰. These previously high temperatures were thought to be due to the incorrect use of the neutral metal oxide dissociation energies. However, the combination of metal oxides used in this study enabled the determination of the temperature using the dissociation energies of the metal oxide ions, which were available for these species. The temperature calculated using the $D_0(\text{MO}^+)$ values were slightly higher than those for $D_0(\text{MO})$, varying between 7400 and 16,000 K. These values are higher than temperatures reported by other workers using optical methods to determine the temperature (4000 - 7000 K), but apart from at the extreme edges of the radial profile, the calculated temperatures lie within the range expected for the plasma (5000 - 10,000 K)³³².

The metal oxides species used in this study have $D_0(\text{MO})$ values similar to their $D_0(\text{MO}^+)$ values, and this could explain the similar temperatures calculated using the two sets of dissociation energies, whereas previous studies reported temperatures up to 21,000 K using the $D_0(\text{MO})$ values. The metal oxide species used in these previous studies were different to those used in this study and the $D_0(\text{MO}^+)$ values were not necessarily available for these species. If the $D_0(\text{MO})$ and $D_0(\text{MO}^+)$ values for these

species are not similar, this might result in the extremely high temperatures calculated in these studies using the D_0 (MO) values.

Therefore, the problem of extremely high calculated temperatures previously associated with this method were overcome by using the correct D_0 (MO⁺) values. However, this was only possible because the D_0 (MO⁺) values were obtainable for the metal oxide species used in this study. There is very limited MO⁺ data available, with that which does exist being difficult to obtain, and therefore the use of the correct D_0 (MO⁺) values may not be possible with other metal oxides.

4.4.2 Method B

The temperature calculated using Method B (6200 - 15,000 K) was very similar to that calculated for method A using D_0 (MO) values, and were within the range expected for the plasma, except for the extreme edges of the radial profile. This method uses a calculation which compensates for the use of D_0 (MO) values and so it is not necessary to use the D_0 (MO⁺) values which are difficult to obtain. The only problem with this method is that to compensate for the use of the D_0 (MO) values the partition functions are included into the calculation. The partition functions are by definition a temperature dependent term and so care should be taken when using them to calculate the temperature, as an assumption about the temperature of the plasma is necessary to determine the value of the partition function.

4.4.3 Method C

The temperatures calculated using Method C varied with each individual species, however, they all lay within the range 4000 - 7000 K, well within the range expected in the plasma. The trends in the radial profile of the temperature for several of the species

studied were different to those exhibited using Methods A and B, due to the significantly lower raw signals for the oxide ions of these species.

This method also has the problem of the inclusion of partition functions in the calculation. However, this was overcome by their incorporation into the spreadsheet, so that the value of the partition function changed as the temperature was altered. Due to the format of the spreadsheet used to determine the temperature it was not possible to use this method for overcoming the temperature dependence of the partition functions in the other methods used (i.e. Methods B and D).

Another problem associated with this method was the lack of spectroscopic data for the metal oxide ions, making it necessary to use the spectroscopic data for the neutral metal oxides. The author noted that many workers wrongly use the data for the neutral metal oxides (particularly the dissociation energy) when calculating the temperature by this method. However, the references cited within this paper only contained data for the neutral metal oxides, with no references providing any data for the metal oxide ions, with the exception of AlO^+ . As seen with previous studies using Method A, the use of data for the neutral metal oxide rather than the correct MO^+ data can result in extreme deviations from the expected temperature, and so it is not advisable to use this method until more extensive MO^+ data becomes available.

4.4.4 Method D

The temperatures calculated using Method D were higher than those calculated using the previous methods. This higher temperature would be expected as the second ionisation energy of barium (10.0 eV) is higher than the dissociation energies of the metal oxides studied in the other methods. Hence, it would require more energy to further ionise ionic barium than it would to dissociate the metal oxides, and so the

temperature calculated for this process would also be greater. Due to the inhomogeneity of the plasma it would be expected that the ionisation temperature is greater than the dissociation temperature within the plasma.

This method also suffers from the inclusion of the partition functions into the calculation, which are not only temperature dependent but difficult to calculate for Ba^{2+} .

4.4.5 Method E

The temperatures calculated using Method E were much lower than those calculated for Methods A - D, and lower than would be expected in the plasma. The temperature calculated for the interface was even lower than that calculated for the plasma, but both these temperatures were within the range expected for the interface region, suggesting that ArO^+ is formed in the interface. Therefore, it may be possible to determine where in the plasma a species is being formed using this method.

4.4.6 Overall Conclusions

All of the methods discussed utilise mass spectrometric data to calculate the temperature of the plasma. If the results obtained in Section 4.3.1 are used to calculate the temperature of the plasma using these different methods it would be reasonable to expect temperatures which, although not identical, would be similar, assuming that thermal equilibrium exists. This is because all the species used to determine the temperature were being aspirated into the plasma at the same time and so experienced the same conditions within the plasma. This is particularly so for the three methods which were used to determine the temperature from the dissociation of the metal oxides, since the raw data used to calculate the temperature was identical for all three methods. However, all of these methods depend upon different assumptions and also on the

availability of the fundamental data needed to calculate the temperature. Therefore, although all of the methods would be expected to give similar temperatures and to lie within the accepted range of temperatures for the plasma, i.e. 5000 - 10,000 K, this would depend upon how accurate the assumptions were.

Therefore, the temperature calculated would be expected to differ from method to method depending upon the assumptions inherent within that method, and this can be seen in Figure 4.14 and Table 4.4 where the temperatures calculated for all the methods are compared.

Table 4.4: Comparison of the temperature calculated using all methods

Temperature Method	Temperature Range (K)
Method A (MO)	6190 - 14,400
Method A (MO ⁺)	7410 - 15,900
Method B (MO)	6230 - 14,640
Method C (AlO)	5400 - 6220
Method C (BaO)	5400 - 6950
Method C (LaO)	5330 - 5740
Method C (MnO)	3900 - 5780
Method C (TiO)	4680 - 4900
Method C (YO)	5260 - 5950
Method C (ZrO)	5030 - 5440
Method C (AlO ⁺)	1980 - 2330
Method D	9280 - 9940
Method E (plasma)	660 - 2220
Method E (interface)	370 - 580

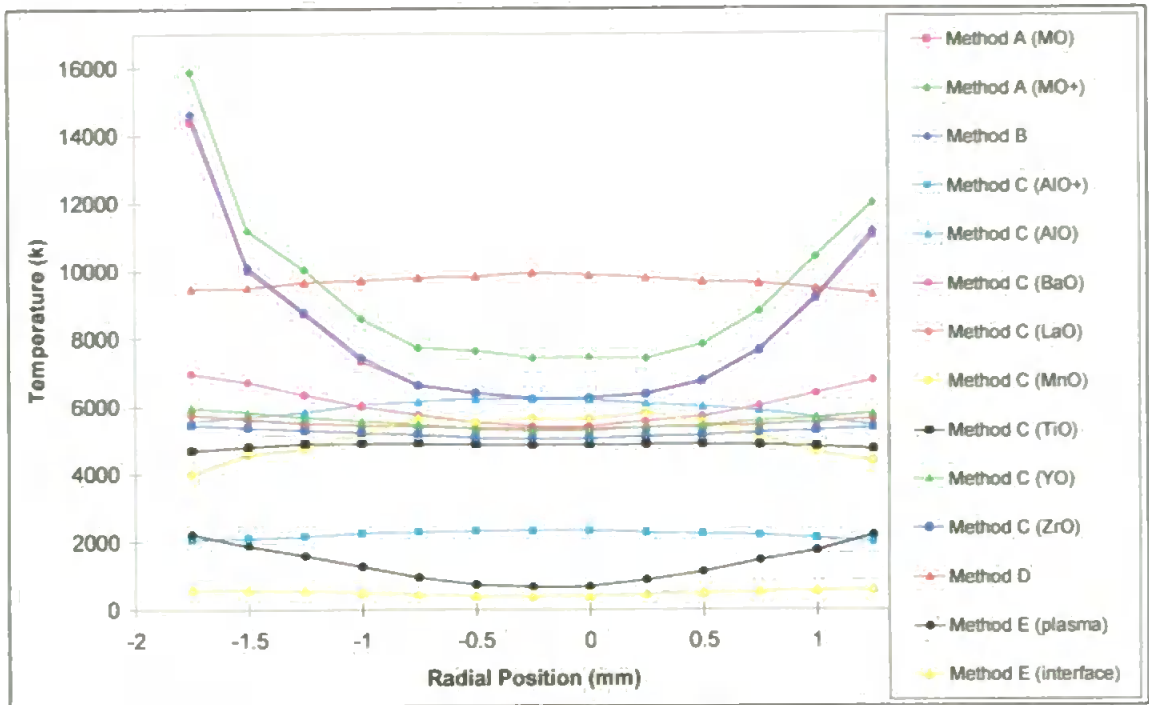


Figure 4.14: Comparison of the radial profiles for the temperature calculated using all methods. Errors = 3σ for $n = 3$.

These show that there were large differences in the temperatures calculated, depending upon which method was used, with nearly 15,500 K difference between the lowest and the highest temperature calculated. This emphasises how critical it is to select the appropriate method when determining the temperature of the plasma.

All of these methods suffer from a lack of fundamental data, and hence certain assumptions have to be made regarding this if it is to be possible to determine the temperature. A list of all the fundamental data available is given in Appendix 1. One assumption which affects all of the temperature methods is that in order to calculate the temperature it is assumed that the plasma is in local thermal equilibrium. However, it is well established^{125,325} that this is not the case and that the plasma is inhomogeneous and composed of several different zones^{125,332}, which will be at different temperatures. Therefore, the temperature value calculated will depend upon the region of the plasma being sampled, and this is investigated in Chapter 5.

The most popular method of determining the temperature of the plasma using mass spectrometric data is the dissociation of the metal oxides, although the three methods used to do this vary in both the temperature calculated and the assumptions used in the calculation. However, all three methods suffer from the lack the fundamental data for the metal oxide ions, although the calculation for Method B compensates for this lack of MO^+ data. With the combination of metal oxides studied it was possible to determine the temperature using MO^+ data for Method A, although this may not be possible for other metal oxides due to the lack of MO^+ data. Method C suffers the most from the lack of MO^+ data, although it has the advantage of being the same as Method E, which would allow for the direct comparison between two different types of interferences. The necessary data for ArO^+ exists and so it is possible to use this method to calculate the ArO^+ dissociation temperature, but until MO^+ data is available it should not be used to calculate MO^+ dissociation temperatures.

Therefore, in all further experiments the temperature of the plasma will be determined from the metal oxides using Methods A (MO^+ data) and B and from the argon polyatomics using Method E.

CHAPTER 5

Effect Of Sampling Depth On Polyatomic Ions And Their Dissociation Temperatures

5 EFFECT OF SAMPLING DEPTH ON POLYATOMIC IONS AND THEIR DISSOCIATION TEMPERATURES

5.1 INTRODUCTION

As mentioned in Chapter 4 the ICP is not homogeneous, but composed of several different zones with different temperatures^{125,332}, as shown in Figure 5.1.

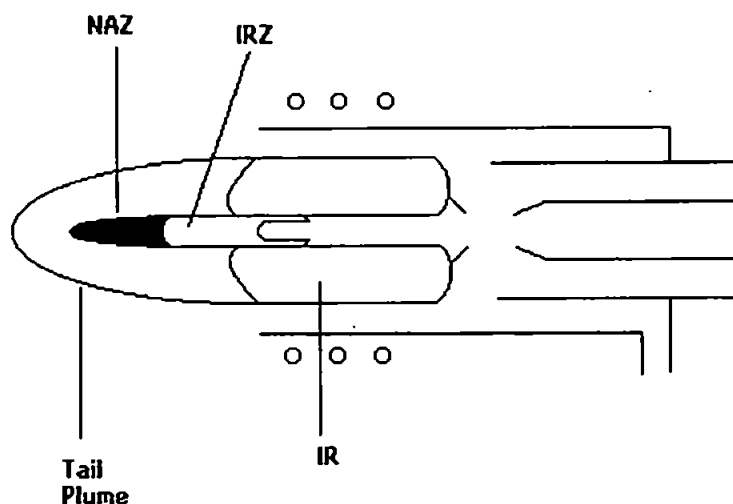


Figure 5.1: Schematic diagram of an ICP showing the different zones within the plasma³⁴².

Energy is transferred from the load coil to the plasma through the induction region (IR), where argon atom emission is observed in optical spectroscopy³⁰⁴. The axial channel consists of three distinct zones: the initial radiation zone (IRZ), normal analytical zone (NAZ) and plasma tail²⁴⁹. The IRZ contains mostly molecular species and neutral atoms, atomic analyte ions are mostly abundant in the NAZ, while the plasma tail contains neutral atoms and oxides formed by reactions of atomic ions with oxygen from

entrained air^{136,249}. In ICP - MS the characteristics of the mass spectrum depend on the position of the sampler relative to the IRZ and NAZ. Generally, the signal from analyte ions is maximum somewhere in - between the IRZ and NAZ at a position 1 - 5 mm downstream from the tip of the IRZ^{136,249}, which can be visualised by the aspiration of Y into the plasma¹³⁶. This position corresponds to a zone of the plasma which is at a sampling depth of approximately 5 - 15 mm³⁰³. Therefore, it would be expected that the region of the plasma being sampled would have a great effect on both the raw analyte signals and temperatures calculated using mass spectral data.

5.2 EXPERIMENTAL

Experiments were conducted using a PlasmaQuad 3 ICP - MS (VG Elemental, Ion Path, Road Three, Winsford, Cheshire, UK), as described in Section 2.1.2. Both ArX^+ and MO^+ interferences were studied at the m/z shown in Table 5.1.

Ion sampling depth profiles of the plasma were obtained from 16 - 39 mm by moving the torchbox as far forward as possible and then moving it back at 1.25 mm intervals. These were obtained using standard conditions (1350 W), using a shield torch (620 W), and at 620 W without a shield (to act as a control to ensure any differences observed were not merely a power effect). A solution of 10 ng ml⁻¹ MASSCAL (Be, Mg, Co, In, Pb and U) and 100 ng ml⁻¹ Al, Ba, La, Mn, Ti, Y and Zr (in order to obtain MO^+ signals) was aspirated into the plasma. At each sampling depth monitored all other operating parameters, i.e. lens settings and position of torchbox in the other two axes were adjusted to give maximum signal for $^{115}\text{In}^+$.

Table 5.1: Isotopes studied during effect of sampling depth experiment

Species	Mass	Abundance	Species	Mass	Abundance
Al ⁺	27	100	Ar ₂ ⁺	80	99.2
Ar ⁺	38	0.1	Y ⁺	89	100
ArH ⁺	39	0.1*	Zr ⁺	96	2.8
AlO ⁺	43	99.8*	YO ⁺	105	99.8*
Ti ⁺	50	5.3	ZrO ⁺	106	51.3*
ArN ⁺	54	99.2	In ⁺	115	95.8
Mn ⁺	55	100	Ba ⁺	134	2.6
ArO ⁺	56	99.4*	La ⁺	139	99.9
TiO ⁺	64	73.6*	BaO ⁺	154	71.6*
MnO ⁺	71	99.8*	LaO ⁺	155	99.7*

* The abundances for the molecular species were calculated by combining the abundances of the two constituent elements.

5.3 RESULTS AND DISCUSSION

5.3.1 Variation of Dissociation Temperature with Sampling Depth

5.3.1.1 Dissociation Temperature of MO⁺

These methods for calculating the dissociation temperatures of the metal oxides have been described previously for Methods A and B in Sections 4.3.2.1 and 4.3.2.2, respectively.

Comparisons of the temperatures calculated, using Methods A and B, for the metal oxide species at 1350 W, with the shield torch and at 620 W are shown in Figure 5.2.

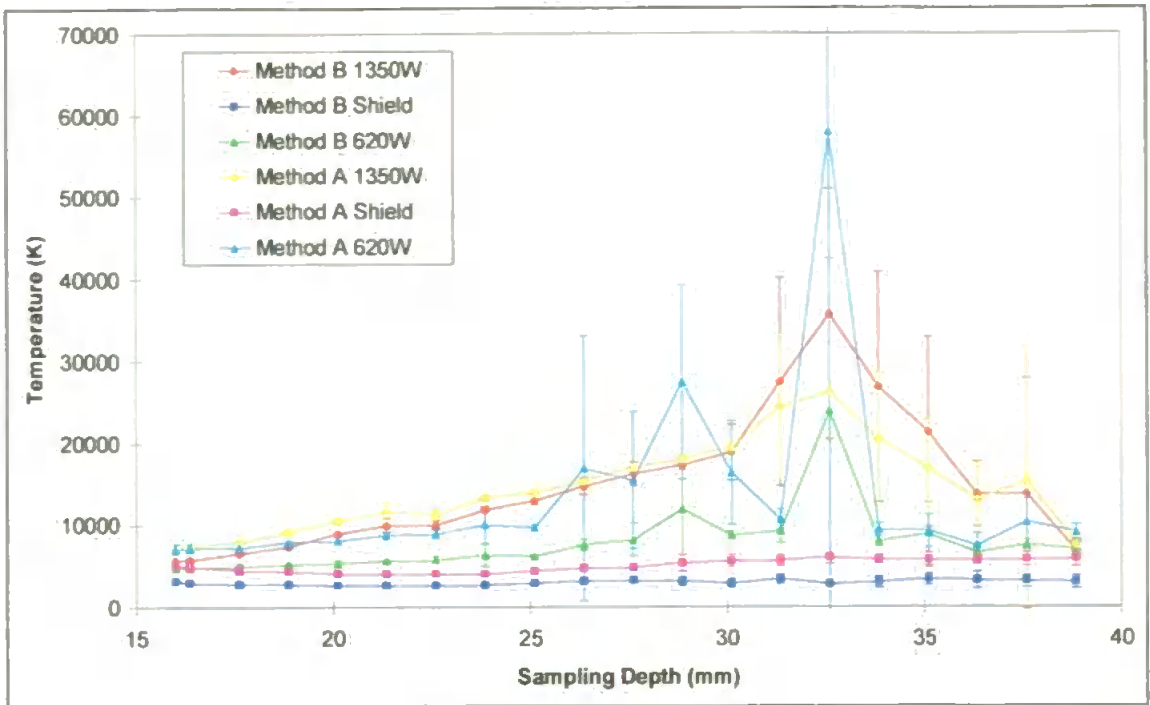


Figure 5.2: Comparison of the sampling depth profiles for the MO⁺ temperature.

Errors = 3 σ for n = 3.

These results show that the temperature at 1350 W increased as the sampling depth was increased, to a maximum at a sampling depth of 32.5 mm and then decreased as the sampling depth was increased further. For both the temperature methods used the temperatures calculated for sampling depths greater than 25 mm were very large (greater than 13,000 K) with poor reproducibility, particularly at sampling depths greater than 30 mm. This poor reproducibility at sampling depths above 25 mm meant that it was difficult to interpret the data below 25 mm, and so the temperature profiles up to a sampling depth of 25 mm are shown in Figure 5.3, for a clearer comparison of the signals.

The temperature calculated at 1350 W using Method A increased from 7100 K at a sampling depth of 16 mm to 14,000 K at 25 mm, while the temperature calculated using Method B increased from 5650 K at 16 mm to 13,000 K at 25 mm.

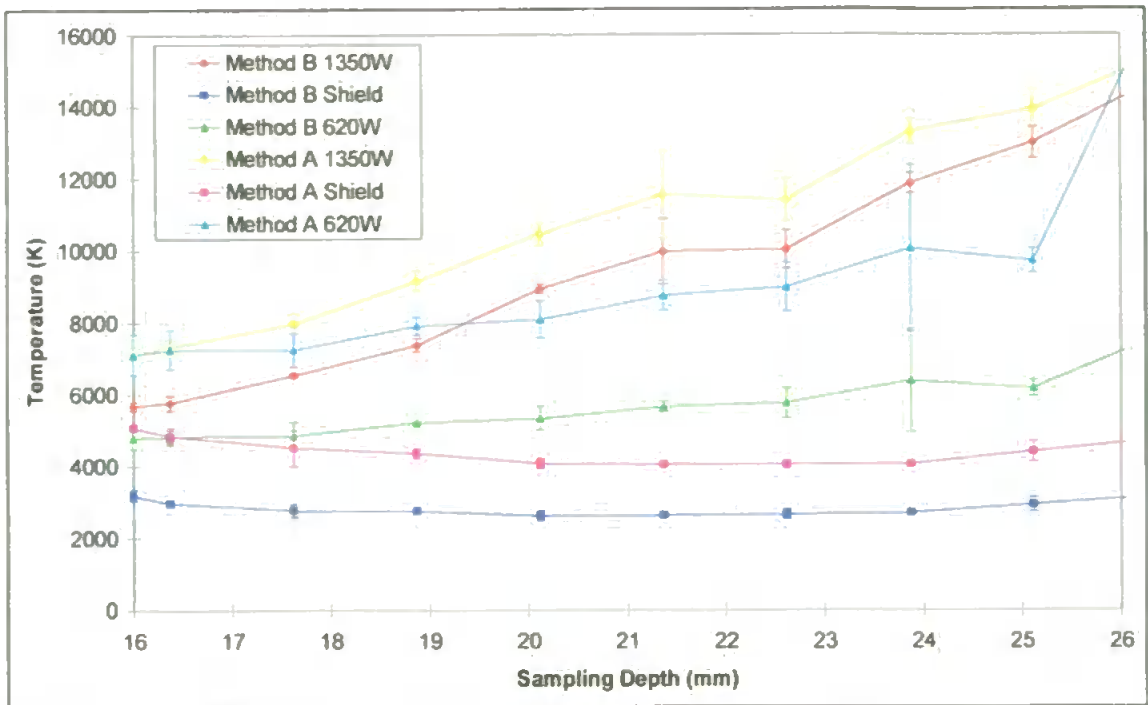


Figure 5.3: Comparison of the sampling depth profiles for the MO^+ temperature up to a sampling depth of 25 mm. Errors = 3σ for $n = 3$.

At 620 W the temperatures calculated were lower than those calculated at 1350 W, although they exhibited the same trend, in that they increased as the sampling depth was increased, up to a maximum at a sampling depth of 32.5 mm and then decreased as the sampling depth was increased further. These temperature profiles also exhibited poor reproducibility at sampling depths greater than 25 mm. The temperature calculated using Method A increased from 7100 K at a sampling depth of 16 mm to 9700 K at 25 mm, while the temperature calculated using Method B increased from 4800 K at 16 mm to 6200 K at 25 mm.

With the shield torch the temperatures calculated were lower than those calculated at both 1350 W and 620 W, and they exhibited a different trend, with the temperature decreasing as the sampling depth was increased, up to a sampling depth of 24 mm. At sampling depths greater than 24 mm the temperature began to increase as the sampling depth was increased further, although they exhibited poor reproducibility at

sampling depths greater than 25 mm. The temperature calculated using Method A decreased from 5050 K at a sampling depth of 16 mm to 4000 K at 24 mm, while the temperature calculated using Method B decreased from 3150 K at 16 mm to 2650 K at 24 mm.

The calculated dissociation temperatures were greatest at 1350 W, with lower temperatures at 620 W, and with the temperatures calculated for the shield torch being lower than both those at 1350 W and 620 W. At 1350 W the positive plasma potential would be large, since there was a large amount of forward power to couple both to the load coil and the sampler cone. Therefore, a large temperature would be expected. At 620 W the coupling between the plasma and both the load coil and the sampler cone would still occur, but would be reduced since there was less forward power available for the coupling. Hence, the temperature would be greater at 1350 W than at 620 W. With the shield torch, not only was the coupling reduced but there was no secondary discharge, and hence an even lower temperature would be expected.

The typical "doughnut" form of an ICP, in which the RF energy is coupled into the outer "skin" of the gas stream, provides a region (the induction region) with a gas temperature of about 10,000 K from which energy is transferred to the central channel flow of initially cold gas. Within this central channel the gas temperature rises from ambient, at the entrance to the plasma, to about 8000 K by the time the gas has reached the mouth of the torch. Once the central channel gas leaves the torch the temperature begins to fall, and by a sampling depth of 30 mm it has dropped to about 6000 K or less^{343,344}. Therefore, the temperature in the plasma should be hottest at low sampling depths and decrease as the sampling depth is increased, and this was found with the shield torch for sampling depths up to 24 mm. However, this was found not to be the case, at 1350 W and 620 W where the temperature increased until a sampling depth of 32.5 mm.

At 1350 W and 620 W a prominent secondary discharge was easily observed at the tip of the sampling cone, especially at large sampling depths where the secondary discharge was not obscured by the light emitted from the plasma. This secondary discharge, which promotes the dissociation of MO^+ , becomes more intense as the sampler is retracted further downstream in the plasma¹⁴⁹. Therefore, as the sampling depth was increased the secondary discharge would increase, resulting in an increase in the plasma potential. An increase in plasma potential would increase the energy coupling to the plasma, resulting in an increase in temperature. Therefore, although the temperature would be expected to decrease with increasing sampling depth, the increased secondary discharge results in an increase in temperature with increased sampling depth at 1350 W and 620 W. With the shield torch no secondary discharge was observed at the power used (620 W), although a discharge has been observed when using a shield torch at powers above 1200 W¹⁵². Therefore, with the shield torch the secondary discharge, which causes an increase in temperature at larger sampling depths, has been removed and so the temperature decreases as expected with increasing sampling depths.

With all three sets of conditions used it was not possible to interpret any meaningful trends at sampling depths greater than 25 mm due to the poor reproducibility of the calculated temperatures.

The majority of temperature determination methods use optical measurements to determine the excitation or ionisation temperature of the plasma, whereas this study determined the dissociation temperature using mass spectrometric measurements. The calculated dissociation temperature would be expected to be greatest with conditions where complete dissociation has occurred. At low sampling depths dissociation is incomplete, resulting in lower temperatures than at greater sampling depths where effective dissociation of the metal oxide has occurred. Therefore, the unexpected trend,

with the temperature increasing with increasing sampling depth, could be due to the type of temperature being determined. Dissociation occurs at higher sampling depths than excitation, which typical plasma temperature calculations are based on, and so the maximum dissociation temperature would occur at higher sampling depths than expected.

Previous studies on the effect of sampling depth on temperature have mainly been carried out using optical measurements. However, Crain *et al.*³¹¹ investigated the effect of sampling depth (10 - 14 mm) on the ionisation temperature of As, using mass spectrometric measurements. The temperature decreased from 6500 K at 10 mm to 6400 K at 14 mm, although the sampling depth range studied was very limited. Furuta³⁰⁴ investigated the effect of sampling depth (4 - 30 mm) on the ionisation temperature for both Ar and Ca, using optical measurements. The ionisation temperature for Ca increased from 6300 K at 12 mm to a maximum of 7000 K at a sampling depth of 16 mm. The temperature then decreased to 5700 K as the sampling depth was increased further. The ionisation temperature for Ar increased from 6600 K at 12 mm to a maximum of 7300 K at a sampling depth of 18 mm. The temperature then decreased to 6500 K as the sampling depth was increased further. Nonose *et al.*¹⁴² measured the ionisation temperature for Mg with and without a shield torch, using optical measurements. The temperature with the shield was lower than with the conventional ICP, but only slightly (7300 K with the shield torch compared to 7400 K with the conventional ICP).

Therefore, previous studies have found that the ionisation temperature also increased at lower sampling depths³⁰⁴. At low sampling depths ionisation is also not complete³⁰³⁻³⁰⁵, which could affect the calculated temperature in the same way as for the dissociation temperature. It was also found that the use of the shield torch reduced the temperature of the plasma¹⁴².

5.3.1.2 Dissociation Temperature of ArX^+

This method for calculating the dissociation temperature of the argon polyatomic ions has been described previously for Method E in Section 4.3.2.5.

The sampling depth profile of the temperature calculated for ArO^+ is shown in Figure 5.4. These results show that the temperature for ArO^+ at 1350 W in the plasma increased from 650 K at a sampling depth of 16 mm to a maximum of 1550 K at 31 mm. The temperature then decreased as the sampling depth was increased further. At 620 W in the plasma the temperature increased from 450 K at 16 mm to 600 K at 31 mm. The temperature then remained constant as the sampling depth was increased further. With the shield torch the raw signal for Ar^+ was so negligible that it was not possible to calculate the temperature.

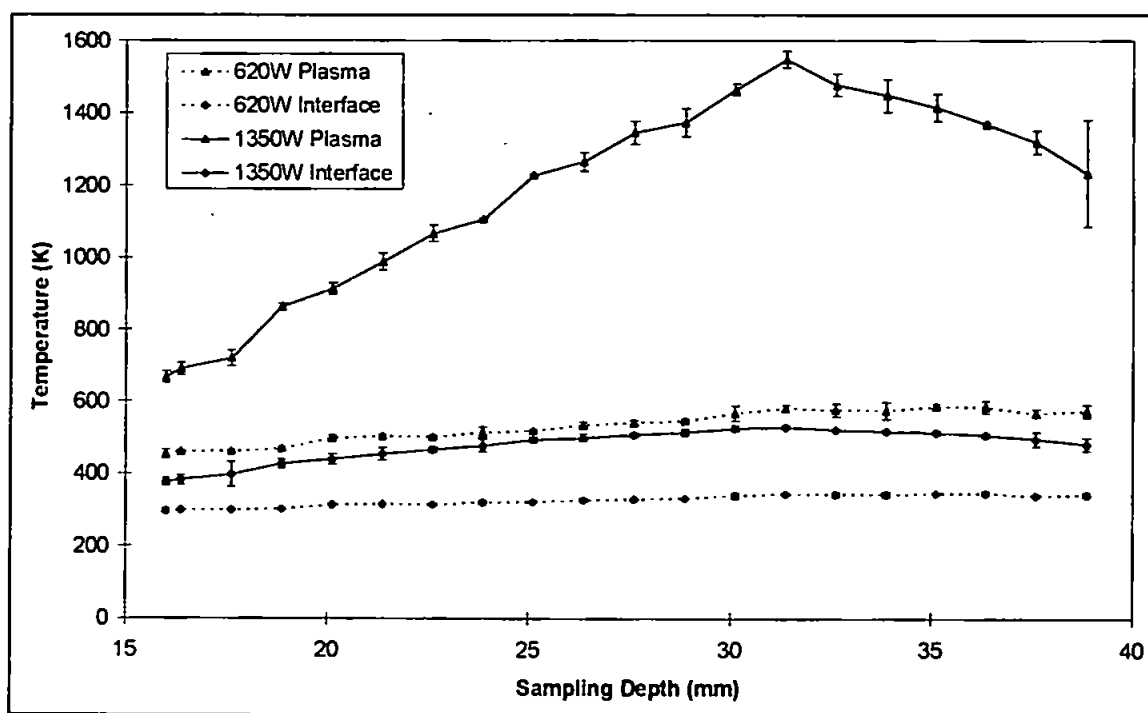


Figure 5.4: Comparison of the sampling depth profiles for the ArO^+ temperature.

Errors = 3σ for $n = 3$.

The temperatures calculated for the dissociation of ArO^+ exhibited a similar trend to those shown for the dissociation of the metal oxides, with the temperature increasing as the sampling depth was increased. The secondary discharge, which promotes the formation of ArX^+ species, becomes more intense as the sampler is retracted further downstream in the plasma¹⁴⁹. Therefore, as the sampling depth was increased the secondary discharge would increase, resulting in an increase in the plasma potential, which in turn would result in an increase in temperature. Therefore, as for the metal oxides, although the temperature would be expected to decrease with increasing sampling depth, the increased secondary discharge results in an increase in temperature with increasing sampling depth.

The temperature calculated for ArO^+ was much lower than those calculated for the metal oxides, varying between 650 K and 1550 K at 1350 W. This was much lower than would be expected in the plasma (5000 - 10,000 K), and this could be due to the low dissociation energy of ArO^+ , which is only 0.43 eV. AlO^+ also has a low dissociation energy (1.71 eV) and the temperatures calculated for this species (< 2500 K) in Chapter 4 were also much lower than those expected within the plasma. Therefore, the low temperature calculated for ArO^+ may be due to its low dissociation energy.

Argon polyatomics, such as ArO^+ , are thought to possibly be formed in the interface rather than in the plasma¹⁴², and this may reflect the low temperature. The temperature calculated for the interface was even lower than that calculated for the plasma. At 1350 W the temperature for ArO^+ in the interface increased from 350 K at a sampling depth of 16 mm to 550 K at 31 mm, while the temperature at 620 W increased from 300 K at 16 mm to 350 K at 31 mm. It was not possible to calculate the temperature with the shield torch due to the negligible values for the Ar^+ raw data.

These temperatures calculated for both the plasma and interface are much lower than expected for the plasma. The temperature calculations are based on p - LTE

conditions within the plasma, and therefore the low temperatures calculated using ArO^+ may indicate a deviation from LTE conditions. LTE conditions are not thought to exist in the interface region of the ICP - MS, suggesting that the ArO^+ species is formed in the interface rather than the plasma. The low temperatures calculated correspond to those thought to prevail in the interface ($< 3500 \text{ K}$)¹⁴², also suggesting formation in the interface rather than the plasma.

5.3.2 Effect of Sampling Depth on M^+ Signal

An example of the sampling depth profile for the metals studied is shown in Figure 5.5 for Ba^+ .

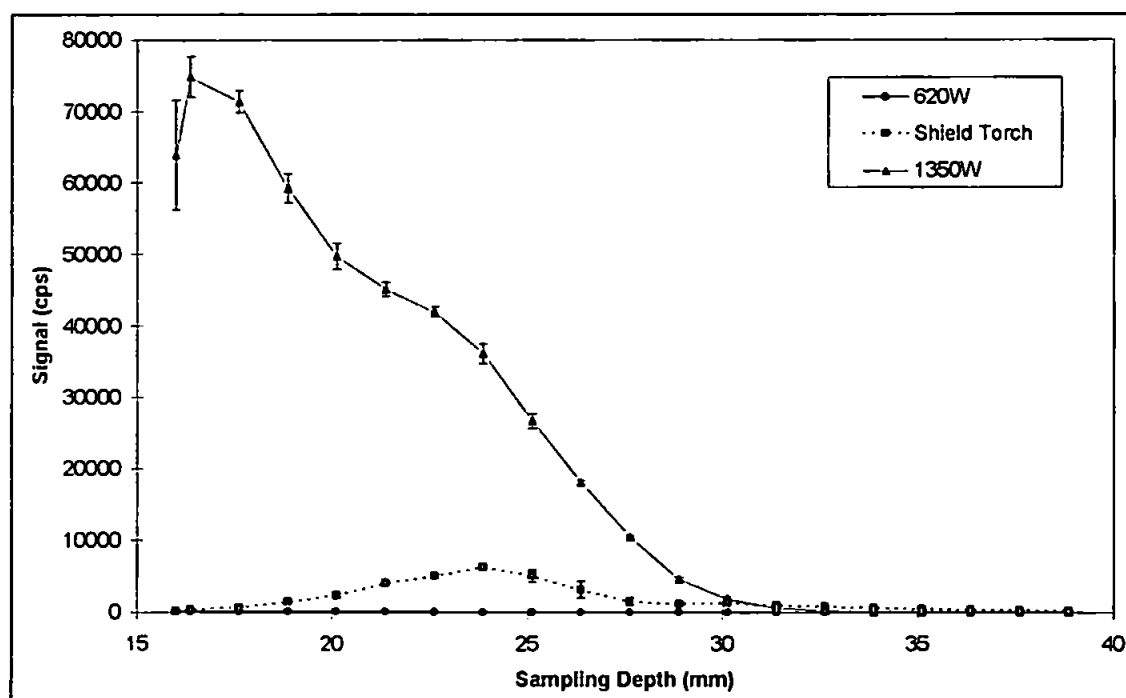


Figure 5.5: Sampling depth profile for Ba^+ . Errors = 3σ for $n = 3$.

These results showed that the signal for Ba⁺ at 1350 W reached a maximum at a sampling depth just after 16 mm and then steadily decreased as the sampling depth was increased further, until a sampling depth of 30 mm where the signal became negligible. With the shield torch the signal for Ba⁺ was much lower than that at 1350 W. The signal increased to a maximum at a sampling depth of 24 mm and then decreased as the sampling depth was increased further. At 620 W the signal for Ba⁺ was negligible at all sampling depths.

This behaviour can be explained with reference to the two main zones in the ICP, the initial radiation zone (IRZ) and the normal analytical zone (NAZ). In ICP - AES the NAZ is generally associated with the position at which the most intense ion line emission is observed, while the IRZ is where the most intense neutral atom line emission is observed^{136,249}. In ICP - MS the best observation zone is somewhere between the IRZ and NAZ¹³⁶, which is at a sampling depth of approximately 5 - 15 mm³⁰³.

At small sampling depths, corresponding to the IRZ, analytes introduced into the plasma have a short residence time in the plasma. This short residence time in the plasma leads to insufficient ionisation of the analyte species. However, as the sampling depth is increased the residence time of analytes in the plasma increases. Hence, the analytes are present in the plasma long enough for efficient ionisation to occur³⁰³. Therefore, as the sampling depth is increased from the IRZ to the NAZ, the analyte signal intensity increases, as the analyte is being more effectively ionised^{304,305}. However, at greater sampling depths the plasma gas becomes cooler and so the ion population is lower, as the analyte is no longer being effectively ionised at the lower temperatures and hence the analyte signal decreases¹³⁸. Therefore a zone of maximum intensity is exhibited⁵⁸. Therefore, at the sampling depths studied, which started at 16 mm, the maximum signal intensity at 1350 W had already occurred lower down in the plasma, and only the decrease in signal, as the sampling depth was increased from this position, was being

observed. With the shield torch the zone of maximum intensity covered a wide range and occurred at a greater sampling depth than at 1350 W, typically 25 mm. With the shield torch the plasma was cooler than at 1350 W, and so a longer residence time in the plasma was necessary for effective ionisation to occur¹⁵², and so the maximum signal intensity would occur at a larger sampling depth than at 1350 W. At 620 W the Ba⁺ signal also exhibited a maximum at a greater sampling depth than at 1350 W, at a sampling depth of 20 mm, although the signal was negligible. The temperature of the plasma at 620 W was less than that at 1350 W, and so it would also be expected to exhibit a maximum signal at a sampling depth greater than that at 1350 W, since a longer residence time would be necessary for effective ionisation to occur. However, the temperature at 620 W was greater than with the shield torch, and so a shorter residence time in the plasma would be necessary for ionisation to occur, and so the maximum signal at 620 W would occur at a smaller sampling depth than with the shield torch.

Previous studies^{138,139,144} have shown that the majority of species reached a maximum signal intensity at sampling depths between 5 and 10 mm. The remainder of the species were studied at sampling depth ranges which started above 15 mm. These species all reached a maximum signal intensity at the lowest sampling depth studied. Therefore, other studies show that the maximum analyte ion signal occurred at a sampling depth of 16 mm or lower, and decreased as the sampling depth was increased further, as seen in this study at 1350 W.

5.3.3 Effect of Sampling Depth on MO⁺ Signal

The metal oxides exhibited a different trend, with increasing sampling depth, to that shown for the metal analyte ions, as shown in Figure 5.6 for BaO⁺.

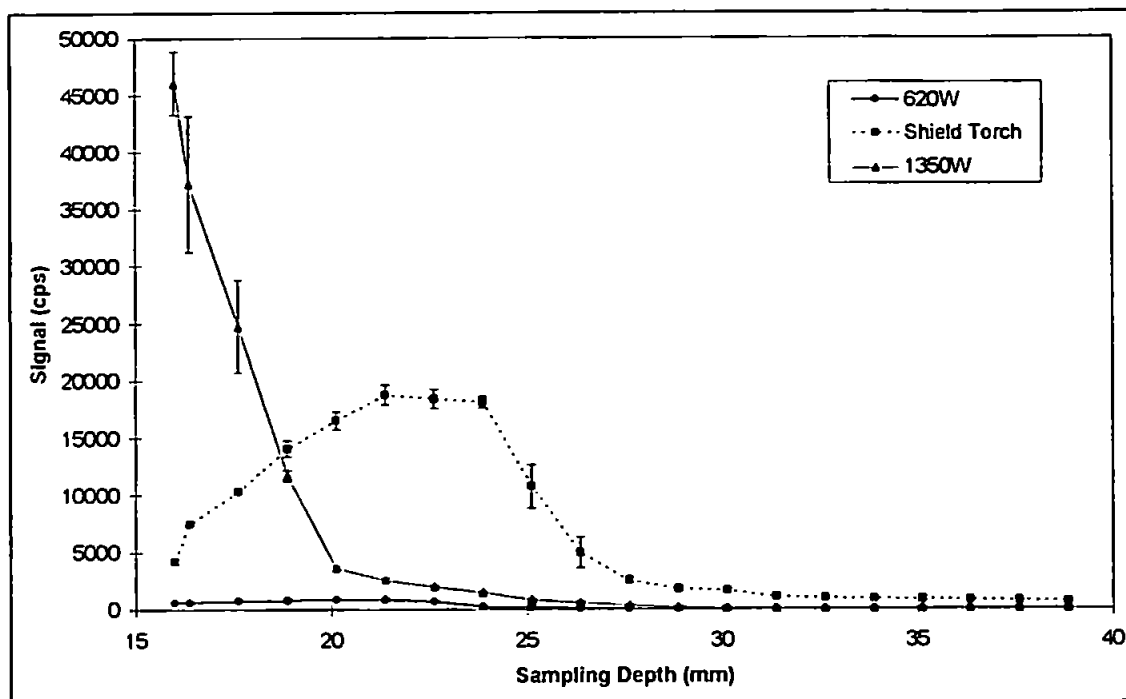


Figure 5.6: Sampling depth profile for BaO^+ . Errors = 3σ for $n = 3$.

These results show that the metal oxide signal at 1350 W was initially very large but rapidly decreased as the sampling depth was increased, with minimal signal at sampling depths greater than 20 mm. With the shield torch the signal increased to a maximum around 24 mm, before decreasing as the sampling depth was increased further. With the shield torch the metal oxide signal was large compared to that at 1350 W, and at sampling depths above 20 mm was much greater than that at 1350 W. At 620 W the signal was negligible compared to those at 1350 W and with the shield torch. However, the signal did increase to a maximum around 21 mm, before decreasing as the sampling depth was increased further.

At low sampling depths the analytes are sampled from the IRZ, where a short residence time in the plasma can lead to insufficient dissociation of any metal oxide species present in the plasma¹⁴⁴. As the sampling depth is increased the sampling region of the ICP moves from the IRZ to the NAZ, resulting in promotion of MO^+ dissociation^{58,142}. Molecular dissociation occurs progressively along the axial channel of

the plasma³⁰⁸, because at larger sampling depths a long residence time in the plasma results in effective dissociation of the metal oxide. Therefore, at low sampling depths a large MO^+ signal would be expected due to insufficient dissociation, but as it is more efficiently dissociated at larger sampling depths the MO^+ signal would decrease, as observed at 1350 W.

With the shield torch the forward power is much lower than at 1350 W and so there is less energy available within the plasma to dissociate the metal oxides¹⁵². Hence, a greater amount of metal oxides would be expected with the shield torch, especially at sampling depths which would correspond to the NAZ (15 - 25 mm). At 1350 W, at these sampling depths the residence time in the plasma was sufficient for effective dissociation of the metal oxides to occur, and so there was little metal oxide signal at these sampling depths. With the shield torch, although the residence time in the plasma was identical, the plasma was operating at 620 W compared to 1350 W, so there was insufficient energy to dissociate the metal oxides effectively. Therefore, with the shield torch significant metal oxide signal was observed at sampling depths between 15 and 25 mm and it was only at greater sampling depths that the metal oxide was effectively dissociated.

At 620 W the forward power is again much lower than at 1350 W, with less energy available to dissociate the metal oxides¹⁵², and so the MO^+ signal would be expected to be comparable to that with the shield torch. However, the shield torch effectively removes the secondary discharge which promotes the formation of metal oxide ions, while at 620 W this secondary discharge is still present. Therefore, at 620 W the power is lower than that at 1350 W, resulting in reduced ionisation of the metal oxide. In addition the secondary discharge effectively dissociates any MO^+ ions which are formed, resulting in negligible MO^+ signal at 620 W. With the shield torch the secondary discharge which promotes the dissociation of MO^+ is removed, resulting in enhanced MO^+ signals compared to those at both 620 W and 1350 W.

Previous studies have investigated the effect of sampling depth on various metal oxide species, including CeO^+ ^{125,139}, BaO^+ ¹³⁹, GdO^+ ⁵⁸ and TbO^+ ⁵⁸. In all cases it was found that either the metal oxide signal or the MO^+ / M^+ ratio decreased as the sampling depth was increased, as was the case in this study at 1350 W.

A comparison of the metal oxide signals, (Figures 5.7 - 5.9) show that the relative signal intensity of the metal oxide increased as the dissociation energy of the metal oxide increased. This is best illustrated at 1350 W (Figure 5.7), which shows that all of the metal oxides studied, as given in Table 5.1, exhibited the same trend, in that the maximum signal was observed at a sampling depth of 16 mm and then decreased as the sampling depth was increased further. However, the maximum intensity reached varied considerably between each metal oxide species. It can be seen that the intensity of the metal oxide signal varied according to its dissociation energy.

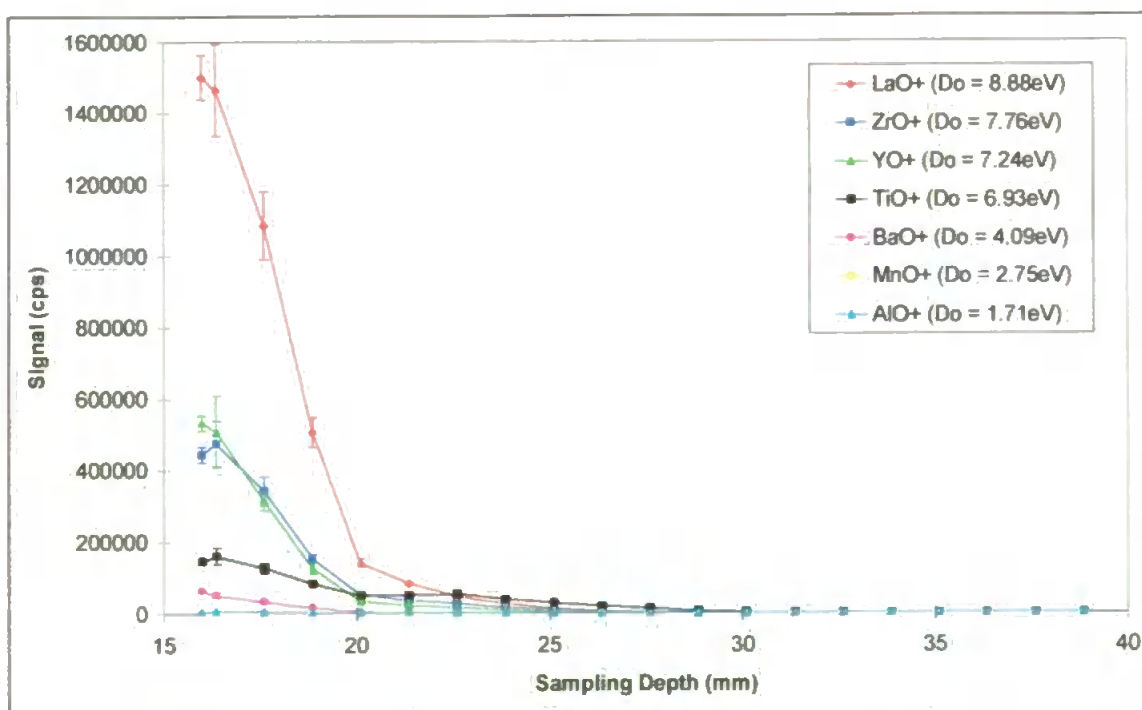


Figure 5.7: Comparison of the sampling depth profiles for MO^+ at 1350 W. Signals normalised to 100% abundance. Molecular abundances of metal oxides are given in Table 5.1. D_0 values given are for MO^+ . Errors = 3σ for $n = 3$.

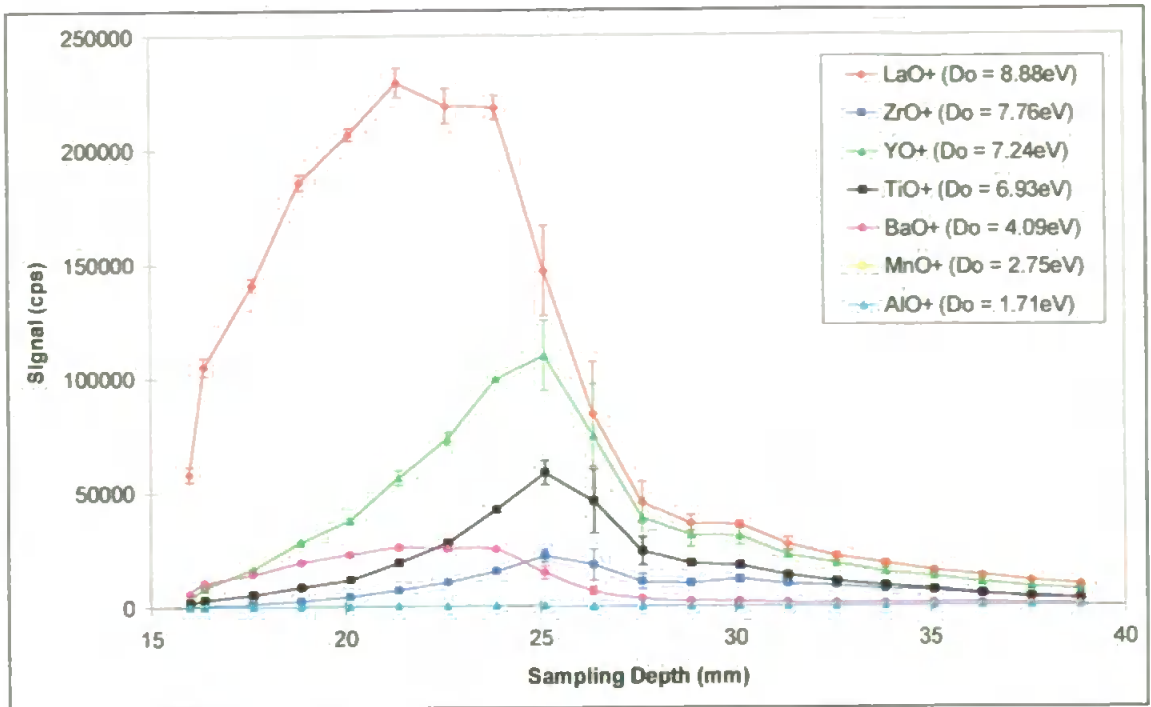


Figure 5.8: Comparison of the sampling depth profiles for MO^+ with shield torch. Signals normalised to 100% abundance. Molecular abundances of metal oxides are given in Table 5.1. D_0 values given are for MO^+ . Errors = 3σ for $n = 3$.

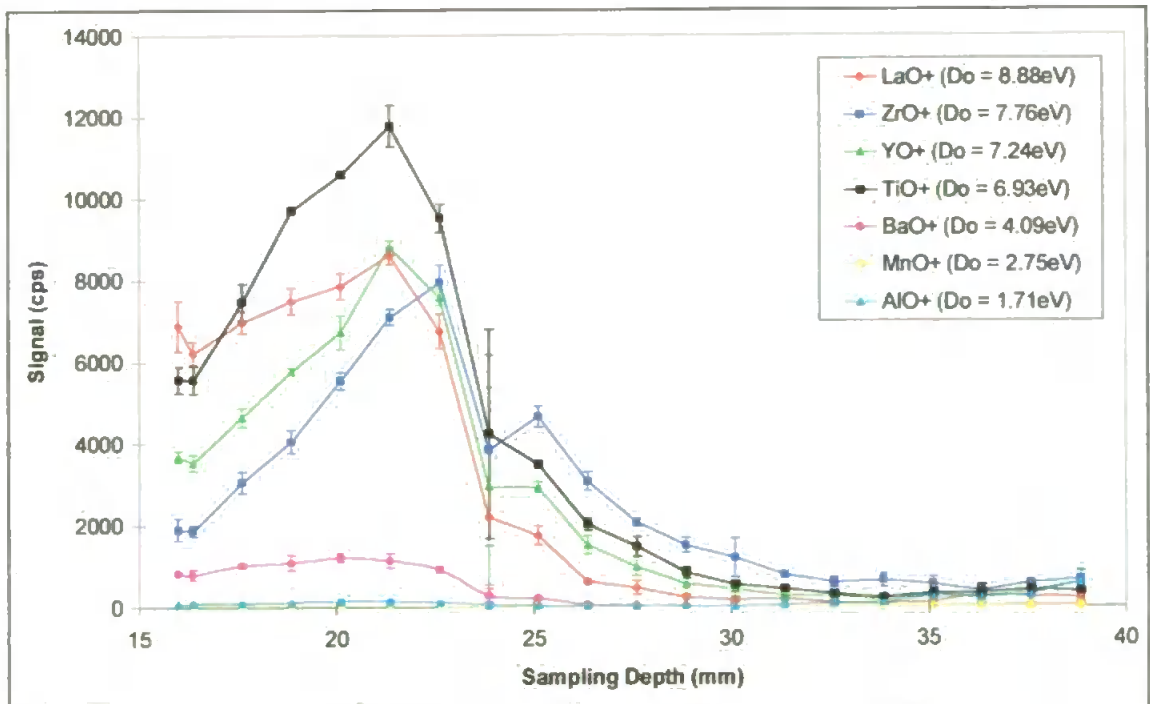


Figure 5.9: Comparison of the sampling depth profiles for MO^+ at 620 W. Signals normalised to 100% abundance. Molecular abundances of metal oxides are given in Table 5.1. D_0 values given are for MO^+ . Errors = 3σ for $n = 3$.

Species with a large dissociation energy require large amounts of energy to break the metal oxide bond so were persistent in the plasma, and a large signal was therefore observed. Conversely, species with low dissociation energies require little energy to break the metal oxide bond, were less persistent in the plasma because they dissociated to a greater extent, so relatively little signal was observed. This can be seen in Figure 5.7 where LaO^+ , with a high dissociation energy of 8.88 eV, gave rise to a very large signal and AlO^+ , with a low dissociation energy of 1.71 eV, resulted in virtually no signal. With the use of the shield torch (Figure 5.8) the metal oxides show the same trend, in that the metal oxide signal increased as the dissociation energy was increased. At 620 W (Figure 5.9) the correlation between signal intensity and dissociation energy was less obvious, due to negligible signals at 620 W.

5.3.4 Effect of Sampling Depth on ArX^+ Signal

An example of the sampling depth profile for the ArX^+ species studied is shown in Figure 5.10 for ArO^+ .

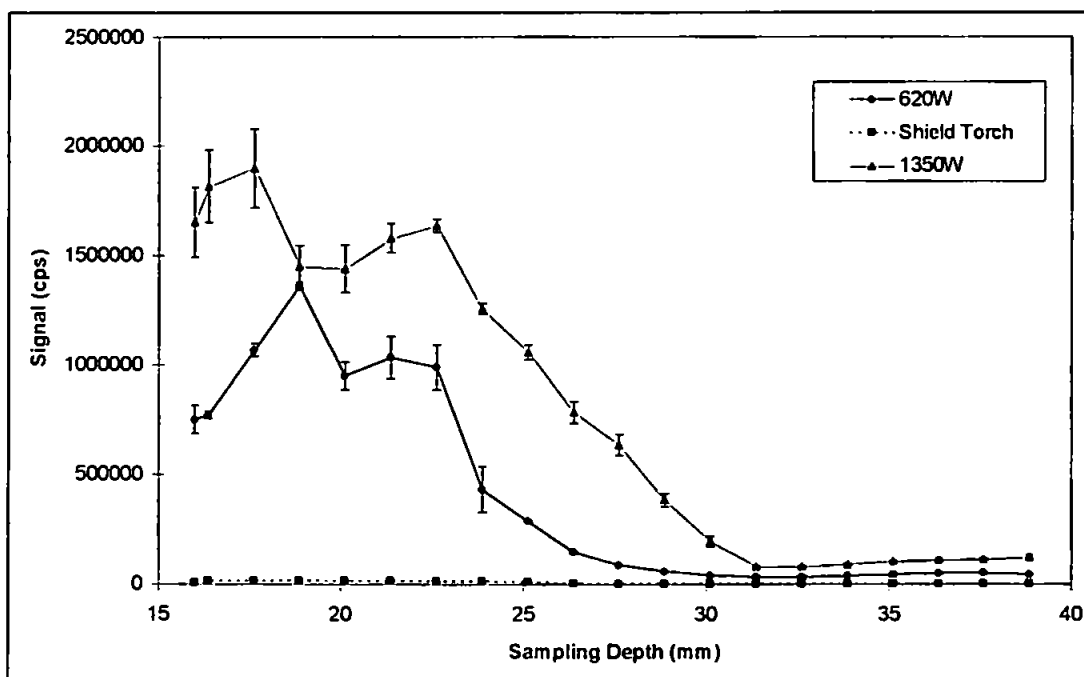


Figure 5.10: Sampling depth profile for ArO^+ . Errors = 3σ for $n = 3$.

These results show that the signal for ArO^+ at 1350 W reached a maximum at a sampling depth of 17 mm, remained fairly constant between 18 and 24 mm and then decreased as the sampling depth was increased further. After a sampling depth of 31 mm the signal began to increase slightly, although the signal was negligible compared to that at smaller sampling depths. At 620 W the signal for ArO^+ was lower than that at 1350 W, remained fairly constant until a sampling depth of 24 mm, after which the signal decreased as the sampling depth was increased further. At sampling depths greater than 31 mm the signal began to increase slightly. With the shield torch the signal for ArO^+ was negligible at all sampling depths.

Capacitive coupling between the plasma and the load coil creates a potential in the plasma, which forms a secondary discharge between the plasma and the sampling orifice^{249,250} if the plasma potential is too high. This secondary discharge can promote the formation of polyatomic ions behind the sampling cone²⁴⁸. At 1350 W the large forward power would create a large plasma potential, resulting in large ArX^+ signals. At 620 W the forward power is less and so a smaller plasma potential would occur, resulting in less ArX^+ signal at 620 W than at 1350 W. With the shield torch the capacitive coupling is reduced and the secondary discharge removed, resulting in negligible ArX^+ signal.

Comparison of the sampling depth profiles of ArX^+ species, as given in Table 5.1, at 1350 W, 620 W and with the shield torch are shown in Figures 5.11, 5.12, and 5.13, respectively. These results show that at 1350 W (Figure 5.11) the argon polyatomic species exhibit three different trends. The signal for ArH^+ exhibited a similar trend to that observed for ArO^+ , with maximum signal at low sampling depths which decreased as the sampling depth was increased further.

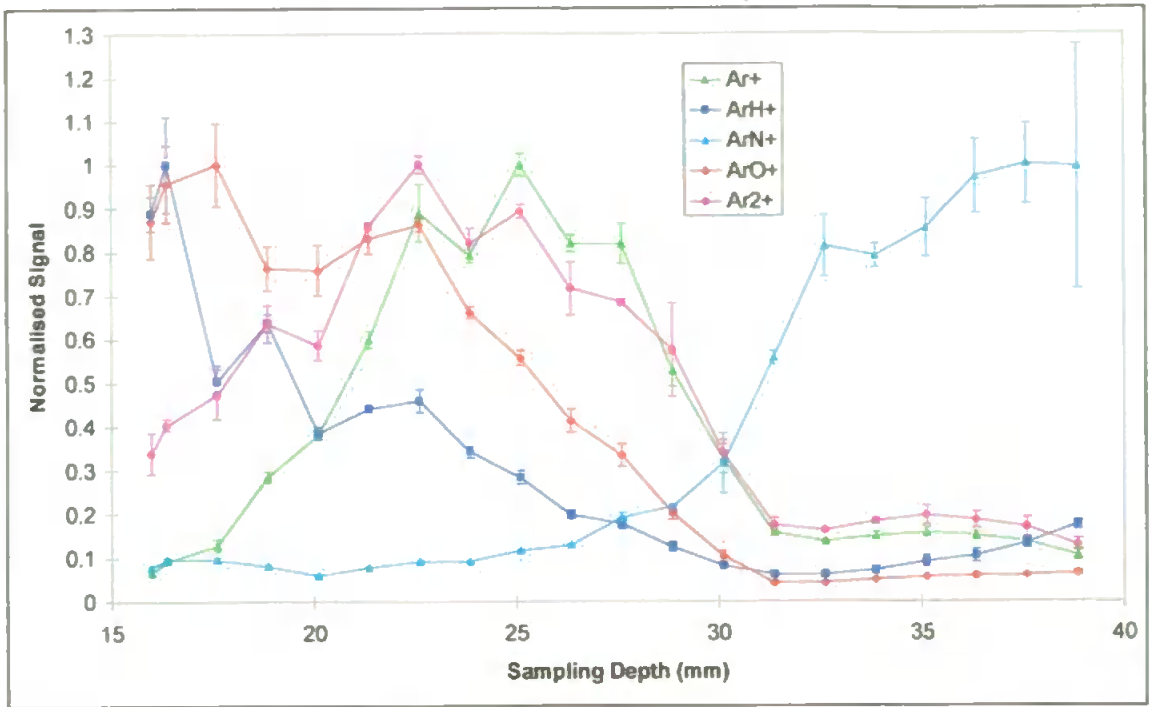


Figure 5.11: Comparison of the sampling depth profiles for the ArX^+ species at 1350 W. Signals normalised (Signals divided by highest signal in profile).

Errors = 3σ for $n = 3$.

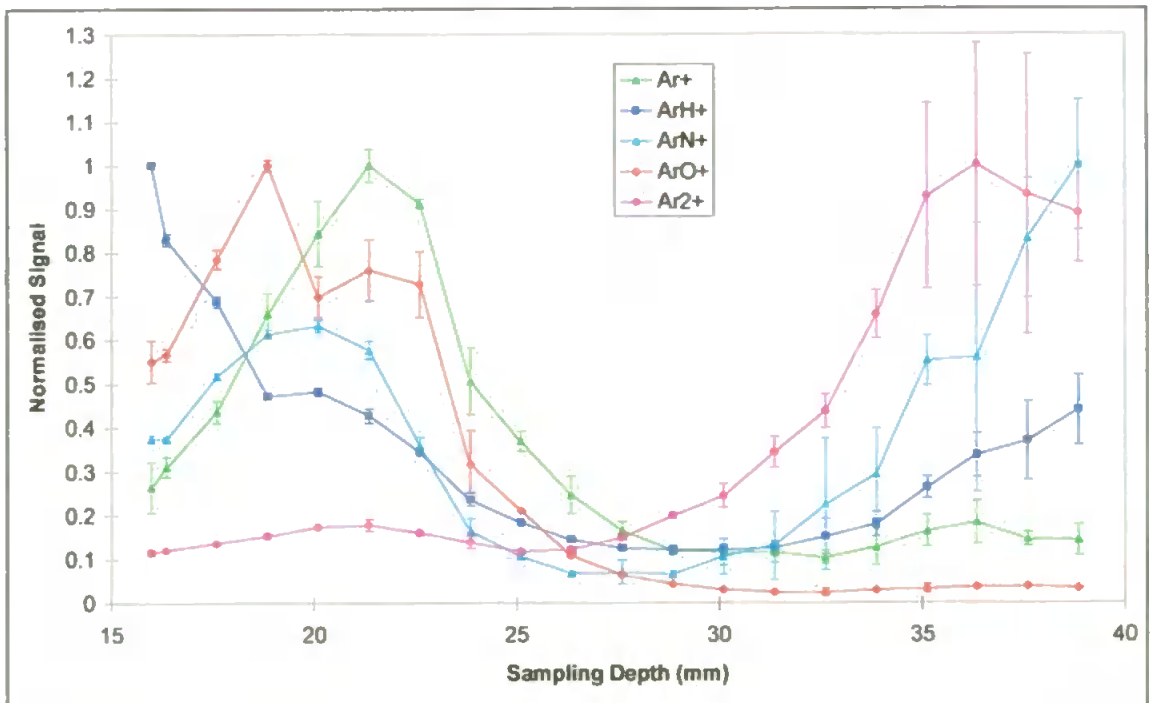


Figure 5.12: Comparison of the sampling depth profiles for the ArX^+ species at 620 W. Signals normalised. Errors = 3σ for $n = 3$.

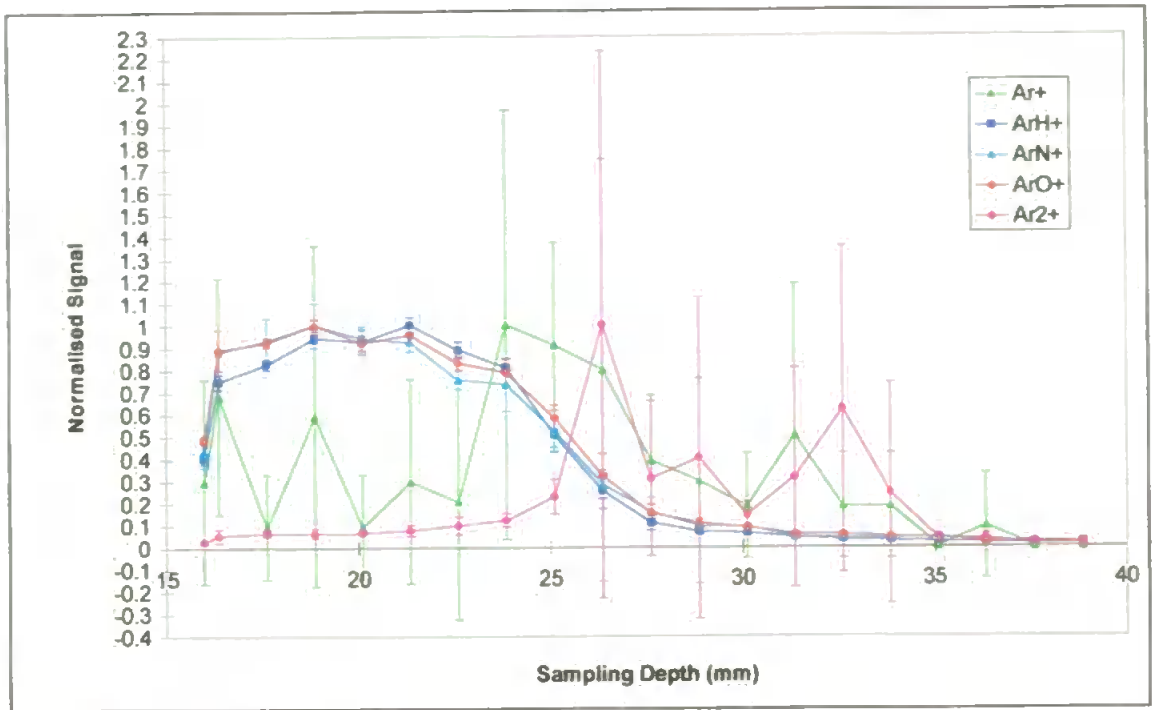


Figure 5.13: Comparison of the sampling depth profiles for the ArX^+ species with the shield torch at 620 W. Signals normalised. Errors = 3σ for $n = 3$.

The signals for Ar^+ and Ar_2^+ exhibited a slightly different trend from ArO^+ and ArH^+ at low sampling depths, with the signals increasing to a maximum at 22 mm, remaining fairly constant between 22 and 27 mm, and then decreasing as the sampling depth was increased further. The signal for ArN^+ increased as the sampling depth was increased.

At 1350 W the behaviour of the ArO^+ and ArH^+ signals exhibited a similar trend to those observed for MO^+ , in that there were large signals at low sampling depths which decreased as the sampling depth was increased, although the signals decreased much less sharply than the MO^+ signals. Therefore, at low sampling depths there was little dissociation of ArO^+ and ArH^+ , and so these signals were large at low sampling depths. As the sampling depth was increased more efficient dissociation occurs and so these signals decrease with increasing sampling depth. However, ArX^+ species are thought to form in the interface, as well as in the plasma, due to the formation of a secondary

discharge behind the sampler cone. This secondary discharge, which promotes the formation of ArX^+ , becomes more intense as the sampler is retracted further downstream in the plasma¹⁴⁹. Therefore, due to an increase in the secondary discharge the ArX^+ signals would be expected to increase as the sampling depth was increased, and this was observed at sampling depths greater than 31 mm, where the ArO^+ and ArH^+ signals began to increase again as the sampling depth was increased beyond 31 mm.

The Ar^+ signal exhibited a trend similar to the metal analytes, although the maximum signal occurred at a larger sampling depth than that exhibited for the metal ions. At low sampling depths the short residence time in the plasma leads to insufficient ionisation of the argon atom. As the sampling depth increases the Ar^+ signal increases, due to more efficient ionisation. As the sampling depth is increased further less efficient ionisation occurs at the lower temperatures at these sampling depths, and so the Ar^+ signal decreases. The maximum Ar^+ signal occurred at a larger sampling depth than the metal ions due to its higher ionisation potential. The ionisation potential of Ar at 15.76 eV is almost double that of the metals studied, which are typically less than 8 eV, and so a longer residence time in the plasma is required for effective ionisation of Ar to occur, compared to that for the metals, resulting in a maximum signal at a larger sampling depth.

The Ar_2^+ signal followed an identical trend to that observed for the Ar^+ signal. Ar_2^+ is thought to be formed in the plasma by collisional reactions, rather than by ionisation of the neutral species¹³⁸, e.g.



As the population of Ar^+ increases at increasing sampling depths, the Ar_2^+ signal would increase as more collisional reactions with Ar occur within the plasma, and then decrease again as less Ar^+ is formed in the plasma at greater sampling depths.

The signal for ArN^+ exhibited a completely different trend to those exhibited by the other ArX^+ species, with the signal increasing as the sampling depth was increased. This can be explained by air entrainment. As the sampling depth was increased the plasma was moved further away from the sampling cone, increasing the air entrainment into the system.

At 620 W (Figure 5.12) the ArX^+ signals are similar to those exhibited at 1350 W. However, at large sampling depths (greater than 30 mm) the ArX^+ signals increase to significant levels. This can be explained by the secondary discharge which becomes more intense as the sampler is retracted further downstream in the plasma¹⁴⁹. Therefore, at larger sampling depths the secondary discharge becomes more intense, promoting the formation of ArX^+ species. This trend was also observed at 1350 W but was not so pronounced due to the large ArX^+ signals at low sampling depths. At 620 W the ArX^+ signals were lower than those at 1350 W, due to the reduced plasma power, and so the signals at larger sampling depths were of comparable intensity to those at low sampling depths. At both 1350 W and 620 W a prominent secondary discharge was easily observed at the tip of the sampler cone, especially at large sampling depths when the secondary discharge was not obscured by the light emitted from the plasma. However, at the power used with the shield torch (620 W) no secondary discharge was observed, although a secondary discharge has been observed when using a shield torch at powers above 1200 W¹⁵².

With the shield torch (Figure 5.13) the signals for ArO^+ , ArH^+ and ArN^+ , exhibited a similar trend, in that the signals remained fairly constant to a sampling depth of 24 mm, before decreasing as the sampling depth was increased further. Unlike the

signals at 1350 W and 620 W the ArX^+ signals with the shield torch did not increase at sampling depths above 30 mm, due to the removal of the secondary discharge which causes this effect. The maximum signal observed occurred over a wider range of sampling depths than at 1350 W and 620 W. With the shield torch the plasma potential is greatly reduced and so effective dissociation of these species occurs at a greater sampling depth. The signals for Ar^+ and Ar_2^+ did not exhibit a determinable trend with sampling depth, due to the reduced potential with the shield torch which was not sufficient to effectively ionise the argon in the plasma.

Previous studies on argon polyatomic species are not as common as for the metals or their oxides, and those that have been carried out are very patchy. Evans and Ebdon¹³⁸ investigated the effect of sampling depth (8.75 - 11.5 mm) on ArO^+ , ArN^+ and Ar_2^+ at conditions comparable to those at 1350 W in this study. The signal for all of these ions gradually increased as the sampling depth was increased. Kawaguchi *et al.*¹⁴⁰ also investigated the effect of sampling depth (4 - 10 mm) on ArO^+ and Ar_2^+ at 1200 W, although it was only in the form of the effect of carrier gas flow rate at various sampling depths. The signal for ArO^+ decreased as the sampling depth was increased, while the signal for Ar_2^+ increased as the sampling depth was increased, at a carrier gas flow rate of 0.9 l min^{-1} . Nonose *et al.*¹⁴² investigated the effect of sampling depth (12 - 16 mm) on ArO^+ with a shield torch at several different forward powers. At 800 W the signal for ArO^+ increased to a maximum at 15 mm and then decreased as the sampling depth was increased further. At higher powers the signal increased as the sampling depth was increased, over the range of sampling depths studied.

Therefore, previous studies have found that argon polyatomic signals increased at low sampling depths. However, all these studies were carried out at sampling depths which were beyond the range of this study and so a valid comparison is not possible.

5.4 CONCLUSIONS

The sampling depth had a significant effect on the signal for metal analytes and polyatomic ions, showing how important it is to optimise the sampling depth for maximum response, and also to reduce interferences. At a sampling depth of 20 mm the analyte ion signal was two thirds of the signal at 16 mm. However, the metal oxide signal at 20 mm had dropped to less than one tenth of the signal at 16 mm. Therefore, simply by careful selection of the sampling depth it is possible to greatly reduce the metal oxide interferences, with minimal loss of signal. This eliminates the need for other, more expensive or time consuming, methods for oxide reduction, such as desolvation. However, this is not effective for the argon polyatomic species, which are still present in the plasma in significant amounts at sampling depths beyond 25 mm.

These argon polyatomic species are greatly reduced, in most cases to negligible levels, with the use of the shield torch, while maintaining a reasonable level of metal analyte signal. Unfortunately, with the shield torch the levels of metal oxides greatly increased, especially at sampling depths up to 25 mm. This difference in behaviour between the metal oxides and argon polyatomics, with the shield torch, suggests that they may be formed by different mechanisms¹⁴². This can also be seen in the temperatures calculated for the different species, where temperatures of 5000 - 14,000 K suggest that metal oxides are formed in the plasma, and temperatures below 1500 K suggest that argon polyatomics are formed in the interface region of the plasma. The use of temperature calculations to investigate the possible site of formation for interference ions is investigated in a later chapter.

The presence of the secondary discharge has a great influence on both the raw signals and the dissociation temperatures. While the signals for both the metal oxides and the argon polyatomics decrease with increasing sampling depths, at sampling depths greater than 30 mm the ArX^+ signals at 1350 W and 620 W began to increase again. At

these sampling depths the region of the plasma being sampled is beyond the tail plume, and so it is the secondary discharge which is being sampled. The secondary discharge promotes the formation of ArX^+ species and this was observed at sampling depths above 30 mm, where the ArX^+ signals increased as the sampling depth was increased. With the shield torch, where no secondary discharge is formed, the ArX^+ signals did not increase at sampling depths greater than 30 mm.

The temperatures calculated for both the metal oxides and argon polyatomic species increased as the sampling depth was increased, at both 1350 W and 620 W. At both 1350 W and 620 W a prominent secondary discharge was observed at the tip of the sampler cone, which becomes more intense as the sampler is retracted further downstream in the plasma¹⁴⁹. As the sampling depth was increased the secondary discharge would increase, resulting in an increase in the plasma potential. An increase in the plasma potential would increase the energy coupling to the plasma, resulting in an increase in temperature. Therefore, although the temperature would be expected to decrease with increasing sampling depth, the increased secondary discharge results in an increase in temperature with increasing sampling depth at 1350 W and 620 W. With the shield torch no secondary discharge was observed, and the temperature decreased with increasing sampling depth as expected.

In this investigation the minor isotopes of many of the species studied were used in order to prevent the overloading of the detector. However, it was found that although the minor isotopes gave ample signal at 1350 W this was not always the case. At 620 W and with the shield torch the signals for some species dropped significantly, especially at larger sampling depths. While these greatly reduced signals could still be used to calculate the temperature, it would introduce unnecessary errors into the temperature calculation. In the case of Ar^+ the signal with the shield torch was so low that it was not possible to calculate the temperature. Therefore, in all further experiments more major

isotopes of the analytes under investigation will be used, in order to prevent these errors in the temperature calculations.

The shield torch was operated with compromise conditions, so that while the argon polyatomics were reduced there was also some loss of analyte signal, by about an order of magnitude. Throughout the experiment it was impossible to reduce the argon polyatomic species further without reducing the metal ion signal to lower than this recommended amount. The shield torch was operated at 620 W because that was the default power setting which the plasma was set at when the shield was in operation. Therefore, it was assumed that since that was the default power setting that it was also the optimum power at which the shield torch operated. However, subsequent investigations revealed that the plasma was not stable with the shield torch at the recommended power of 620 W, so further experiments were performed at 700 W.

CHAPTER 6

Effect of Power on Polyatomic Ions and their Dissociation Temperatures

6 EFFECT OF POWER ON POLYATOMIC IONS AND THEIR DISSOCIATION TEMPERATURES

6.1 INTRODUCTION

Plasma operating conditions, such as nebuliser gas flow rate, power and solvent loading, influence the relative positions of the initial radiation zone (IRZ) and normal analytical zone (NAZ), and are thus related to the sampling position²⁴⁹. If the RF power is increased, the IRZ and NAZ move closer to the load coil because the central channel of the ICP contracts⁵⁸. Therefore, at a fixed sampling depth, increasing the RF power moves the sampling region of the ICP from the IRZ to the NAZ^{58,142}. As shown in Chapter 5, the sampling position greatly affects the signal obtained for both metal analyte species and polyatomic ion interferences. Therefore, it would be expected that plasma operating conditions which are related to the sampling depth would also affect the signals of metal analyte ions and polyatomic ion interferences.

6.2 EXPERIMENTAL

Experiments were conducted using a PlasmaQuad 3 (VG Elemental, Ion Path, Road Three, Winsford, Cheshire, UK), as described in Section 2.1.2. Both ArX^+ and MO^+ interferences were studied at the m/z shown in Table 6.1.

A power profile of the plasma was obtained from 550 to 1600 W at 50 W intervals, at a sampling depth of 16 mm. When using the shield torch the power profile was obtained from 650 to 1400 W at 50 W intervals, due to the unpredictable stability of the plasma with the shield torch at lower powers and the possibility of damaging the Ni

shield with prolonged use at high powers. At each power monitored all other operating parameters, i.e. lens settings and position of torchbox were adjusted to give maximum signal for $^{115}\text{In}^+$.

Table 6.1: Isotopes studied during effect of power experiment

Species	Mass	Abundance	Species	Mass	Abundance
Al^+	27	100	Ar_2^+	80	99.2
Ar^+	36	0.34	Y^+	89	100
ArH^+	39	0.1*	Zr^+	90	51.4
AlO^+	43	99.8*	YO^+	105	99.8*
Ti^+	48	73.8	ZrO^+	106	51.3*
ArN^+	54	99.2	In^+	115	95.8
Mn^+	55	100	Ba^+	138	71.7
ArO^+	56	99.4*	La^+	139	99.9
TiO^+	64	73.6*	BaO^+	154	71.6*
MnO^+	71	99.8*	LaO^+	155	99.7*

* The abundances for the molecular species were calculated by combining the abundances of the two constituent elements.

6.3 RESULTS AND DISCUSSION

6.3.1 Variation of Dissociation Temperature with Power

6.3.1.1 Dissociation Temperature of MO^+

The methods used for calculating the dissociation temperature of the metal oxides have been described previously for Methods A and B in Sections 4.3.2.1 and 4.3.2.2, respectively.

Comparisons of the dissociation temperatures, using Methods A and B, calculated for the different metal oxide species with standard conditions and with the shield torch are shown in Figure 6.1.

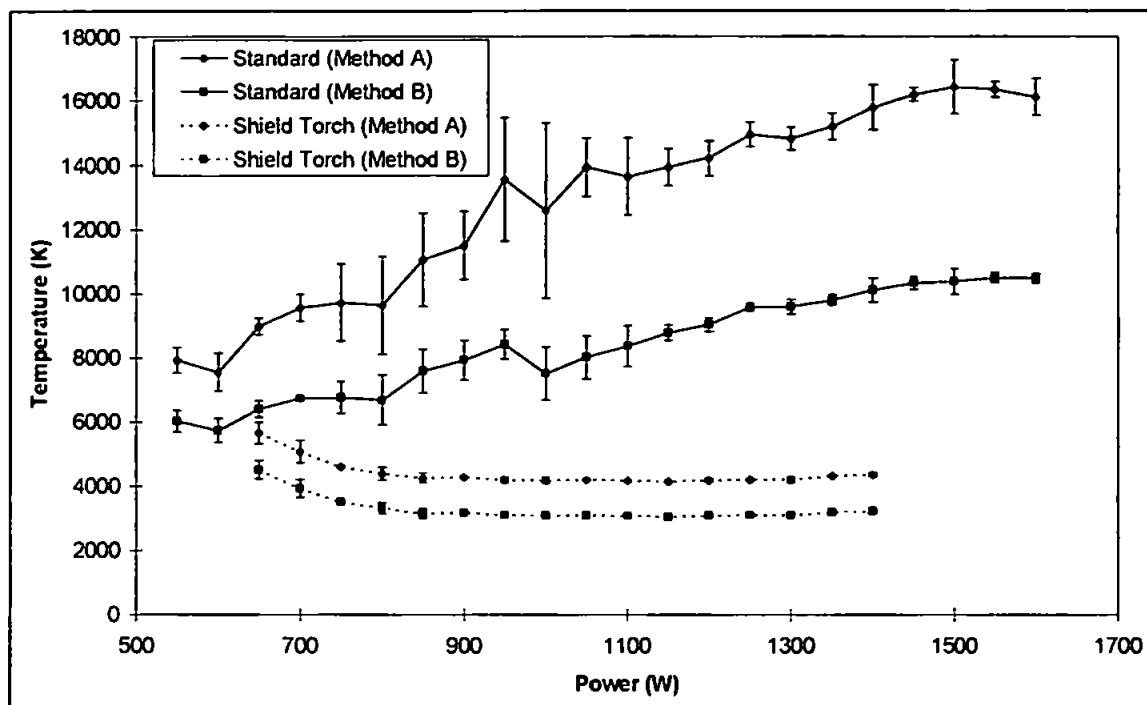


Figure 6.1: Comparison of the effect of power for the MO^+ temperature.

Errors = 3σ for $n = 3$.

With standard conditions the metal oxide dissociation temperatures increased as the power was increased. The temperature calculated using Method A increased from 7900 K at a power of 550 W to 16,500 K at 1600 W, while the temperature calculated using Method B increased from 6000 K at a power of 550 W to 10,500 K at 1600 W. The temperatures calculated at higher powers using Method A were higher than the range expected within the plasma (4000 - 10,000 K)³³², but the temperatures calculated using Method B were within this range expected within the plasma.

As the power was increased more energy would enter the plasma and so the temperature within the plasma would increase. Therefore, the temperature would be

expected to increase as the power was increased. Longerich³¹⁴ and Crain *et al.*³¹¹ have investigated the effect of power on the dissociation temperature of metal oxides and the ionisation temperature of Sb and As, respectively. They found that the temperature increased as the power was increased.

With the shield torch the temperatures initially decreased as the power was increased but then remained fairly constant as the power was increased above 800 W. The temperature calculated using Method A decreased from 5650 K at a power of 650 W to 4250 K at 850 W, while the temperature calculated using Method B decreased from 4500 K at a power of 650 W to 3150 K at 850 W. At powers above 800 W the temperature with the shield torch remained fairly constant as the power was increased. Previous studies³⁰² have shown that the plasma potential with the shield torch varies much less with the plasma operating parameters than with a standard coil. Therefore, the power has little effect on the plasma potential, and hence the temperature, with the shield torch.

The temperatures calculated with the shield torch were lower than those calculated with standard conditions. This would be expected because the use of the shield torch removes the capacitive coupling and the secondary discharge within the plasma, removing some of the energy within the plasma. Therefore, with less energy within the plasma the temperature would be expected to be lower.

6.3.1.2 Dissociation Temperature of ArX^+

This method for calculating the dissociation temperature of the argon polyatomic ions has been described previously for Method E in Section 4.3.2.5.

The power profile of the temperature for ArO^+ is shown in Figure 6.2. These results show that the temperature for ArO^+ with standard conditions increased from 480 K at 550 W to a maximum of 830 K at 1100 W. The temperature then decreased to 700

K at 1200 W, after which the temperature varied very little as the power was increased further. With the shield torch the temperature increased from 500 K at 650 W to a maximum of 830 K at 1350 W. As the power was increased more energy would enter the plasma and so the temperature within the plasma would increase. Therefore, the temperature would be expected to increase as the power was increased.

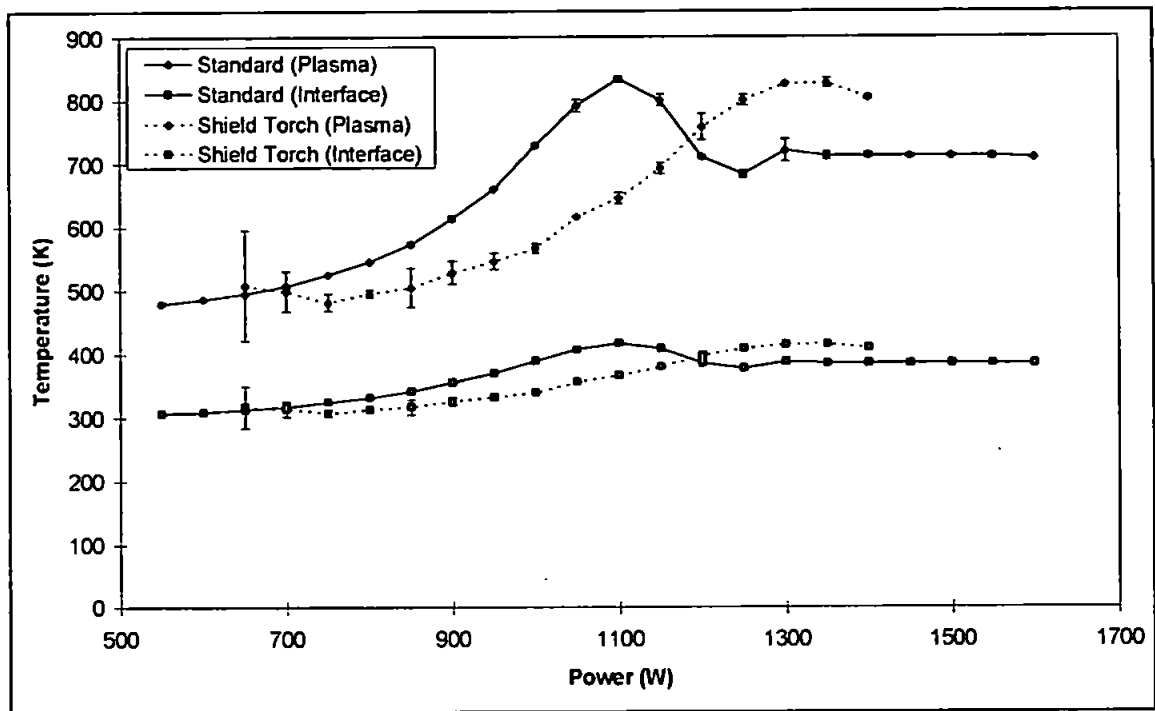


Figure 6.2: Comparison of the effect of power for the ArO^+ temperature. Errors = 3σ for $n = 3$.

The temperatures calculated with the shield torch were slightly lower than those calculated with standard conditions. This would be expected because the use of the shield torch removes the capacitive coupling and the secondary discharge within the plasma, removing some of the energy within the plasma. Therefore, with less energy within the plasma the temperature would be expected to be lower.

Argon polyatomics, such as ArO^+ , are thought to possibly be formed in the interface rather than in the plasma¹⁴², and this may reflect the low temperature. The temperature calculated for the interface was even lower than that calculated for the plasma. With standard conditions the temperature for ArO^+ in the interface increased from 300 K at 550 W to a maximum of 420 K at 1100 W. The temperature then decreased to 380 K at 1200 W, after which the temperature varied very little as the power was increased further. With the shield torch the temperature increased from 300 K at 650 W to a maximum of 415 K at 1350 W.

These temperatures calculated for both the plasma and interface are much lower than expected for the plasma. The temperature calculations are based on p - LTE conditions within the plasma, and therefore the such low temperatures calculated using ArO^+ may indicate a deviation from LTE conditions. LTE conditions are not thought to exist in the interface region of the ICP - MS, suggesting that the ArO^+ species is formed in the interface rather than the plasma. The low temperatures calculated correspond to those thought to prevail in the interface ($< 3500 \text{ K}$)¹⁴², also suggesting formation in the interface rather than the plasma.

6.3.2 Effect of Power on M^+ Signal

The metal ion signals with standard conditions increased as the power was increased, as shown in Figure 6.3 for La^+ , although the signal was negligible below 1050 W. With the shield torch the signal for La^+ was negligible at all powers, although the signal increased as the power was increased.

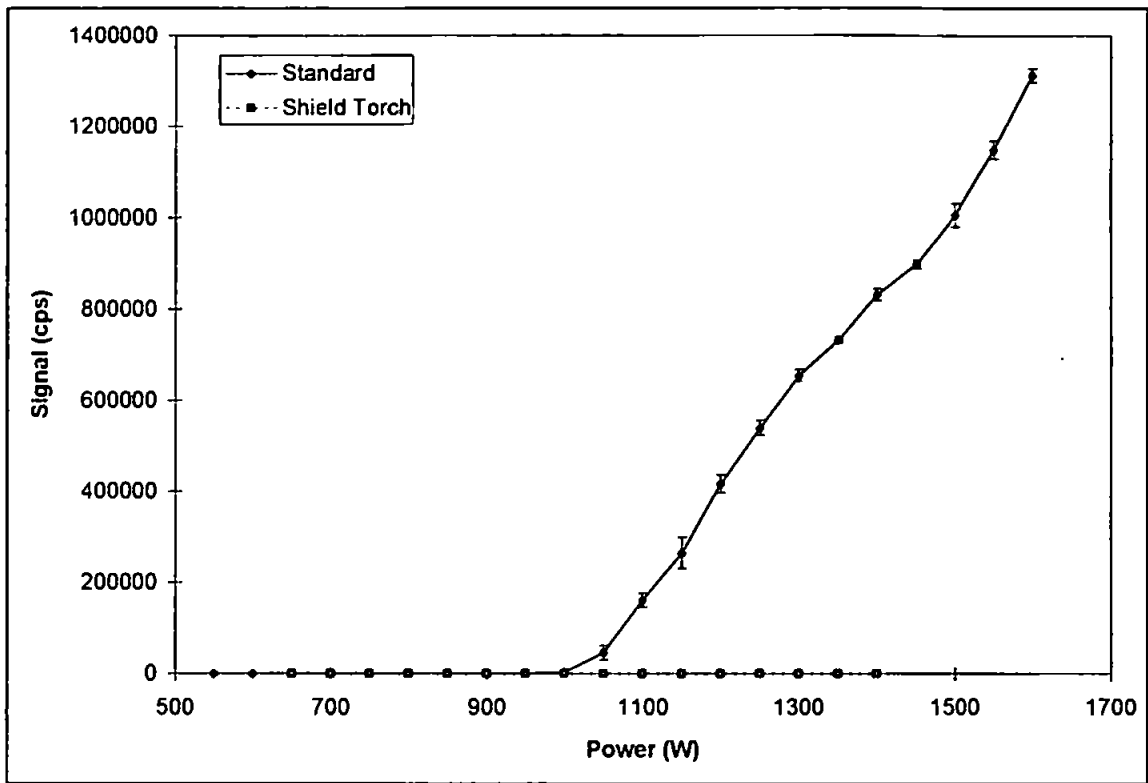


Figure 6.3: Effect of power on the signal for La^+ . Errors = 3σ for $n = 3$.

All the metal ions studied, as given in Table 6.1, exhibited the same trend with standard conditions, with the signals increasing as the power was increased. This trend would be expected, because as the power was increased there would be more energy available within the plasma to ionise analytes present in the plasma. As the power was increased an increase in analyte ionisation would therefore lead to an increase in metal ion signal.

With the shield torch all of the metal ions studied also increased as the power was increased, with several species reaching a maximum signal and then decreasing as the power was increased further. However, not all the metal ion signals with the shield torch were negligible in comparison to those with standard conditions. The signals for Al^+ , Mn^+ and the internal reference ion In^+ exhibited a different trend to that observed for La^+ , as shown in Figure 6.4 for Al^+ . The signal for Al^+ with the shield torch was much greater than that with standard conditions. This was particularly pronounced at powers below

1100 W, where the signals with the shield torch were more than ten times greater than the signals with standard conditions. Even at high powers the signals with the shield torch were twice that of the signals with standard conditions.

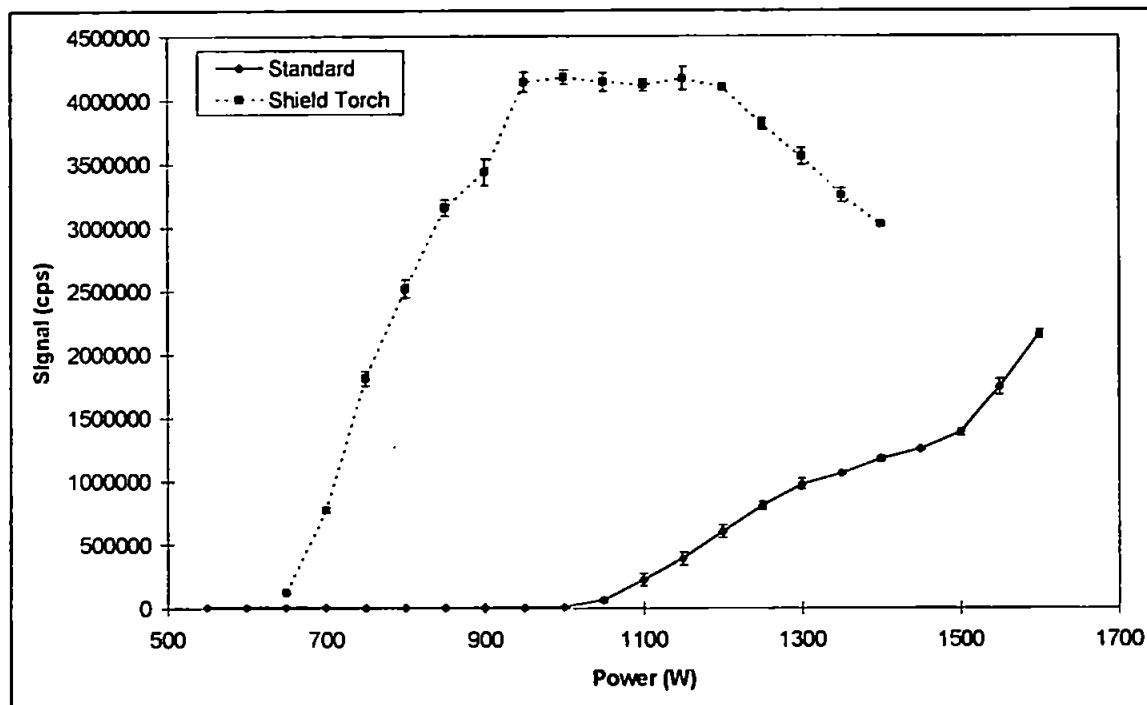


Figure 6.4: Effect of power on the signal for Al^+ . Errors = 3σ for $n = 3$.

The signal with the shield torch would be expected to be lower than with standard conditions, since the plasma would be cooler with the shield due to the removal of the capacitive coupling and secondary discharge within the plasma. Therefore, at the same operating power there would be less energy within the plasma to ionise metal analytes and so there would be less signal with the shield torch.

The difference in M^+ signal with the shield torch could possibly be explained due to the oxide forming potential of the metal analytes. La readily forms oxides, the promotion of which with the use of the shield torch, was shown in Section 5.3.3. Therefore, due to the high probability of oxide formation with the shield torch, the signal for La^+ would be expected to be small since any La present in the plasma would form

LaO⁺. In addition the reduced energy with the shield torch does not promote the dissociation of the oxide, due to the high dissociation energy of this species, resulting in large LaO⁺ signals. However, metals such as In, Al and Mn form oxides less readily than La, hence giving rise to higher M⁺ signals with the use of the shield torch.

Previous studies on the effect of power on metal analyte species include Li⁺^{134,136,138}, B⁺^{136,137}, Na⁺¹³⁷, Mg⁺^{134,136,137}, Al⁺^{134,137}, Ti⁺^{136,137}, V⁺¹³⁷, Cr⁺^{136,137}, Mn⁺^{137,150}, Fe⁺¹³⁷, Co⁺^{134,137-139,150}, Ni⁺^{136,137}, Cu⁺¹³⁷, Cd⁺¹³⁹, Rb⁺¹³⁷, Sc⁺²⁸¹, Ba⁺^{130,134,138,139,150,314}, Pb⁺^{136,137,139,150}, Ce⁺^{125,134,150,304}, Pd⁺¹³⁶, Pt⁺¹³⁶, Ga⁺¹³⁶, Ge⁺¹³⁶, As⁺¹³⁶, Zr⁺¹³⁶, Mo⁺^{136,150}, Hf⁺¹³⁶, W⁺¹³⁶, In⁺^{136,138}, Sn⁺¹³⁶, Sb⁺¹³⁶, Tl⁺¹³⁶, Bi⁺¹³⁶, Sr⁺¹⁵⁰, U⁺¹⁵⁰ La⁺¹⁴⁰, Be⁺¹³⁸ and Cs⁺¹²⁵. These have found that the signal for metal analytes, with standard conditions, increased as the power was increased, although one investigation¹²⁵ found that a maximum in signal was reached depending upon the mass of the analyte. These findings correspond to the results of this investigation, where with standard conditions the metal analyte signals increased as the power was increased.

Sakata *et al.*¹⁵² investigated the effect of power on Co⁺, with the use of a shield torch. They found that the signal for Co⁺ increased as the power was increased. This corresponds to the findings of this investigation, where the signals for the metal analytes increased as the power was increased.

6.3.3 Effect of Power on MO⁺ Signal

An example of the effect of power on metal oxide signals is shown in Figure 6.5 for LaO⁺. These results show that with standard conditions the signal for LaO⁺ increased as the power was increased. With the shield torch the signal for LaO⁺ increased as the power was increased. The signal for LaO⁺ with the shield torch was much greater than that with standard conditions, particularly at powers above 900 W. The signal for LaO⁺

would be expected to decrease with increasing power¹²⁵, due to more effective dissociation of the metal oxide with increasing power²⁹³.

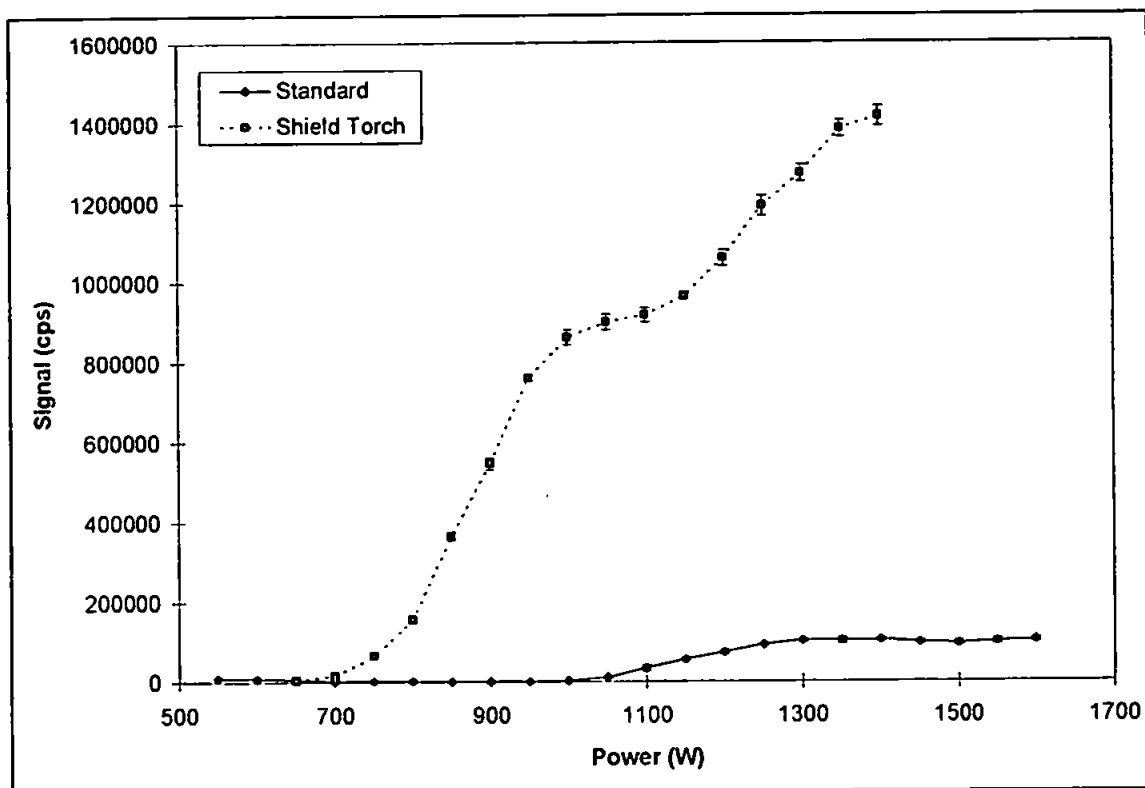


Figure 6.5: Effect of power on the signal for LaO^+ . Errors = 3σ for $n = 3$.

Metal oxide signals are more commonly expressed as a MO^+ / M^+ , and these MO^+ / M^+ ratios are shown in Figures 6.6 and 6.7 for standard conditions and with the shield torch respectively.

These results show that with standard conditions the MO^+ / M^+ ratio decreased, for all the species studied, despite the raw MO^+ signal increasing with increasing power. At low powers there was less energy within the plasma to dissociate the metal oxide while, at high powers there was more energy within the plasma and so the metal oxides were more effectively dissociated.

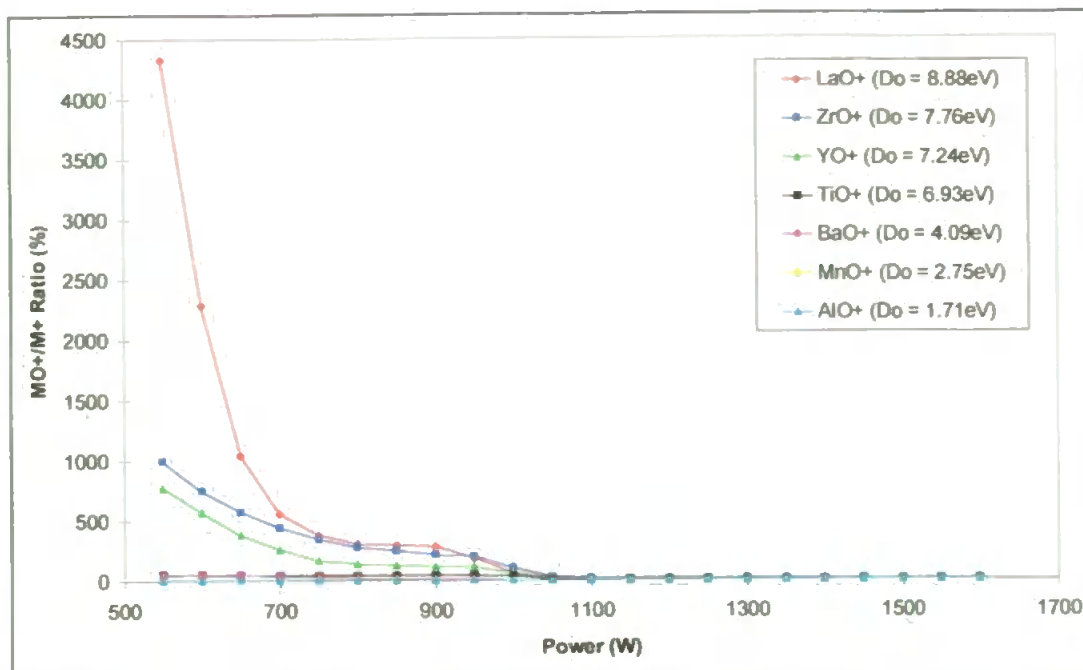


Figure 6.6: Comparison of the effect of power for the MO^+ / M^+ ratio with standard conditions. MO^+ and M^+ signals normalised to 100%. Molecular and atomic abundances are given in Table 6.1. D_0 values given are for MO^+ .

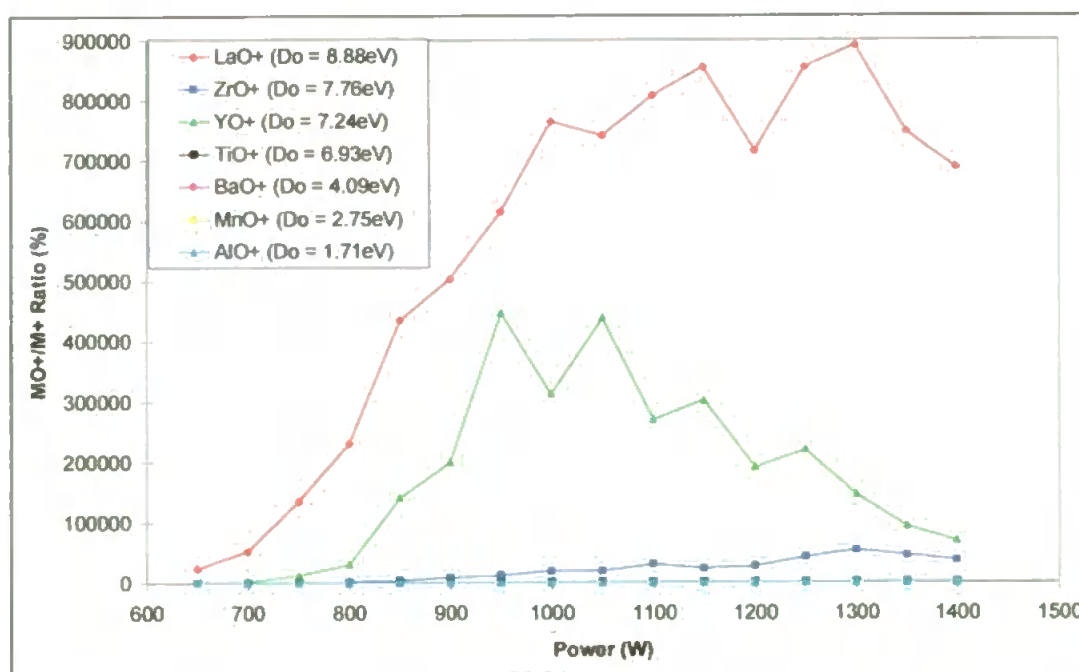


Figure 6.7: Comparison of the effect of power for the MO^+ / M^+ ratio with the shield torch. MO^+ and M^+ signals normalised to 100%. Molecular and atomic abundances are given in Table 6.1. D_0 values given are for MO^+ .

Comparisons of the MO^+ / M^+ ratios show that the MO^+ / M^+ ratio increased as the dissociation energy of the metal oxide increased. Species with a large dissociation energy require large amounts of energy to break the metal oxide bond, so were persistent in the plasma, and a large signal was therefore observed in relation to the metal signal, resulting in a large MO^+ / M^+ ratio. Conversely, species with low dissociation energies require little energy to break the metal oxide bond, were less persistent in the plasma, so relatively little signal was observed in relation to the metal signal, resulting in a small MO^+ / M^+ ratio. At low powers the MO^+ / M^+ ratios were extremely high, greater than 50 % for all species except Al and Mn, and several of these were much greater than 100 % (i.e. the oxide signal was greater than the metal signal). It was only at powers above 1200 W that the MO^+ / M^+ ratios dropped below 10 %, and even at the highest powers the MO^+ / M^+ ratio for La did not fall below 5 %.

With the shield torch the MO^+ / M^+ ratios were different to those exhibited with standard conditions, and did not exhibit the same trend as each other, as shown in Figure 6.7. These results show that, with the exception of Al and Mn, the MO^+ / M^+ ratios were much higher than those with standard conditions. The MO^+ / M^+ ratio for Al and Mn remained fairly constant with the increase of power, while the MO^+ / M^+ ratio for Ba decreased as the power was increased. For all other species the MO^+ / M^+ ratio increased as the power was increased, with Ti and Y reaching a maximum at about 1000 W and La and Zr reaching a maximum at a power of about 1300 W.

The shield torch greatly promoted the formation of the metal oxides, well beyond the level which would be expected, and this is particularly prominent at high powers. At high powers the MO^+ / M^+ ratios with standard conditions were negligible, due to increased dissociation of the metal oxide at these higher powers. With the shield torch the plasma is cooler than with standard conditions, and the metal oxides are not so

effectively dissociated at these lower temperatures, resulting in greater MO^+ / M^+ ratios, particularly at higher powers.

Previous studies on the effect of power on metal oxide species have been performed, using standard conditions, on CeO^+ ^{125,150}, BaO^+ ^{130,314}, TbO^+ ⁵⁸, GdO^+ ⁵⁸, ThO^+ ²⁹³, and LaO^+ ¹⁴⁰. In all cases it was found that the MO^+ / M^+ ratio decreased as the power was increased, as found during this investigation for standard conditions.

6.3.4 Effect of Power on ArX^+ Signal

An example of the effect of power on ArX^+ is shown in Figure 6.8 for ArO^+ . These results show that the signal for ArO^+ increased to a maximum at 650 W and then decreased as the power was increased up to 1100 W. Beyond 1100 W the signal rose until a power of 1250 W, after which the signal remained fairly constant.

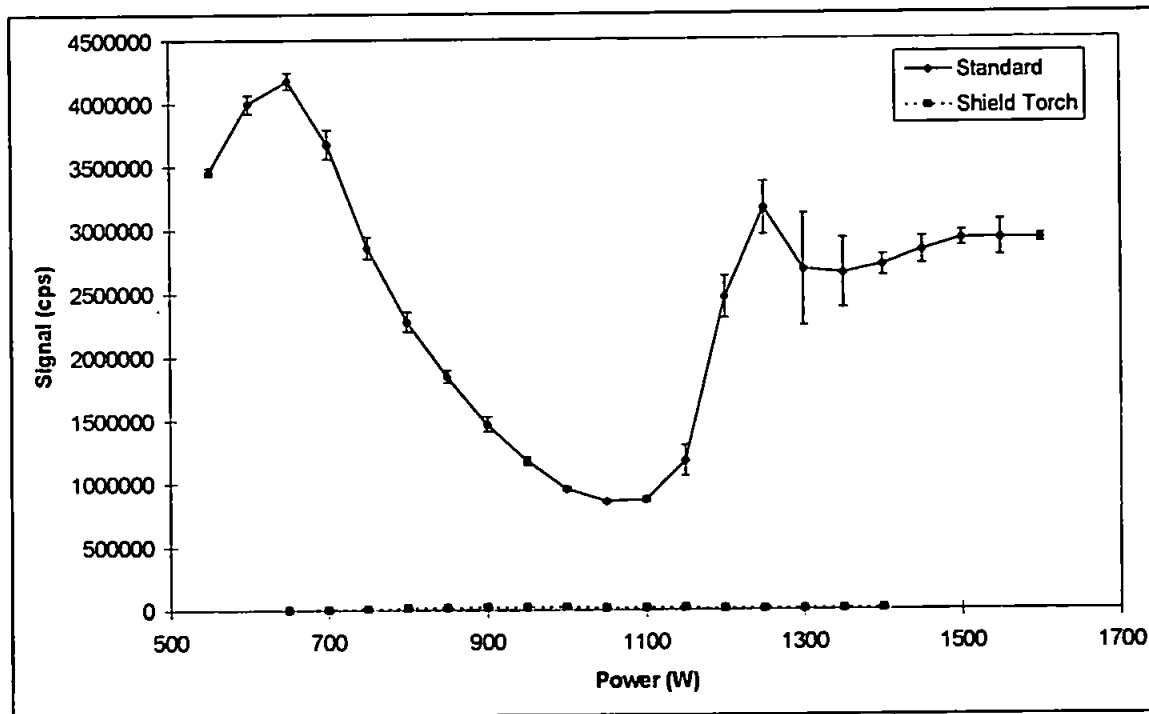


Figure 6.8: Effect of power on the signal for ArO^+ . Errors = 3σ for $n = 3$.

The signals for the argon polyatomic species would be expected to increase as the power was increased, as more energy is introduced into the plasma promoting the formation of argon polyatomic species. At powers above 1100 W the ArO^+ signals followed this expected trend, in that the signals increased as the power was increased. However, at powers below 1100 W the ArO^+ signal increased as the power was decreased below 1100 W. This can be explained by the formation of the secondary discharge, which is strongest at low powers¹⁴⁹. The secondary discharge, which promotes the formation of argon polyatomic species¹⁴², is correlated with the plasma potential, which has been found to be three times higher at 800 W than 1400 W³⁰². Therefore, this increase in plasma potential, and hence secondary discharge, at low powers would be expected to enhance the ArX^+ signals at low powers.

With the shield torch the signal for ArO^+ increased as the power was increased until 1000 W. Beyond 1000 W the signal decreased as the power was increased further, until a power of 1300 W, after which the signal began to increase again. The ArO^+ signal could initially increase as the power was increased, due to the increased ionisation of O precursors from the nebuliser gas, resulting in an increased signal¹³⁸. However, ArO^+ has very low dissociation energies (0.4 eV) compared to the ionisation potentials of its constituent species (14 eV), hence as the power was increased further the dissociation of ArO^+ would become the predominant effect. However, at powers above 1300 W the signals began to increase again with a further increase in power. Sakata *et al.*¹⁵² observed that even with the use of the shield torch the secondary discharge was present in the plasma at powers above 1200 W. Therefore, this increase in ArO^+ signal above 1300 W could be due to the secondary discharge reappearing in the plasma, which promotes the formation of ArX^+ species. The signal with the shield torch was negligible compared to that without the shield.

The effect of power, with standard conditions, on various ArX^+ species, as given in Table 6.1, is shown in Figure 6.9. These results show that the signals for ArH^+ , ArN^+ , and ArO^+ all showed a similar trend, although the effect was much more pronounced for ArO^+ , while the signals for Ar^+ , and Ar_2^+ exhibited a similar trend, with the signals increased as the power was increased. The signal for Ar^+ would be expected to be similar to those observed for metal analyte species because although the plasma is composed of argon, only about 0.1 % is ionised²⁵. In addition, argon is introduced into the plasma in the same way as analyte species in the form of the nebuliser gas. Therefore, as the power was increased the Ar would be more efficiently ionised, leading to an increase in Ar^+ signal.

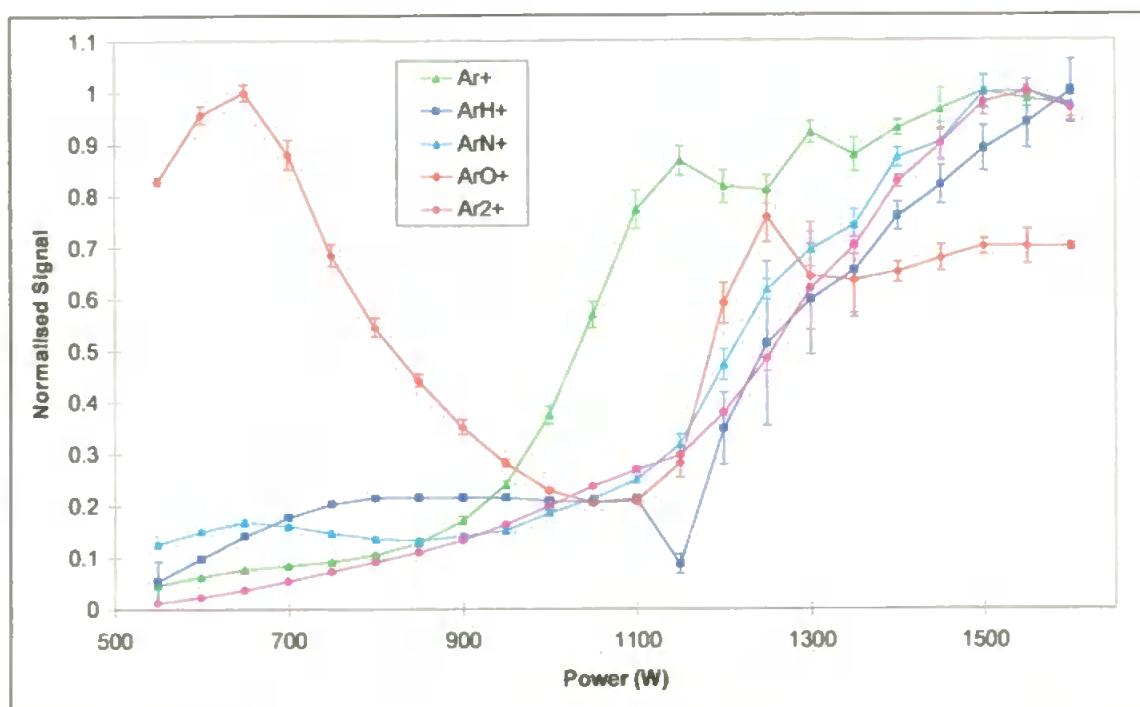


Figure 6.9: Comparison of the effect of power for the ArX^+ species with standard conditions. Signals normalised. Errors = 3σ for $n = 3$.

Ar_2^+ is thought to be formed in the plasma by collisional reactions, rather than by ionisation of the neutral species¹⁴², e.g.



As the population of Ar^+ increased at high powers the Ar_2^+ signal would be expected to increase as more collisional reactions with Ar occur within the plasma.

The effect of power, with the shield torch on various ArX^+ species is shown in Figure 6.10. The signals for ArH^+ , and ArN^+ exhibited a trend similar to that observed for ArO^+ . With the shield torch the signal for Ar^+ exhibited the same trend as that shown with standard conditions, in that the signal increased as the power was increased. Therefore, both with and without the shield torch Ar^+ exhibited the same trend as the metal analytes introduced into the plasma.

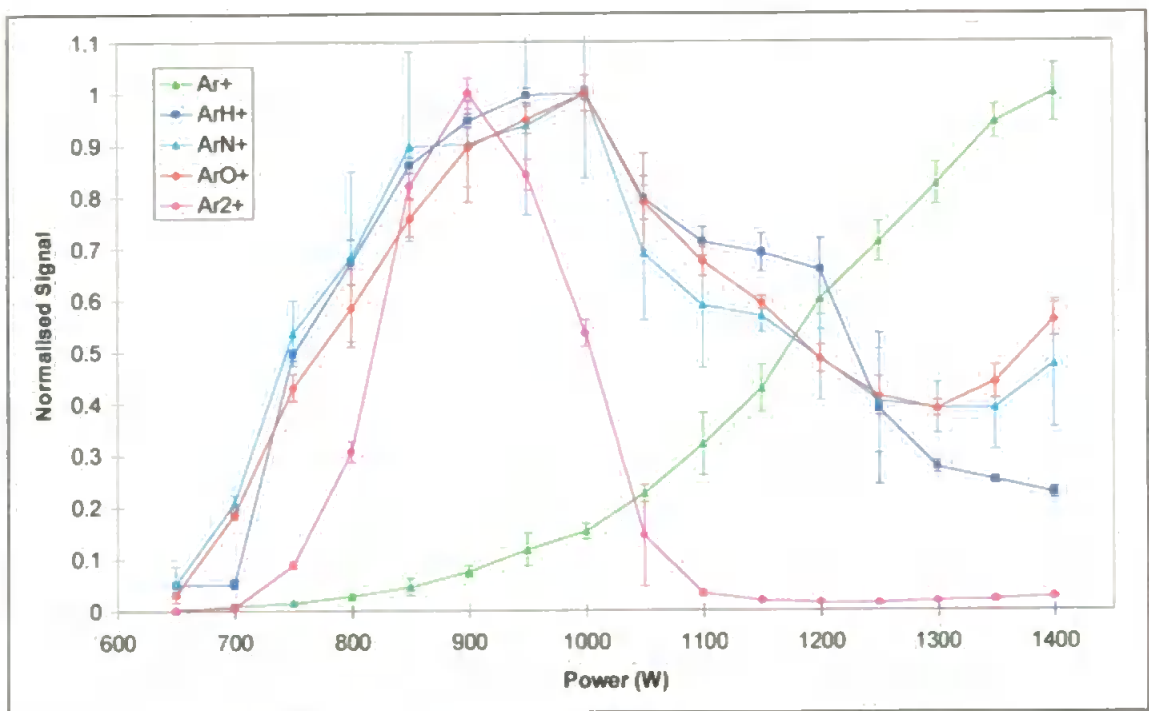


Figure 6.10: Comparison of the effect of power for the ArX^+ species with the shield torch. Signals normalised. Errors = 3σ for $n = 3$.

The signal for Ar_2^+ increased to a maximum at 900 W before decreasing as the power was increased further. If Ar_2^+ was formed according to Equation 6.1 the Ar_2^+ signal would be expected to increase as the power was increased, as more Ar was ionised. However, the dissociation energy of Ar_2^+ is very low (1.05 eV), and so as the power was increased further the dissociation of Ar_2^+ would rapidly become the predominant process occurring within the plasma, leading to a decrease in the Ar_2^+ signal.

Previous studies on the effect of power on ArX^+ have mainly investigated the effect of power with standard conditions. Gray and Williams¹³⁴ and Kawaguchi *et al.*¹⁴⁰ investigated the effect of power (1.1 - 1.5 kW) on Ar_2^+ and ArO^+ . They both found that the signal for Ar_2^+ increased as the power was increased. Gray and Williams¹³⁴ also found that the signal for ArO^+ increased as the power was increased. However, Kawaguchi *et al.*¹⁴⁰ found that the ArO^+ signal decreased as the power was increased, to a power of 1300 W and then increased slightly as the power was increased further. Evans and Ebdon¹³⁸ also investigated the effect of power (1.0 - 1.8 kW) on ArO^+ , ArN^+ , and Ar_2^+ . They found that the signals for ArO^+ and ArN^+ decreased as the power was increased, while the signal for Ar_2^+ varied little over the range studied. Therefore, none of the previous studies have investigated the effect of power below 1000 W. However, they found that the signals for all the ArX^+ species increased as the power was increased^{134,140}, as expected, and as seen in this study at powers above 1100 W.

Sakata *et al.*¹⁵² and Nonose *et al.*¹⁴² investigated the effect of power (0.7 - 1.4 kW) with the use of the shield torch on Ar^+ , Ar_2^+ , ArO^+ and ArH^+ . They found that the signals for Ar^+ ¹⁵², Ar_2^+ ¹⁵² and ArO^+ ^{142,152} increased as the power was increased, although the signals were negligible below 1.2 kW¹⁵². The signal for ArH^+ was much larger and exhibited a different trend to that shown by the other argon polyatomic species¹⁵². The signal for ArH^+ increased as the power was increased up to a power of 0.9 kW, after which it decreased as the power was increased further up to a power of 1.2

kW. Beyond 1.2 kW the signal began to increase again as the power was increased further. Therefore, although the results from this study differed from most of the previous studies, they did follow a similar trend to that seen by Sakata *et al.*¹⁵² for ArH^+ .

6.4 CONCLUSIONS

The operating power had a great effect on the signals for metal analytes and polyatomic ions. With standard conditions the metal analyte signals were negligible at powers below 1100 W, showing how important it is to operate at a high enough power to ionise the analytes of interest. However, at these higher powers polyatomic ion signals were also higher, although the MO^+ / M^+ ratios were lower at high powers.

The use of the shield torch effectively reduced the argon polyatomic ion species, particularly at high powers. The use of the shield torch also significantly enhanced the signal for certain metal analytes, at all powers. Therefore, the use of the shield torch at high powers significantly reduces the argon polyatomic species and also increases analyte sensitivity by at least double. However, the formation of metal oxides was greatly enhanced with the shield torch, particularly at high powers, and this is reflected in the low signals for the metal analytes, such as La, which readily form oxides.

Therefore, while the operation of the shield torch at high powers has significant potential for both increased analyte sensitivity and removal of interferences, the nature of the analyte being studied must be carefully considered, with oxide forming analytes causing a specific problem. Not only is the sensitivity of these species greatly reduced with the shield at high powers, but the formation of oxide species may cause interference problems on other analytes being studied.

CHAPTER 7

Effect of Solvent Loading on Polyatomic Ions and their Dissociation Temperatures

7 EFFECT OF SOLVENT LOADING ON POLYATOMIC IONS AND THEIR DISSOCIATION TEMPERATURES

7.1 INTRODUCTION

Samples are most commonly introduced into an ICP by aspiration of aqueous samples in the form of an aerosol, which is a mixture of gases, droplets, particles and solvent vapour, although gaseous sample introduction is also possible.

Water vapour introduced into the plasma region influences the coupling of the plasma with the RF field, which in turn affects the power absorbed by the plasma³⁰⁶. Water dissociation must also be taken into account as this process requires a large amount of energy²³², hence, this would lower the amount of energy available for analyte atomisation and ionisation³⁴⁵. In addition, the power required to desolvate aerosol droplets, atomise solvent molecules and then excite the solvent pyrolysis products is supplied at the expense of the power available to vaporise, atomise and excite the analyte³⁴⁵. Therefore, the solvent loading of the plasma may greatly affect the energy within the plasma available to ionise the analyte species. It has been proposed that the influence of variations in water aerosol loadings on plasma properties is substantially greater than that of water vapour³⁴⁶, because, for a certain water loading containing both liquid aerosol droplets and water vapour, energy is required to vaporise the liquid droplets before atomisation and ionisation of the resulting vapour can be achieved. This should result in a significant difference in the intensity of both analyte and interference signals for samples consisting of nebulised droplets and vapour, and vapour only, particularly at similar solvent loadings.

Many of the most serious polyatomic interferences in ICP - MS are caused by species which contain oxygen in combination with another element^{30,158-162}. The presence of water when aspirating aqueous samples is a major source of oxygen in the plasma, and hence also oxygen containing interferences. Therefore, the introduction of the sample as a vapour rather than as vapour / droplets should reduce the solvent loading, by removing the droplets, and so should also reduce the amount of oxygen containing interferences.

7.2 EXPERIMENTAL

Experiments were conducted using a PlasmaQuad 3 ICP - MS (VG Elemental, Ion Path, Road Three, Winsford, Cheshire, UK), as described in Section 2.1.2. Water vapour was introduced directly into the back of the ICP torch using the apparatus shown in Figure 7.1.

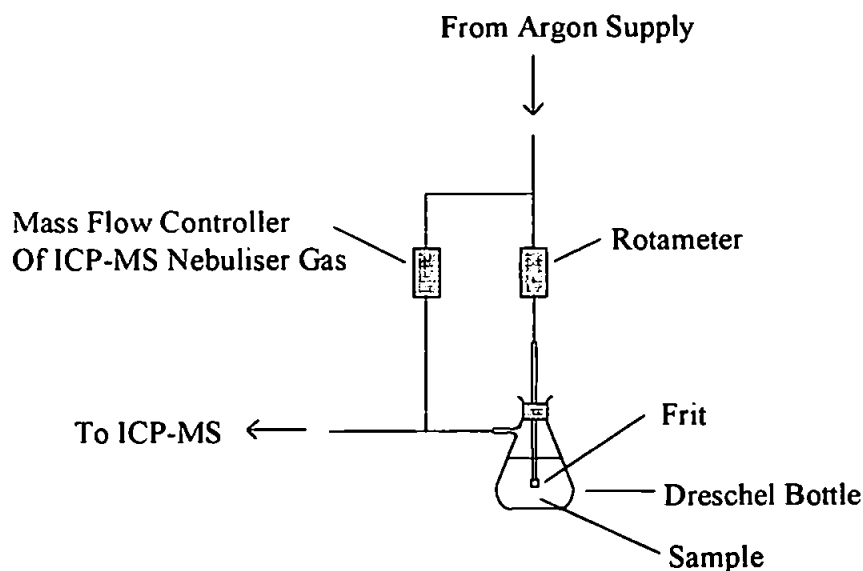


Figure 7.1: Schematic diagram of apparatus used for the introduction of water vapour via a temperature controlled Dreschel bottle.

Argon gas, in the range 0 to 0.9 l min⁻¹, was bubbled through a frit into a Dreschel bottle containing water in order to saturate the argon with water vapour. The amount of argon entering the bottle was controlled using a rotameter. The gas coming from the Dreschel bottle was made up with another supply of argon, controlled by a mass flow controller, in order to maintain a constant total flow rate of 0.9 l min⁻¹ entering the plasma. The water in the Dreschel bottle was kept at a constant temperature of 19 °C, using a water bath, in order to maintain a constant vapour pressure. Care was taken to ensure that this temperature was lower than room temperature in order to avoid condensation of the water in the gas lines. The amount of water vapour entering the plasma was altered by adjusting the gas flow through the Dreschel bottle, which had previously been calibrated. The detector was set up to monitor the ions shown in Table 7.1. A vial containing a small droplet of mercury and covered with six layers of Teflon tape was attached to the arm of the frit to facilitate tuning of the lenses on the signal for ¹⁹⁶Hg at an abundance of 0.14 %. Milli - Q deionised water was aspirated into the ICP - MS at a flow rate of 1.2 ml min⁻¹ using a peristaltic pump, to provide a reference solvent loading representing standard introduction with a nebuliser.

Table 7.1: Isotopes studied during the effect of solvent loading experiment

Species	Mass	Abundance	Species	Mass	Abundance
N ⁺	14	99.64	Ar ⁺	36	0.34
N ⁺	15	0.37	ArH ⁺	39	0.1*
O ⁺	16	99.76	ArN ⁺	54	99.2*
O ⁺	17	0.037	ArO ⁺	56	99.4*
N ₂ ⁺	28	99.28*	Ar ₂ ⁺	80	99.2*

* The abundances for the molecular species were calculated by combining the abundances of the two constituent elements.

7.3 RESULTS AND DISCUSSION

7.3.1 Effect of Solvent Loading on Dissociation Temperature

This method for calculating the dissociation temperature of the argon polyatomic ions has been described previously for Method E in Section 4.3.2.5.

The effect of solvent loading on the dissociation temperature of ArO^+ is shown in Figure 7.2.

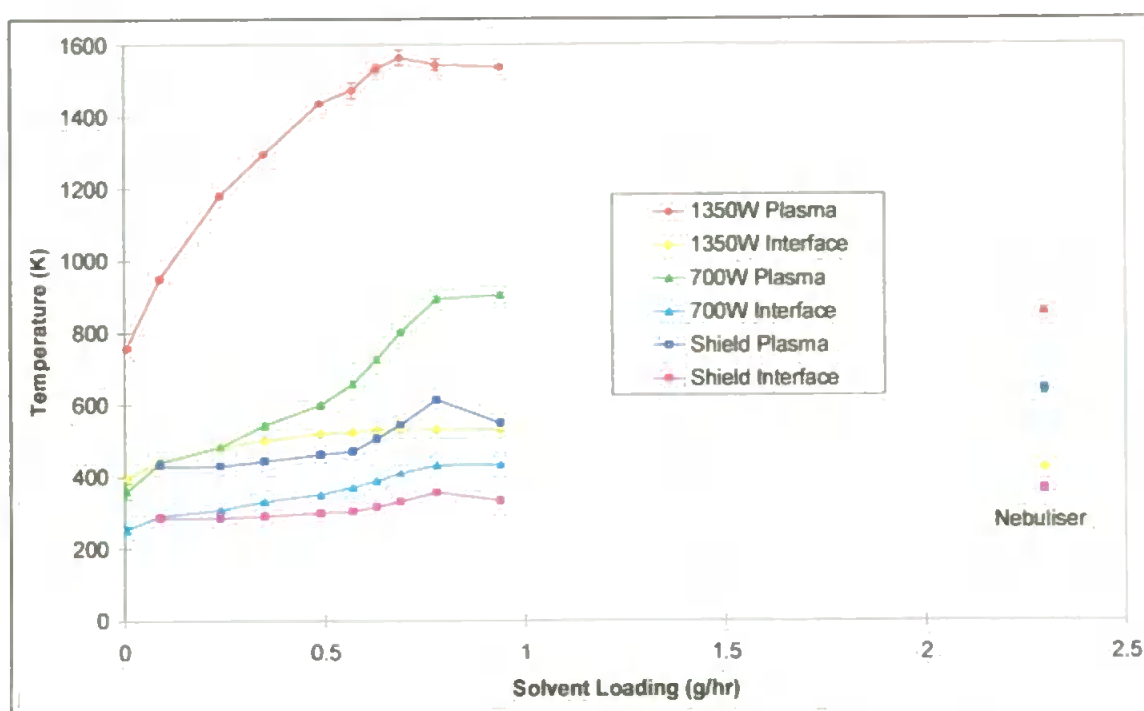


Figure 7.2: Effect of solvent loading for the ArO^+ temperature.

Errors = 3σ for $n = 3$.

These results show that at 1350 W the ArO^+ dissociation temperature in the plasma increased as the solvent vapour loading was increased, from 750 K at a solvent loading of 0.01 g / hr to 1550 K at a solvent loading of 0.94 g / hr. At 700 W the ArO^+ dissociation temperature in the plasma also increased as the solvent vapour loading was increased, from 350 K at a solvent loading of 0.01 g / hr to 900 K at a solvent loading of

0.94 g / hr. With the shield torch the ArO^+ dissociation temperature in the plasma also increased as the solvent vapour loading was increased, from 400 K at a solvent loading of 0.01 g / hr to 600 K at a solvent loading of 0.94 g / hr. For all three conditions used the temperature with the nebuliser was lower than that with the vapour.

As the solvent vapour loading was increased the amount of atomic hydrogen entering the plasma would be increased. The thermal conductivity of hydrogen is about ten times higher than that of argon³⁴⁷, and improves the heat transfer towards the central channel²³², and so an increase in temperature would be expected. With the nebuliser the solvent loading has increased, increasing the amount of atomic hydrogen entering the plasma, and so the temperature would be expected to be greater than that with the vapour. However, the temperature did not increase as the solvent loading was increased with the nebulised droplets. The nebulised droplets introduced into the plasma require a large amount of energy for vaporisation. This would reduce the energy within the plasma, even though the presence of atomic hydrogen improves the heat transfer, and so led to a reduction in the temperature calculated. Therefore, with the nebuliser, the temperature decreased due to the extra energy required to vaporise the droplets.

Previous studies investigating the effect of solvent loading on the temperature have been carried out by Alder *et al.*³³⁹, Tang and Trassy³⁴⁷, and Murillo and Mermet²³², who investigated the effect of desolvation on the temperature. It was found that the presence of water increased the temperature^{232,339,347} by 1000 K²³².

For the ArO^+ dissociation temperature, calculated using equilibrium conditions in the interface, the temperatures calculated were much lower than those calculated for the plasma, at all three operating conditions used, but followed the same trends as those shown by the temperatures calculated for equilibration in the plasma, (i.e. the temperatures increased as the solvent vapour loading was increased, with the temperature for the nebuliser being lower than for the vapour).

These temperatures calculated for both the plasma and interface were much lower than expected for the plasma. The temperature calculations are based on p - LTE conditions within the plasma, and therefore the low temperatures calculated using ArO^+ may indicate a deviation from LTE conditions. LTE conditions are not thought to exist in the interface region of the ICP - MS, suggesting that the ArO^+ species is formed in the interface rather than the plasma. The low temperatures calculated correspond to those thought to prevail in the interface ($< 3500 \text{ K}$)¹⁴², also suggesting formation in the interface rather than the plasma.

7.3.2 Effect of Solvent Loading on Polyatomic Ion Signals

The effect of solvent loading at 1350 W on the interference species studied, as given in Table 7.1, is shown in Figure 7.3. These results show that as the solvent vapour loading was increased the interference signals increased, reached a maximum at a solvent loading of 0.7 g / hr and then decreased as the solvent loading was increased further.

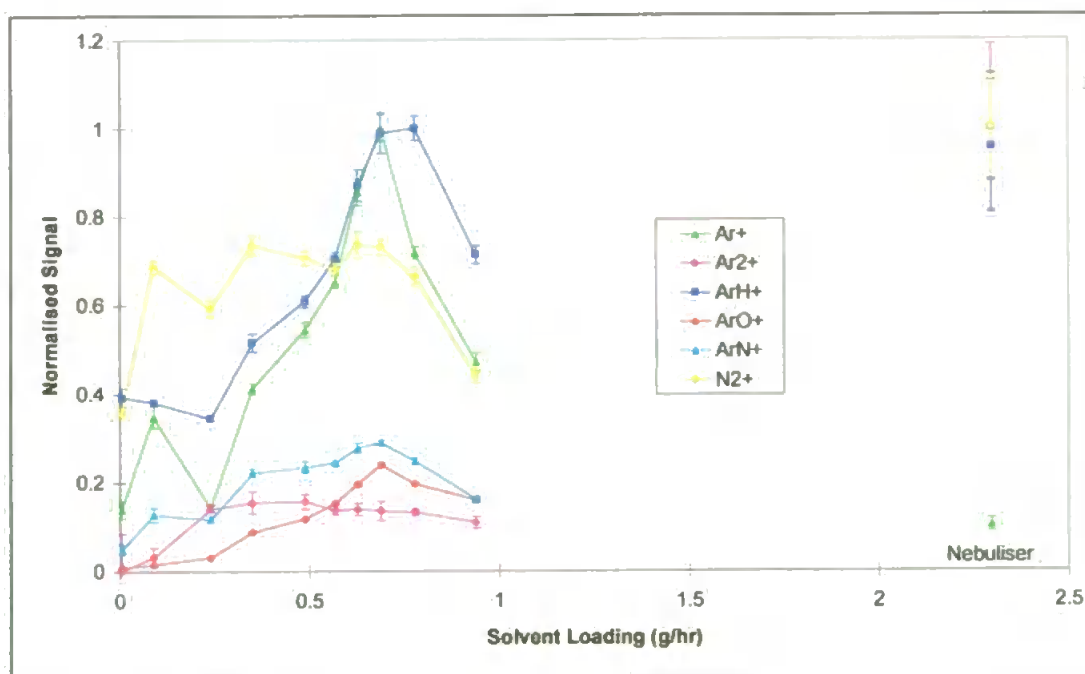


Figure 7.3: Effect of solvent loading for the ArX^+ species at 1350 W. Signals normalised. Errors = 3σ for $n = 3$.

With the increase in solvent vapour loading the signals would be expected to increase, due to the increase in analyte mass transport³⁴⁸. However, as the vapour loading was increased there would be more water vapour present in the plasma, which would require more energy for atomisation, leading to less energy available within the plasma for the ionisation of analyte species. This would lead to a decrease in signal at higher vapour loadings.

The signal for species such as ArO^+ , and ArH^+ would be expected to increase as the solvent vapour loading was increased due to an increase in the analyte mass transport³⁴⁸, which in this case is water. However, it was also found that the signals for species such as Ar^+ , and Ar_2^+ also increase as the solvent vapour loading was increased, even though they are not formed by any of the constituent species formed by the atomisation of water. Hutton and Eaton¹⁴⁸ also reported a strong dependence of the Ar_2^+ signal on the water loading. Therefore, the increased presence of water in the plasma not only acts to increase the species which are directly formed from its constituent species, but also it increases the signal of other species in the plasma.

The increase in solvent vapour loading introduces more atomic hydrogen into the plasma, improving the heat transfer toward the central channel and leading to an increase in temperature²³². This increase in thermal conductivity and temperature would explain the strong dependence of signals such as Ar_2^+ on the solvent loading, as more atomic argon would be ionised, resulting in greater amounts of Ar_2^+ being formed. As with the signals for ArO^+ , the signals would then begin to decrease as the solvent loading was increased further due to the increase in water vapour, which would require more energy to atomise.

With the nebuliser the signal for Ar^+ decreased compared to those for the vapour, but the signals for the other ArX^+ species increased compared to those with the vapour. These signals would be expected to increase due to the much greater volume of solvent

entering the plasma as nebulised droplets compared to the vapour. With the nebuliser the temperature was lower than for the vapour, and so the Ar^+ signal would be expected to be lower, due to a reduction in ionisation at the lower temperature with the nebuliser.

Previous studies investigating the effect of solvent loading have concentrated on the reduction of the solvent loading by desolvation techniques^{28,30,31,161,164,166}, such as membrane separators^{28,161,164} or cryogenic desolvation^{30,164}, or the reduction of the solvent loading by cooling the temperature of the spray chamber^{31,148,306}. Several studies have investigated the effect of aerosol water loading on the spectral characteristics observed in ICP - MS by incrementally adjusting the spray chamber temperature^{31,148,306}. These studies found that the ArO^+ and Ar_2^+ signals were dependent on the solvent loading¹⁴⁸, decreasing as the spray chamber temperature was reduced from 30 to 0 °C (decreasing solvent loading). These species have also been investigated using desolvation techniques^{28,30,31,161,164,166,347}, comparing signals with water present in the sample and when the water had been removed from the sample. These studies showed that the polyatomic ion interferences, such as ArO^+ , ClO^+ , ArCl^+ and ArOH^+ were reduced when the desolvation techniques were used^{30,161,166}.

Therefore, previous studies have found that interference ion signals decreased as the solvent loading of the plasma was reduced.

The effect of solvent loading at 700 W and with the shield torch on the interference species studied are shown in Figures 7.4 and 7.5 respectively.

These signals exhibited a similar trend to that observed at 1350 W, with the signals increasing as the solvent vapour loading was increased, reached a maximum and then decreased as the solvent vapour loading was increased further. At 700 W the signals with the nebuliser were greater than those for the vapour, except for Ar^+ , due to the greater volume of solvent entering the plasma.

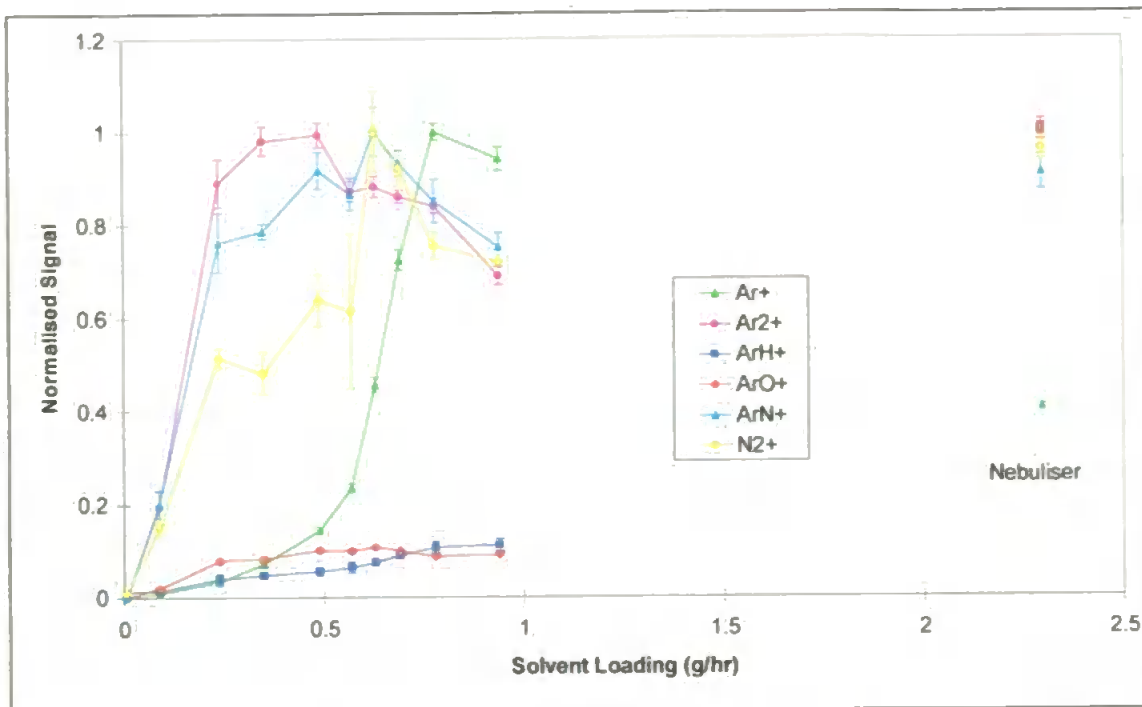


Figure 7.4: Effect of solvent loading for the ArX⁺ species at 700 W. Signals normalised. Errors = 3 σ for n = 3.

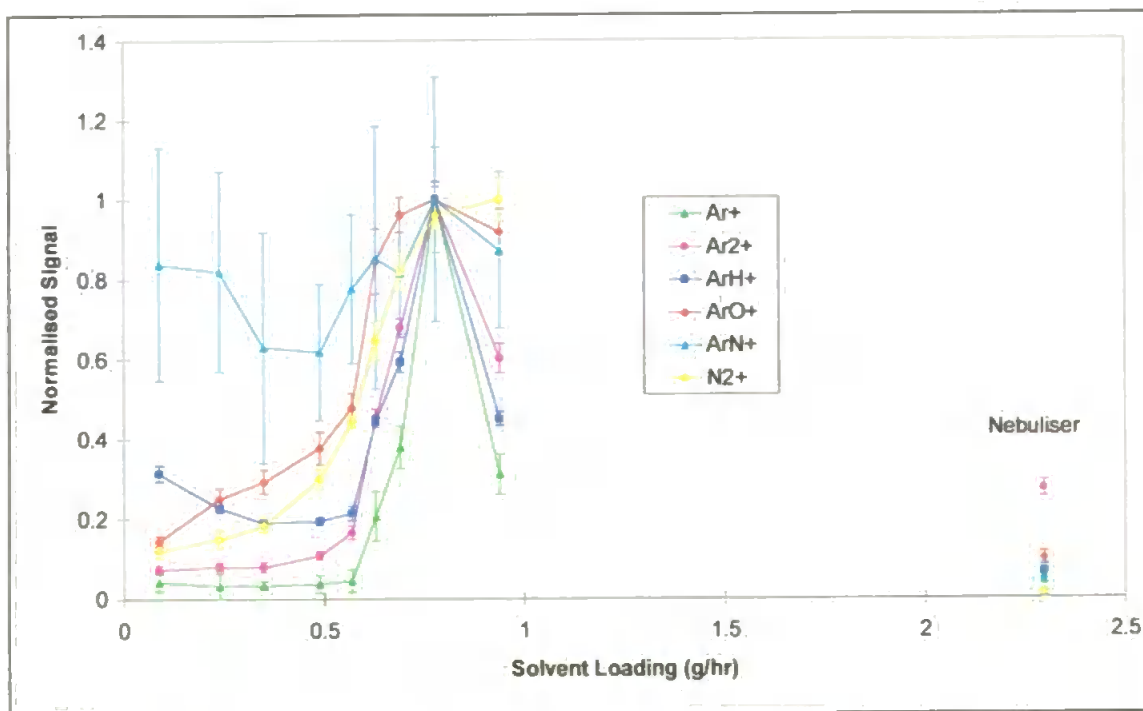


Figure 7.5: Effect of solvent loading for the ArX⁺ species with the shield torch. Signals normalised. Errors = 3 σ for n = 3.

With the shield torch the signals with the nebuliser were lower than those for the vapour. The temperature with the shield torch was lower than at 1350 W and 700 W and so, the large amount of energy required to vaporise the droplets would reduce the energy available for ionisation of the analytes, resulting in a decrease in signal with the nebuliser compared to the vapour.

The signals at 1350 W were greater than those at 700 W, with the signals using the shield torch being negligible compared with both these signals. This reflects the amount of energy within the plasma, at each of these conditions, available to vaporise the solvent and ionise analyte species.

7.4 CONCLUSIONS

The introduction of solvent in the form of nebulised droplets, compared with a vapour, affected both the raw ArX^+ signals and the temperature calculated from them. With the nebuliser the ArX^+ signals were greater than those for the vapour, due to the increased volume of solvent entering the plasma. The introduction of solvent as nebulised droplets reduced the temperature within the plasma, compared with that for the vapour, due to the increased energy required to vaporise the water droplets. This reduction in temperature would result in less energy available within the plasma to ionise analyte species, although this is not the case for the argon polyatomic species.

The introduction of solvent in the form of a vapour rather than as nebulised droplets reduced the interference signals and increased the temperature of the plasma, which would improve analyte signals. Therefore, if the nature of the sample allows, the introduction of the sample as a vapour would be beneficial, both due to the reduction in interferences and the enhancement of analyte signals.

CHAPTER 8

Determination Of The Site And Mechanisms Of Formation Of Polyatomic Ion Interferences

8 DETERMINATION OF THE SITE AND MECHANISMS OF FORMATION OF POLYATOMIC ION INTERFERENCES

8.1 INTRODUCTION

Since the development of ICP - MS, fundamental studies have been performed to elucidate ionisation and / or excitation mechanisms within the plasma^{284-286,288-290}. Analyte ions are not the only species formed within the ICP, with molecular interference ions such as oxides, hydroxides and background species due to plasma gases and / or solvent being formed. These species can cause a significant problem and much work has been carried out to reduce these interferences (as discussed in Section 1.2.2), however, the mechanisms and site of formation of these interfering species are not well understood. A clear interpretation of formation mechanisms and the site of formation of these interfering species would greatly enhance the understanding of these interferences and could lead to design modifications of the instrument, rather than relying on modification of the analytical method, to reduce them.

One complication in the determination of the formation of polyatomic ions in ICP - MS is related to the insertion of a sampling interface made of cooled metal between the ICP and the mass spectrometer, and the resulting reactions occurring in the interface region¹⁴². The secondary discharge occurring at the sampling region was thought to affect the formation of M^{2+} and MO^+ species^{130,143,150,151,250,349}, due to an increase in n_e at the surface of the sampling cone. However, this secondary discharge has been shown to result from a large RF voltage swing in the plasma to the grounded interface²⁵⁰, and that

reduction in this plasma potential greatly affected the formation of ArX^+ species but had little effect on M^{2+} and MO^+ formation²⁵⁰.

Therefore, comparison of the formation of polyatomic interferences and their relationship to physical properties of the plasma with a standard plasma and with a shield torch, which is known to affect the formation of polyatomic ions, may result in a better understanding of the formation mechanisms and sites of formation of these species.

8.2 EXPERIMENTAL

Experiments were conducted using a PlasmaQuad 3 (VG Elemental, Winsford, UK) using the experimental conditions described in Section 2.1.2.

Various solvents were introduced into the plasma at a flow rate of 1.2 ml min^{-1} using a peristaltic pump, including 2 % HNO_3 , 1 % methanol, 1 % HCl and 10 ng ml^{-1} MO solution. Various interferences were studied at the m/z shown in Tables 8.1 - 8.4.

Table 8.1: Isotopes studied during the introduction of 2 % HNO_3 for the site of formation experiment

Species	Mass	Abundance	Species	Mass	Abundance
N^+	14	99.64	O_2^+	32	99.52*
N^+	15	0.37	Ar^+	36	0.34
O^+	16	99.76	ArH^+	39	0.1*
O^+	17	0.037	ArN^+	54	99.2*
N_2^+	28	99.28*	ArO^+	56	99.4*
NO^+	30	99.40*	Ar_2^+	80	99.2*

* The abundances for the molecular species were calculated by combining the abundances of the two constituent elements.

Table 8.2: Isotopes studied during the introduction of 1 % HCl for the site of formation experiment

Species	Mass	Abundance	Species	Mass	Abundance
Cl ⁺	35	75.8	Cl ₂ ⁺	70	57.5*
Ar ⁺	36	0.02	ArCl ⁺	75	75.5*
ClO ⁺	51	75.6*			

Table 8.3: Isotopes studied during the introduction of 1 % MeOH for the site of formation experiment

Species	Mass	Abundance	Species	Mass	Abundance
C ⁺	12	98.9	Ar ⁺	36	0.02
C ₂ ⁺	24	97.8*	ArC ⁺	52	98.5*
CO ⁺	28	98.7*			

Table 8.4: Isotopes studied during the introduction of 10 ng ml⁻¹ MO Solution for the site of formation experiment

Species	Mass	Abundance	Species	Mass	Abundance
Al ⁺	27	100	YO ⁺	105	99.8*
AlO ⁺	43	99.8*	ZrO ⁺	106	51.3*
Ti ⁺	48	73.8	In ⁺	115	95.7
Mn ⁺	55	100	Ba ⁺	138	71.7
TiO ⁺	64	73.7*	La ⁺	139	99.9
MnO ⁺	71	99.8*	BaO ⁺	154	71.6*
Y ⁺	89	100	LaO ⁺	155	99.7*
Zr ⁺	90	51.4			

* The abundances for the molecular species were calculated by combining the abundances of the two constituent elements.

The experiment was carried out at 1350 W, 700 W and 700 W with a shield torch. With each solvent studied the lens settings and torchbox position were adjusted to give maximum signal for $^{115}\text{In}^+$ prior to each analysis.

8.3 RESULTS AND DISCUSSION

8.3.1 Temperature Determination

The methods for calculating the dissociation temperature of the metal oxide and argon polyatomic ions have been described previously for Methods A, B and E in Sections 4.3.2.1, 4.3.2.2 and 4.3.2.5, respectively. The determination of the temperature of molecular species XY^+ , i.e. CO^+ , required more complicated calculation since both the constituent species were being introduced into the plasma. Also, the dissociation mechanism is more complicated, since either species may form the positive ion, e.g.



Therefore, the temperature was calculated using both possible mechanisms. The concentration of the neutral species was calculated using Equation 8.3, using carbon in methanol as an example.

$$\text{density of C atoms} = \left(\frac{(\text{vapour loading} / 3600) \times \% \text{ in solution} \times N_0}{(\text{Molecular weight} \times \text{nebuliser gas flow})} \right) \times (T_{\text{bath}} / T_{\text{plasma}}) \quad (8.3)$$

This was then multiplied by the experimental O^+ / CO^+ ratio in order to obtain an experimental $K_d (CO^+)$ value, which could then be used to calculate the temperature using the method described previously. Alternatively, the density of O atoms was calculated using Equation 8.3, which was then multiplied by the experimental C^+ / CO^+ ratio in order to obtain an experimental $K_d (CO^+)$ value, which was then used to calculate the temperature.

The calculation of the temperatures for the species $ArCl^+$ and ClO^+ was not possible due to the lack of available data for these ions, nor was it possible to calculate the temperature for ArH^+ , due to the lack of data to calculate the partition function for H^+ .

Polyatomic ions are thought to be formed in the interface as well as in the plasma, and so the dissociation temperatures were calculated for equilibration in the interface as well as in the plasma.

The dissociation temperatures calculated using this method are given in Table 8.5. These results show that at 1350 W the dissociation temperatures calculated for the metal oxide ions ranged from 7350 - 9150 K, which correspond to the temperature thought to prevail in the plasma. The MO^+ dissociation temperatures calculated at 700 W were lower than those calculated for 1350 W, being in the range 5200 - 7900 K. This would be expected due to the reduced power being introduced to the plasma, which would result in lower plasma temperatures. The MO^+ dissociation temperatures calculated with the shield torch were lower than the temperatures calculated at both 1350 W and 700 W. With the shield torch, not only was less power introduced into the plasma, but the plasma potential was reduced, resulting in an even lower temperature.

Table 8.5: Dissociation temperatures calculated for the polyatomic ions (K)

Species	1350W		700W		Shield	
	Plasma	Interface	Plasma	Interface	Plasma	Interface
ArO ⁺ (O ⁺)	2245	584	828	415	2090	575
ArO ⁺ (Ar ⁺)	867	424	619	356	726	388
ArN ⁺ (N ⁺)	5222	2180	3148	1726	3810	1901
ArN ⁺ (Ar ⁺)	2544	1531	1500	1083	1076	835
N ₂ ⁺	4995	3890	3845	3157	2770	2395
ArC ⁺ (C ⁺)	2795	1067	1505	814	4170	1202
ArC ⁺ (Ar ⁺)	1325	759	1405	785	1625	846
C ₂ ⁺	4518	3174	4500	3165	3260	2500
CO ⁺ (O ⁺)	5423	4040	5020	3812	5121	3870
CO ⁺ (C ⁺)	3732	4803	5738	4277	5897	4364
Cl ₂ ⁺	4401	2831	3045	2205	3184	2276
MO ⁺	7368		5205		2752	
(Kubota)						
MO ⁺	9145		7897		4355	
(Longerich)						

Due to the nature of the MO⁺ dissociation temperature calculation it was not possible to calculate the temperature within the interface. However, the calculated MO⁺ dissociation temperatures show that they are probably formed in the plasma, with little indication of formation in the interface.

The dissociation temperatures calculated for argon polyatomic species, such as ArO⁺, were much lower than those calculated for the metal oxides, with temperatures below 2800 K, with the exception of ArN⁺. Argon polyatomic ions are thought to be

formed in the interface rather than the plasma¹⁴², and this may reflect the low temperature. The temperatures calculated for the interface were even lower than those calculated for the plasma, with temperatures in the range 400 - 2200 K. With a dissociation temperature of less than 3000 K calculated at 1350 W it would seem unlikely that the ArX^+ species were formed in the plasma, and this is reflected in the dissociation temperatures calculated for the interface, which were generally less than 1000 K. This suggests that while there may be some ArX^+ formed in the plasma, it is predominantly formed in the interface.

These temperatures calculated for both the plasma and interface were much lower than expected for the plasma. The temperature calculations are based on p - LTE conditions within the plasma, and therefore the low temperatures may indicate a deviation from LTE conditions. LTE conditions are not thought to exist in the interface region of the ICP - MS, suggesting that the ArX^+ species are formed in the interface rather than the plasma.

ArN^+ , however, exhibited a different trend to the other ArX^+ species, with a dissociation temperature of 5200 K at 1350 W. This temperature corresponds to temperatures thought to prevail in the plasma. However, the dissociation temperature calculated for the interface was 2200 K, which is much less than thought to exist in the plasma. Therefore, it is possible that ArN^+ is formed in the plasma, probably due to air entrainment, and also in the interface in the same way as the other ArX^+ species.

Other polyatomic species, such as N_2^+ , exhibit dissociation temperatures in the range 3700 - 5500 K at 1350 W. These temperatures correspond to the temperature thought to prevail in the plasma. The temperatures calculated for the interface are in the range 2800 - 4800 K, which still correspond to temperatures within the plasma rather than the interface. Therefore, this suggests than the other polyatomic species, such as

N_2^+ , are formed in the plasma rather than in the interface like the argon polyatomic species.

Polyatomic ions can be divided into two groups according to their formation mechanisms, with argon polyatomic ions probably forming in the interface, and metal oxides, and other species such as CO^+ and N_2^+ probably forming in the plasma.

Previous studies into the formation mechanisms and site of formation of polyatomic interferences are scarce. Nonose *et al.*¹⁴² theoretically calculated the monoxide to analyte (MO / M) ratio, assuming the dissociation equilibrium in the ICP. They proposed that the MO^+ due to analytes was derived from undissociated MO in the ICP because the theoretical MO / M ratios in the ICP agreed satisfactorily with the experimental MO^+ / M^+ ratios. Similar calculations with ArO^+ ¹⁴² showed little relationship between the signal behaviour of ArO^+ and its dissociation equilibrium in the ICP, suggesting that a collision - induced reaction of neutral argon and O^+ was a dominant process for the formation of ArO^+ ¹⁴². Becker *et al.*²⁹¹ investigated the formation of several metal argide molecular ions, and from the similar distribution of metal argide ions and metal ions they assumed that an association reaction was dominant for their formation.

Nonose *et al.*¹⁴² also carried out theoretical calculations to determine the site of formation of various polyatomic ion species. The signal behaviour of MO^+ species seemed to reflect the physical properties of the ICP rather than the interface, and was not influenced by the secondary discharge occurring at the tip of the sampling cone. Theoretical calculations were used to determine the equilibrium dissociation temperature for ArO^+ and ArH^+ ¹⁴². The theoretical ArH^+ / ArO^+ ratio which corresponded to the experimental ratio produced a temperature of 3500 K, suggesting that the dissociation equilibrium for ArX^+ species was reached in the interface region of the ICP.

Therefore, previous studies into the site and mechanisms of formation for polyatomic ions suggest that they can be divided into two groups. Metal oxide ions seem to be formed in the ICP by the ionisation of undissociated MO in the ICP. Argon polyatomic species, however, seem to be formed in the interface by collision - induced reactions of neutral Ar with X^+ .

8.4 CONCLUSIONS

Comparison of the dissociation temperatures calculated for different polyatomic molecular ions shows that there was a wide range of temperatures determined, depending on the molecular ion used for the calculation.

Dissociation temperatures calculated for metal oxide ions, at 1350 W were within the range expected for the plasma. It was not possible to calculate the MO^+ dissociation temperature in the interface, but there was little to suggest that metal oxide ions are formed in the interface. Therefore, the dissociation temperatures calculated for the metal oxide ions indicate that they are formed in the plasma.

Dissociation temperatures calculated for argon polyatomic species were much lower than both those calculated for the metal oxides and those expected in the plasma, with the temperatures calculated for the interface even lower than those calculated for the plasma. This suggests that the argon polyatomic ions are not present in the plasma, but formed within the interface. These low temperatures calculated for the ArX^+ ions, both in the plasma and the interface, suggest a deviation from LTE conditions, further indicating formation in the interface, where LTE conditions are thought not to prevail.

The exception to this was ArN^+ , for which the dissociation temperature at 1350 W suggests formation in the plasma. A likely source of ArN^+ is air entrainment, which would result in the formation of ArN^+ in the plasma. However, the ArN^+ dissociation

temperature calculated for the interface was much lower than both that calculated for the plasma and that expected within the plasma, suggesting that ArN^+ was formed in the interface in a similar method to the other ArX^+ ions. Therefore, the dissociation temperatures for ArN^+ suggest that it is formed both in the plasma and the interface.

Dissociation temperatures calculated for other polyatomic ion species, such as N_2^+ , C_2^+ , and CO^+ , for both the plasma and interface, were within the range expected for the plasma, indicating that they were formed in the plasma.

The dissociation temperature calculated for the polyatomic ion interferences suggest that they can be divided into two groups, depending on their site of formation, with ArX^+ species formed in the interface, and metal oxides and other molecular ions formed in the plasma.

The differing sites of formation for the different types of molecular ions suggests that these species are also formed by different mechanisms. The preliminary optical studies in Chapter 3 showed that the neutral metal oxide signal increased as the MO^+ signal decreased, suggesting that the MO^+ ion was reduced to neutral metal oxide. This suggests that the metal oxide ions are most probably formed from undissociated neutral metal oxide in the plasma. However, while the dissociation temperatures provide an indication to the site of formation, further information is necessary in order to determine possible formation mechanisms.

The determination of the dissociation temperature can provide a useful indication of the site of formation of the molecular ion. This method can be used to determine the site of formation of any molecular ion species, providing the necessary fundamental data is available for that species. Therefore, this method provides a simple, non - invasive technique for determining the site of formation of any potential interference molecular ion.

CHAPTER 9

Conclusions and Future Work

9 CONCLUSIONS AND FUTURE WORK

9.1 CONCLUSIONS

- 1) The temperature method used and the species used to determine the temperature have a considerable effect on the calculated temperature value. Many of the previous mass spectrometric temperature determinations have erroneously used data for the neutral metal oxide species, rather than the data for the metal oxide ions. Some authors have highlighted this problem but then still use the data for the neutral metal oxides, resulting in some cases in extremely high calculated temperatures. Therefore, it is of utmost importance to use the correct spectroscopic and thermochemical data in order to obtain correct temperature values. However, extreme care must be taken when choosing the metal oxide species to study, as the fundamental data is very patchy and difficult to obtain, and the data for many metal oxide ions is not available. Similarly, the fundamental data is not available for all argon polyatomic ions.

- 2) The operating conditions used have a large influence on both analyte and interference signals, highlighting the importance of careful optimisation of the operating parameters for successful use of the ICP - MS. Careful optimisation of the operating conditions can reduce the metal oxide interferences to below 5 %, although interferences such as argon polyatomic ions exhibit similar trends to the metal analytes with differing operating conditions. Therefore, operating conditions which successfully reduce argon polyatomic ions often also reduced analyte signals, and so other methods, such as desolvation of the sample or the use of a shield torch, must be utilised to reduce such interferences.

3) The temperature of the plasma with the shield torch was generally lower than the temperature at 1350 W. This difference in temperature could explain the difference in the trends of the raw signals observed at 1350 W and with the shield torch. However, the temperature at 700 W was also lower than the temperature at 1350 W. In general the raw signals at 700 W exhibited similar trends to those observed at 1350 W, although displaced slightly due to the increased residence time required for efficient ionisation / dissociation to occur at the lower power. Therefore, if the difference in raw signal behaviour with the shield torch compared to 1350 W was due to the decreased temperature with the shield torch, the raw signals with the shield torch would be expected to exhibit similar trends to those at 1350 W. However, while the raw signals at 700 W exhibited similar trends to those at 1350 W, the signals with the shield torch exhibited trends different to both those at 1350 W and 700 W. Therefore, the difference in raw signals with the shield torch can not be explained by the reduction in temperature compared to that at 1350 W.

4) The presence of the secondary discharge had a significant effect on the raw signals observed. In general, the signals at 1350 W and 700 W exhibited similar trends, although they were sometimes different to those expected, due to the influence of the secondary discharge. At both 1350 W and 700 W a prominent secondary discharge was observed at the tip of the sampler cone, although at standard operating conditions it was obscured by the light emitted from the plasma. The secondary discharge promotes both the formation of ArX^+ species and the dissociation of metal oxides, and this was reflected in the raw signals observed. At both 1350 W and 700 W the signals for the ArX^+ species were large, due to the large secondary discharge present, while negligible ArX^+ signals were observed with the shield torch, where the secondary discharge was removed. Conversely, the metal oxide signals were larger

with the shield torch than at 1350 W and 700 W, due to the removal of the secondary discharge which promotes metal oxide dissociation.

The presence of the secondary discharge also affected the behaviour of the raw signals at 1350 W and 700 W, and this was most pronounced for the effect of sampling depth, where the secondary discharge became more intense at larger sampling depths. At these sampling depths the tip of the sampler cone was not obscured by the plasma, and the secondary discharge was clearly visible. At large sampling depths the signals for the ArX^+ species increased, due to the more intense secondary discharge at these sampling depths, which promoted the formation of these species. However, with the shield torch, where the secondary discharge had been removed, there was no increase in ArX^+ signal at these large sampling depths. Therefore, the presence of the secondary discharge greatly affected the raw signals observed, although it did not have a significant influence on the temperature of the plasma.

- 5) The use of the shield torch at low powers greatly reduced the signals for the ArX^+ species, but the metal analyte signals were also reduced. The use of the shield torch at high powers, however, maintained the low ArX^+ signals but enhanced the metal analyte signals, in most cases to higher levels than with standard conditions. The signals for the metal oxides with the shield torch at high powers, however, were greatly enhanced, to levels much greater than expected. The use of the shield torch at high powers could potentially be a very useful analytical tool for increasing analyte signals, while reducing argon polyatomic ions. However, this method would not be suitable for the analysis of refractory metals or for species which suffer from metal oxide interferences.

- 6) The determination of the dissociation temperature can provide a useful indication of the site of formation of the molecular ion, indicating whether they are formed in the plasma or the interface region of the ICP - MS. This method can be used to determine the site of formation of any molecular ion species, providing the necessary fundamental data is available for that species. Therefore, this method provides a simple, non - invasive technique for determining the site of formation of any potential interference molecular ion.

After considering these conclusions, the following areas for future work can be identified.

9.2 SUGGESTIONS FOR FUTURE WORK

- 1) The determination of the dissociation temperatures provided an indication of the site of formation of the polyatomic interferences, or at least an indication of the predominant site of equilibrium, providing that thermal equilibrium prevailed. However, the behaviour of species such as ArX^+ suggested that they behaved in a non - equilibrium manner, so were less useful to predict plasma temperature.

The use of a fibre optic to determine an optical temperature, such as the excitation temperature of argon, would provide a non - invasive method for determining the temperature of the plasma. The use of the fibre optic for optical temperature measurements would also allow for the determination of the temperature in the interface, using the modified interface described in Chapter 3. This would allow a direct comparison between the temperature of the plasma and interface, which is not possible with mass spectrometric temperature determinations. Methods such as laser induced fluorescence could provide a better way of determining the temperature.

2) The difference in signal behaviour observed with the shield torch compared with 1350 W, cannot be explained by the difference in temperature between the two different operating conditions. The use of the shield torch removes the secondary discharge at the tip of the sampler cone, and so the use of the shield torch may have a greater influence on the electron number density rather than the temperature of the plasma. The fibre optic arrangement used for the optical measurement of the plasma could also be used to determine the electron number density of the plasma. Argon polyatomic species are thought to be formed in the interface region of the ICP, due to the secondary discharge, and the fibre optic system could also be used to determine the electron number density in the interface. This would allow a direct comparison between the electron number density of the plasma and interface, which could explain the formation of argon polyatomic species in the interface.

3) The use of the shield torch at high powers was shown in Chapter 6 to enhance metal analyte signals, while maintaining low argon polyatomic signals, providing a potentially useful analytical tool. The shield torch operated at low powers is not capable of ionising analytes with high ionisation potentials due to inefficient ionisation at these low powers. However, the shield torch operated at higher powers may have sufficient energy to effectively ionise these species, while still successfully reducing the argon polyatomic interference. Therefore, the use of the shield torch at high powers could possibly be used to analyse species such as As and Se, which suffer from argon polyatomic interferences, but cannot be analysed with the conventional low power shield torch system due to their high ionisation potentials. Further work would also be required on the shield torch system at high powers to reduce the metal oxide signals, which were greatly enhanced using these conditions.

References

REFERENCES

- 1) Sheppard, B. S., and Caruso, J. A., *J. Anal. At. Spectrom.*, 1994, **9**, 145.
- 2) Gray, A. L., *J. Anal. At. Spectrom.*, 1986, **1**, 403.
- 3) Jarvis, K. E., Gray, A. L., and Houk, R. S., *Handbook Of Inductively Coupled Plasma Mass Spectrometry*, Blackie, Glasgow, 1992, p1.
- 4) Reed, T. B., *J. Appl. Phys.*, 1961, **32**, 821.
- 5) Reed, T. B., *J. Appl. Phys.*, 1961, **32**, 2534.
- 6) Reed, T. B., *Int. Sci. Tech.*, 1962, **6**, 42.
- 7) Greenfield, S., Jones, I. L., and Berry, C. T., *Analyst*, 1964, **89**, 713.
- 8) Wendt, R. H., and Fassel, V. A., *Anal. Chem.* 1965, **37**, 920.
- 9) Gray, A. L., *Proc. Soc. Anal. Chem.*, 1974, **11**, 182.
- 10) Gray, A. L., *Analyst*, 1975, **100**, 289.
- 11) Gray, A. L., *Spectrochim. Acta*, 1985, **40B**, 1525.
- 12) Houk, R. S., Fassel, V. A., Flesch, G. D., Svec, H. J., Gray, A. L., and Taylor, C. E., *Anal. Chem.*, 1980, **52**, 2283.
- 13) Douglas, D. J., and French, J. B., *Anal. Chem.*, 1981, **53**, 37.
- 14) Douglas, D. J., Quan, E. S. K., and Smith, R. G., *Spectrochim. Acta*, 1983, **38B**, 39.
- 15) Gray, A. L., and Date, A. R., *Analyst*, 1983, **108**, 1033.
- 16) Date, A. R., and Gray, A. L., *Spectrochim. Acta*, 1983, **38B**, 29.
- 17) Date, A. R., and Gray, A. L., *Analyst*, 1983, **108**, 159.
- 18) Douglas, D. J., *J. Can. Res.*, 1983, **16**, 55.
- 19) Instrument Literature, PQ Excell, TJA Solutions, Winsford, Cheshire, UK, 2000.
- 20) Denoyer, E. R., Tanner, S. D., and Vollkopf, U., *Spectroscopy*, 1999, **14**, 43.

- 21)Jarvis, K. E., Gray, A. L., and Houk, R. S., Handbook Of Inductively Coupled Plasma Mass Spectrometry, Blackie, Glasgow, 1992, p10.
- 22)Thompson, M., and Walsh, J. N., Handbook Of Inductively Coupled Plasma Spectrometry, Blackie, Glasgow, 1989, p239.
- 23)Gray, A. L., in "Inorganic Mass Spectrometry", Adams, F., Gybels, R., and van Grieken, R., (eds), Wiley, New York, 1988, p258.
- 24)Willard, H. H., Merritt, L. L., Dean, J. A., and Settle, F. A., Instrumental Methods Of Analysis, Wadsworth, Belmont, 1988, p267.
- 25)Jarvis, K. E., Gray, A. L., and Houk, R. S., Handbook Of Inductively Coupled Plasma Mass Spectrometry, Blackie, Glasgow, 1992, p16.
- 26)Sharp, B., L., *J. Anal. At. Spectrom.*, 1988, **3**, 613.
- 27)Wang, S. R., and Jiang, S. J., *J. Chinese Chem. Soc.*, 1991, **38**, 327.
- 28)Montaser, A., Tan, H., Ishii, I., Nam, S. H., and Cai, M., *Anal. Chem.*, 1991, **63**, 2660.
- 29)Brenner, I. B., Zander, A., Plantz, M., and Zhu, J., *J. Anal. At. Spectrom.*, 1997, **12**, 273.
- 30)Alves, L. C., Wiederin, D. R., and Houk, R. S., *Anal. Chem.*, 1992, **64**, 1164.
- 31)Vanhoe, H., Moens, L., and Dams, R. J., *J. Anal. At. Spectrom.*, 1994, **9**, 815.
- 32)Vanhoe, H., Saverwijn, S., Parent, M., Moens, L., and Dams, R. J., *J. Anal. At. Spectrom.*, 1995, **10**, 575.
- 33)Shum, S. C. K., and Houk, R. S., *Anal. Chem.*, 1993, **65**, 2972.
- 34)Shum, S. C. K., Neddersen, R., and Houk, R. S., *Analyst*, 1992, **117**, 577.
- 35)Crain, J. S., and Kiely, J. T., *J. Anal. At. Spectrom.*, 1996, **11**, 525.
- 36)Vela, N. P., Olson, L. K., and Caruso, J. A., *Anal. Chem.*, 1993, **65**, 585A.
- 37)Hill, S. J., Bloxham, M. J., and Worsfold, P. J., *J. Anal. At. Spectrom.*, 1993, **8**, 499.
- 38)Vela, N. P., and Caruso, J. A., *J. Anal. At. Spectrom.*, 1993, **8**, 787.

- 39)Lobinski, R., Rodriguez Pereiro, I., Chassaingne, H., Wasik, A., and Szpunar, J., *Anal. At. Spectrom.*, 1998, **13**, 859.
- 40)McLaren, J. W., Siu, K. W. M., Lam, J. W., Willie, S. N., Maxwell, P. S., Palepu, A., Koether, M., and Berman, S. S., *Fresenius J. Anal. Chem.*, 1990, **337**, 721.
- 41)Feldman, J., *Anal. Comm.*, 1996, **33**, 11.
- 42)Heumann, K. G., Rottmann, L., and Vogl, J., *J. Anal. At. Spectrom.*, 1994, **9**, 1351.
- 43)Van Loon, J. C., Alcock, L. R., Pinchin, W. H., and French, J. B., *Spectroscopy Letters*, 1986, **19**, 1125.
- 44)Burguera, J. L., and Burguera, M., *J. Anal. At. Spectrom.*, 1997, **12**, 643.
- 45)Ebdon, L., Fisher, A. S., Worsfold, P. J., Crews, H., and Baxter, M., *J. Anal. At. Spectrom.*, 1993, **8**, 691.
- 46)Fairman, B., Sanz-Medel, A., and Jones, P., *J. Anal. At. Spectrom.*, 1995, **10**, 281.
- 47)Richner, P., *J. Anal. At. Spectrom.*, 1993, **8**, 927.
- 48)Viczian, M., Lasztity, A., Wang, X., and Barnes, R. M., *J. Anal. At. Spectrom.*, 1990, **5**, 125.
- 49)Vickers, G. H., Ross, B. S., and Hieftje, G. M., *Appl. Spectrosc.*, 1989, **43**, 1330.
- 50)Tomlinson, M. J., Liu, L., and Caruso, J. A., *Analyst*, 1995, **120**, 583.
- 51)Shen, W. L., Vela, N. P., and Sheppard, B. S., *Anal. Chem.*, 1991, **63**, 1491.
- 52)Tangen, A., Trones, R., Greibrokk, T., and Lund, W., *J. Anal. At. Spectrom.*, 1997, **12**, 667.
- 53)Howard, A. G., *J. Anal. At. Spectrom.*, 1997, **12**, 267.
- 54)Karanassios, V., and Horlick, G., *Spectrochim. Acta*, 1989, **44B**, 1301.
- 55)Hughes, D. M., Chakrabarti, C. L., Goltz, D. M., Gregoire, D. C., Sturgeon, R. E., and Byrne, J. P., *Spectrochim. Acta*, 1995, **50B**, 425.
- 56)Shibata, N., Fudagawa, N., and Kubota, M., *Spectrochim. Acta*, 1992, **47B**, 505.

- 57) Marshall, J., and Franks, J., *Atomic Spectroscopy*, 1990, **11**, 177.
- 58) Shibata, N., Fudagawa, N., and Kubota, M., *Spectrochim. Acta*, 1993, **48B**, 1127.
- 59) Ediger, R. D., and Beres, S. A., *Spectrochim. Acta*, 1992, **47B**, 907.
- 60) Gregoire, D. C., and Sturgeon, R. E., *Spectrochim. Acta*, 1993, **48B**, 1347.
- 61) Hall, G. E. M., Pelchat, J. C., Boomer, D. W., and Powell, M., *J. Anal. At. Spectrom.*, 1988, **3**, 791.
- 62) Omenetto, N., *J. Anal. At. Spectrom.*, 1998, **13**, 385.
- 63) Shuttleworth, S., and Kremser, D. T., *J. Anal. At. Spectrom.*, 1998, **13**, 697.
- 64) Longerich, H. P., Jackson, S. E., and Gunther, D., *J. Anal. At. Spectrom.*, 1996, **11**, 899.
- 65) Ebdon, L., Foulkes, M., and Sutton, K., *J. Anal. At. Spectrom.*, 1997, **12**, 213.
- 66) Fonseca, R. W., and Miller - Ihli, N. J., *Appl. Spectrosc.*, 1995, **49**, 1403.
- 67) Gregoire, D. C., Miller - Ihli, N. J., and Sturgeon, R. E., *Anal. At. Spectrom.*, 1994, **9**, 605.
- 68) Jarvis, K. E., Gray, A. L., and Houk, R. S., *Handbook Of Inductively Coupled Plasma Mass Spectrometry*, Blackie, Glasgow, 1992, p14.
- 69) Olesik, J. W., *Appl. Spectrosc.*, 1997, **51**, 158A.
- 70) Instrument Literature "AAS, FAAS, ICP or ICP-MS? Which technique should I use?", TJA Solutions, Winsford, Cheshire, UK, 2000.
- 71) Goenaga Infante, H., Fernandez Sanchez, M. L., and Sanz Medel, A., *J. Anal. At. Spectrom.*, 1998, **13**, 899.
- 72) De Boer, J. L. M., De Joode, P., and Ritsema, R., *J. Anal. At. Spectrom.*, 1998, **13**, 971.
- 73) Sariego Muniz, C., Marchante Gayon, J. M., Garcia Alonso, J. I., and Sanz Medel, A., *J. Anal. At. Spectrom.*, 1998, **13**, 283.

- 74)Caddia, M., and Iversen, B. S., *J. Anal. At. Spectrom.*, 1998, **13**, 309.
- 75)Latkoczy, C., Prohaska, T., Stingeder, G., and Teschler-Nicola, M., *J. Anal. At. Spectrom.*, 1998, **13**, 561.
- 76)Moreton, J. A., and Delves, H. T., *J. Anal. At. Spectrom.*, 1998, **13**, 659.
- 77)Krachler, M., Alimonti, A., Petrucci, F., Forastiere, F., and Caroli, S., *J. Anal. At. Spectrom.*, 1998, **13**, 701.
- 78)Townsend, A. T., Miller, K. A., McLean, S., and Aldous, S., *J. Anal. At. Spectrom.*, 1998, **13**, 1213.
- 79)Gwiazda, R., Woolard, D., and Smith, D., *J. Anal. At. Spectrom.*, 1998, **13**, 1233.
- 80)Fecher, P. A., Goldman, I., and Nagengast, A., *J. Anal. At. Spectrom.*, 1998, **13**, 977.
- 81)Menegario, A. A., Gine, M. F., Bendassolli, J. A., Bellato, A. C. S., and Trivelin, P. C. O., *J. Anal. At. Spectrom.*, 1998, **13**, 1065.
- 82)Woller, A., Garraud, H., Boisson, J., Dorthe, A. M., Fodor, P., and Donard, O. F. X., *J. Anal. At. Spectrom.*, 1998, **13**, 141.
- 83)Klueppel, D., Jakubowski, N., Messerschmidt, J., Stuewer, D., and Klockow, D., *J. Anal. At. Spectrom.*, 1998, **13**, 255.
- 84)Townsend, A. T., and Edwards, R., *J. Anal. At. Spectrom.*, 1998, **13**, 463.
- 85)Karunasagar, D., Arunachalam, J., and Gangadharan, S., *J. Anal. At. Spectrom.*, 1998, **13**, 679.
- 86)Yang, L., Lam, J. W. H., Sturgeon, R. E., and McLaren, J. W., *J. Anal. At. Spectrom.*, 1998, **13**, 1245.
- 87)Sturup, S., Dahlgaard, H., and Nielsen, S. C., *J. Anal. At. Spectrom.*, 1998, **13**, 1321.
- 88)Watling, R. J., *J. Anal. At. Spectrom.*, 1998, **13**, 927.
- 89)Shibuya, E. K., Sarkis, J. E., Enzweiler, J., Jorge, A. P. S., and Figueiredo, A. M. G., *J. Anal. At. Spectrom.*, 1998, **13**, 941.

- 90) Gunther, D., Audetat, A., Frischknecht, R., and Heinrich, C. A., *J. Anal. At. Spectrom.*, 1998, **13**, 263.
- 91) Norman, M. D., Griffin, W. L., Pearson, N. J., Garcia, M. O., and O'Reilly, S. Y., *J. Anal. At. Spectrom.*, 1998, **13**, 477.
- 92) Townsend, A. T., Yu, Z., McGoldrick, P., and Hutton, J. A., *J. Anal. At. Spectrom.*, 1998, **13**, 809.
- 93) Barefoot, R. R., *J. Anal. At. Spectrom.*, 1998, **13**, 1077.
- 94) Eroglu, A. E., McLeod, C. W., Leonard, K. S., and McCubbin, D., *J. Anal. At. Spectrom.*, 1998, **13**, 875.
- 95) Barrero Moreno, J. M., Betti, M., and Garcia Alonso, J. I., *J. Anal. At. Spectrom.*, 1997, **12**, 355.
- 96) Richter, R. C., Koirtiyohann, S. R., and Jurisson, S. S., *J. Anal. At. Spectrom.*, 1997, **12**, 557.
- 97) Pilon, F., Lorthioir, S., Birolleau, J. C., and Lafontan, S., *J. Anal. At. Spectrom.*, 1996, **11**, 759.
- 98) Magnuson, M. L., Creed, J. T., and Brockhoff, C. A., *J. Anal. At. Spectrom.*, 1997, **12**, 689.
- 99) Montes Bayon, M., Garcia Alonso, I., and Sanz Medel, A., *J. Anal. At. Spectrom.*, 1998, **13**, 1027.
- 100) Tao, H., Murakami, T., Tominaga, M., and Miyazaki, A., *J. Anal. At. Spectrom.*, 1998, **13**, 1085.
- 101) Coedo, A. G., Dorado, M. T., Padilla, I., and Alguacil, F. J., *J. Anal. At. Spectrom.*, 1998, **13**, 1193.
- 102) Becker, J. S., Soman, R. S., Becker, T., Panday, V. K., and Dietze, H. J., *J. Anal. At. Spectrom.*, 1998, **13**, 983.

- 103) Nonose, N., and Kubota, M., *J. Anal. At. Spectrom.*, 1998, **13**, 151.
- 104) Wildner, H., *J. Anal. At. Spectrom.*, 1998, **13**, 573.
- 105) Mierzwa, J., and Yang, M. H., *J. Anal. At. Spectrom.*, 1998, **13**, 667.
- 106) Atatsuka, K., Suzuki, T., Nobuyama, N., Hoshi, S., Haraguchi, K., Nakagawa, K., Ogata, T., and Kato, T., *J. Anal. At. Spectrom.*, 1998, **13**, 271.
- 107) Kumagai, H., Yamanaka, M., Sakai, T., Yokoyama, T., Suzuki, T. M., and Suzuki, T., *J. Anal. At. Spectrom.*, 1998, **13**, 579.
- 108) Waggoner, J. W., Belkin, M., Sutton, K. L., Caruso, J. A., and Fannin, H. B., *J. Anal. At. Spectrom.*, 1998, **13**, 879.
- 109) Cocherie, A., Negrel, P., Roy, S., and Guerrot, C., *J. Anal. At. Spectrom.*, 1998, **13**, 1069.
- 110) Vanhaecke, F., Moens, L., and Dams, R., *J. Anal. At. Spectrom.*, 1998, **13**, 1189.
- 111) Rosland, E., and Lund, W., *J. Anal. At. Spectrom.*, 1998, **13**, 1239.
- 112) Balaram, V., *Atomic Spectroscopy*, 1993, **14**, 174.
- 113) Gregoire, D. C., *J. Anal. At. Spectrom.*, 1990, **5**, 623.
- 114) Haraldsson, C., Lyven, B., Pollak, M., and Skoog, A., *Anal. Chim. Acta*, 1993, **284**, 327.
- 115) Bersier, P. M., Howell, J., and Bruntlett, C., *Analyst*, 1994, **119**, 219.
- 116) Bayon, M. M., Garcia Alonso, J. I., and Sanz Medel, A., *J. Anal. At. Spectrom.*, 1998, **13**, 277.
- 117) Ornemark, U., Taylor, P. D., and De Bievre, P., *J. Anal. At. Spectrom.*, 1997, **12**, 567.
- 118) Held, A., Taylor, P., Inglebrecht, C., De Bievre, P., Brockaert, S., Van Straaten, M., and Gijbels, R., *J. Anal. At. Spectrom.*, 1995, **10**, 849.
- 119) Furuta, N., *Anal. Sci.*, 1991, **7**, 823.

- 120) Vanhaecke, F., Goossens, J., Dams, R., and Vandecasteele, C., *Talanta*, 1993, **40**, 975.
- 121) Evans, E. H., and Giglio, J. J., *J. Anal. At. Spectrom.*, 1993, **8**, 1.
- 122) Park, C. J., Cho, K. H., Suh, J.K., and Han, M. S., *J. Anal. At. Spectrom.*, 2000, **15**, 567.
- 123) Vanhoe, H., Goossens, J., Moens, L., and Dams, R., *J. Anal. At. Spectrom.*, 1994, **9**, 177.
- 124) Date, A. R., Cheung, Y. Y., and Stuart, M. E., *Spectrochim. Acta*, 1987, **42B**, 3.
- 125) Longerich, H. P., Fryer, B. J., Strong, D. F., and Kantipuly, C. J., *Spectrochim. Acta*, 1987, **42B**, 75.
- 126) Shao, Y., and Horlick, G., *Appl. Spectrosc.*, 1991, **45**, 143.
- 127) Wilson, D. A., Vickers, G. H., and Hieftje, G. M., *J. Anal. At. Spectrom.*, 1987, **2**, 365.
- 128) Van Heuzen, A. A., and Nibbering, N. M. M., *Spectrochim. Acta*, 1993, **48B**, 1013.
- 129) Tan, S. H., and Horlick, G., *Appl. Spectrosc.*, 1986, **40**, 445.
- 130) Vaughan, M. A., and Horlick, G., *Appl. Spectrosc.*, 1986, **40**, 434.
- 131) Munro, S., Ebdon, L., and McWeeny, D. J., *J. Anal. At. Spectrom.*, 1986, **1**, 211.
- 132) Houk, R.S., *Anal. Chem.*, 1986, **58**, 97A.
- 133) May, T. W., and Wiedmeyer, R. H., *At. Spectrosc.*, 1998, **19**, 150.
- 134) Gray, A. L., and Williams, J. G., *J. Anal. At. Spectrom.*, 1987, **2**, 599.
- 135) Longerich, H. P., Strong, D. F., and Kantipuly, C. J., *Can. J. Spectrosc.*, 1986, **31**, 111.
- 136) Vaughan, M. A., Horlick, G., and Tan, S. H., *J. Anal. At. Spectrom.*, 1987, **2**, 765.
- 137) Horlick, G., Tan, S. H., Vaughan, M. A., and Rose, C. A., *Spectrochim. Acta*, 1985, **40B**, 1555.

- 138) Evans, E. H., and Ebdon, L., *J. Anal. At. Spectrom.*, 1991, **6**, 421.
- 139) Zhu, G., and Browner, R. F., *Appl. Spectrosc.*, 1987, **41**, 349.
- 140) Kawaguchi, H., Tanaka, T., and Mizuike, A., *Spectrochim. Acta*, 1988, **43B**, 955.
- 141) Gray, A. L., *Spectrochim. Acta*, 1986, **41B**, 151.
- 142) Nonose, N. S., Matsuda, N., Fudagawa, N., and Kubota, M., *Spectrochim. Acta*, 1994, **49B**, 995.
- 143) Lepla, K., Vaughan, M. A., and Horlick, G., *Spectrochim. Acta*, 1991, **46B**, 967.
- 144) Kubota, M., Fudagawa, N., and Kawase, A., *Anal. Sci.*, 1989, **5**, 701.
- 145) Vanhaecke, F., Dams, R., and Vandecasteele, C., *J. Anal. At. Spectrom.*, 1993, **8**, 433.
- 146) Uchida, H., and Ito, T., *J. Anal. At. Spectrom.*, 1994, **9**, 1001.
- 147) Vickers, G. H., Wilson, D. A., and Hieftje, G. M., *J. Anal. At. Spectrom.*, 1989, **4**, 749.
- 148) Hutton, R. C., and Eaton, A. N., *J. Anal. At. Spectrom.*, 1987, **2**, 595.
- 149) Amad, M. H., and Houk, R. S., *J. Anal. At. Spectrom.*, 1998, **13**, 223.
- 150) Ross, B. S., Yang, B., Chambers, D. M., and Hieftje, G. M., *Spectrochim. Acta*, 1991, **46B**, 1667.
- 151) Gray, A. L., *J. Anal. At. Spectrom.*, 1986, **1**, 247.
- 152) Sakata, K., and Kawabata, K., *Spectrochim. Acta*, 1994, **49B**, 1027.
- 153) Ketterer, M. E., Reschl, J. J., and Peters, M. J., *Anal. Chem.*, 1989, **61**, 2031.
- 154) Van Veen, E. H., Bosch, S., and De Loos - Vollebregt, M. T. C., *Spectrochim. Acta*, 1994, **49B**, 1347.
- 155) Casetta, B., *At. Spectrosc.*, 1990, **11**, 102.
- 156) Selby, M., *At. Spectrosc.*, 1994, **15**, 27.

- 157)Zhu, W., DeLeer, E. W. B., Kennedy, M., Kelderman, P., and Alaerts, G. J. F. R., *J. Anal. At. Spectrom.*, 1997, **12**, 661.
- 158)Evans, E. H., and Ebdon, L., *J. Anal. At. Spectrom.*, 1990, **5**, 425.
- 159)Browner, R. F., and Zhu, G., *J. Anal. At. Spectrom.*, 1987, **2**, 543.
- 160)McLaren, J. W., Lam, J. W., and Gustavsson, A., *Spectrochim. Acta*, 1990, **45B**, 1091.
- 161)Tao, H., and Miyazaki, A., *J. Anal. At. Spectrom.*, 1995, **10**, 1.
- 162)Louie, H., and Yoke-Peng Soo, S., *J. Anal. At. Spectrom.*, 1992, **7**, 557.
- 163)Weir, D. G. J., and Blades, M. W., *Spectrochim. Acta*, 1990, **45B**, 615.
- 164)Minnich, M. G., and Houk, R. S., *J. Anal. At. Spectrom.*, 1998, **13**, 167.
- 165)Minnich, M. G., Woodin, M. A., Christiani, D. C., and Houk, R. S., *J. Anal. At. Spectrom.*, 1997, **12**, 1345.
- 166)Fitzgerald, N., Tyson, J. F., and Leighty, D. A., *J. Anal. At. Spectrom.*, 1998, **13**, 13.
- 167)Shabani, M. B., Sahoo, S. K., and Masuda, A., *Analyst*, 1992, **117**, 1477.
- 168)Batterham, G. J., Munksgaard, N. C., and Parry, D. L., *J. Anal. At. Spectrom.*, 1997, **12**, 1277.
- 169)Katoh, T., Akiyama, M., Ohtsuka, H., Nakamura, S., Haraguchi, K., and Akatsuka, K., *J. Anal. At. Spectrom.*, 1996, **11**, 69.
- 170)Vircavs, M., Pelne, A., Rone, V., and Vircava, D., *Analyst*, 1992, **117**, 1013.
- 171)Ebdon, L., Fisher, A. S., Hill, S. J., and Worsfold, P. J., *J. Automatic Chem.*, 1991, **13**, 281.
- 172)Ebdon, L., Fisher, A. S., and Worsfold, P. J., *J. Anal. At. Spectrom.*, 1994, **9**, 611.
- 173)Goossens, J., Moens, L., and Dams, R., *J. Anal. At. Spectrom.*, 1993, **8**, 921.

- 174)Seubert, A., Petzold, G., and McLaren, J. W., *J. Anal. At. Spectrom.*, 1995, **10**, 371.
- 175)Bloxham, M. J., Hill, S. J., and Worsfold, P. J., *J. Anal. At. Spectrom.*, 1994, **9**, 935.
- 176)Shabani, M. B., Akagi, T., and Masuda, A., *Anal. Chem.*, 1992, **64**, 737.
- 177)Greenway, G. M., Nelms, S. M., and Koller, D., *Anal. Comm.*, 1996, **33**, 57.
- 178)Beauchemin, D., and Berman, S. S., *Anal. Chem.*, 1989, **61**, 1857.
- 179)Akatsuka, K., McLaren, J. W., Lam, J. W., and Berman, S. S., *J. Anal. At. Spectrom.*, 1992, **7**, 889.
- 180)Shabani, M. B., and Masuda, A., *Anal. Chim. Acta*, 1992, **261**, 315.
- 181)Miyazaki, A., and Reimer, R. A., *J. Anal. At. Spectrom.*, 1993, **8**, 449.
- 182)Heithmar, E. M., Hinners, T. A., Rowan, J. T., and Riviello, J. M., *Anal. Chem.*, 1990, **62**, 857.
- 183)Plantz, M. R., Fritz, J. S., Smith, F. G., and Houk, R. S., *Anal. Chem.*, 1989, **61**, 149.
- 184)Taylor, D. B., Kingston, H. M., Nogay, D. J., Koller, D., and Hutton, R., *J. Anal. At. Spectrom.*, 1996, **11**, 187.
- 185)Ebdon, L., Fisher, A., Handley, H., and Jones, P., *J. Anal. At. Spectrom.*, 1993, **8**, 979.
- 186)Stroh, A., Vollkopf, U., and Denoyer, E. R., *J. Anal. At. Spectrom.*, 1992, **7**, 1201.
- 187)Sheppard, B. S., Shen, W. L., Caruso, J. A., Heitkemper, D. T., and Fricke, F. L., *J. Anal. At. Spectrom.*, 1990, **5**, 431.
- 188)Kumar, U. T., Vela, N. P., Dorsey, J. G., and Caruso, J. A., *J. Chromatog. A*, 1993, **665**, 340.
- 189)Lu, P. L., Huang, K. S., and Jiang, S. J., *Anal. Chim. Acta*, 1993, **284**, 181.

- 190)Hall, G. E. M., and Pelchat, J. C., *J. Anal. At. Spectrom.*, 1993, **8**, 1059.
- 191)Gomez, M. M., and McLeod, C. W., *J. Anal. At. Spectrom.*, 1995, **10**, 89.
- 192)Beauchemin, D., McLaren, J. W., Mykytiuk, A. P., and Berman, S. S., *Anal. Chem.*, 1987, **59**, 778.
- 193)Yang, H. J., Huang, K. S., Jiang, S. J., Wu, C. C., and Chou, C. H., *Anal. Chim. Acta*, 1993, **282**, 437.
- 194)Rattray, R., Minoso, J., and Salin, E. D., *J. Anal. At. Spectrom.*, 1993, **8**, 1033.
- 195)Chapple, G., and Byrne, J. P., *J. Anal. At. Spectrom.*, 1996, **11**, 549.
- 196)Yu, L., Koirtyohann, S. R., Rueppel, M. L., Skipor, A. K., and Jacobs, J. J., *J. Anal. At. Spectrom.*, 1997, **12**, 69.
- 197)Alvarado, J. S., and Erickson, M. D., *J. Anal. At. Spectrom.*, 1996, **11**, 923.
- 198)Naka, H., and Gregoire, D. C., *J. Anal. At. Spectrom.*, 1996, **11**, 359.
- 199)Watling, R. J., Lynch, B. F., and Herring, D., *J. Anal. At. Spectrom.*, 1997, **12**, 195.
- 200)Gunther, D., Frischknect, R., Heinrich, C. A., and Kahlert, H. J., *J. Anal. At. Spectrom.*, 1997, **12**, 939.
- 201)Leloup, C., Marty, P., Dall'ava, D., and Perdereau, M., *J. Anal. At. Spectrom.*, 1997, **12**, 945.
- 202)Westheide, J., Becker, J. S., Jager, R., Dietze, H. J., and Broekaert, J. A. C., *J. Anal. At. Spectrom.*, 1996, **11**, 661.
- 203)Stroh, A., and Vollkopf, U., *J. Anal. At. Spectrom.*, 1993, **8**, 35.
- 204)Hwang, C. J., and Jiang, S. J., *Anal. Chim. Acta*, 1994, **289**, 205.
- 205)Huang, M. F., Jiang, S. J., and Hwang, C. J., *J. Anal. At. Spectrom.*, 1995, **10**, 31.
- 206)Branch, S., Corns, W. T., Ebdon, L., Hill, S., and O'Neill, P., *J. Anal. At. Spectrom.*, 1991, **6**, 155.

- 207) Quijano, M. A., Gutierrez, M. A., Perez Conde, M. C., and Camara, C., *J. Anal. At. Spectrom.*, 1995, **10**, 871.
- 208) Tao, H., Lam, J. W. H., and McLaren, J. W., *J. Anal. At. Spectrom.*, 1993, **8**, 1067.
- 209) Haygarth, P. M., Rowland, A. P., Sturup, S., and Jones, K. C., *Analyst*, 1993, **118**, 1303.
- 210) Winefordner, J. D., Wagner, E. P., and Smith, B. W., *J. Anal. At. Spectrom.*, 1996, **11**, 689.
- 211) Evans, E. H., Giglio, J. J., Castellano, T. M., and Caruso, J. A., *Inductively Coupled and Microwave Induced Plasma Sources For Mass Spectrometry*, The Royal Society of Chemistry, Cambridge, 1995.
- 212) O'Connor, G., Ebdon, L., Evans, E. H., Ding, H., Olson, L. K., and Caruso, J. A., *J. Anal. At. Spectrom.*, 1996, **11**, 1151.
- 213) O'Connor, G., Ebdon, L., and Evans, E. H., *J. Anal. At. Spectrom.*, 1997, **12**, 1263.
- 214) Yan, X., Huang, B., Tanaka, T., and Kawaguchi, H., *J. Anal. At. Spectrom.*, 1997, **12**, 697.
- 215) Castellano, T. M., Giglio, J. J., Evans, E. H., and Caruso, J. A., *J. Anal. At. Spectrom.*, 1997, **12**, 383.
- 216) Montaser, A., Ishi, I., Palmer, B. A., and Layman, L. R., *Spectrochim. Acta*, 1990, **45B**, 603.
- 217) Van Der Velde-Koerts, T., and De Boer, J. L. M., *J. Anal. At. Spectrom.*, 1994, **9**, 1093.
- 218) Beauchemin, D., and Craig, J. M., *Spectrochim. Acta*, 1991, **46B**, 603.
- 219) Craig, J. M., and Beauchemin, D., *J. Anal. At. Spectrom.*, 1992, **7**, 937.
- 220) Lam, J. W., and McLaren, J. W., *J. Anal. At. Spectrom.*, 1990, **5**, 419.
- 221) Hill, S. J., Ford, M. J., and Ebdon, L., *J. Anal. At. Spectrom.*, 1992, **7**, 719.

- 222) Bloxham, M. J., Worsfold, P. J., and Hill, S. J., *Anal. Proc.*, 1994, **31**, 95.
- 223) Laborda, F., Baxter, M. J., Crews, H. M., and Dennis, J., *J. Anal. At. Spectrom.*, 1994, **9**, 727.
- 224) Ford, M. J., Ebdon, L., Hutton, R. C., and Hill, S. J., *Anal. Chim. Acta*, 1994, **285**, 23.
- 225) Lam, J. W. H., and Horlick, G., *Spectrochim. Acta*, 1990, **45B**, 1313.
- 226) Wang, J., Evans, E. H., and Caruso, J. A., *J. Anal. At. Spectrom.*, 1992, **7**, 929.
- 227) Raeymaekers, B., Brockaert, J. A. C., and Leis, F., *Spectrochim. Acta*, 1988, **43B**, 941.
- 228) Evans, E. H., and Ebdon, L., *J. Anal. At. Spectrom.*, 1989, **4**, 299.
- 229) Sheppard, B. S., Shen, W., Davidson, T. M., and Caruso, J. A., *J. Anal. At. Spectrom.*, 1990, **5**, 697.
- 230) Miller, G. P., *Spectrochim. Acta*, 1989, **44B**, 395.
- 231) Smith, F. G., Wiederin, D. R., and Houk, R. S., *Anal. Chem.*, 1991, **63**, 1458.
- 232) Murillo, M., and Mermet, J. M., *Spectrochim. Acta*, 1989, **44B**, 359.
- 233) Hill, S. J., Ford, M. J., and Ebdon, L., *J. Anal. At. Spectrom.*, 1992, **7**, 1157.
- 234) Alder, J. J., and Mermet, J. M., *Spectrochim. Acta*, 1973, **28B**, 421.
- 235) Ebdon, L., Ford, M. J., Hutton, R. C., and Hill, S. J., *Appl. Spectrosc.*, 1994, **48**, 507.
- 236) Platzner, I., Sala, J. V., Mousty, F., Trincherini, P. R., and Poletini, A. L., *J. Anal. At. Spectrom.*, 1994, **9**, 719.
- 237) Branch, S., Ebdon, L., Ford, M. J., Foulkes, M. E., and O'Neill, P., *J. Anal. At. Spectrom.*, 1991, **6**, 151.
- 238) Ebdon, L., Ford, M. J., Goodall, P. S., and Hill, S. J., *Microchem. J.*, 1993, **48**, 246.
- 239) Beauchemin, D., *Analyst*, 1993, **118**, 815.

- 240)Allain, P., Jaunault, L., Mauras, Y., Mermet, J. M., and Delaporte, T., *Anal. Chem.*, 1991, **63**, 1497.
- 241)Marriott, P., Fletcher, R., Cole, A., Beaumont, I., Lofthouse, J., Bloomfield, S., and Miller, P., *J. Anal. At. Spectrom.*, 1998, **13**, 1021.
- 242)Moens, L., Vanhaecke, F., Riondato, J., and Dams, R., *J. Anal. At. Spectrom.*, 1995, **10**, 569.
- 243)Reed, N. M., Cairns, R. O., Hutton, R. C., and Takaku, Y., *J. Anal. At. Spectrom.*, 1994, **9**, 881.
- 244)Yamasaki, S. I., Tsumura, A., and Takaku, Y., *Microchem. J.*, 1994, **49**, 305.
- 245)Tittes, W., Jakubowski, N., Stuver, D., Tolg, G., and Broekaert, J. A. C., *J. Anal. At. Spectrom.*, 1994, **9**, 1015.
- 246)Becker, J. S., and Dietze, H. J., *J. Anal. At. Spectrom.*, 1997, **12**, 881.
- 247)Fisher, A. S., and Ebdon, L., in "Advances In Atomic Spectroscopy", Vol. 3, JAI Press Inc., 1997, p13.
- 248)Hewlett Packard HP4500 ICP - MS Applications Handbook, 1996.
- 249)Niu, H., and Houk, R. S., *Spectrochim. Acta*, 1996, **51B**, 779.
- 250)Douglas, D. J., and French, J. B., *Spectrochim. Acta*, 1986, **41B**, 197.
- 251)Douglas, D. J., and Tanner, S. D., in Montaser, M., ICP-MS, 1998, Wiley-VCH, p623-626.
- 252)Du, Z., and Houk, R. S., *J. Anal. At. Spectrom.*, 2000, **15**, 383.
- 253)Eiden, G. C., Baringa, C. J., and Koppenaar, D. W., *J. Anal. At. Spectrom.*, 1999, **14**, 1129.
- 254)Douglas, D. J., and French, J. B., *Am. Soc. Mass Spectrom.*, 1992, **3**, 398.
- 255)Douglas, D. J., *Can. J. Spectrosc.*, 1989, **34**, 38.
- 256)Rowan, J. T., and Houk, R. S., *Appl. Spectrosc.*, 1989, **43**, 976.

- 257)Turner, P., Merren, T., Speakman, J., and Haines, C., *Plasma Source Mass Spectrometry, Developments and Applications*, The Royal Society of Chemistry, Cambridge, UK, 1997, p.28.
- 258)Vollkopf, U., Klemm, K., and Pfluger, M., *At. Spectrosc.*, 1999, **20**, 53.
- 259)Bollinger, D. S., and Schleisman, A. J., *At. Spectrosc.*, 1999, **20**, 60.
- 260)Neubauer, K., and Vollkopf, U., *At. Spectrosc.*, 1999, **20**, 64.
- 261)Bandura, D. R., and Tanner, S. D., *At. Spectrosc.*, 1999, **20**, 69.
- 262)Duckworth, D. C., and Barshick, C. M., *Anal. Chem.*, 1998, **70**, 709A.
- 263)Baringa, C. J., and Koppenaal, D. W., *Rapid Commun. Mass Spectrom.*, 1994, **8**, 71.
- 264)Eiden, G. C., Baringa, C. J., and Koppenaal, D. W., *J. Anal. At. Spectrom.*, 1996, **11**, 317.
- 265)Tanner, S. D., and Baranov, V. I., *At. Spectrosc.*, 1999, **20**, 45.
- 266)Baranov, V. I., and Tanner, S. D., *J. Anal. At. Spectrom.*, 1999, **14**, 1133.
- 267)Marichy, M., Mermet, M., and Mermet, J. M., *Spectrochim. Acta*, 1990, **45B**, 1195.
- 268)Brenner, I. B., Segal, I., Mermet, M., and Mermet, J. M., *Spectrochim. Acta*, 1995, **50B**, 333.
- 269)Brenner, I. B., Mermet, J. M., Segal, I., and Long, G. L., *Spectrochim. Acta*, 1995, **50B**, 323.
- 270)Blades, M. W., and Caughlin, B. L., *Spectrochim. Acta*, 1985, **40B**, 579.
- 271)Kreuning, G., and Maessen, F. J. M. J., *Spectrochim. Acta*, 1989, **44B**, 367.
- 272)Hu, K., and Houk, R. S., *J. Am. Soc. Mass Spectrom.*, 1993, **4**, 28.
- 273)Hieftje, G. M., *Spectrochim. Acta*, 1992, **47B**, 3.
- 274)Wang, J., Shen, W. L., Sheppard, B. S., Evans, E. H., Caruso, J. A., and Fricke, F. L., *J. Anal. At. Spectrom.*, 1990, **5**, 445.

- 275)Beauchemin, D., McLaren, J. W., and Berman, S. S., *Spectrochim. Acta*, 1987, **42B**, 467.
- 276)Goossens, J., Vanhaecke, F., Moens, L., and Dams, R., *Anal. Chim. Acta*, 1993, **280**, 137.
- 277)Rodushkin, I., Ruth, T., and Klockare, D., *J. Anal. At. Spectrom.*, 1998, **13**, 159.
- 278)Evans, E. H., and Caruso, J. A., *Spectrochim. Acta*, 1992, **47B**, 1001.
- 279)Gregoire, D. C., *Appl. Spectrosc.*, 1987, **41**, 897.
- 280)Ross, B. S., and Hieftje, G. M., *Spectrochim. Acta*, 1991, **46B**, 1263.
- 281)Tan, S. H., and Horlick, G., *J. Anal. At. Spectrom.*, 1987, **2**, 745.
- 282)Pretty, J. R., Evans, E. H., Blubaugh, E. A., Shen, W. L., Caruso, J. A., and Davidson, T. M., *J. Anal. At. Spectrom.*, 1990, **5**, 437.
- 283)Beauchemin, D., *Anal. Chem.*, 1995, **67**, 1553.
- 284)Hasegawa, T., Umemoto, M., Haraguchi, H., Hsieh, C., and Montaser, A., in "Inductively Coupled Plasmas in Analytical Atomic Spectrometry", Montaser, A., and Golightly, D. W., (eds), UCH Publishers, New York, 1992, chpt 8.
- 285)Blades, M. W., in "Inductively Coupled Plasma - Emission Spectroscopy, Pt II: Applications and Fundamentals", Boumans, P. W. J. M., (ed), Wiley, New York, 1987, chpt 11.
- 286)Blades, M. W., and Weir, D. G., *Spectroscopy*, 1994, **9**, 14.
- 287)Kalnicky, D. J., Kniseley, R. N., and Fassel, V. A., *Spectrochim. Acta*, 1975, **30B**, 511.
- 288)Mermet, J. M., in "Inductively Coupled Plasma - Emission Spectroscopy, Pt II: Applications and Fundamentals", Boumans, P. W. J. M., (ed), Wiley, New York, 1987, chpt 10.
- 289)Cabannes, F., and Chapelle, J., in "Reactions Under Plasma Conditions", Venugopalan, M., (ed), Wiley, New York, 1971, chpt. 7.

- 290)Fannin, H. B., Seliskar, C. J., and Miller, D. C., *Appl. Spectrosc.*, 1987, **41**, 621.
- 291)Becker, J. S., Seifert, G., Saprykin, A. I., and Dietze, H. J., *J. Anal. At. Spectrom.*, 1996, **11**, 643.
- 292)Houk, R. S., Schoer, J. K., and Crain, J. S., *J. Anal. At. Spectrom.*, 1987, **2**, 283.
- 293)Olivares, J. A., and Houk, R. S., *Anal. Chem.*, 1985, **57**, 2674.
- 294)Douglas, D. J., and French, J. B., *J. Anal. At. Spectrom.*, 1988, **3**, 743.
- 295)Gray, A. L., Houk, R. S., and Williams, J. G., *J. Anal. At. Spectrom.*, 1987, **2**, 13.
- 296)Olivares, J. A., and Houk, R. S., *Appl. Spectrosc.*, 1985, **39**, 1070.
- 297)Lim, H. B., and Houk, R. S., *Spectrochim. Acta*, 1990, **45B**, 453.
- 298)Jakubowski, N., Raeymaekers, B. J., Broekaert, J. A. C., and Steuwer, D., *Spectrochim. Acta*, 1989, **44B**, 219.
- 299)Jiang, S. J., Houk, R. S., and Stevens, M. A., *Anal. Chem.*, 1988, **60**, 1217.
- 300)Duersch, B. S., Patterson, J. E., and Farnsworth, P. B., *J. Anal. At. Spectrom.*, 1999, **14**, 615.
- 301)Tanaka, T., Yonemura, K., Tanabe, M., and Kawaguchi, H., *Anal. Sci.*, 1991, **7**, 537.
- 302)Park, C. J., and Noh, S. M., *J. Anal. At. Spectrom.*, 1998, **13**, 719.
- 303)Hieftje, G. M., and Norman, L. A., *Int. J. Mass Spectrom. Ion Proc.*, 1992, **118/119**, 519.
- 304)Furuta, N., *Spectrochim. Acta*, 1985, **40B**, 1013.
- 305)Furuta, N., *Spectrochim. Acta*, 1986, **41B**, 1115.
- 306)Zhu, G., and Browner, R. F., *J. Anal. At. Spectrom.*, 1988, **3**, 781.
- 307)Olesik, J. W., and Den, S. J., *Spectrochim. Acta*, 1990, **45B**, 731.
- 308)Date, A. R., and Gray, A. L., in "Applications of Inductively Coupled Plasma Mass Spectrometry", Blackie, Glasgow, 1989, p27.

- 309) Davies, J., and Snook, R. D., *J. Anal. At. Spectrom.*, 1986, **1**, 325.
- 310) Smith, T. R., and Denton, M. B., *Appl. Spectrosc.*, 1989, **43**, 1385.
- 311) Crain, J. S., Smith, F. G., and Houk, R. S., *Spectrochim. Acta*, 1990, **45B**, 249.
- 312) Houk, R. S., Montaser, A., and Fassel, V. A., *Appl. Spectrosc.*, 1983, **37**, 425.
- 313) Houk, R. S., Svec, H. J., and Fassel, V. A., *Appl. Spectrosc.*, 1981, **35**, 380.
- 314) Longerich, H. P., *J. Anal. At. Spectrom.*, 1989, **4**, 491.
- 315) Lias, S. G., Bartmess, J. E., Liebman, J. F., Holmes, J. L., and Levin, R. D., "Gas Phase Ion And Neutral Thermochemistry", *J. Phys. Chem. Ref. Data*, Vol.17, Suppl. 1, 1988.
- 316) Chase, M. W., Davies, C. A., Downey, J. R., Frurip, D. J., McDonald, R. A., and Syverud, A. N., "JANAF Thermochemical Tables", *J. Phys. Chem. Ref. Data*, Vol.14, Suppl. 1, 1985.
- 317) Huber, K. P., and Herzberg, G., "Molecular Spectra And Molecular Structure IV: Constants Of Diatomic Molecules", Van Nostrand, New York, 1979.
- 318) Suchard, S. N., "Spectroscopic Data Vol 1: Heteronuclear Diatomic Molecules", IFI / Plenum, New York, 1975.
- 319) Drawin, H. W., and Felenbok, P., "Data For Plasmas In Local Thermodynamic Equilibrium", Gauthier - Villars, Paris, 1965.
- 320) Mavrodineanu, R., and Boiteux, H., "Flame Spectroscopy", Wiley, New York, 1965.
- 321) Frenking, G., Koch, W., Cremer, D., Gauss, J., and Liebman, J. F., *J. Phys. Chem.*, 1989, **93**, 3410.
- 322) Wong, M. W., and Radom, L., *J. Phys. Chem.*, 1989, **93**, 6303.
- 323) Rosmus, P., *Theoret. Chim. Acta*, 1979, **51**, 359.
- 324) Wadt, W. R., *J. Chem. Phys.*, 1978, **68**, 402.

- 325)Clemmer, D. E., Elkind, J. L., Aristov, N., and Armentrout, P. B., *J. Chem. Phys.*, 1991, **95**, 3387.
- 326)Walch, S. P., Wagner, A. F., Dunning, T. H., and Schatz, G. C., *J. Chem. Phys.*, 1980, **72**, 2894.
- 327)Ding, A., Karlau, J., and Weise, J., *Chem. Phys.Letts.*, 1977, **45**, 92.
- 328)Fisher, E. R., Elkind, J. L., Clemmer, D. E., Georgiadis, R., Loh, S. K., Aristov, N., Sunderlin, L. S., and Armentrout, P. B., *J. Chem. Phys.*, 1990, **93**, 2676.
- 329)Sievers, M. R., Chen, Y. M., and Armentrout, P. B., *J. Chem. Phys.*, 1996, **105**, 6322.
- 330)Murad, E., and Hildenbrand, D. L., *J. Chem. Phys.*, 1980, **73**, 4005.
- 331)Johns, J. W. C., *J. Mol. Spectrosc.*, 1970, **36**, 488.
- 332)Jarvis, K. E., Gray, A. L., and Houk, R. S., *Handbook Of Inductively Coupled Plasma Mass Spectrometry*, Blackie, Glasgow, 1992, p12.
- 333)Kornblum, G. R., and De Galan, L., *Spectrochim. Acta*, 1977, **32B**, 71.
- 334)De Galan, L., Smith, R., and Winefordner, J. D., *Spectrochim. Acta*, 1968, **23B**, 521.
- 335)Atkins, P. W., *Physical Chemistry*, 4th Edition, Oxford University Press, Oxford, 1990, p8.
- 336)Hasegawa, T., and Winefordner, J. D., *Spectrochim. Acta*, 1987, **42B**, 773.
- 337)Caughlin, B. L., and Blades, M. W., *Spectrochim. Acta*, 1985, **40B**, 987.
- 338)Kalnicky, D. J., Fassel, V. A., and Knisely, R. N., *Appl. Spectrosc.*, 1977, **31**, 137.
- 339)Alder, J. F., Bombelka, R. M., and Kirkbright, G. F., *Spectrochim. Acta*, 1980, **35B**, 163.
- 340)Jarosz, J., Mermet, J. M., and Robin, J. P., *Spectrochim. Acta*, 1978, **33B**, 55.
- 341)Togashi, H., Hashizume, A., and Niwa, Y., *Spectrochim. Acta*, 1992, **47B**, 561.
- 342)Koirtyohann, S. R., Jones, J. S., and Yates, D. A., *Anal. Chem.* 1980, **52**, 1965.

- 343)Date, A. R., and Gray, A. L., in "Applications of Inductively Coupled Plasma Mass Spectrometry", Blackie, Glasgow, 1989, p12.
- 344)Gray, A. L., in "Inorganic Mass Spectrometry", Adams, F., Gýbels, R., and van Grieken, R., (eds), Wiley, New York, 1988, p263.
- 345)Weir, D. G., and Blades, M. W., *J. Anal. At. Spectrom.*, 1994, **9**, 1311.
- 346)Long, S. E., and Browner, R. F., *Spectrochim. Acta*, 1988, **43B**, 1461.
- 347)Tang, Y. Q., and Trassy, C., *Spectrochim. Acta*, 1986, **41B**, 143.
- 348)You, J., Dempster, M. A., and Marcus, R. K., *J. Anal. At. Spectrom.*, 1997, **12**, 807.
- 349)Vaughan, M. A., and Horlick, G., *Spectrochim. Acta*, 1990, **45B**, 1289.

Appendices

APPENDIX 1: TABLE OF FUNDAMENTAL DATA³¹⁵⁻³³¹

Species	Ionisation Potential (eV)	Dissociation Energy (eV)	ω_c (cm^{-1})	$\omega_c x_c$ (cm^{-1})	B_c (cm^{-1})	α_c (cm^{-1})	r (\AA)	g
Ar	15.76	/	/	/	/	/	/	1
Ar ⁺	27.62	/	/	/	/	/	/	6
ArH		3.40			10.20		1.297	
ArH ⁺		4.03	2810.7	56	10.43	0.364	1.286	
Ar ₂	14.50	0.011	25.74	14.80	0.0598	0.00375	3.758	
Ar ₂ ⁺		1.05	293		0.137		2.43	
ArC								
ArC ⁺		0.88	304	12.7	0.41	0.0147	2.059	
ArN								
ArN ⁺		1.94	515	5.0	0.45	0.0044	1.87	
ArO		3.2					3.31	
ArO ⁺		0.42	289.2		0.280		2.292	
ArCl		4.51	230					
ArCl ⁺								
H	13.60	/	/	/	/	/	/	2
H ⁺	/	/	/	/	/	/	/	1
C	11.26	/	/	/	/	/	/	9
C ⁺	24.38	/	/	/	/	/	/	6
C ₂	12.11	6.21	1854.7	13.34	1.819	0.0176	1.243	1
C ₂ ⁺		5.32	1350		1.659		1.301	
CO	14.01	11.09	2169.5	13.37	1.930	0.0175	1.128	1
CO ⁺	26.8	8.34	2214.2	15.16	1.977	0.0189	1.115	
N	14.53	/	/	/	/	/	/	4
N ⁺	29.61	/	/	/	/	/	/	9

Appendix 1 Cont'd

Species	Ionisation Potential (eV)	Dissociation Energy (eV)	ω_e (cm^{-1})	$\omega_e x_e$ (cm^{-1})	B_e (cm^{-1})	α_e (cm^{-1})	r (\AA)	g
N ₂	15.58	9.76	2358.6	14.32	1.998	0.0173	1.098	3
N ₂ ⁺	27.1	8.71	2207.0	16.10	1.932	0.0190	1.116	2
NO	9.26	6.50	1904.2	14.08	1.672	0.0171	1.151	2
NO ⁺	30.3	10.85	2376.4	16.26	1.997	0.0189	1.063	1
O	13.62	/	/	/	/	/	/	9
O ⁺	35.11	/	/	/	/	/	/	4
O ₂	12.07	5.13	1580.3	11.98	1.446	0.0159	1.208	3
O ₂ ⁺	24.2	6.66	1904.8	16.26	1.691	0.0198	1.116	4
OH	13.00	4.39	3737.8	84.88	18.91	0.724	0.969	2
OH ⁺		5.09	3113.4	78.52	16.79	0.749	1.029	3
Cl	12.97	/	/	/	/	/	/	6
Cl ⁺	23.80	/	/	/	/	/	/	9
Cl ₂	11.48	2.48	559.8	2.68	0.244	0.00149	1.988	
Cl ₂ ⁺		3.95	645.6	3.02	0.269	0.00164	1.892	
ClO	10.95	2.75	853.8	5.5	0.623	0.0058	1.569	
ClO ⁺								
Al	5.99	/	/	/	/	/	/	6
Al ⁺	18.82	/	/	/	/	/	/	1
AlO	9.46	5.27	979.2	6.97	0.641	0.0058	1.618	2
AlO ⁺		1.71	710	4	0.507	0.004	1.82	6
Ba	5.21	/	/	/	/	/	/	1
Ba ⁺	10.00	/	/	/	/	/	/	2
BaO	6.91	5.79	669.8	2.04	0.313	0.00139	1.939	1
BaO ⁺								

Appendix 1 Cont'd

Species	Ionisation Potential (eV)	Dissociation Energy (eV)	ω_e (cm^{-1})	$\omega_e x_e$ (cm^{-1})	B_e (cm^{-1})	α_e (cm^{-1})	r (\AA)	g
La	5.58	/	/	/	/	/	/	10
La ⁺	11.43	/	/	/	/	/	/	21
LaO	4.95	8.23	817.3	3.09	0.352	0.0014	1.826	2
LaO ⁺		8.88						
Mn	7.44	/	/	/	/	/	/	6
Mn ⁺	15.64	/	/	/	/	/	/	7
MnO	8.65	3.71	839.6	4.79	0.435		1.769	
MnO ⁺		2.95						
Ti	6.82	/	/	/	/	/	/	21
Ti ⁺	13.63	/	/	/	/	/	/	28
TiO	6.4	6.87	1009.0	4.49	0.535	0.00303	1.620	2
TiO ⁺		6.93						
Y	6.22	/	/	/	/	/	/	10
Y ⁺	12.4	/	/	/	/	/	/	1
YO		7.39	861.0	2.93	0.388	0.0018	1.790	2
YO ⁺		7.24						
Zr	6.84	/	/	/	/	/	/	21
Zr ⁺	13.13	/	/	/	/	/	/	28
ZrO	6.1	7.85	969.8	4.90	0.423	0.0023	1.712	1
ZrO ⁺		7.76						

/ Molecular constants not applicable to atomic species. Gaps in table represent data not available.

APPENDIX 2

CONFERENCES AND COURSES ATTENDED

- 1) Spectroscopic Techniques For In-Situ Water Monitoring. University of Plymouth, 11 July 1996.
- 2) 8th Biennial National Atomic Spectroscopy Symposium. University of East Anglia, 17-19 July 1996.
- 3) Research And Development Topics In Analytical Chemistry. Nottingham Trent University, 22-23 July 1996.
- 4) Research And Development Topics In Analytical Chemistry. University of Northumbria at Newcastle, 2-3 July 1997.
- 5) EPSRC Graduate School. University of York, 17-22 July 1997.
- 6) XXX Colloquium Spectroscopicum Internationale. Melbourne, Australia, 22-25 September 1997.
- 7) Research And Development Topics In Analytical Chemistry. University of Durham, 6-7 April 1998.
- 8) 9th Biennial National Atomic Spectroscopy Symposium. University of Bath, 8-10 July 1998.

Royal Society of Chemistry lectures and lectures by invited speakers at the University of Plymouth. Various weekly research seminars at the University of Plymouth.

APPENDIX 3
PRESENTATIONS

- 1) *Fundamental Studies Of Interferences In ICP-MS*. Poster presented at Research And Development Topics In Analytical Chemistry. Nottingham Trent University, 22-23 July 1996.

- 2) *Optical And Mass Spectrometric Studies Of Interferences In ICP-MS*. Poster presented at Research And Development Topics In Analytical Chemistry. University of Northumbria at Newcastle, 2-3 July 1997.

- 3) *Spatial Studies Of Interferences In Inductively Coupled Plasma - Mass Spectrometry*. Lecture presented at XXX Colloquium Spectroscopicum Internationale. Melbourne, Australia, 22-25 September 1997.

- 4) *Temperature Measurements Of Interferences In Inductively Coupled Plasma - Mass Spectrometry*. Poster presented at Research And Development Topics In Analytical Chemistry. University of Durham, 6-7 April 1998.

- 5) *Comparison Of Temperature Measurement Techniques In ICP-MS*. Lecture presented at 9th Biennial National Atomic Spectroscopy Symposium. University of Bath, 8-10 July 1998.

Regular lecture presentations at the University of Plymouth research seminars and at VG Elemental, Winsford, Cheshire.

APPENDIX 4
PUBLICATIONS

- 1) Rowley, L.K., Evans, E.H., and Ebdon, L., Mass Spectrometric Techniques For Temperature Determination In ICP-MS: A Review. To be submitted.

- 2) Evans, E.H., Rowley, L.K., Carter, J., and Ebdon, L., Insight Into The Formation Of Molecular Ions In ICP-MS By Studying Deviation From Equilibrium Dissociation Temperature. To be submitted.

- 3) Rowley, L.K., Evans, E.H., and Ebdon, L., Effect Of Operating Parameters And The Influence Of A Shielded Torch System On Interferences In ICP-MS. 1. Effect Of Power. To be submitted.